CARBON DIOXIDE CAPTURE FROM FUEL GAS STREAMS UNDER ELEVATED PRESSURES AND TEMPERATURES USING NOVEL PHYSICAL SOLVENTS

by

Yannick Jacques Heintz

B.S. in Chemical Engineering and Chemistry, CPE Lyon, France, 2002

Submitted to the Graduate Faculty of

the Swanson School of Engineering in partial fulfillment

of the requirements for the degree of

Doctor of Philosophy

University of Pittsburgh

2011

UNIVERSITY OF PITTSBURGH

SWANSON SCHOOL OF ENGINEERING

This dissertation was presented

by

Yannick Jacques Heintz

It was defended on

November 29, 2011

and approved by

Badie I. Morsi, PhD, Professor, Department of Chemical and Petroleum Engineering

Shiao-Hung Chiang, PhD, Professor, Department of Chemical and Petroleum Engineering

Brian M. Gleeson, PhD, Professor, Department of Mechanical Engineering and Materials Science

Kenneth L. Jones, PhD, National Energy Technology Laboratory - U.S. Department of Energy

George E. Klinzing, PhD, Professor, Department of Chemical and Petroleum Engineering

David R. Luebke, PhD, National Energy Technology Laboratory - U.S. Department of Energy

Dissertation Director: Badie I. Morsi, PhD, Professor, Department of Chemical and Petroleum Engineering

CARBON DIOXIDE CAPTURE FROM FUEL GAS STREAMS UNDER ELEVATED PRESSURES AND TEMPERATURES USING NOVEL PHYSICAL SOLVENTS

Yannick Jacques Heintz, PhD

University of Pittsburgh, 2011

The conventional processes for acid gas removal (AGR), including CO_2 in the Integrated Gasification Combined Cycle (IGCC) power generation facilities are: a chemical process, using methyl-diethanolamine (MDEA); a physical process, using chilled methanol (Rectisol) or a physical process, using mixtures of dimethylethers of polyetheleneglycol (Selexol). These conventional processes require cooling of the fuel gas streams for CO_2 capture and subsequent reheating before sending to turbines, which decreases the plant thermal efficiency and increases the overall cost. Thus, there is a pressing need for developing an economical process which can capture CO_2 from the hot fuel gas stream without significant cooling.

The overall objective of this study is to investigate the potential use of physical solvents for selective capture of CO_2 from post water-gas-shift streams under relatively elevated pressures and temperatures. In order to achieve this objective, a comprehensive literature review was conducted to define an "ideal solvent" for CO_2 capture and to identify six different physical solvents which should obey such a definition.

The first physical solvents identified were perfluorocarbons (PFCs), which are known to have low reactivity, high chemical stability and relatively low vapor pressures. Three different PFCs, known as PP10, PP11, and PP25, were selected as potential candidates for CO_2 capture. The equilibrium solubilities of CO_2 and N_2 were measured in these PFCs under different

operating conditions up to 30 bar and 500 K. These PFCs have relatively low viscosity at 500 K, very good thermal and chemical stabilities and showed high CO_2 solubilities; hence they were considered as "ideal solvents." The CO_2 solubilities in PP25 were found to be greater than in the other two PFCs. Due to its superior behavior, PP25 was selected for the development of a conceptual process for CO_2 capture form Pittsburgh No. 8 shifted fuel gas mixture using Aspen Plus simulator. Unfortunately, during the pressure-swing option for solvent regeneration, the solvent loss was significant due to the fact that the boiling point of PP25 is 533 K which is close to the absorber temperature (500 K). Also, other drawbacks of PFCs include, high cost, and absorption of other gases (light hydrocarbons) along with CO_2.

It was then decided to seek different physical solvents, which have negligible vapor pressure, in addition to the other attractive properties of the "ideal solvent" in order to use in the Aspen Plus simulator. Extensive literature search led to Ionic Liquids (ILs), which are known to have unique properties in addition to extremely low vapor pressures, and therefore they were considered excellent candidates for the CO_2 capture from fuel gas streams under elevated pressures and temperatures. Three ILs, namely TEGO IL K5, TEGO IL P9 and TEGO IL P51P, manufactured by Evonik Goldschmidt Chemical Corporation, were selected as potential solvents for CO_2 capture. The solubilities of CO_2, H_2, H_2S and N_2 were measured in the TEGO IL K5 and the solubilities of CO_2 and H_2 were measured in the TEGO IL K5 at pressures up to 30 bar and temperatures from 300 to 500 K. Also, the density and viscosity of these three ILs were measured within the same pressure and temperature ranges, and the surface tension for TEGO IL K5 and TEGO IL P51P were measured from 296 to 369 K. Due to their superior performance for CO_2 capture, the TEGO IL K5 and the TEGO IL P51P were selected to be used in the Aspen simulator for the conceptual process development. The density and surface tension data for the

TEGO IL K5 and the TEGO IL P51P were used in Aspen Plus, employing the Peng-Robinson Equation of state (P-R EOS) to obtain the critical properties of the two ILs; and the measured solubility data were also used to obtain the binary interaction parameters between the shifted gas constituents and two ILs.

The Aspen Plus simulator was employed to develop a conceptual process for CO_2 capture from a shifted fuel gas stream (102.52 kg/s) generated using Pittsburgh # 8 coal for a 400 MWe power plant. The conceptual process developed consisted mainly of 4 adiabatic absorbers (2.4 m ID) arranged in parallel and packed with Plastic Pall Rings of 0.025 m for CO_2 capture; 3 flash drums arranged in series for solvent regeneration using the pressure-swing option; and 2 pressure-intercooling systems for separating and pumping CO_2 to the sequestration sites. The compositions of all process steams, CO_2 capture efficiency, and net power were calculated using Aspen Plus for each solvent. The results indicated that, based on the composition of the inlet gas stream to the absorbers, 87.6 and 81.42 mol% of CO_2 were captured and sent to sequestration sites; and 97.69 and 97. 86 mol% of H_2 were separated and sent to turbines using the TEGO IL K5 and the TEGO IL P51P, respectively. Also, the two solvents exhibited minimum loss of 0.06 and 0.17 wt% with a net power balance of -26.44 and -14.72 MW for the TEGO IL K5 and the TEGO IL P51P, respectively. Thus, the TEGO IL K5 could be selected as a physical solvent for CO_2 capture from shifted hot fuel gas streams since large quantities of CO_2 are absorbed.

DESCRIPTORS

Absorption

Aspen Plus

CO_2 Capture

Gas-Inducing Reactor

Gas-Liquid Interfacial Area

Hydrodynamics

Ionic Liquids

Mass Transfer Coefficient

Sauter Mean Bubble Diameter

Solubility

Statistical Experimental Design

Volumetric Mass Transfer Coefficient

TABLE OF CONTENTS

LIST OF TABLES

LIST OF FIGURES

NOMENCLATURE

a	Gas-liquid interfacial area per unit liquid volume, m^{-1}
a_e	Effective area per unit volume of the column, m^{-1} [=] $m^2.m^{-3}$
a^I	Total interfacial area for mass transfer, m^2
a_p	Specific area of packing, m^{-1} [=] $m^2.m^{-3}$
A_t	Cross-sectional area of the column, m^2
bp	Boiling point, °C
C^*	Equilibrium gas solubility in the liquid, $kmol.m^{-3}$
C_G	Concentration in the gas phase, $kmol.m^{-3}$
C_L	Concentration of gas in the liquid phase, $kmol.m^{-3}$
C_L	Mass transfer coefficient parameters for liquid, characteristic of the shape and structure of the packing, -
D^0	Bond dissociation energy, $kcal.mol^{-1}$
D_{AB}	Diffusivity of the gases in solvents, $m^2.s^{-1}$
d_B	Bubble diameter, m
d_h	Hydraulic diameter, m $\quad d_h = \dfrac{4\varepsilon}{a_p}$
$D_{i,k}^L$	Diffusivity of the liquid, $m^2.s^{-1}$
d_{Imp}	Diameter of the impeller, m
d_S	Sauter mean bubble diameter, m
d_T	Diameter of the tank, m
d_W	Width of the impeller blade, m
E_0	Coefficient in Equations (7-36) and (8-1)
E_1	Coefficient in Equations (7-36) and (8-1)
EA	Electron Affinity, $kcal.mol^{-1}$

Fr_L	Froude number for the liquid, - $Fr_L = \frac{a_p (u_S^L)^2}{g}$
g	Gravitational constant, m.s^{-2}
H	Liquid height from the bottom of the reactor, m
$H_{2,1}$	Henry's law constant for solute 2 dissolved in solvent 1, Mpa
He	Henry's law constant, bar
He'	Henry's law constant, Mpa.kg.mol^{-1}
He_{∞}	Henry's law constant at infinite dilution, bar
$He_{0,\infty}$	Coefficient in Equation (8-3)
H_L	Liquid height above the impeller of the reactor, m
h_p	Height of the packed section, m
IP	Ionization Potential, kcal.mol^{-1}
$k_G a$	Volumetric gas-side mass transfer coefficient, s^{-1}
k_L	Liquid-side mass transfer coefficient, m.s^{-1}
$k_L a$	Volumetric liquid-side mass transfer coefficient, s^{-1}
$k_{i,k}^L$	Binary mass transfer coefficient for the liquid, m.s^{-1}
$K_{i,k}^L$	Liquid-phase binary overall mass transfer coefficient, kmol.s^{-1} $K_{i,k}^L = k_{i,k}^L \overline{\rho}_L a^I$
L	Molar flow rate of liquid, kmol.s^{-1}
M	Molality, mol.kg^{-1}
MW	Molecular weight, kg.kmol^{-1}
N	Mixing speed, rpm
$n^{25}{}_D$	Refractive index at 25°C, -
N_{CR}	Critical mixing speed for gas inducing, rpm
N_F	Number of factorial points
N_P	Power number, -
P	Pressure, bar
P^*	Total power input, W
P_c	Critical pressure, bar
P_S or P^s	Vapor pressure, bar
P_S	Spectral Polarity Index

Q_{GI}	Induced gas flow rate, $m^3.s^{-1}$
Re_L	Reynolds number for the liquid, - $Re_L = \frac{\rho_L u_S^L}{a_p \mu^L}$
R_s	Mass transfer rate, $mol.m^{-3}.s^{-1}$
r_v	Van der Waals' radius, Å
T	Temperature, K
T_b	Boiling point temperature, K
T_c	Critical temperature, K
T_r	Reduced temperature, K
U_G	Superficial gas velocity, $m.s^{-1}$
u_s^L	Superficial velocity for the liquid, $m.s^{-1}$ $u_s^L = \frac{L}{\rho_L A_t}$
V_A	Molar volume of the diffusing gas at its normal boiling point, $m^3.kmol^{-1}$
V_c	Critical molar volume, $m^3.kmol^{-1}$, $cm^3.mol^{-1}$ (when specified)
v_L	Molar volume, $kmol/m^3$
V_P	Preheater volume, m^3
V_R	Reactor volume, m^3
W	Baffle width, m
We_L	Weber number for the liquid, - $We_L = \frac{\rho_L (u_S^L)^2}{a_p \sigma}$
x^*	Equilibrium gas solubility in the liquid (mole of gas per total number of mole), -
x_1	Solubility of gas 1 in solvent 2 in mole fraction, -
x_2	Solubility of solute 2 in solvent 1 in mole fraction, -
y_1	Mole fraction in the gas phase of component 1, -
y_2	Mole fraction in the gas phase of component 2, -
Z	Compressibility factor, -
Z_c	Critical compressibility factor, -

Greek symbols:

α_v	Atom polarizability, Å^3
β	Compressibility, atm^{-1}
δ_{ij}	Peng-Robinson binary interaction parameter, -
δ'	Solubility parameter, MPa$^{1/2}$
Δ	Film thickness, m
ΔE	Apparent activation energy of absorption, kJ.kmol^{-1}
ΔH^0	Standard heat of solution of a gas, kJ.kmol^{-1}
ΔH_v	Heat of vaporization, kcal.mol^{-1}
ΔP_c	Contribution to the critical pressure in the Modified Lydersen-Joback-Reid method, bar
ΔT_b	Contribution to the normal boiling temperature in the Modified Lydersen-Joback-Reid method, K
ΔT_c	Contribution to the critical temperature in the Modified Lydersen-Joback-Reid method, K
ΔV_c	Contribution to the critical volume in the Modified Lydersen-Joback-Reid method, cm^3.mol^{-1}
ε	Void fraction of the packing, -
ε_1	Dielectric constant, -
ε_G	Gas holdup, %
η	Viscosity, Pa.s or cP (when specified)
μ_L	Liquid viscosity, Pa.s
ψ	Associate factor in Equation (6-8)
ρ_L	Liquid density, kg.m^{-3} or g.cm^{-3} (when specified)
$\bar{\rho}_L$	Molar density of liquid, kmol.m^{-3}
σ_L	Liquid surface tension, N.m^{-1} or dyn.cm^{-1} (when specified)
χ_p	Electronegativity Pauling, -
ω	Acentric factor, -

Subscript:

C	Critical condition
CR	Critical
F	Final
G	Gas phase
i	Component i
L	Liquid phase
m	Mean
1	Component 1: Gas
2	Component 2: Liquid

Acronyms:

AGR	Acid Gas Removal
CCD	Charge-Coupled Device
CFC	Chlorofluorocarbons
ECF	Electrochemical Fluorination
FC-47	Perfluorotributylamine, $[F_3C\text{-}(CF_2)_3]_3N$ (3M Company)
FC-80	Perfluorinated butyltetrahydrofuran (3M Company)
GIR	Gas-Inducing Reactor
GSR	Gas Sparging Reactor
HC	Hydrocarbon
HFC	Partially perfluorinated hydrocarbon
L-1822	$C_{10}F_{18}$ (3M Company)
PCB	Polychlorinated Biphenyl
PFC	Perfluorocarbon
PTFE	Polytetrafluoroethylene
P-R EOS	Peng-Robinson Equation-of-State
SAR	Surface Aeration Reactor

PREFACE

To my grandparents, Louise and François-Xavier Schmitt

I am thankful and grateful to my parents for their help, sacrifices at any condition, and teachings. I would also like to take this opportunity to thank my brothers: Patrice and Eric, my extended family, and family friends for their continuous moral support and encouragement.

I would like to express my gratitude and appreciation to my thesis advisor Professor Badie I. Morsi for his support and valuable guidance throughout my PhD at the University of Pittsburgh. In conjunction I would also like to thank Professors Shiao-Hung Chiang, Brian Gleeson, and George Klinzing, along with Kenneth Jones, PhD and David Luebke, PhD for serving on my thesis committee. Additionally, I want to thank Professors Robert Enick and Sachin Velenkar for their mentorship.

I would like to acknowledge the following institutions for either their financial or technical support:

- US NETL-DOE Pittsburgh for financial support of my thesis,
- Evonik Goldschmidt Chemical Corporation, Charles Milburn, for providing the ionic liquids used as solvents to complete my thesis

- Chemical and Petroleum Engineering faculty and staff, especially Ron Bartlett, Bob Maniet, and
- the School of Engineering Machine Shop for prompt repairs.

Further, I am grateful for the valuable contribution, help, and constructive criticism from the previous and current members of my research group whom include Benoit Fillion, PhD, Arsam Behkish, PhD, Romain Lemoine, PhD, Jean-Philippe Soriano, Laurent Sehabiague, Mariela Sanoja, Stoyan Nedeltchev, PhD, Yeldos Rakymkul, Peiqian Yu, PhD and Manuel Götz.

Many thanks also to the friends who supported me during these years and special thanks to my former roommate and dear friend Abhishek Soni, PhD.

Finally I would like to express great gratitude to Sanna Gaspard, PhD who supported me emotionally during this endeavor for the past five years, and was on my side during the difficult and challenging times but also for the great periods.

1.0 INTRODUCTION

The goal of the 2002 Global Climate Change Initiative (GCCI) is to significantly reduce the greenhouse gas (GHG) intensity of the U.S. economy over the next 10 years while sustaining the economic growth needed to finance investment in new, clean energy technologies. The initiative calls for increased emphasis on carbon sequestration and for increased investment in research and development to provide the technical basis for optimum future decisions. By the year 2012, the DOE is expected to develop commercial CO_2 capture/sequestration systems which would capture at least 90% of emissions and result in less than 10% increase in the cost of energy services.[1,2]

Combustion- and gasification-based systems are the two main fossil fuel technologies currently being developed for power generation. In the former, pulverized coal is directly combusted to generate high-pressure steam which runs a turbine, which in turn runs a power generator with an overall thermal efficiency of about 35%. In the latter, coal and/or biomass mixed with steam and oxygen (or air) is gasified at high-pressure and temperature to produce syngas which is sent to an Integrated Gasification Combined-Cycle (IGCC) process for power generation with an overall thermal efficiency nearing 40%.[1,3]

The IGCC power generation facilities enjoy several advantages over the coal-fired power technologies, such as (1) the discharge of solid byproducts and wastewater is reduced by roughly 50%; (2) the emission of pollutant (NO_x, SO_x, CO, etc.) is lower; (3) the emission of trace hazardous air pollutants, including gaseous mercury (Hg) is low; and (4) carbon dioxide (CO_2) emission is reduced by at least 10% per equivalent net production of electricity.[1] The CO_2 emission from IGCC units, however, is by far the largest contributor to greenhouse gas when compared with that of other produced gaseous constituents, including N_2O and NH_3. Fortunately, the IGCC is remarkably suitable for near total CO_2 removal and subsequent sequestration.[1,2,4,5] This is because CO_2 can be captured more efficiently from IGCC than from pulverized coal (PC) combustion technology due to the following: (1) the fuel gas stream has higher CO_2 concentration than the flue gas stream, which can be further increased by converting more CO into CO_2 prior to combustion through the water-gas-shift (WGS) reaction, while simultaneously producing more hydrogen; and (2) the IGCC gasifiers typically operate under relatively high pressure, making CO_2 capture from the syngas much easier than that from flue gas.

The temperature and pressure of the fuel gas stream produced via gasification technologies strongly depend on the type of gasifier used.[6,7] For instance, after a 2-stage or a 3-stage WGS reactor, the shifted fuel gas temperature is expected to be about 508 K.[7] Actually, the IGCC is considered as the most promising process for power generation because of its high thermal efficiency and low emissions, and its ability to use different feedstocks.[4] For the IGCC process to become commercially viable, however, all contaminants in the syngas have to be removed before combustion, and the emission control technologies should target the removal of Hg, As, Cd, Se, SO_x, NO_x and particulates, in addition to the other contaminants present in high concentration, such as H_2S and CO_2 (acid gas). Currently, technologies for removal of acid gases from the syngas stream used in the IGCC processes fall into three categories, namely cold-, warm-, and hot-gas cleanup.[4]

In cold-gas cleanup, H_2S and CO_2 are removed from syngas by first concentrating them either with amine-based chemical solvents, such as methyldiethanolamine (MDEA), or refrigerated physical solvents, such as chilled methanol[8] (Rectisol process), mixtures of dimethyl ethers of polyethylene glycol[9,10] (Selexol process), or n-formylmorpholine/n-acetylmorpholine[11,12] (Morphysorb process).[2,4,5,13] These solvents were reported to be effective in removing nearly all of the undesirable contaminants from syngas. Table 1.1 shows a few commercially available processes employing physical solvents for AGR.

Table 1.1: Physical solvents used in commercial processes[14]

Process	Physical solvent
Purisol[8]	N-methyl-2-pyrrolidone
Estasolvan	Tributyl-phosphate
Fluor Solvent[15]	Propylene carbonate
Rectisol[8] and IFPEXOL	Methanol
Selexol[10,16], Sepasolv MPE, and Genosorb	Polyethylene glycol dialkyl ethers

Generally, these physical processes have the following similar features: (1) high selectivity for H_2S and COS over CO_2; (2) high loadings at high acid gas partial pressures; (3) strong solvent stability; and (4) low heat requirements, since most of the solvents can be regenerated by a simple pressure letdown, meaning that there is no significant heat of reaction or solution.[4,5] Also, physical-solvent processes can be easily configured to take advantage of their high H_2S/CO_2 selectivity together with high levels of CO_2 recovery. Usually, this can be accomplished by staging absorption for high H_2S removal, followed by CO_2 removal.

In general, physical methods are favored when the acid gas pressure is high. This is because the concentration gradient (or the partial pressure difference) between the acid gas and the physical (non-reactive) solvent is the driving force for AGR. On the other hand, chemical methods are more effective when the acid gas pressure or concentration in the gas stream is low. This is because the reaction rate or the chemical potential between the acid gas and the reactant (reactive solvent) is the driving force for AGR. This can be schematically illustrated in Figure 1.1 in terms of loading (mole acid gas/mole of solvent).

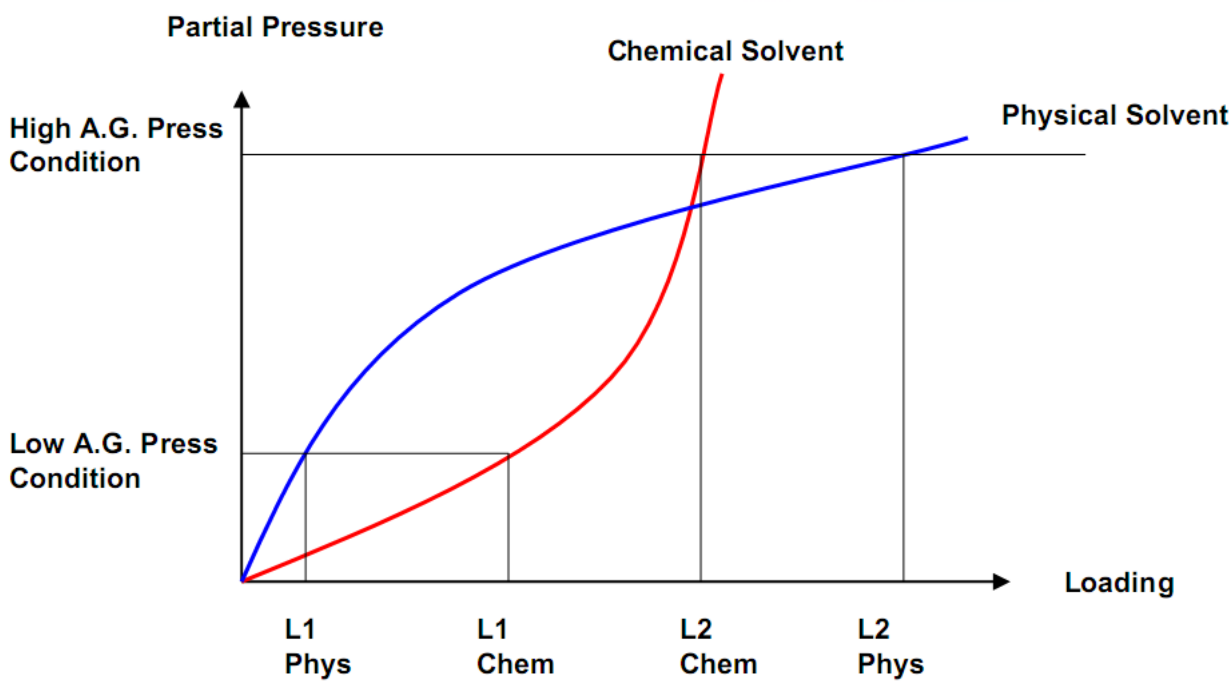

Figure 1.1: Physical versus Chemicals Solvents[17]

A comparison among chemical and physical solvent-based processes reveals the following: (1) the heat requirements for solvent regeneration in the MDEA chemical process are greater than those needed for the physical solvent-based processes; (2) the glycol process is generally more expensive than the MDEA process, however, its package, including total acid gas removal (AGR), sulfur recovery, and tail gas treatment could be more cost effective than the MDEA process, particularly when the syngas pressure is high and deep sulfur removal is required (e.g., down to 10-20 ppmv); and (3) the refrigeration and complexity of the chilled methanol process make it the most expensive AGR process, and accordingly its use is generally restricted to applications in which almost pure syngas (containing as low as <0.1 ppmv total sulfur) is required.[2] For sulfur recovery in these cold-gas cleanup technologies, often conducted using the Claus process, H_2S-rich acid gas feed is required, implying that the absorption process should be more selective towards H_2S than CO_2. On the other hand, for CO_2 sequestration, the selected absorption process should be more selective towards CO_2 than H_2S. Although these two objectives appear to be conflicting, those two gases have been successfully removed by staging the absorption process into separate steps.[2,4,5] It should be pointed out that the major drawback of the cold-gas cleanup technologies is that the entire syngas stream has to be cooled prior to H_2S and CO_2 removal to 311 K for amine-based absorption processes and to 211 or 233 K for the refrigerated physical solvent processes.[4] Unfortunately, cooling the syngas to such low temperatures leads to the condensation of most of the water vapor present in the syngas stream, which significantly reduces the overall thermal efficiency of the process and increases the capital costs of the system.

In hot-gas cleanup, carried out at temperatures approaching that of the gasifier (~1144 K), solid sorbents such as zinc ferrite are reacted with H_2S to form sulfides. The sorbents are usually regenerated by oxidation with air in a separate vessel. The oxidation converts H_2S in the syngas into a gas stream containing SO_2 which is treated separately. There are many technical difficulties associated with cleanup, including sorbent stability and the need for SO_2 removal. In addition, the cost of the hot-gas cleanup is high because the process must be carried out in high-cost alloy equipment. Also, hot-gas cleanup effectively removes H_2S, but does not significantly remove Hg and other contaminants.[4]

In warm-gas cleanup, carried out at moderate temperatures (~ 478 K), H_2S and other contaminants such as Hg, As, Se and Cd, which were not removed by hot-gas cleanup, can be effectively removed. In 2007, Vidaurri et al.[3] developed a warm-gas cleanup process where H_2S is oxidized in-situ with small amount of air (or O_2) at temperatures (383 – 493 K) in the presence of a catalyst to liquid elemental sulfur without H_2 consumption. This liquid elemental sulfur was also capable of removing low concentrations of Hg from the syngas streams. Even though some cooling of the fuel gas from the gasifier temperature is required, leading to some energy efficiency penalty, the warm-gas cleanup temperature is above the steam dew point, which prevents water vapor condensation from the syngas stream.[4] Indeed, warm-gas cleanup is obviously more attractive than cold- and hot- syngas cleanups because it allows the removal of multi-contaminants from the syngas while using low-cost alloy equipment at an energy penalty lower than that of the cold-gas cleanup.

Thus, there is a pressing need to develop warm-gas cleanup technologies in order to allow control of the emissions of sulfur, ammonia, chlorides and Hg, Se, As and Cd. The prime mover for this development stems from the fact that the syngas, at a relatively high temperature, can easily be used in the downstream power generation facilities or as a fuel for chemical production plants (e.g. Fisher-Tropsch and methanol synthesis).

The focus of this research is the use of physical solvents for CO_2 capture from warm gas streams.

2.0 BACKGROUND

2.1 SELEXOL AND RECTISOL PROCESSES FOR CO_2 CAPTURE

The two most-widely-used physical processes for AGR are Selexol and Rectisol. The Selexol process is more expensive than the MDEA process which requires high thermal energy (heat) for solvent regeneration, and the chilling option could increase the process costs. The Rectisol process is complex, and refrigeration makes it the most expensive AGR process. These processes are briefly discussed in the following. The only composition found in the open literature[10] for the solvent used in the Selexol process is given in Table 2.1; and the solvent used in the Rectisol process is methanol. The solubilities of various gases in the Selexol solvent, expressed in terms of that of methane (CH_4), are given in Table 2.2; and the absorption coefficients for various gases in the Rectisol solvent, as a function of temperature, are depicted in Figure 2.1. The physical properties of solvents used in the Selexol and Rectisol Processes are given in Table 2.3. From the table, it can be sees that at 298 K the vapor pressure of methanol is high (16678.4 Pa), whereas that of the Selexol solvent is extremely low (0.093 Pa). Also, at 298 K the viscosity of the Selexol solvent (0.0059 Pa.s) is much greater than that of methanol (0.000539 Pa.s).

Table 2.1: Composition of the Selexol process solvent[10]

$CH_3(CH_2CH_2O)_nCH_3$			
Component n	**Mol%**	**Molecular Weight**	
		kg.kmol^{-1}	*kg.kmol^{-1}*
3	10.69	178.2	19.05
4	26.94	222.3	59.88
5	26.57	266.3	70.77
6	18.42	310.4	57.17
7	10.75	354.4	38.10
8	4.78	398.5	19.05
9	1.85	442.5	8.19
	100		**272.21**

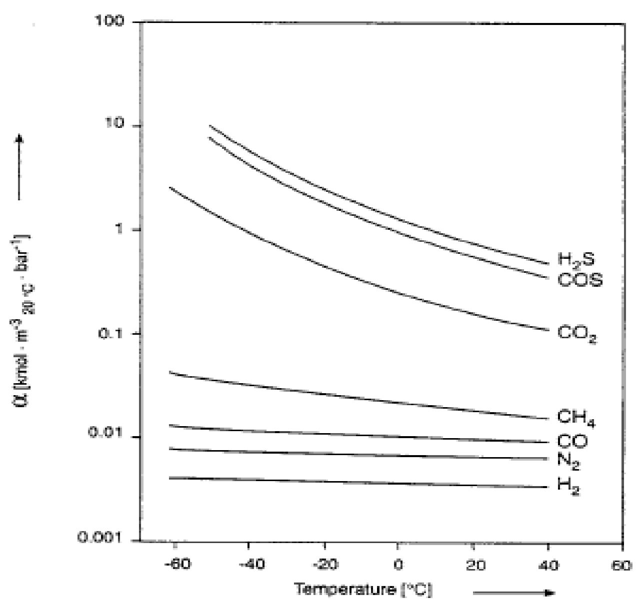

Figure 2.1: Absorption coefficient (α) of various gases in methanol

(Partial pressure: 1 bar)

Table 2.2: Solubilities of gases in the Selexol solvent

(Component Solubility Index relative to CH_4)

Component	Component Solubility Index Solubility	$Ncm^3/g.bar$, @25°C
CH_4	1.0	0.20
H_2	0.2	0.03
CO	0.8	0.08
CO_2	15	3.10
COS	35	7.0
H_2S	134	21
CH_3SH	340	68
C_6H_6	3,800	759
H_2O	11,000	2,200
HCN	38,000	6,600

Table 2.3: Physical properties of solvents used in the Selexol and Rectisol processes

Process	Selexol	Rectisol
Solvent Name	Dimethylethers of Polyethylene glycol	Methanol
Formula	$CH_3(CH_2CH_2O)_nCH_3$ $3<n<9$	CH_3OH
MW (kg/kmol)	178 - 442.5	32.04
Density at 298K (kg/m3)	1030	753
Viscosity at 298K (Pa.s)	0.0059	0.000539
Melting Point (K)	244-251	175.62
Boiling Point at 1.013 Bar (K)		321.25
Cp at 298K (J/kg/K)	2090	2498
Thermal Conductivity at 298K (W/m/K)	0.19	0.2011
Vapor Pressure at 298K (Pa)	0.093	16678.4
Surface Tension (N/m)	0.0283 - 0.0346	0.0188

It should be mentioned that for any physical-solvents to be economically feasible they must have:[2,4] (1) low vapor pressures in order to prevent solvent losses; (2) high selectivity for acid gases when compared with those of CH_4, H_2 and CO; (3) low viscosity; (4) thermal stability; and (5) non-corrosive behavior to metals. Unfortunately, only a few commercially employed solvents as given in Table 1.1 meet some of these criteria.

2.2 PHYSICAL GAS ABSORPTION INTO LIQUID SOLVENTS

The physical gas absorption into liquid solvents involves the following steps:

Step 1: Transport of the gas species through the bulk gas to the gas-film boundary;

Step 2: Transport of the gas species from the gas-film boundary through the gas-film (gas-side) to the gas-liquid interface;

Step 3: Transport of the gas species from the gas-liquid interface through the liquid-film (liquid-side) to the liquid-film boundary; and

Step 4: Transport of the gas species from the liquid-film boundary through the bulk liquid.

For steps 2 and 3, according to the two-film theory, a steady state mass transfer across a stagnant gas-liquid interface can be described for the gas-film and the liquid-film, as shown schematically in Figure 2.2, by the following equations:

$$R_S = k_G a\left(P - P^*\right) = k_G a\, He\left(C_G - C^*\right) \tag{2-1}$$

$$R_S = k_L a\left(C^* - C_L\right) \tag{2-2}$$

The overall rate of mass transfer in terms of the bulk gas and liquid concentrations of a gas component can thus be expressed as:

$$R_S = \frac{C_G - C_L}{\dfrac{1}{k_G a He} + \dfrac{1}{k_L a}} \tag{2-3}$$

Generally, the partial pressure of the physical solvents in the gas-phase is so small that the gas-phase resistance ($1/k_G$) can be neglected. This assumption suggests that Equation (2-3) can be reduced to Equation (2-2), and accordingly, the knowledge of the solubility (C^*) and the volumetric liquid-side mass transfer coefficient ($k_L a$) is essential in order to determine the rate of mass transfer in the gas absorption process.

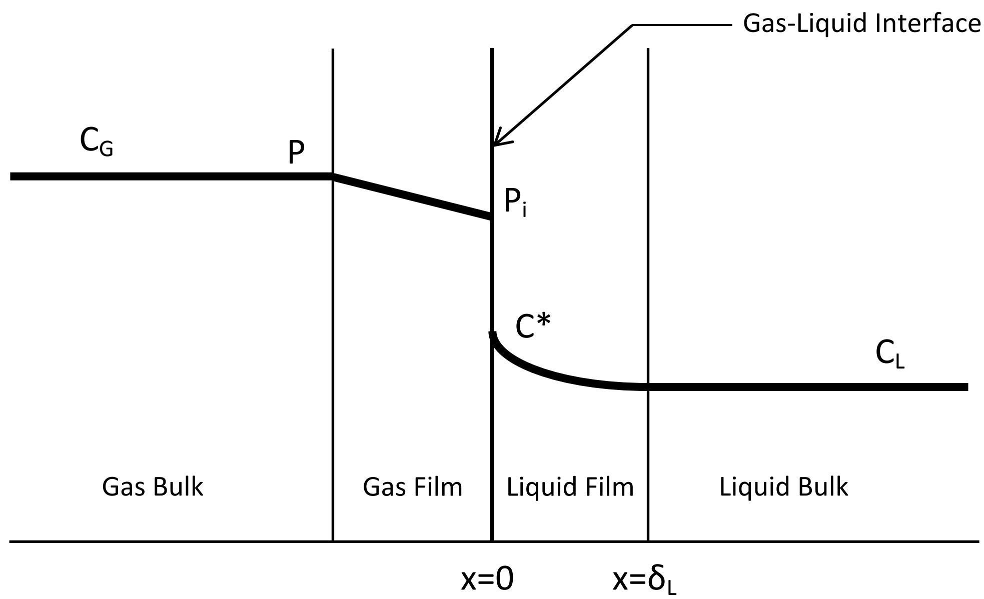

Figure 2.2: Gas concentration profile in liquid solvents

The gas absorption process is usually carried out in a unit operation (reactor) where the gas under given pressure and temperature is physically absorbed into the liquid solvent. In general, the gas a form of bubbles is brought into contact with the liquid solvent using a gas distributor where the difference between the concentration of the gas in the gas-bulk (C_G) and the concentration of the gas dissolved in the liquid-bulk (C_L) is the driving force; and the resistance to mass transfer is thus located in the liquid-film (k_L). In general, the physical absorption process continues until the thermodynamic equilibrium is reached, where C_L equals the equilibrium gas solubility (C^*). Under such conditions, there is no driving force and subsequently there is no mass transfer.

The unit operation used to carry out the absorption process can be: (1) a packed-bed reactor, operating in a countercurrent or concurrent mode where different open or structured packing are employed; (2) a bubble column reactor, where the gas is injected through the liquid-phase via a gas distributor located at the bottom of the reactor; and (3) an agitated reactor provided with a motor, in order to induce proper mixing of the gas bubbles throughout the liquid-phase for mass transfer enhancement. The accepted geometrical ratios of agitate reactors are shown in Table 2.4.

Based on the mode of gas mixing throughout the liquid, agitated reactors are generally classified into (1) surface-aerated reactor (SAR); (2) gas-inducing reactor (GIR); and (3) gas-sparging reactors (GSR) as depicted in Figure 2.3.

Table 2.4: Geometrical ratios of agitated reactors

Ratios	Ranges[18]
H/d_T	1
$d_{Imp.}/d_T$	1/4-1/2
H_L/d_T	1/2-5/6
$d_W/d_{Imp,}$	1/4-1/6
W/d_T	1/10-1/12

H: Liquid height from the bottom of the rector, m; d_T: diameter of the tank, m; H_L: Liquid height above the impeller of the reactor, m; d_W: Width of the impeller blade, m; $d_{imp.}$: Diameter of the impeller, m; W: baffle width, m

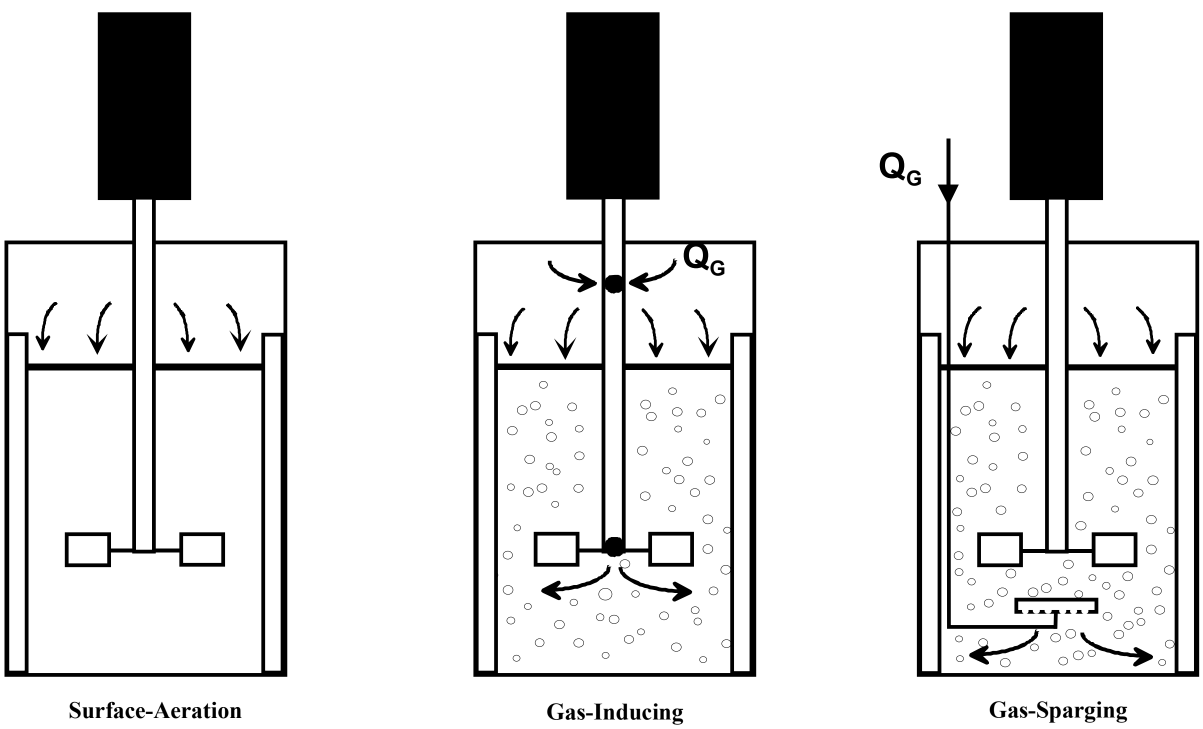

Figure 2.3: Operating modes of agitated reactors

In this study, the physical absorption for CO_2 as a single component or in a mixture in a liquid solvent was carried out in one-gallon gas-inducing reactor (GIR), where the gas was induced through the hollow shaft of the reactor; and hence the criteria need for the design and scaleup of only GIRs are here reviewed.

2.2.1 Hydrodynamic regimes in GIRs

In GIRs, different hydrodynamic regimes could occur depending on the mixing speed, relative position of the impeller to the gas-liquid surface, impeller and reactor sizes and design.[19-27] At low mixing speed, gas-inducing reactors behave as surface aeration reactors, since no gas is induced into the liquid. As the mixing speed increases the pressure near the impeller decreases until at a critical mixing speed, the pressure around the impeller becomes so small that gas bubbles are induced into the reactor. Further increase of the mixing speed increases the pumping capacity of the impeller, which results in an increase of the induced gas flow rate. Thus, more gas bubbles are induced and dispersed throughout the liquid. Under these conditions, Aldrich and van Deventer[28] and Patwardhan et al.[29] reported that the circular motion of the impeller creates a flow separation, which forms a wake region below the impeller. Consequently, gas cavities appear behind the impeller, which reduce subsequently the average density of the mixture and decrease the power input. These cavities can also be perceived as a local gas holdup in the vicinity of the impeller. In fact, when such cavities are observed behind the blades, the impeller is considered flooded. Thus, the following regimes can prevail in GIRs: (1) Surface aeration regime until the critical mixing speed for gas induction, (2) At the critical mixing speed, bubbling[30] commences, (3) Continuous bubbling[30] occurs as the mixing speed is increased, and (4) Gas jet[30] or flooding at very high mixing speeds, i.e. high gas induction rate.

Table 2.5: Hydrodynamic studies in GIRs

Authors	Gas/Liquid	Reactor characteristics	Remarks
Zlokarnik[31]	Air/Water	d_T /$d_{Imp.}$: 2.42-5.00/hollow shaft 4 types: 0.06, 0.12	Effect of mixing speed, liquid height and impeller submergence on Q_{GI}
Zlokarnik[32]	Air/Water	d_T: 0.15-1.00/Hollow Shaft 4 types: 0.06	Effect of N on Q_{GI}
Martin[19]	Air/water	d_T: 0.28/Baffles/Hollow Shaft Flat, angles T: 0.254	Q_{GI} is function of the contact angle. Scale-up of GIR
Topiwala and Hamer[33]	O_2/K_2SO_4 sol., bacterial broth	d_T: 0.158/4-Baffles Hollow T: 0.075	Q_{GI} increases with N and decreases with K_2SO_4. Effect of liquid properties on d_S , ε_G
Joshi and Sharma[20]	Air/water, DEG, Sodium dithionite	d_T: 0.41-1.00/4-Baffles, Hollow shaft/Pipe T: 0.2-0.5 Flat cylind. T: 0.250-0.395	Q_{GI} increases with orifice area, N, $d_{Imp.}$, and decreases with H and μ_L. No effect of σ_L on Q_{GI}
White and de Villiers[34]	Air/Tap water, glycerin-water-teepol	d_T: 0.29/Stator, Hollow shaft 12-vanes rotor: 0.056	Q_{GI} increases with μ_L
Sawant and Joshi[21]	Air/water, isopropanol, PEG	Denver d_T: 0.1-0.172 , $d_{Imp.}$: 0.070-0.115 Wenco d_T: 0.3 $d_{Imp.}$: 0.050	Q_{GI} increases with N and $d_{Imp.}$, decreases with H and μ_L, and is independent of σ_L and ρ_L. N_{CRI} affected by μ_L
Zundelevich[22]	Air/Water	d_T: 0.4/Stator, Hollow shaft Rotor Stator: 0.08, 0.10, 0.12	Effect of $d_{Imp.}$ and H on Q_{GI} and P_G*
Sawant et al.[35]	Air/Water, PEG/dolomite	d_T: 0.30/ Stator, Hollow shaft Wenco: 0.10	Q_{GI} increases with N and decreases with H, and μ_L
Sawant et al.[36]	Air/Water, PEG/dolomite	d_T: 0.1-0.172, 0.380 $d_{Imp.}$: 0.070-0.115/Stator	Q_{GI} increases with N and $d_{Imp.}$, decreases with H and μ_L
Joshi et al.[37]	-	-	Review on agitated gas-liquid contactors
Raidoo et al.[38]	Air/Water	d_T: 0.57/Stator, Hollow shaft 6-B DT: 0.15-0.25 6-B T/6-B PT: 0.25	Q_{GI} increases with ΔP, $d_{Imp.}$ and N. At high N, Q_{GI} flattens off
Chang[39]	H_2,N_2, CO,CH_4/n-C_6H_{14},n-$C_{10}H_{22}$, n-$C_{14}H_{30}$, c-C_6H_{12}	d_T: 0.127/4 Baffles 6-B RT: 0.0635, Hollow shaft	Determination of N_{CR}

Table 2.5 (continued)

Authors	Gas/Liquid	Reactor characteristics	Remarks
He et al.[40]	Air/Water+CMC, water+triton-X-114	d_T: 0.075/4 Baffles 6-B DT: 0.032	N_{CR} increases with μ_L, H and σ_L,; a, ε_G increases with N, and decreases with H, σ_L. ε_G increases and decreases with μ_L
Rielly et al.[41]	Air/Water	d_T: 0.30, 0.45, 0.60/4 Baffles 2-B Flat Pa: 0.215 2-B Concave T: 0.215	Bubble coalescence increases with Q_{GI}. Model to determine N_{CR} and Q_{GI}
Aldrich and van Deventer[42]	Air/H_2O, resin, brine sol., sucrose/nylon, polystyrene	d_T: 0.19/Baffles, Draft tube 6, 12-B RT: 0.05, 0.057 4-B Pipe T: 0.065	Q_{GI} decreases with μ_L and ρ_L
Aldrich and van Deventer[28]	Air/Water, aqueous ethyl alcohol, sucrose, glycerin	d_T: 0.19/Baffles, Draft tube 6, 12-B RT: 0.05, 0.057	At low μ_L, Q_{GI} increases with μ_L, and decreases with μ_L at high μ_L. Q_{GI} decreases with ρ_L
Saravanan et al.[43]	Air/H_2O	d_T: 0.57, 1.0, 1.5/Baffles 6-B DT: 0.19-0.55, Draft tube	Scale-up effect on N_{CRI} and Q_{GI}.
Al Taweel and Cheng[44]	Air/water + PGME	d_T: 0.19/Baffles, Draft tube 8-B RT: 0.096	Effect of liquid properties on a and ε_G. Additives retards the coalescence
Aldrich and van Deventer[23]	Air/water, sucrose, ethanol, brine solution	d_T: 0.19/Baffles, Draft tube 6, 12-B RT: 0.05, 0.057	Effect of H, $d_{\mathrm{Imp.}}$, μ_L and ρ_L on Fr_C and Ae
Heim et al.[24]	Air/water-fermentation mixture	d_T: 0.30/4-Baffles/hollow shaft 4-B Pipe/6-B Pipe T: 0.125 6-B DT: 0.100, 0.150	Q_{GI} is a function of N, $d_{Imp.}$, H, μ_L, and increases with μ_L
Hsu and Huang[45]	Ozone/water	d_T: 0.170/Baffles, Draft tube 6-B PT: 0.060	Bubble coalescence Increases with Q_{GI}
Saravanan and Joshi[46]	Air/H_2O	d_T: 0.57, 1.0, 1.5/Baffles 6-B DT: 0.19-0.55, Draft tube	Review on modeling and experimental studies of N_{CR}, ε_G and Q_{GI} in GIR
Hsu and Huang[25]	Ozone/water	d_T: 0.29/4-Baffles 2 6-B PT: 0.09-0.12	Effect of impeller submergence on N_{CR} and the mixing time
Hsu et al.[26]	Ozone/water	d_T: 0.170/Baffles, Draft tube 6-B PT: 0.35-0.50 d_T	Effect of N and $d_{Imp.}$ on N_{CR}, ε_G, d_S, Q_{GI} and a

Table 2.5 (continued)

Authors	Gas/Liquid	Reactor characteristics	Remarks
Patwardhan and Joshi[47]	Air/H_2O	d_T: 1.5/Baffles, Draft tube 2 6-B DT: 0.50	Review on modeling and experimental studies of N_{CR}, ε_G and Q_{GI} in GIR
Tekie[48]	N_2, O_2/Cyclohexane	d_T: 0.1154-Baffles 6-B RT: 0.0508, Hollow shaft	No effect of pressure, temperature, mixing speed and liquid height on d_S
Forrester et al.[30]	Air/Water	d_T: 0.45/4 Baffles, hollow Shaft 26-B Concave T: 0.154	Q_{GI} increases with number of gas outlets
Hsu et al.[27]	Ozone/water	d_T: 0.29/4-Baffles 2 6-B PT: 0.09-0.12	Effect of N and $d_{Imp.}$ on N_{CR}, and P_G*
Patwardhan and Joshi[49]	-	-	Review of hydrodynamic studies in agitated reactors
Patil and Joshi[50]	Air/H_2O	d_T: 1.0/Baffles, Draft tube 12-B PT: -/4-24 vanes Stator T:-	Q_{GI} exhibit a hysteresis behavior. Effect of impeller design on Q_{GI}
Patwardhan and Joshi[29]	-	-	Review of experimental and modeling studies on GIR
Fillion[51]	H_2, N_2/Soybean oil	d_T: 0.115/4-Baffles hollow shaft, 6 blades RT	Effect of P, T, N, H and Q_{GI} on d_S and ε_G
Lemoine[52]	N_2, O_2, Air / Toluene, mixtures of toluene, benzaldehyde and benzoic acid	d_T: 0.115/4-Baffles hollow shaft $d_{Imp.}$: 0.051, 6 blades RT	Effect of P, T, N, H and Q_{GI} on d_S and ε_G
Lemoine and Morsi[53]	N_2, O_2, Air/Toluene, mixtures of toluene, benzaldehyde and benzoic acid	d_T: 0.115/4-Baffles hollow shaft $d_{Imp.}$: 0.051, 6 blades RT	Effect of P, T, N, H, Q_{GI} (U_G), gas nature and liquid nature on d_S and ε_G

B: Blade, DT: Disk turbine, RT: Rushton turbine, PT: Pitched turbine, P: Propeller, Pa: Paddles

2.2.2 Critical mixing speeds for gas induction in GIRs

In GIRs, several correlations have been proposed in the literature in order to predict the critical speed for gas induction (N_{CR}).[21-26,43,47,51] Using a hollow shaft, Evans et al.[54,55] extended the earlier model proposed by Martin[19] and employed the theory of flow past immersed body along with Bernoulli's equation to obtain the critical mixing speed for gas induction in GIRs as follows:

$$P(\theta) = (P_T + \rho_L g H_L) - \frac{1}{2}\rho_L C_P(\theta) \times \left(2\pi N \frac{d_{\mathrm{Im}\,p.}}{2}(1-K) \right)^2 \tag{2-4}$$

where $P(\theta)$ and $C_P(\theta)$ are defined as the pressure and the pressure coefficients at any angular position θ, respectively, and K is a factor accounting for the slip between the impeller and the fluid. Therefore, the critical speed of induction is:

$$N_{CR} = \sqrt{\frac{2gH_L}{C_P(\theta) \times (\pi \times d_{\mathrm{Im}\,p.}(1-K))^2}} \tag{2-5}$$

The values of $Cp(\theta)$ are calculated from the potential flow theory for inviscid flow around a cylinder in an infinite medium:

$$C_P(\theta) = 4\sin^2(\theta) \tag{2-6}$$

Saravanan and Joshi[46] and White and de Villiers[34] used a similar model in a hollow shaft stator-diffuser type impeller. Increasing liquid viscosity has been reported to increase the critical mixing speed of gas induction[21,23,51] to a power ranging from 0.1 to 0.13, while negligible effects of liquid density and surface tension were reported. On the other hand, increasing liquid height or decreasing impeller diameter was found[21,23,51] to increase the critical mixing speed of gas induction. Several techniques have been developed to determine critical mixing speeds in agitated reactors. The most commonly used method is the photographic technique, which had been successfully carried out in the GIR.[20,23,51] Another commonly accepted technique developed by Clark and Vermeulen,[56] consists of monitoring the mixing speed at which the power input decreases steeply.

2.2.3 Induced gas flow rate in GIRs

In GIRs, extensive studies on the rate of gas induction can be found in the literature.[19,22-26,28,33-36,38,42,43,46,51] While the effect of liquid surface tension on the induction rate appears to be negligible, the impact of the liquid viscosity is critical. In fact, several investigators reported a decrease of the gas flow rate with increasing liquid viscosity,[20,22,35,51] whereas others reported an increase.[23,34] Furthermore, recent studies found that the rate of gas induction was first increased and then decreased with increasing liquid viscosity.[28,42] Liquid density, however, has been reported to decrease the gas induction rate,[23,28,42] due to the increase of the buoyancy. While the effects of temperature and pressure on the induced gas flow rate have been scarcely reported,[51] the effects of mixing speed, liquid height, impeller and reactor diameter are well established. In fact, Fillion[51] found that the effect of increasing temperature on gas induction rate was similar to the effect of decreasing viscosity, whereas an increase of pressure decreases the induction rate by influencing the cavities structure. Decreasing the liquid height, vessel diameter or increasing the impeller diameter increases the pumping capacity of the impeller, hence the induction rate, as generally reported.[19,22,24,34-36,38,43] In GIRs, Fillion[51] used a sealed bearing device and re-circulation loop to measure the gas flow rate with a Coriolis mass flowmeter.

2.2.4 Gas bubble size and distribution in GIRs

The quality of the gas in the liquid-phase is often characterized by the gas bubble size and distribution, which, along with the gas holdup, control the gas-liquid interfacial area, the bubble rise velocity, and the contact time. In GIRs, the gas bubbles are formed near the impeller, and therefore, the gas bubble size can be controlled by the energy of the gas stream, impeller type and size, as well as liquid properties. The formation of a single gas bubble is subject to the competition between the forces of buoyancy and surface tension. In agitated reactors, however, multiple bubbles are formed, which can collide, break up, coalesce or be consumed by reaction.

The bubble size measurement techniques can be classified into two main categories:[48] (1) direct optical techniques; and (2) indirect techniques. Several direct techniques have been used to measure the gas bubble sizes in gas-liquid contactors. High speed flash photography[48,51,57-74] as well as light scattering[75,76] have been used in order to evaluate statistically the Sauter mean bubble diameter and the bubble size distribution in gas-liquid contactors. Indirect techniques, such as ultra-sound,[77] electrical resistivity probe,[78-81] photoelectric capillary,[82] acoustic,[83] capillary probe[57] and gas disengagement[61,84-87] have also been used to measure the gas bubble size. Since most of these techniques provide local measurement of the bubble size, it should be mentioned that unless tedious study of the entire reactor at different positions is carried out, extreme care should be taken to use these measurements in overall calculations. It is also important to point out that most of these techniques have been extensively used at atmospheric pressure and room temperature, but due to the lack of adequate instrumentation only few studies have been completed under typical industrial conditions, i.e. high temperatures and pressures.[88]

The mixing speed and superficial gas velocity, i.e. the mixing power input, have been reported to decrease the bubbles diameter,[51,69,76,89-93] whereas the effect of temperature and pressure on the gas bubble sizes has been scarcely reported. It seems, however, that increasing temperature, which decreases the liquid viscosity, decreases the bubble diameter. Fillion[51] reported that the reactor type has an important impact on the bubble size, which is the result of different modes of bubble formation in the different reactor types. Literature data showed that the d_S values are supposed to increase with increasing liquid surface tension,[51,69,89,91-95] and decrease with increasing liquid density. Vermeulen et al.[93] and Matsumura et al.[89] reported that d_S values decrease with increasing liquid viscosity. Also, it should be mentioned that the effect of gas holdup on the bubble diameter reported by Calderbank,[76] Miller,[90] Sridhar and Potter[91] and Hughmark[92] reflects the coalescing behavior of the liquid employed.

2.2.5 Gas Holdup in Agitated Reactors

The gas holdup, ε_G, defined as the gas volume fraction present in the expanded volume of the reactor, has tremendous impact on the hydrodynamics and heat as well as mass transfer, since it can control the gas-liquid interfacial area.[85] Thus, it is necessary to study the effect of operating conditions, physical properties and reactor design on ε_G in order to assess the parameters influencing the gas-liquid interfacial area.

A number of methods have been developed in order to measure the gas holdup in gas-liquid contactors. The dispersion height technique is a direct method, where the liquid height is measured under gassed and ungassed conditions.[96] This method, however, has been reported to lack accuracy when waves or foam are formed at the liquid surface.[88] An alternative to this technique is the manometric method or gas disengagement technique,[48,85-87,94,97,98] which indirectly measures the gas holdup. In fact, by using high accuracy differential pressure (DP) cells, the pressure difference between two points in the reactor is measured. The gas holdup is then calculated precisely even under high temperatures and pressures. Other techniques such as ultrasound and real time neutron radiography,[77] X- and γ-ray[99] and electrical resistivity probe[100] have also been employed but less frequently in gas-liquid contactors to measure the gas holdup.

Literature findings indicated that ε_G decreases with increasing liquid surface tension[44,89-92,94,101-105] and decreasing liquid density[24,46,89-91,94,103,104] in agitated reactors. The effect of liquid viscosity on ε_G, on the other hand, appears to be controversial, since Matsumura et al.[89] in the SAR, Saravanan and Joshi,[46] Heim et al.[24] and Tekie[48] in the GIR, and Loiseau et al.[105] in the GSR found that ε_G decreases with increasing liquid viscosity, whereas Murugesan found that ε_G values increase with increasing liquid viscosity in the GSR. Furthermore, He et al.[40] in the GIR and Rushton and Bimbinet[106] in the GSR found that ε_G first increases and then decreases with increasing liquid viscosity, revealing a maximum. In addition, Sridhar and Potter[91] reported an increase of ε_G with increasing gas density, which was attributed to the increase of gas momentum.[107] The effects of mixing speed,[24,44,48,51,89,92,104,108] superficial gas velocity[46,89-92,94,104-106] and power input[36,40,46,90,91,94,101,102,105,106,109] have been reported to increase ε_G whereas the effect of temperature on ε_G appeared to be reactor dependent. Fillion[51] found that ε_G decreases with temperature in the GIR and increases in the GSR. Few and controversial studies on the effect of pressure on ε_G can be found, since for instance, Fillion[51] reported negligible effect of pressure on ε_G, while Sridhar and Potter[91] found an increase of ε_G with pressure in agitated reactor. The effect of impeller and reactor types and diameter has been reported to have an important influence on the gas holdup.[24,46,89,92,101,102,104,110,111] An increase of the number of impellers and diameter has been observed to increase ε_G, whereas an increase of reactor diameter was found to decrease ε_G. Although extensive studies on ε_G have been carried out, it should be stressed that the experimental data under typical industrial conditions, i.e. high pressures[51,91,112] and temperatures[91] are very scarce. ε_G is directly reflect the interfacial area (a), therefore if ε_G increases then a increases.

2.2.6 Mass Transfer Parameters

2.2.6.1 Volumetric Mass Transfer Coefficient, k_La

Depending on the systems used, either chemical or physical methods[113,114] have been employed to measure k_La in gas-liquid contactors. In the physical methods, the physical gas absorption or desorption is monitored by pressure transducers or gas probes[48] as a function of time under defined conditions. The transient pressure decline technique appears to be the most successful method used.[39,48,115] For instance, Chang and Morsi[116-118] developed a powerful model to describe the transient pressure decline, based on a modified Peng-Robinson EOS and mass balance. The improvement brought by this model is discussed elsewhere.[39] In the chemical methods, reviewed by Danckwerts et al.,[119] k_La data are obtained by combining known kinetics and mass transfer under chemical reaction conditions. The difficulty of temperature control, as well as the lack of kinetics data, however, seems to set the boundaries of the chemical method. The direct determination of k_L is only possible through the chemical method,[96] but can, however, be indirectly calculated from the measurement of k_La and a.[94,96,113,119,120]

Empirical and statistical correlations have been used to predict the volumetric mass transfer coefficient in agitated reactors. In the SAR, it appears that k_La follows essentially the trend of the mass transfer coefficient, k_L[39,48,51,115,121] since the absorption takes place at the free gas-liquid interface. Thus, an increase in mixing speed, power input, impeller diameter or a decrease in the liquid height and vessel diameter, will result in an increase of the volumetric mass transfer coefficient.[39,48,51,115,121] The diffusivity, on the other hand, has been reported in all correlations to be proportional to k_La raised to a power ranging between 0.5 and 1, which is in good agreement with the penetration theory and film model, respectively. While it appears that there is a good agreement on the effect of liquid viscosity on k_La, the effect of liquid density and surface tension are controversial. In fact, increasing liquid viscosity is generally found in Table 2.6 to decrease k_La, whereas increasing liquid density and surface tension were reported to increase or decrease[48,115,121-124] k_La. Additional controversial findings on the effect of pressure were reported k_La. In contrast, the temperature was generally reported to increase k_La in the SAR.[48,51,115,121]

In the GIR, below the critical mixing speed for gas induction, the reactor performs exactly as an SAR, since no gas bubbles are induced in the liquid phase. When the critical mixing for gas induction is reached, however, gas bubbles start to be induced and dispersed in the liquid phase, increasing considerably a and therefore k_La. Consequently, both a and k_L can influence k_La values, sometimes only a or k_L have an impact on k_La. Increasing the mixing speed, power input, impeller diameter or decreasing the liquid height and vessel diameter increases the turbulences inside the reactor and the pumping capacity of the impeller. Thus, both a and k_L increase and subsequently k_La as often found.[20,24,30,36,39,48,51,117,118,125-130] On the other hand, the effect of physical properties on k_La appears to be system-dependent since the overall trends of k_La with liquid viscosity, density and surface tension are different. It appears also that increasing temperature leads to a decrease of k_La[48,51] in the GIR, whereas the effect of pressure seems more complex and was generally found to be negligible.[48,51]

2.2.6.2 Gas-liquid interfacial area, *a*

Several methods have been developed in order to measure the gas-liquid interfacial area, *a* in gas-liquid contactors. The gas-liquid interfacial area can be measured using physical or chemical methods. Optical methods, such as photographic,[94] light reflection[94,131] and light scattering[132] were used as physical techniques; however, they were restricted to transparent contactors having low gas holdup.[77] Other physical methods including γ–ray radiography[77] and real time neutron radiography[77] have also been used to estimate *a*. Midoux and Charpentier[133] reviewed various chemical reactions, where it is possible to measure *a*. The limitation of this method is that the reaction kinetics are needed before measuring a. While these previous procedures mainly help to reveal the bubble contributions to *a*, other measuring techniques have been used in ripple tank to determine *a* at the gas-liquid interface. Muenz and Marchello,[134,135] measured the wave frequency using a stroboscope and determined the amplitude through the analysis of the refractive surface properties via a photo-volt photometer and densitometer. Recently, Vazquez-Una et al.[136] used a CDD camera viewing the surface at a 45° angle to calculate through digitized images analysis the wave length, λ. The surface peak-to-peak amplitude and frequency were determined from the surface displacement recorded using a vertically oriented laser triple-range distance-measuring device.

Table 2.6: Literature survey on k_La in GIRs

References	Gas /Liquid	Operating Conditions	Remarks
Topiwala et al.[33]	Air /K_2SO_4 (aq.)	303 K	k_La increases with N
Joshi and Sharma[20]	Air/Sodium dithionite sol.	Atm./d_{Imp}.0.2-0.5/d_T 0.41-1	Effect of reactor size and impeller design on a and k_La
Zlokamik et al.[137]	O_2,N_2/Water, Na_2SO_4, NaCl	2 bar / 293 K	k_La increases with $(P^*/V_L)^{0.8}$
Pawlowski and Kricsfalussy[138]	H_2/DNT	41 bar / 393-433 K	k_La is a function of P^*/V_L
Kara et al.[125]	H_2/Tetralin, coal liquid	70-135 bar / 606-684 K	k_La increases with and decreases with
Karandikar et al.[139]	H_2,CO/F-T medium (C_{11}-C_{22}, MW=201.5) liquid containing water	423-498K, 10-40 bar, 11.7-20 Hz	k_La increases strongly with P and N k_La increases with T
Karandikar et al.[126]	CO, CH_4, CO_2, H_2/ F-T liquids (heavy, ≥C_{22}, MW=368.5) containing water	10-50 bar / 373-573 K	k_La increases with P, N, P^*/V_L, decreases with H/d_T
Eiras[140]	H_2, C_2H_4, C_3H_6/n-Hexane	1-40 bar / 313-353 K	k_La increased with N. Effect of P and T was not clear
Lee and Foster[141,142]	O_2, CH_4/Silicon fluid, perfluoroalkyl,polyether	10-70 bar / 293-573 K	k_La increased with N, P and T, $(k_La)_{O2} > (k_La)_{CH4}$
Chang[39]	H_2, N_2, H_2O, CO, CH_4/n-C_6H_{14}, n-$C_{10}H_{22}$, n-$C_{14}H_{30}$, c-C_6H_{12}	1-60 bar 328-528 K	k_La increases with N, decreases with H. Effect of P and T on k_La is system dependent
Chang and Morsi[128]	CO/n-hexane,n-decane, n-tetradecane	328-428K, 1-50 bar, 13.3-20 Hz 4 L reactor	k_La increases slightly with P k_La increases with N
Dietrich et al.[129]	N_2,H_2/Ethanol,water, hydrogenation mixture/Ni Raney particles (10-15μm)	293-353K, 10-50 bar 0.5 L reactor	k_La independent of P k_La increases with increasing T and N
Hichri et al.[143]	H_2/2-propanol,o-cresol,mixture (2/3 2-propanol+ 1/3 o-cresol)/ Pyrex beads ($40<d_p<300$μm)	303-393K, 13.3-25 Hz, 0-30 bar, solid up to 5 vol.%	No influence of P k_La increases with T k_La increases strongly with N
Al Taweel et al.[44]	Air/Water+ propylene glycol methyl ether	298 K / Atm.	Effect of surface tension on a

Table 2.6 (Continued)

References	Gas /Liquid	Operating Conditions	Remarks
Hsu et al.[26]	Ozone/Water	298 K, 8.3-26.7 Hz	k_La increases with N, due to the increase of ε_G, level off at 23.3 Hz
Lekhal et al.[144]	H_2,CO/n-Octene,ethanol,water	323K, 10-150 bar, 18.3-41.7 Hz	Poor effect of *P* on k_La k_La increases strongly with *N*
Tekie et al.[145]	N_2, O_2/Cyclohexane	7-35 bar /330-430 K 6.7-20 Hz/0.171-0.268m	k_La increases with *N*, decreases with *H*. Effect of *P* on k_La is system dependent. Effect of *T* is not clear
Tekie et al.[146]	N_2,O_2/Cyclohexane	330-430K, 7-35 bar, 6.7-20 RPM	k_La increases slightly with *P* k_La increases with *T* and N
Mohammad[115]	N_2, O_2/Benzoic acid	1-5 bar /423-523 K 100-23.3 Hz	k_La increases with *N*, and slightly with *T* and *P*
Fillion and Morsi[147]	N_2, H_2/Soybean Oil	1-5 bar / 373-473 K 10-23 Hz / 0.171-0.268m	k_La increases with *N*, decreases with *H* and *T*. k_La is independent of *P*.
Alghamdi[148]	H_2,CO,N_2,He/Isopar-M (C_{10}-C_{16}),PAO-8 (C_{30}-C_{70})/solid Al_2O_3	373-473K, 7-35 bar, 13.3-20 Hz, solid up to 50 wt.%	k_La slightly increase with *P* k_La increases with *T* and *N*
Hsu et al.[149]	Ozone/Water	290-303K, 10-21.7 Hz	k_La increases with *N*, levels off above 16.7 Hz
Chen et al.[150]	O_2/water	293-313K, 1-1.2 bar, 15-21.7 Hz	k_La independent of *P* k_La increases with *T* and *N*
Soriano[151]	He, N_2, H_2 ,CO/Polyalphaolefins (PAO-8), Sasol Wax	7-35 bar, 423-523 K, 13.3-20 Hz	k_La increases strongly with *N*, k_La increases with *T* Effect of *P* depends on gas-Liquid system
Lemoine and Morsi[53]	N_2, O_2, Air/ Toluene, mixtures of toluene, benzaldehyde and benzoic acid	4.5-15 bar / 300-453 K 13.3-20.0 Hz / 0.171-0.244m	k_La increases with *N* k_La decreases with *H* and *T*

2.2.6.3 Mass transfer coefficient, k_L

The two-film model ("Whiteman's model") was first introduced by Whiteman[152] in 1923, and considers that the gas is being absorbed by molecular diffusion alone across a stagnant liquid film of thickness, Δ. While the liquid composition is assumed constant due to mixing in the bulk, the resistance is concentrated in the film and results in a concentration gradient (C^*-C_L) between its two edges. This model leads to the following equation of k_L:

$$k_L = \frac{D_{AB}}{\Delta} \tag{2-7}$$

Despite the simplistic physical meaning of this model, it integrates important aspects of the real behavior of the gas-liquid absorption, which are the dissolution and molecular diffusion of the gas into the liquid before its transport by convection. This simplistic model predicts results similar to more complex and realistic models.[75,119,153] It is also worth mentioning that the effects of the hydrodynamic parameters on k_L are described by the behavior of the film thickness, whereas the effect of physical properties could have an impact on both the diffusivity and the film thickness. For instance, increasing the viscosity or decreasing the temperature decreases the diffusivity, which reduces k_L. The effects of pressure, liquid surface tension and density on k_L are more complex and appear to be system dependent.[48,51]

In 1935, Higbie[154] proposed the penetration theory or "Higbie's model" based on the postulate that transfer occurs by a penetration process, which in fact overlooks the assumption of steady-state transfer. In this model, it is assumed that all liquid surface elements are exposed to the gas for the same amount of time before being replaced. During this exposure time, also called contact time, the element absorbs the same amount of gas per unit area as if it was stagnant and infinitely deep. The contact time is related to k_L as:

$$k_L = 2\times\sqrt{\frac{D_{AB}}{\pi\times t_C}} \tag{2-8}$$

Assuming that the bubbles slip through the stationary liquid, the contact time in gas-liquid contactors is usually calculated[155,156] as follows:

$$t_C = \frac{d_B}{U_T} \tag{2-9}$$

Thus, the effects of physical properties, operating conditions and reactor design on k_L are the resulting consequence on their effects on d_B, U_T and D_{AB}.

The Danckwerts model also called "surface renewal theory" proposed in 1951[119,157] is similar to Higbie's model.[154] In fact, instead of assuming that all surface elements are exposed to the gas for the same amount of time t_C, it assumes that there is a stationary distribution of the surface exposure. Hence, an element of surface being replaced by a fresh liquid element is independent of the exposure time. The only parameter taking into account the hydrodynamics is in this case the single parameter s, which has the dimensions of reciprocal time (s^{-1}) and represents the fractional rate of surface renewal.[119]

$$k_L = \sqrt{D_{AB}\times s} \tag{2-10}$$

Several investigators have introduced empirical and semi-empirical models based on the previously discussed theory, such as the "film-renewal model".[158,159] Kishinevskii et al.[160] and King[153] have proposed a different approach wherein the turbulences were extended to the liquid surface and the gas absorption was a combination of molecular and eddy-diffusivity. Literature studies showed that in all reactor types, the mass transfer coefficient increases with the degree of turbulences, i.e. with increasing superficial velocity, mixing speed, impeller diameter and power input. k_L values were also found to increase with liquid density and decrease with liquid viscosity, while the effect of liquid surface tension is not clear.[70,156,161] k_L was always found to be proportional to the diffusivity to a power ranging between 0.5 and 1, which corresponds to the penetration theory and the film model, respectively. It should also be mentioned that k_L values were commonly found to increase with the bubble size in all gas-liquid contactors.[75] Nevertheless, no experimental data on the mass transfer coefficient have been reported in the literature under high temperature and high pressure for gas absorption in liquid solvents.

3.0 OBJECTIVE

As can be concluded from the preceding section, the existing conventional chemical processes (MEA, MDEA) and physical processes (Rectisol,[8] Selexol,[9] Morphysorb[11,12]) for acid gases removal (including CO_2) from warm fuel gas steams require cooling the entire gas from the gasifier temperature down to ambient or sub-ambient temperature, leading to a significant increase of the cost of CO_2 capture process and a dramatic decrease of the thermal efficiency of the IGCC facilities. The overall objective of this study is to investigate new chemically and thermally stable physical solvents, which allow selective CO_2 capture from shifted warm fuel gas streams available at high pressures and moderate temperatures (~ 478 K).[3]

In order to achieve this objective, the following research is proposed:

1. Define an “ideal” physical solvent for selective CO_2 capture from a warm fuel gas mixture, which contains CO_2, CO, H_2S, H_2O, and H_2 in amounts typifying those of post-shift reaction; and select 6 different physical solvents which follow such a definition;
2. Measure the solubilities (x^*) and mass transfer coefficients (k_La) for the gaseous constituents of the fuel gas stream into the selected physical solvents under high pressures and temperatures, similar to those of warm fuel gas streams. A one-gallon gas-inducing agitated reactor available in our laboratory will be used for this purpose;

3. Develop conceptual process design for CO_2 capture from warm fuel gas stream using ASPEN Plus Simulator for CO_2 capture using the "best" physical solvents, which will be selected based on the definition of the "ideal" physical solvent.

4.0 DEFINITION OF AN "IDEAL" SOLVENT

An "Ideal" solvent for CO_2 capture from warm gas streams should enjoy the following characteristics:

1. The solvent should contain a hard base, which will permit a strong affinity to CO_2 considered as a hard Lewis acid, according to Pearson's hard soft [Lewis] acid base (HSAB) principle, which states that: hard [Lewis] acids prefer to bind to hard [Lewis] bases, and soft [Lewis] acids prefer to bind to soft [Lewis] bases.[162] Hard Lewis acid is defined as that where the acceptor atom is of high electronegativity. Hard base could be defined in a similar way by considering the high electronegativity of the donor atom. Ethers, R-O-R', are among the best examples of Pearson hard bases. Selexol solvent, which is a well-known benchmark for CO_2 capture, contains polyether groups, which are responsible for the solvent's ability to solubilize relatively large amounts of CO_2. Other examples of Pearson's hard Lewis bases include: $CH_3CO_2^-$, NO_3^-, SO_4^{--}, NH_3, CO_3^{--}, and ROH.[163]

Pearson defined the "absolute hardness" parameter as:[164]

$$\eta = \frac{(I - A)}{2} \tag{4-1}$$

He also defined “absolute electronegativity” as:[164]

$$x = \frac{(I + A)}{2} \tag{4-2}$$

where I is the ionization potential; and A is the electron affinity of any atom, ion, radical, or molecule.

The ionization potential of an element is a measure of its ability to enter into chemical reactions requiring ion formation or donation of electrons and is related to the nature of the chemical bonding in the compounds formed by elements. The electron affinity of an element is the energy given off when a neutral atom gains an extra electron to form a negatively charged ion. These two parameters defined by Pearson for each acid and base may be found from experimental results.[164]

2. The solvent should have a solubility parameter (δ') which is as close as possible to that of CO_2 under actual CO_2 capture process conditions. The solubility parameter indicates the relative solvency behavior of a specific solvent. It is derived from the cohesive energy density of the solvent, which is derived from the heat of vaporization. The heat of vaporization is the energy required to vaporize the liquid, regardless of the temperature at which it boils. Thus, the liquid that vaporizes readily has less intermolecular stickiness than the liquid which requires considerable addition of heat in order to vaporize.[165]

From the heat of vaporization of liquid, the cohesive energy density (C) can be obtained from the following expression:

$$C = \frac{(\Delta H - RT)}{V_m} \tag{4-3}$$

where:

C = Cohesive energy density, $cal.cm^{-3}$

ΔH = Heat of vaporization, $cal.mol^{-1}$

R = Universal gas constant, $cal.mol^{-1}.K^{-1}$

T = Temperature, K

V_m = Molar volume, $cm^3.mol^{-1}$

The cohesive energy density is a direct reflection of the degree of van der Waals forces holding the molecules of the liquid together. Thus, this correlation between heat of vaporization and van der Waals forces translates into a correlation between heat of vaporization and solubility behavior. This is due to the fact that the same intermolecular attractive forces have to be overcome to vaporize a liquid as to dissolve a solute in it. This can be illustrated by considering what happens when two liquids are allowed to mix: the molecules of one liquid are physically separated by the molecules of the other liquid, similar to the separations that happen during vaporization. The same intermolecular van der Waals forces must be overcome in both cases.[165]

In 1936, Joel H. Hildebrand proposed the square root of the cohesive energy density as a numerical value indicating the solvency behavior of a specific solvent:

$$\delta' = \sqrt{C} = \sqrt{\frac{(\Delta H - RT)}{V_m}} \tag{4-4}$$

It was not until the third edition of his book in 1950 that the term "solubility parameter" was proposed. Table 4.1 lists several solvents in order of increasing solubility parameter.[165] The solubility parameter values are expressed in Standard Hildebrand units (square root of calories per centimeter cube, $(cal.cm^{-3})^{0.5}$) and in International System (SI) units (square root of Mega-Pascal, $MPa^{0.5}$). The relationship between the two units is:

$$\delta' \,(MPa)^{1/2} = 2.0455(\delta)\,(cal \cdot cm^{-3})^{1/2} \tag{4-5}$$

Table 4.1: Hildebrand solubility parameters of different solvents[165]

Solvent	δ'		Reference
	$(cal/cm^3)^{0.5}$	$(MPa)^{0.5}$	
Perfluoro-n-hexane (C_6F_{14})	5.9	12.1	166
Perfluoro-n-heptane (C_7H_{16})	6.0	12.3	
Perfluorocyclohexane (C_6F_{12})	6.1	12.5	
Perfluoro(methylcyclohexane) (C_7F_{14})	6.1	12.5	
n-Pentane	7[167]	14.4	
CO_2	7.14	14.6	168
n-Hexane	7.24	14.9	
n-Heptane	7.4[167]	15.3	
Diethyl ether	7.62	15.4	
n-Dodecane	-	16.0	
Cyclohexane	8.18	16.8	
Methyl ethyl ketone	9.27	19.3	
Acetone	9.77	19.7	
Diacetone alcohol	10.18	20.0	
Ethylene dichloride	9.76	20.2	
Methylene chloride	9.93	20.2	
Pyridine	10.61	21.7	
Water	23.5	48.0	

In this table, the Standard Hildebrand values are from Hansen[169] and SI Hildebrand values are from Barton.[170]

It should be mentioned that the solubility of CO_2 (x_1) in a solvent (component 2) is related to the solubility parameters of the two components as follow:[166]

$$x_1 \ \alpha \ \exp\left(\frac{-v_1(\delta_1'-\delta_2')^2\Phi_2^2}{RT}\right) \tag{4-6}$$

where Φ_2 represents the volume fraction of the solvent and v_1 is the CO_2 molar volume. This relationship indicates that a smaller difference between δ_1 and δ_2 should result in high solubility of CO_2 in the solvent.

3. The solvent should be thermally and chemically stable to prevent degradation and formation of unwanted products under the capture process conditions. For instance, Selexol solvent would not be viable if it were used at temperatures greater than 39 °C (312 K). This is because at such temperatures the dimethylethers of polyetheleneglycol [$CH_3(CH_2CH_2O)_nCH_3$, where $3<n<9$] representing the composition of the Selexol solvent (see Table 2.1) as given by McKetta[171] would decompose.

4. The solvent should have a negligible vapor pressure (similar to that of ionic liquids) under the CO_2 capture process conditions in order to minimize solvent loss. The total solvent recovery in the process should be the critical objective for the overall process economics. It was graphically reported by Wölfer[172] that the vapor pressure of Selexol solvent with the given composition mentioned above[171] is about 0.1 Pa at 298 K. Figure 4.1 shows the Selexol vapor pressure as a function of temperature compared to another physical solvent NMP (N-Methyl-2-pyrrolidone). Also, Shah[16] and Dow Chemical Company[173] reported a value of 0.093 Pa at 298 K, which is extremely small. Other properties of the Selexol solvent can be found in Appendix A. Thus, the solvent to be developed or used for CO_2 capture should have a vapor pressure similar to that mentioned for the Selexol solvent under the actual process conditions.

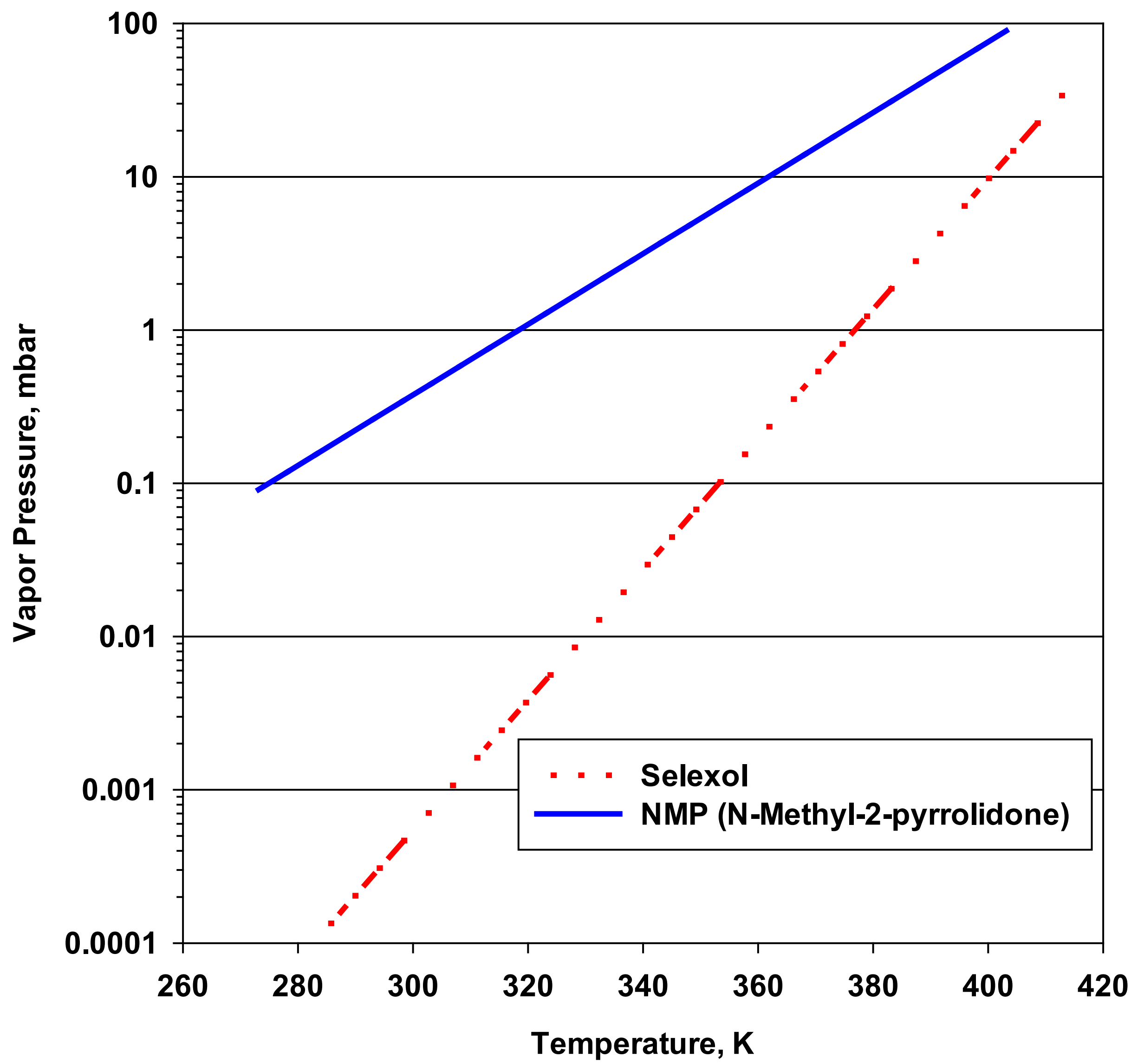

Figure 4.1: Selexol solvent vapor pressure as a function of temperature[172] compared to N-Methyl-2-pyrrolidone

5. The solvent should have low viscosity under the actual capture process conditions. For instance, the performance of centrifugal pumps is affected when pumping viscous liquids. A dramatic increase in brake-Horsepower and a reduction of flowrate and head occurs with increasing liquid viscosity,[174] leading to the increase of the cost of liquid solvent circulation to

the absorber and regenerator. The viscosity of an "ideal" CO_2 capture solvent should be less or equal to that of Selexol solvent, which has been reported to be 0.0059 Pa.s[173] at 298 K (see Appendix A). The viscosity (η) of a Selexol solvent purchased from Univar USA Inc.[175] measured in our laboratory, which is presented in Figure 4.2, can be modeled as a function of temperature using the following expression.

$$\ln(\eta) = A + \frac{B}{T} + C \cdot T + DT^2 \tag{4-7}$$

where $A = -125.96$

$B = 15755.04$

$C = 0.31145$

$D = -2.7986 \times 10^{-4}$

In this equation, T is in K and η is in Pa.s

It should be mentioned that Equation (4-7), which is different from the well-known Andrade Equation[176,177] expresses as [ln(η)=A+B/T] and fits the experimental viscosity data with high accuracy.

6. The solvent used in the entire CO_2 capture process, including the absorber and regenerator should have a useful net enthalpy taking into account the cooling systems (heat exchanger) for bringing the shifted gas temperature to that of the absorber; compression system (compressor) for delivering the CO_2 to the sequestration sites and increasing the H_2 pressure up to the turbine conditions; and pumping system (pump) for recirculation of the liquid solvent back to the absorber. The useful net enthalpy could be used for heating H_2 prior to entering the turbine or generating high-quality steam to be sold or used for other purposes.

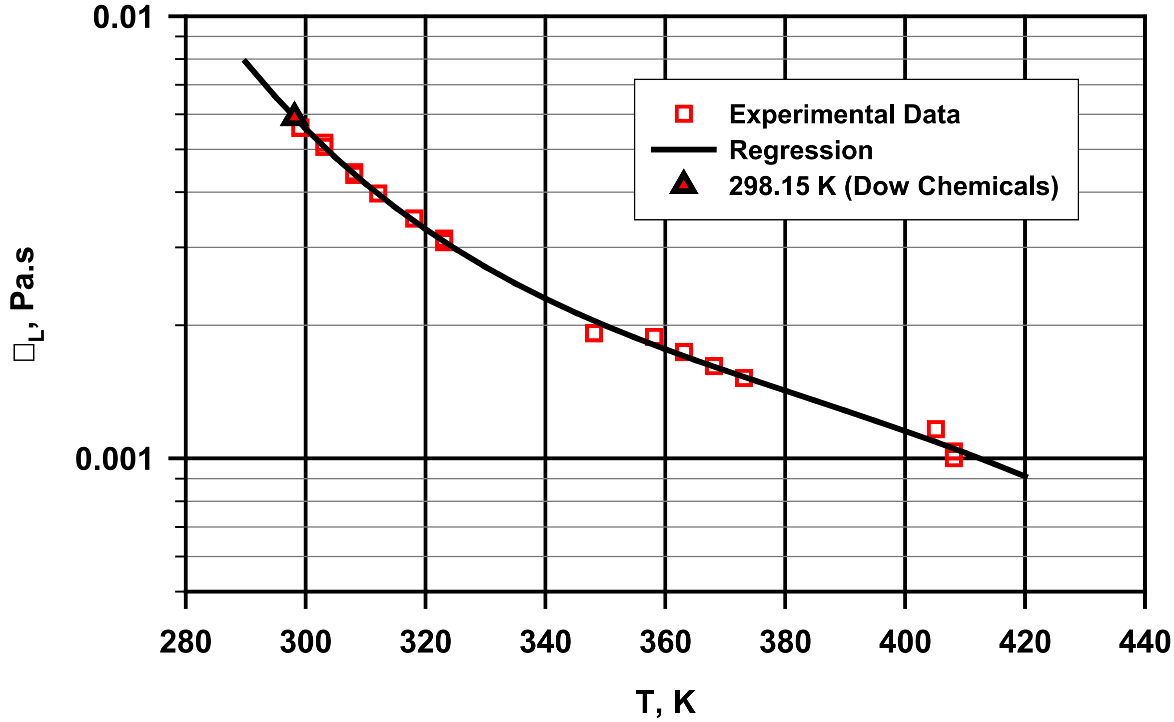

Figure 4.2: Selexol solvent viscosity as a function of temperature

5.0 SELECTION OF PHYSICAL SOLVENTS

A comprehensive literature review was conducted in order to select potential solvents which encompass the characteristics of the "ideal" physical solvents outlined in the preceding section. Table 4.1 shows that the Hildebrand solubility parameters of perfluorinated and hydrocarbon solvents are close to that of CO_2, however, the vapor pressures of the perfluorinated solvent are much lower than those of the hydrocarbons. This initiated an extensive literature search on the properties of the perfluorinated solvents as detailed below. The rational for selecting such perfluorinated solvents in the experimental program is also given.

5.1 PERFLUORINATED SOLVENTS FOR CO_2 CAPTURE

Perfluorinated compounds are characterized by different physical properties when compared with their analogous hydrocarbons (HCs).[178-181] A comparison among some physical properties of saturated perfluorohexane (n-C_6F_{14}), and saturated n-hexane (n-C_6H_{14}) is given in Table 5.1. In general, n-C_6F_{14} has significantly greater compressibilities, viscosities and densities than those of n-C_6H_{14}. The saturated n-C_6F_{14} has lower dielectric constant, refractive index, and surface tension than those of n-C_6H_{14} at 298 K, which reflect its nonpolar character and low polarizability.[182] Table 5.1 shows that the molecular weight of the n-C_6F_{14} is greater than that of n-C_6H_{14}. Branching was reported to have a negligible effect on the boiling points of perfluorinated compounds, which is in contrast with the behavior of the corresponding HCs.[179-181,183] This behavior of the boiling points indicates extremely low intermolecular interactions in PFCs, which make them behave as ideal liquids.[179-181] Table 5.1 also indicates that the surface tension of n-C_6F_{14} is smaller than that of n-C_6H_{14} at 298 K.

Table 5.1: Comparison among physical properties of different hexanes[178]

Property	n-C_6F_{14}	n-C_6H_{14}
Molecular weight, kg.kmol^{-1}	338.0	86.2
Boiling Point, bp (°C)	57	69
Heat of Vaporization, ΔH_v (kcal.mol^{-1})	6.7	6.9
Critical Temperature, T_c (°C)	174	235
Density at 25 °C, d (g.cm^{-3})	1.672	0.655
Viscosity at 25 °C, η (cP)	0.66	0.29
Surface Tension at 25 °C, σ (dyn.cm^{-1})	11.4	17.9
Compressibility at 1 atm, β (10^{-6} atm^{-1})	254	150
Refractive index, n^{25}_D (-)	1.252	1.372
Dielectric constant, ε_1 (-)	1.69	1.89

The high strength of C–F and C–C bonds in PFCs contributes to their outstanding thermal and chemical stabilities.[184] The PFC's thermal stability is limited only by the strength of their C–C bonds, which decreases with increasing the chain length or chain branching.[185] Perfluorinated compounds are nonpolar and are poor solvents for all materials except those with very low cohesive energies, such as gases. Saturated PFCs are practically insoluble in water and HF, but slightly soluble in HCs, and dissolve relatively well in low-molecular weight HCs.[170,179] The cohesive pressures of PFCs are only about half those of their corresponding HCs;[170] the heats of solution of PFCs are much different from those of HCs;[170,186,187] and the enthalpies of interaction between PFCs and HCs are smaller than those between HCs.[186,187] In terms of solvent-solute interactions, PFCs are more like Ar and Kr than HCs.[178] The distinct difference between interaction energies of PFCs and those of HCs is related to their boiling-point trends, and is manifested by the non-ideal behavior of their mixtures.[166,188-193]

A useful property of PFCs is their ability to dissolve oxygen and other gases.[194,195] PFCs dissolve about two to three times more oxygen than their analogous HCs, and about ten times more than water, which explain their use as oxygen carriers in artificial blood and organ perfusion applications.[196] The high solubility of O_2 in PFCs is not due to any specific attractive interaction between these two compounds,[197-200] but rather results from the existence of large cavities (free volume) in PFC liquids which can accommodate the gas molecules. Dias et al.[201] measured the solubility of oxygen in n-C_6F_{14} and n-C_6H_{14}, and found that the solubility of O_2 in the former is twice as that in the latter; and increasing temperature decreased the oxygen solubility in both liquid. Costa Gomes et al.[202] also investigated the solubilities of O_2 and CO_2 in the same liquids and reported an improvement of almost 100% for the solubility of O_2 in n-C_6F_{14} when compared with that in n-C_6H_{14}. In the case of CO_2, as shown in Table 5.2, the increase is not as significant, but it is important to notice that n-C_6F_{14} dissolves between 2-20 times more CO_2 than O_2 depending on the temperature.

Table 5.2: Solubility (x_1, 1×10^3) of O_2 and CO_2 in n-C_6F_{14} and n-C_6H_{14}[202]

T	O_2		CO_2	
K	n-C_6H_{14}	n-C_6F_{14}	n-C_6H_{14}	n-C_6F_{14}
200	5.9±0.4	10±1	174±30	231±39
300	3.0±0.1	5.4±0.1	16.6±0.4	24.3±0.8
400	3.1±0.1	5.1±0.1	7.9±0.1	11.2±0.2

In addition, CO_2 displays greater solubility in PFCs when compared with other gases, as can be seen in Table 5.3. Also the solubility of N_2 in perfluorohexane is greater than that in water, acetone, and cyclohexane as can be observed in Table 5.4. This behavior can be attributed to the absence of dipole in the perfluorinated solvent.

Table 5.3: Solubility of gases in PFCs

Gas solubility mL(gas)/100 g (solvent) at 25 °C and 1 atm					
Gas	Perfluoro-hexane	Perfluoro methyl-cyclohexane	1,3-dimethyl-cyclohexane	Perfluoro-decalin	Perfluoro-methyl decalin
He	6.6	5.5	4.6	3.9	3.4
H_2	10.7	9.0	7.4	6.3	5.6
N_2	26.3	22.0	18.3	15.6	13.8
CO	26.3	24.2	20.0	17.1	15.0
O_2	41	34.6	28.6	24.4	22.0
CO_2	156	132.0	109.0	93.0	82.0

Table 5.4: Solubility of N_2 in various solvents

Solvent	Solubility mL(N_2)/100g (solvent) at 25 °C and 1 atm	Bonding
Water	1.6	Hydrogen-bonding
Acetone	17.7	Dipole-dipole
Cyclohexane	18.5	Cyclohexane has no dipole but dipole can be induced
Perfluorohexane	44.2	No dipole

Thus, PFCs could be employed as attractive physical solvents for CO_2 capture from fuel gas streams at elevated temperatures and pressures based on the following: (1) CO_2 displays greater solubility in PFCs than in the corresponding hydrocarbons, about twice as much;[203] (2) PFCs are extremely chemically and thermally stable, due to the high energy of C–F bond; (3) PFCs' vapor pressures are low, which will minimize solvent loss at high temperature; (4) PFCs have low viscosities at high temperatures, which would minimize the pumping and re-circulation costs of solvents; and (5) PFCs are non-toxic and completely safe under high pressures and temperatures. It should be mentioned, however, that some of the drawbacks of PFCs include, high cost, and absorption of other gases (light hydrocarbons) along with CO_2.

The two main processes currently used for the manufacture of PFCs are electrochemical fluorination (ECF) and cobalt fluoride processes. The ECF process enjoys lower cost when compared with cobalt fluoride, but suffers from producing lower yields and selectivity, as well as extensive molecular rearrangement. The electrochemical, physical and thermodynamic properties, manufacture, and existing industrial applications of perfluorinated compounds (PFCs) are given in Appendix B.

5.2 RATIONALE BEHIND SELECTING PERFLUORINATED SOLVENTS

The rationale behind selecting the perfluorinated solvents for CO_2 capture from post water-gas-shift reactor gas streams at elevated temperatures and pressures is based on the following principles:

(1) Typically, CO_2 displays much higher solubility in perfluorinated solvents when compared with other gases, as can be seen in Table 5.3. The solubility of CO_2 in perfluorinated solvents is expected to be greater than that in the corresponding hydrocarbons, as illustrated in Table 5.4. The reason for this behavior can be explained by the absence of dipole in perfluorinated solvents as can be observed for N_2 solubility in different solvents as shown in Table 5.4.

(2) Perfluorinated compounds are extremely thermally stable. The C-F bond is very high energy, allowing perfluorinated compounds to be routinely used in very high temperature applications, such as Teflon's use in cooking ware.

(3) Perfluorinated compounds are extremely chemically stable. Therefore, they are not expected to be chemically degraded by either high operating temperatures or the presence of reactive compounds such as H_2S.

(4) Vapor pressure of perfluorinated solvents is extremely low, minimizing solvent losses. Vapor pressure can be controlled using mixtures with different molecular weights.

(5) Perfluorinated solvents have low viscosity, minimizing pumping and solvent recirculation costs.

(6) Water has low solubility in perfluorinated compounds, minimizing dilution of the solvents.

Thus, it is expected that these solvents will have good solvation properties toward CO_2, be fairly selective for solvating CO_2 compared to other gaseous constituents, and be stable in a liquid phase at elevated temperatures [e.g. greater than 260 °C (500 °F)].

5.3 PERFLUORINATED SOLVENTS USED IN THIS STUDY

In this study, the three perfluorinated compounds (Flutec fluids), namely Perfluoro-perhydrofluorene ($C_{13}F_{22}$), Perfluoro-perhydrophenanthrene ($C_{14}F_{24}$), and Perfluoro-cyclohexylmethyldecalin ($C_{17}F_{30}$), given in Table 5.5 were selected for CO_2 capture under elevated pressures and temperatures.

Table 5.5: Physical properties of the selected solvents[204,205]

	PP10	PP11	PP25
Molecular Formula	$C_{13}F_{22}$	$C_{14}F_{24}$	$C_{17}F_{30}$
Main molecular species	Perfluoro - perhydrofluorene	Perfluoro-perhydro-phenanthrene	Perfluoro - (cyclohexylmethyldecalin)
Molecular Weight	574	624	774
Density ($kg.m^{-3}$)	1984	2030	2049
Boiling Point (°C) at 1 atm	194	215	260
Pour Point (°C)	-40	-20	-10
Viscosity (kinematic) ($mm^2.s^{-1}$) at 25 C	4.84	14.0	56.1
Viscosity (dynamic) (mPa.s) at 25 C	9.58	28.4	114.5
Surface Tension ($mN.m^{-1}$) at 25 C	19.7	19	-
Vapor Pressure (mbar)	<1	<1	<1
Heat of Vaporization at Boiling Point ($kJ.kg^{-1}$)	71*	68*	67.9*
Specific Heat ($kJ.kg^{-1}.°C^{-1}$)	0.92*	1.07*	0.957*
Critical Temperature (°C)	357.2*	377*	400.4*
Critical Pressure (bar)	16.2*	14.6*	11.34*
Critical Volume ($L.kg^{-1}$)	1.59*	1.58*	1.574*
Thermal Conductivity ($mW.m^{-1}.°C^{-1}$)	56*	52.6*	63.8*
Coefficient of Expansion at 0°C	0.00078	0.00075	0.00084
Refractive Index n^{20}_D	1.3289	1.3348	1.3376

* estimated by F2 Chemicals Ltd., UK.[204]

The perfluorocarbons have the following structures:

PP10

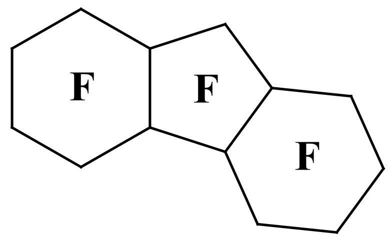

PP11

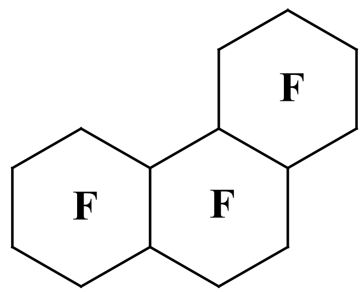

PP25

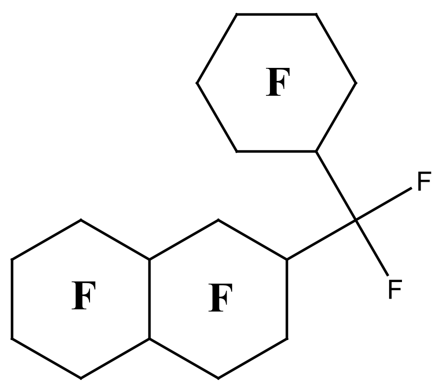

6.0 EXPERIMENTAL

6.1 EXPERIMENTAL SETUP

The experimental setup used in this study, schematically shown in Figure 6.1 and illustrated in Figure 6.2 is similar to that employed by Tekie et al.,[145] Fillion and Morsi,[147] and Lemoine et al.[206] It consists of the following main units: 1. Reactor, 2. Preheater, 3. Vacuum system, and 4. Computer/data acquisition system. The reactor is a gas-inducing 4-liter ZipperClave vessel provided with two Jerguson sight-windows (as can be seen in Figure 6.3) and has an effective volume of 3.83×10^{-3} m^3. The reactor is rated at a maximum allowable pressure of 137 bar for a temperature of 530 K. The reactor is equipped with four symmetrically located baffles (measurement details are in Figure 6.3), a cooling coil, a specially designed heating jacket, a thermo-well and an agitator with a six flat blades impeller and a hollow shaft (more details are shown in Figure 6.4). Four holes of 0.0016 m (1/16 in) diameter each located at the upper and lower end of the shaft allow the reactor to operate in a gas-inducing mode. The agitator is driven by a magnetic drive that has enough capacity of dumping any eccentricity. Two K-type Chromel-Alumel thermocouples are used to measure the gas and liquid phase temperature, whereas the pressure inside the reactor is measured using a Setra Model No. 205-2 pressure transducer rated at 0 – 500 psia. For safety purposes, the reactor is fitted with a relief valve and a 3/16” rupture disk rated at 72 bar at 295 K. As also illustrated in Figure 6.1, a leak-free special device was mounted on the shaft and an external re-circulation loop was designed to measure in the GIR the induced gas flow rate through the agitator hollow shaft.

A digital video camera (DVCAM: DSR-PD100A 3CCD Progressive Scan Compact Digital Camcorder, 12× Optical Zoom), manufactured by Sony, is used to record the gas bubbles and measure the gas holdup through the Jerguson sight-windows shown in Figure 6.1. Also, the gas flow rate was measured during the experiment with the re-circulation loop illustrated in Figure 6.1, using a Coriolis mass flow meter type CMF-010M, manufactured by Micro Motion Inc., Boulder CO, USA.

A high-pressure bomb with an effective volume of 1.176×10^{-3} m^3 is used to heat the gas to the desired temperature before it is charged to the reactor. The preheater is maintained at a constant temperature in a convection furnace controlled with a thermostat. A K-type shielded thermocouple and a pressure transducer Setra -14.7 – 1000 psig are installed to record both temperature and pressure readings during the experiments.

The vacuum pump used is a Welch duo-seal model 1400, which is an oil sealed mechanical vacuum pump that can reach down to 1000 Pa. The system is used to degas the liquid in the reactor before the start of the experiment. A liquid trap is connected between the reactor outlet and the vacuum pump inlet to collect any possible condensed vapor. The gas from the vacuum pump is then vented to the exhaust.

All pressure transducers and thermocouples used in the setup are interfaced with an on-line personal computer through an interfacing board from Keithley Instruments, Inc. (Model 575) for the agitated reactor used for the mass transfer and hydrodynamic measurements. User-friendly computer programs developed in our laboratory were used to assign the channels for the interface board and to monitor on-line the system pressures and temperatures. At any given condition, the pressures and temperatures of both phases are displayed on the computer screen. During gas absorption, the pressure decline is recorded and displayed as a function of time. Also, the pressures and temperatures in the preheater are recorded before and after the gas is charged into the reactor to build a mass balance on the gas phase.

A Balzers quadrupole Mass Spectrometer QME 200 (Quad Mass Spectrometer), equipped with 2 roughing pumps (Vacuubrand Diaphragm vacuum pump MZ 2T and Trivac D8A) and a molecular pump (Pfeiffer TMU 065), and a pressure gauge PKR 250 to monitor the pressure inside the mass spectrometer is connected to the experimental setup. It allows instantaneous "on-line" monitoring of the composition of the multi-component gaseous system used in the experiments under the actual operating conditions. The different molecules are detected using a Faraday cup detector. This mass spectrometer is connected to a computer interface and is controlled using the Balzers AG QUADSTAR 422 software version 6.02.

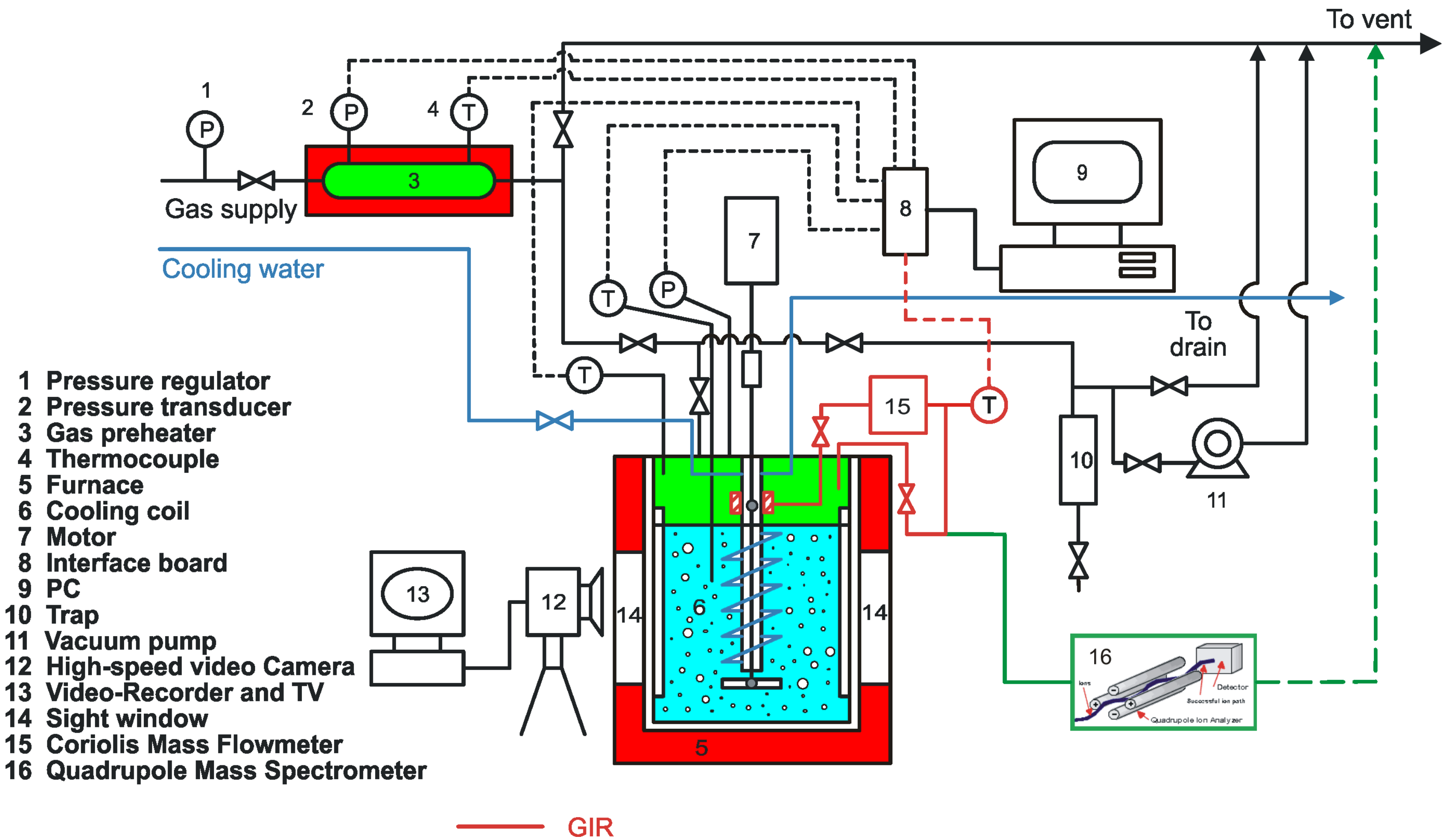

Figure 6.1: Schematic of the experimental setup used for hydrodynamic and mass transfer measurements

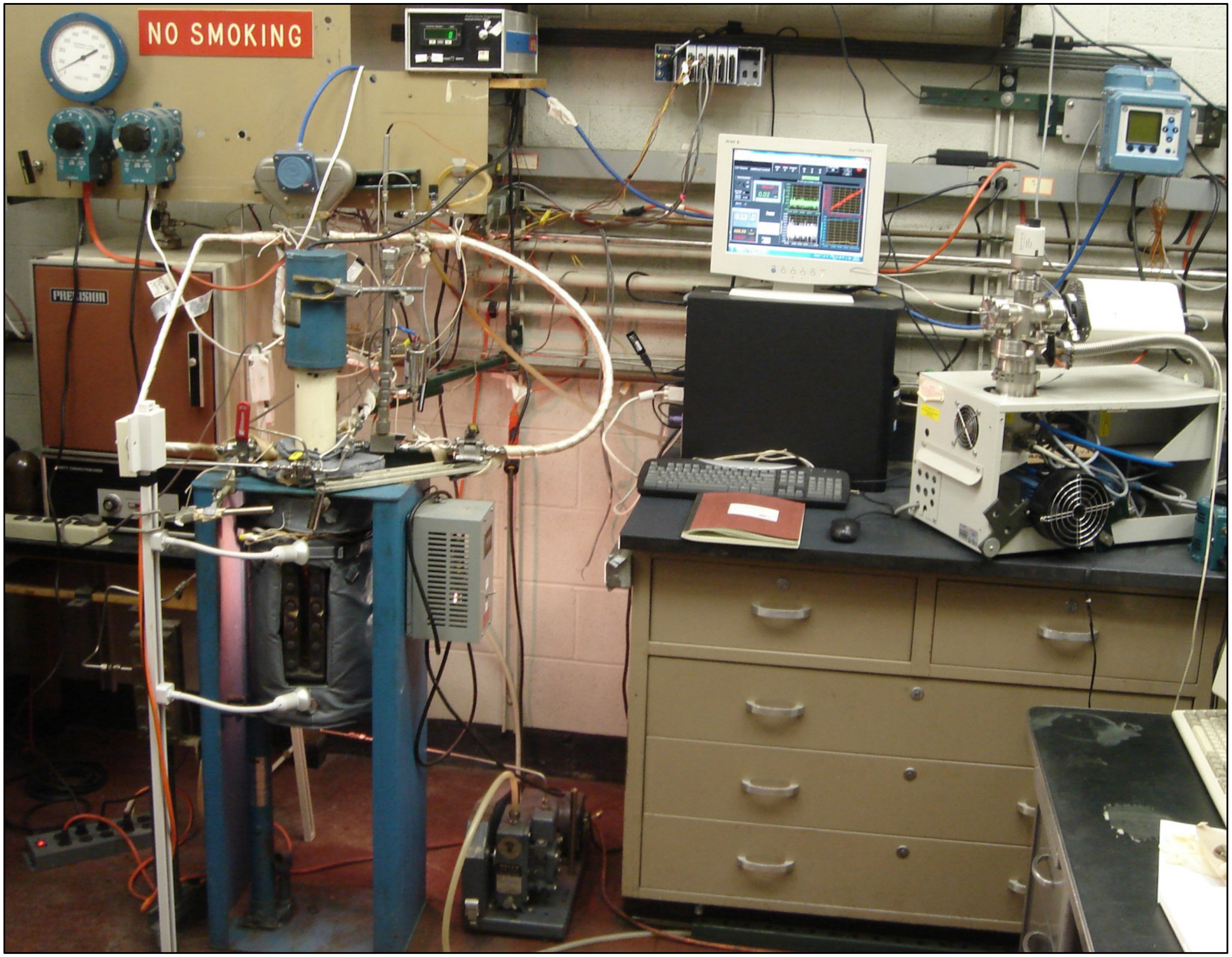

Figure 6.2: 4-Liter zipper clave reactor equipment

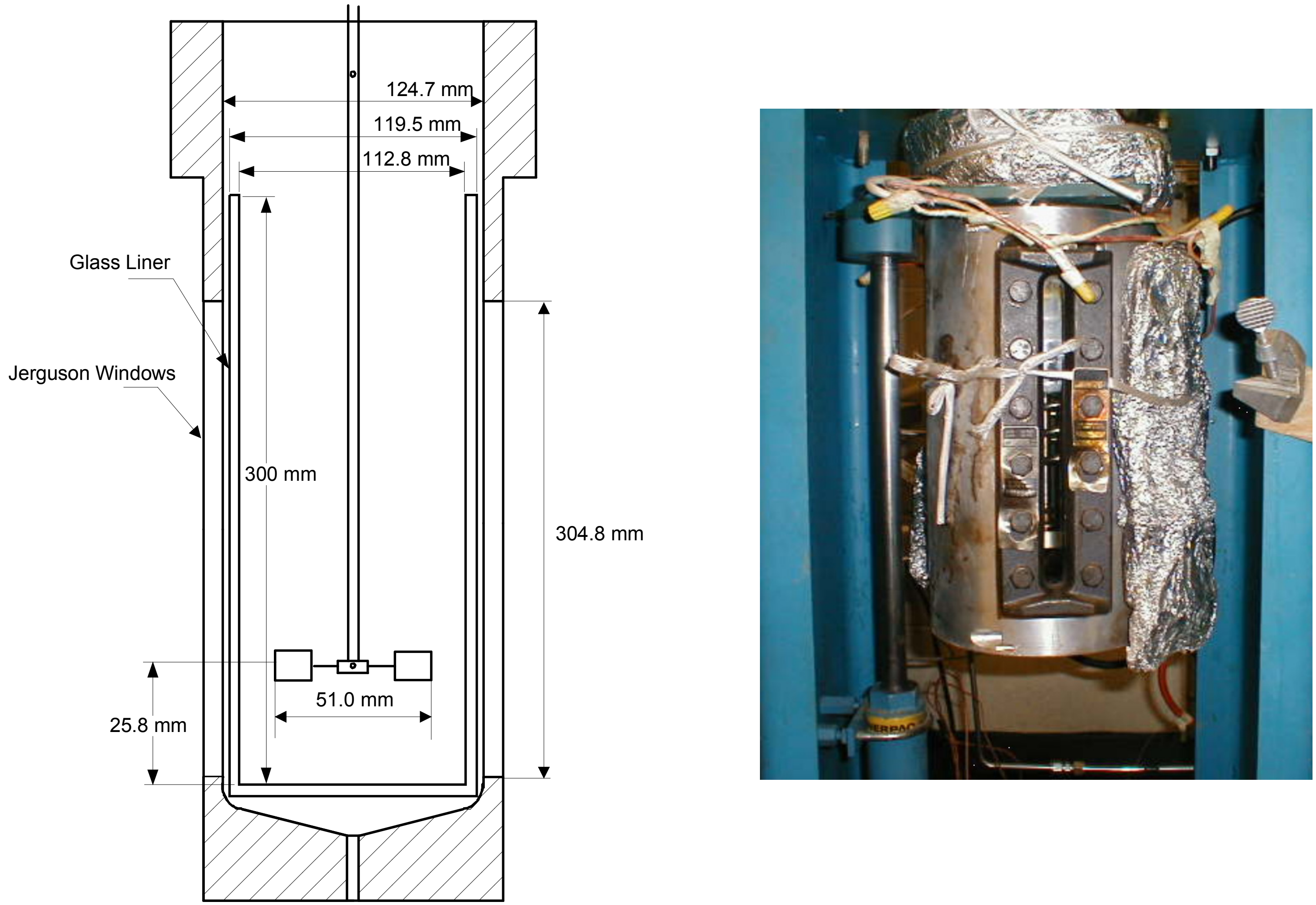

Figure 6.3: Design of the Jerguson windows and position of the impeller

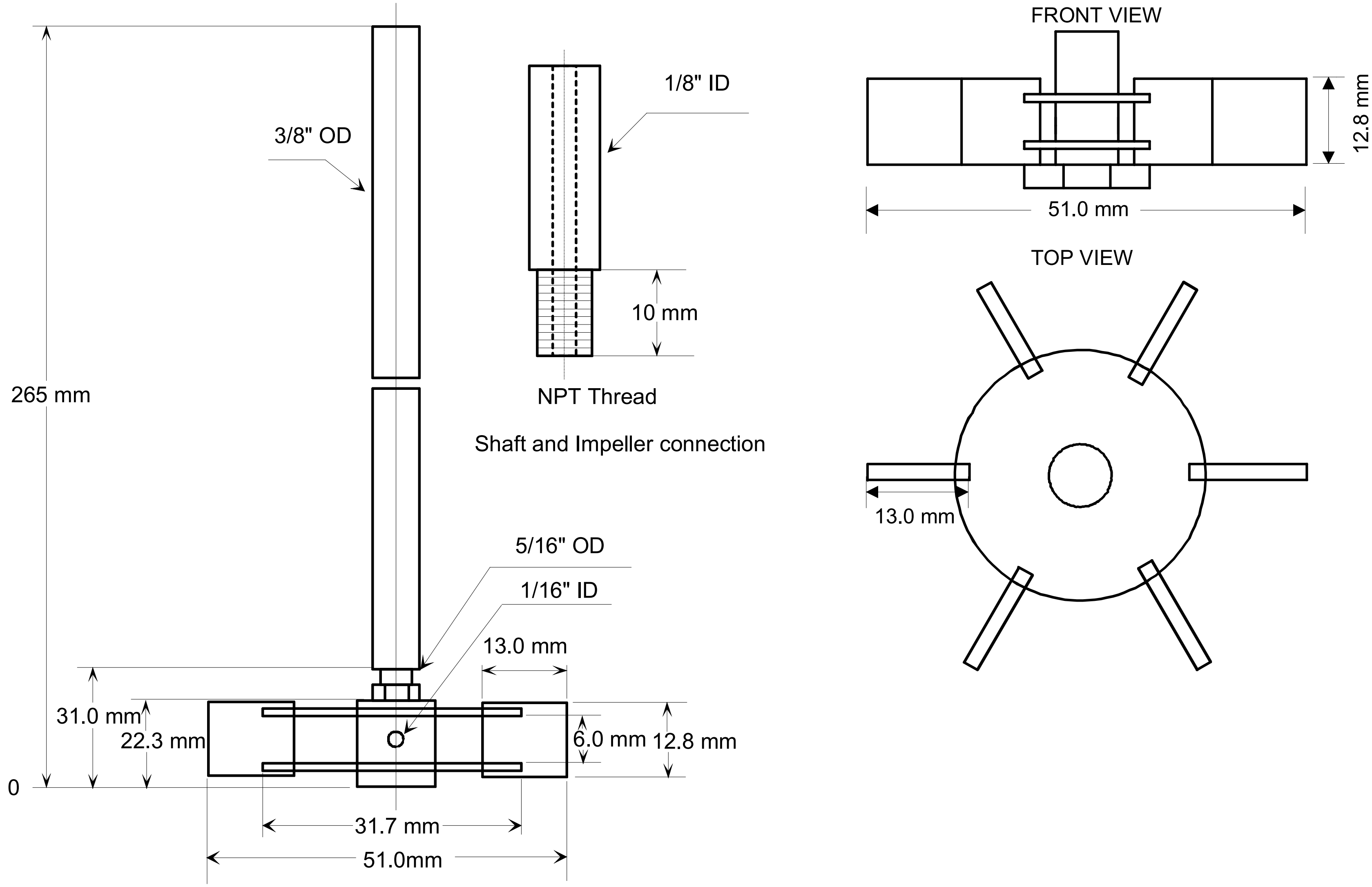

Figure 6.4: Impeller and shaft design in the agitated reactors

6.2 FIRST GAS-LIQUID SYSTEMS USED

Three perfluorocarbons (PFCs), namely PP10, PP11, and PP25 were initially employed in this study. The reactor, gas-liquid system and ranges of the operating variables used are:

Reactors	:	Gas Inducing Reactor (GIR)
Gases	:	CO_2, N_2, gas mixture (H_2, CO_2, CO, CH_4, Ar)
Liquids	:	PP10, PP11, PP25
Pressure	:	6-30 bar
Temperature	:	300-500 K
Mixing Speed	:	10-20 Hz (600-1200 rpm)
Liquid Height	:	0.14-0.22 m

CO_2 and N_2 with purity of 99.99% (Grade 4.0 gases) were purchased from Valley National Gases Inc., USA,[207] whereas He was commercial-grade gas and the three perfluorinated liquids were ordered from F2 Chemicals Ltd., UK.[204] The composition of the gas mixtures shown in Table 6.1 were ordered from Valley National Gases Inc., USA, and delivered in 300 Cylinders at 1400 psia. Some thermodynamic properties of the gas-liquid systems used are listed in Table 6.2;[168,208] and additional properties for PP10, PP11 and PP25 can be found in Table 6.5. Also, other properties, including density, viscosity, surface tension and vapor pressure for the three PFCs can be estimated using the equations given in Table 6.6.

Table 6.1: Gas mixtures compositions

Components	Formula	Mixture
		%
Argon	Ar	0.70
Methane	CH_4	0.77
Carbon monoxide	CO	0.83
Carbon dioxide	CO_2	41.21
Hydrogen	H_2	56.49
Water	H_2O	0.00
Total	**-**	**100.00**

Table 6.2: Thermodynamics properties of the gases and PFCs used[204,209]

Component	Formula	MW kg.kmol^{-1}	T_b K	T_c K	P_c bar	V_c m^3.mol^{-1}	ω -
Carbon Dioxide	CO_2	44.010	194.7	304.19	73.82	0.09407	0.228
Nitrogen	N_2	28.013	77.35	126.1	33.94	0.09010	0.04
Helium	He	4.003	4.22	5.2	2.28	0.05730	-0.39
Argon	Ar	39.948	87.28	150.86	48.98	0.0746	0.00
Methane	CH_4	16.043	111.66	190.58	46.04	0.0993	0.011
Carbon Monoxide	CO	28.01	81.7	132.92	34.99	0.0931	0.066
Hydrogen	H_2	2.016	20.39	33.18	13.13	0.0642	-0.22
Water	H_2O	18.015	373.15	647.13	220.55	0.056	0.345
PP10	$C_{13}F_{22}$	574.10	467	630.2	16.2	2.7696	0.491
PP11	$C_{14}F_{24}$	624.11	488	650.0	14.6	2.5316	0.513
PP25	$C_{17}F_{30}$	774.13	533	673.6	11.34	2.0333	0.745

6.2.1 Vapor pressure of the PFCs

The vapor pressure of PP10, PP11 and PP25 could not be found in the literature and therefore they were measured in our laboratory up to a temperature of 500 K. Also, the experimental data were used to obtain the coefficients C_1 through C_6 in the Antoine Equation (Equation (6-1)) used in the Aspen Plus 13.1 as Riedel's method. Equation (6-1) appears to predict with R^2>92% the vapor pressure values for the three fluorocarbons as shown in Figure 6.5.

$$\ln P_S = C_1 + \frac{C_2}{T} + C_5 \ln(T) + C_6 T^6 \qquad (6\text{-}1)$$

in Equation (6-1), P_S is in Pa.

The values for the constants C_1 through C_6 are listed in Table 6.3.

Table 6.3: Values for the constants in the extended Antoine type equation for the liquid vapor pressure

	PP10	PP11	PP25
C_1	75.76	78.04	100.04
C_2	-8495.91	-8981.91	-11617.36
C_5	-7.501	-7.783	-10.646
C_6	5.98×10^{-18}	5.09×10^{-18}	5.13×10^{-18}

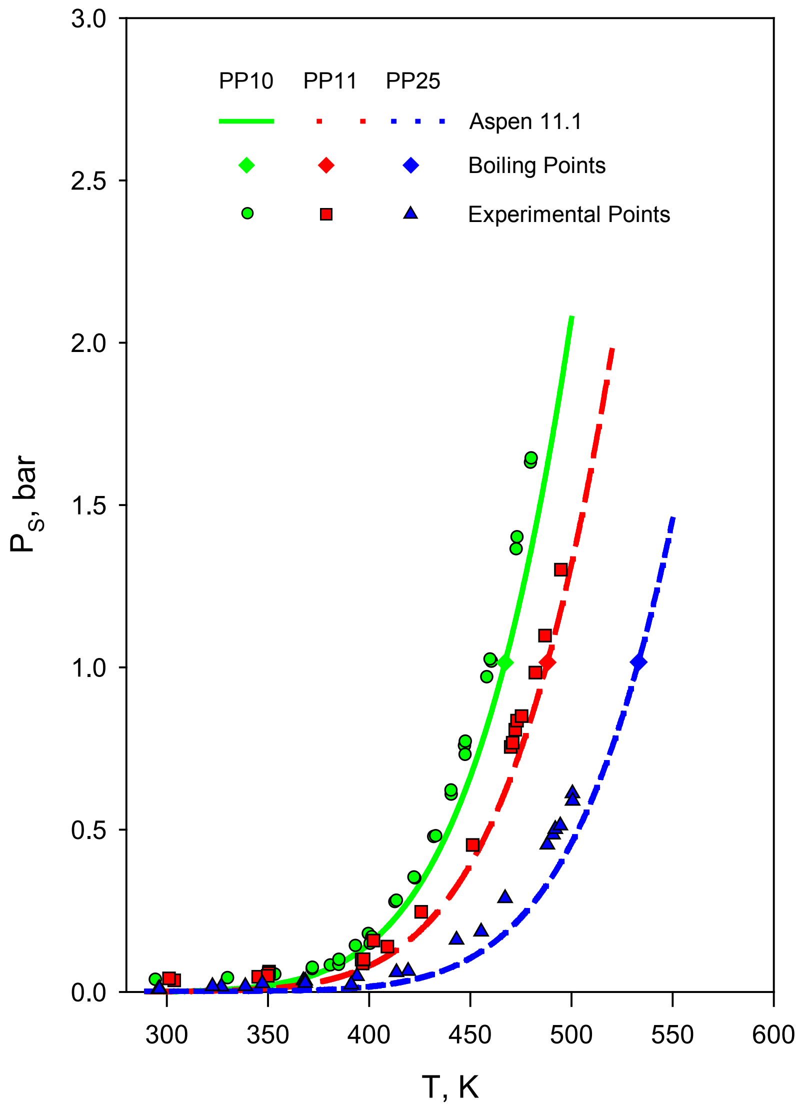

Figure 6.5: Vapor pressure of the fluorocarbons as a function of temperature

6.2.2 Density of the fluorocarbons

The density values of fluorocarbons were measured experimentally and then correlated as a function of temperature using a Rackett-type equation,[168,208,210] Equation (6-2) which has the following general form with $T_r = T/T_c$:

$$\rho_L = A \cdot B^{-\left[(1-T_r)^n\right]} \tag{6-2}$$

Table 6.4 gives the constants for the Rackett-type equation obtained and Figure 6.6 shows the predicted densities of the three fluorocarbons used as a function of temperature. The critical temperatures (T_c) for the three perfluorinated liquids are given in Table 6.2.

Table 6.4: Parameters for the density in the Rackett-type equation

	A	B	n
	kg.m^{-3}	-	-
PP10	628.931	0.2655	0.2532
PP11	632.911	0.2666	0.2192
PP25	635.324	0.2667	0.2136

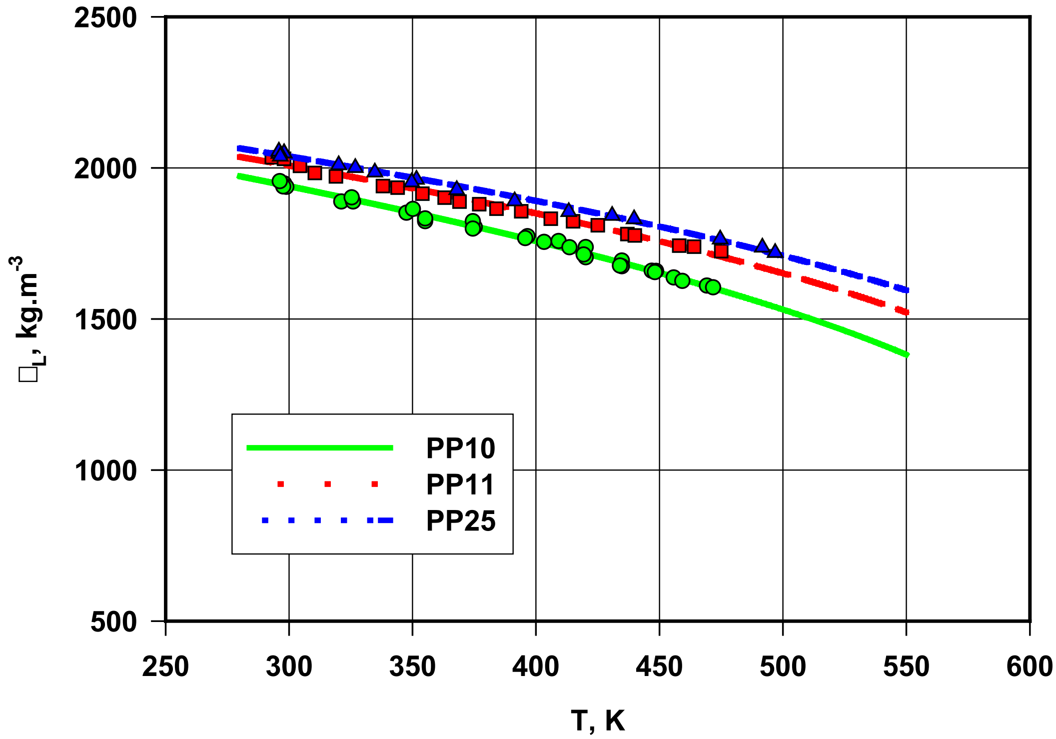

Figure 6.6: Correlation of the fluorocarbon liquid densities using the Rackett-type equation

6.2.3 Viscosity of the fluorocarbons

At 298.15 K the viscosities for PP10, PP11, and PP25 are 0.00958, 0.0284, and 0.1145 Pa.s, respectively. Several viscosity values For PP11 were obtained from F2 Chemicals Ltd.[211] and correlated within the temperature range from 300 to 500 K as follows:

$$\ln(\eta) = -14.533 + \frac{3270.95}{T} \tag{6-3}$$

The viscosity of PP25 was measured using a rheometer from 298 to 373 K and the experimental values were correlated using Equation (6-4):

$$\ln(\eta) = -8.620 - \frac{1305.5}{T} + \frac{959746}{T^2} \tag{6-4}$$

The viscosity of PP10 was estimated using the Sastri-Rao method[212] which was modified in order to fit the viscosity of PP10 of 0.00958 Pa.s at ambient temperature (298.15 K) by the following equation:

$$\eta = 0.1 \times \eta_B P_S^{-N} \qquad (6\text{-}5)$$

where the values of η_B and N for PP10 were estimated using the group contributions described by Sastri-Rao[212] and were found to be 1.11 mPa.s and 0.75 respectively.

The vapor pressure used in equation (6-5) is in atmospheres and is calculated from:

$$\ln(P_S) = \left(4.5398 + 1.0309\ln(T_b)\right) \times \left(1 - \frac{\left(3 - 2\, T/T_b\right)^{0.19}}{T/T_b} - 0.38\left(3 - 2\, T/T_b\right)^{0.19} \ln\left(T/T_b\right) \right) \qquad (6\text{-}6)$$

T_b is the boiling point in K, which is given in Table 6.2.

The correlations for PP10 and PP11 were directly given by F2 Chemicals Ltd., whereas in the case of PP25, the experimental data were correlated using Equation (6-4) since the 3 parameter equation gave a satisfactory fit.

The viscosities of PP10, PP11 and PP25 are plotted as a function of temperature in Figure 6.7.

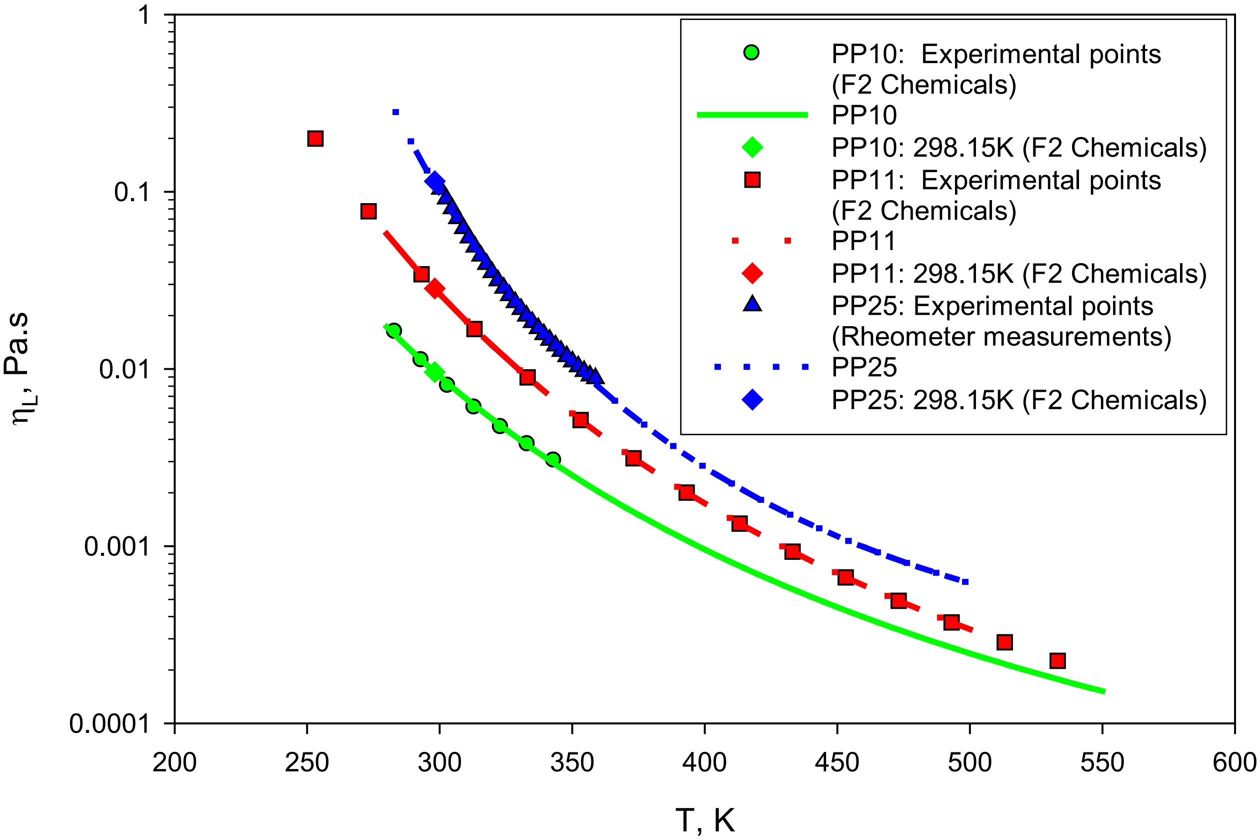

Figure 6.7: Viscosity of the fluorocarbons as a function of temperature

6.2.4 Surface tension of the fluorocarbons

At 298.15 K the surface tensions for PP10, PP11, and PP25 are 0.0197, 0.0190, and 0.0194 $N.m^{-1}$ as given by F2 Chemicals Ltd.[204] The surface tensions of the fluorocarbons were calculated in the temperature range from 280 K to 500K using Equation (6-7);[168,208] and the values obtained are plotted in Figure 6.8.

$$\sigma_L = \sigma_1 \left(\frac{T_c - T}{T_c - T_1} \right)^{11/9} \qquad (6\text{-}7)$$

T_c values for PP10, PP11, and PP25 are 630.2, 650, and 673.6 K, respectively. The T_1 value is 298.15 K.

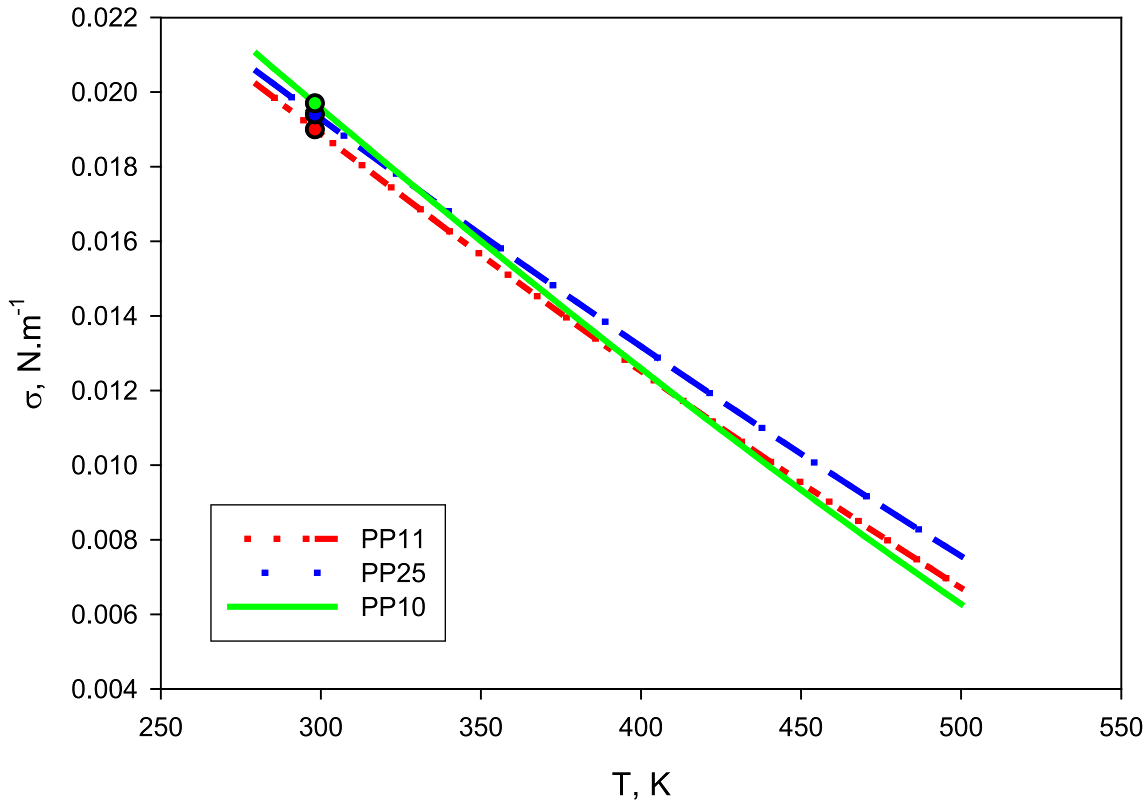

Figure 6.8: Surface tensions of the fluorocarbons as a function of temperature

6.2.5 Gases diffusivity in the fluorocarbons

The diffusivity values of different gases in the three fluorocarbons, D_{AB} ($m^2.s^{-1}$) were calculated as a function of temperature using the Wilke and Chang's Equation[208,213] given below:

$$D_{AB} = 1.1728 \times 10^{-16} \frac{(\psi M_B)^{0.5} T}{\eta_B V_A^{0.6}} \tag{6-8}$$

In this Equation, V_A is the molar volume of the diffusing gas ($m^3.kmol^{-1}$) at its normal boiling point, defined by Tyn and Calus[168,214] as follows:

$$V_A = 10^{-3} \times 0.285 \cdot (V_C)^{1.048} \quad (6\text{-}9)$$

$$V_A = 0.3971 \cdot (V_C)^{1.048}$$

The values of V_c is in $cm^3.mol^{-1}$ are given in Table 6.2, and ψ is the association factor of the solvent which characterizes its polarity and has a value of 1.0 for unassociated solvents.[168] The molecular weight of the solvent, M_B, is in $kg.kmol^{-1}$, the temperature in K and the viscosity of the solvent in Pa.s. The calculated diffusivities of the different gases are represented in Figures 6.9, 6.10 and 6.11 for PP10, PP11 and PP25, respectively.

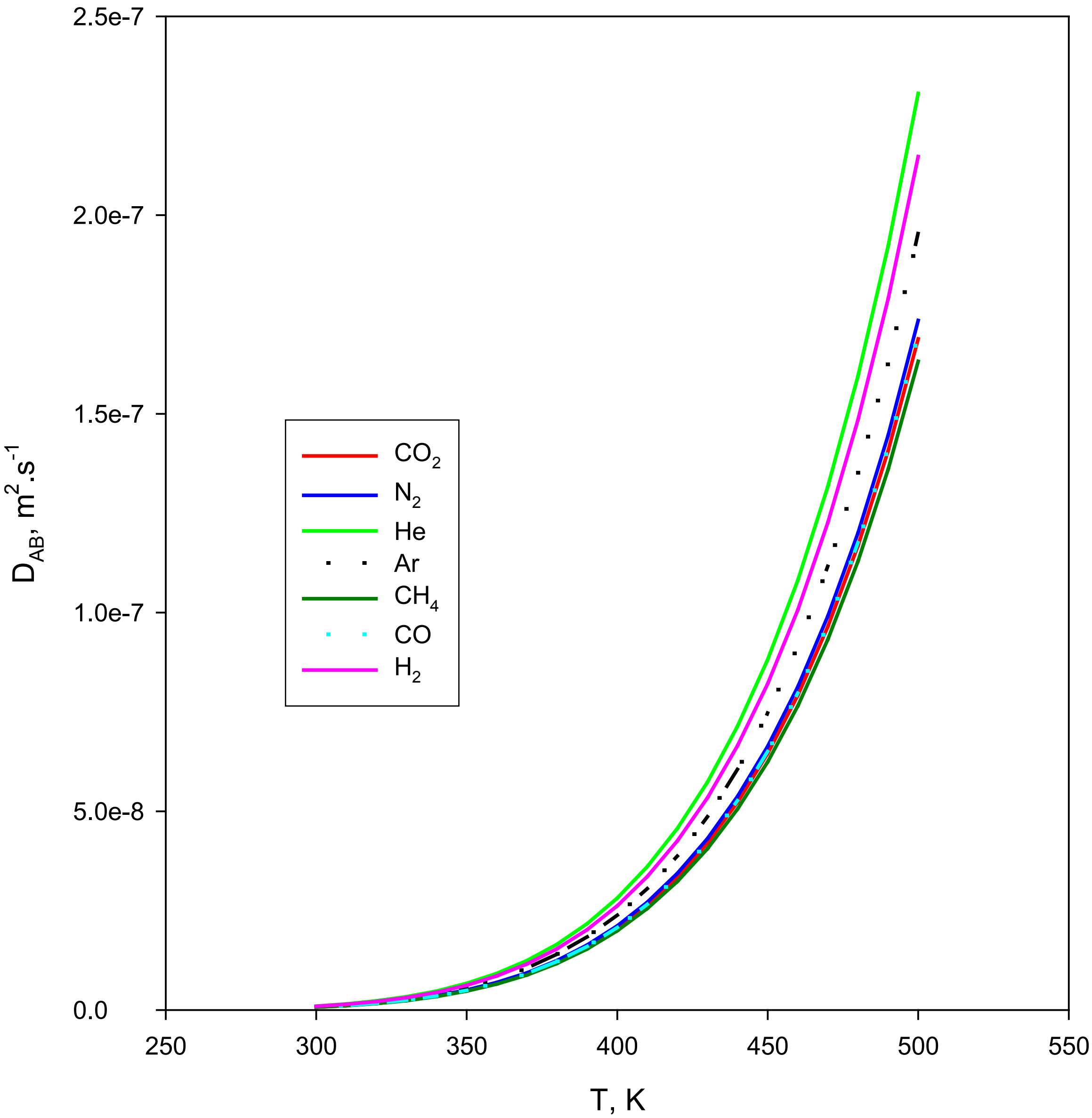

Figure 6.9: Diffusivities of gases in PP10 as a function of temperature

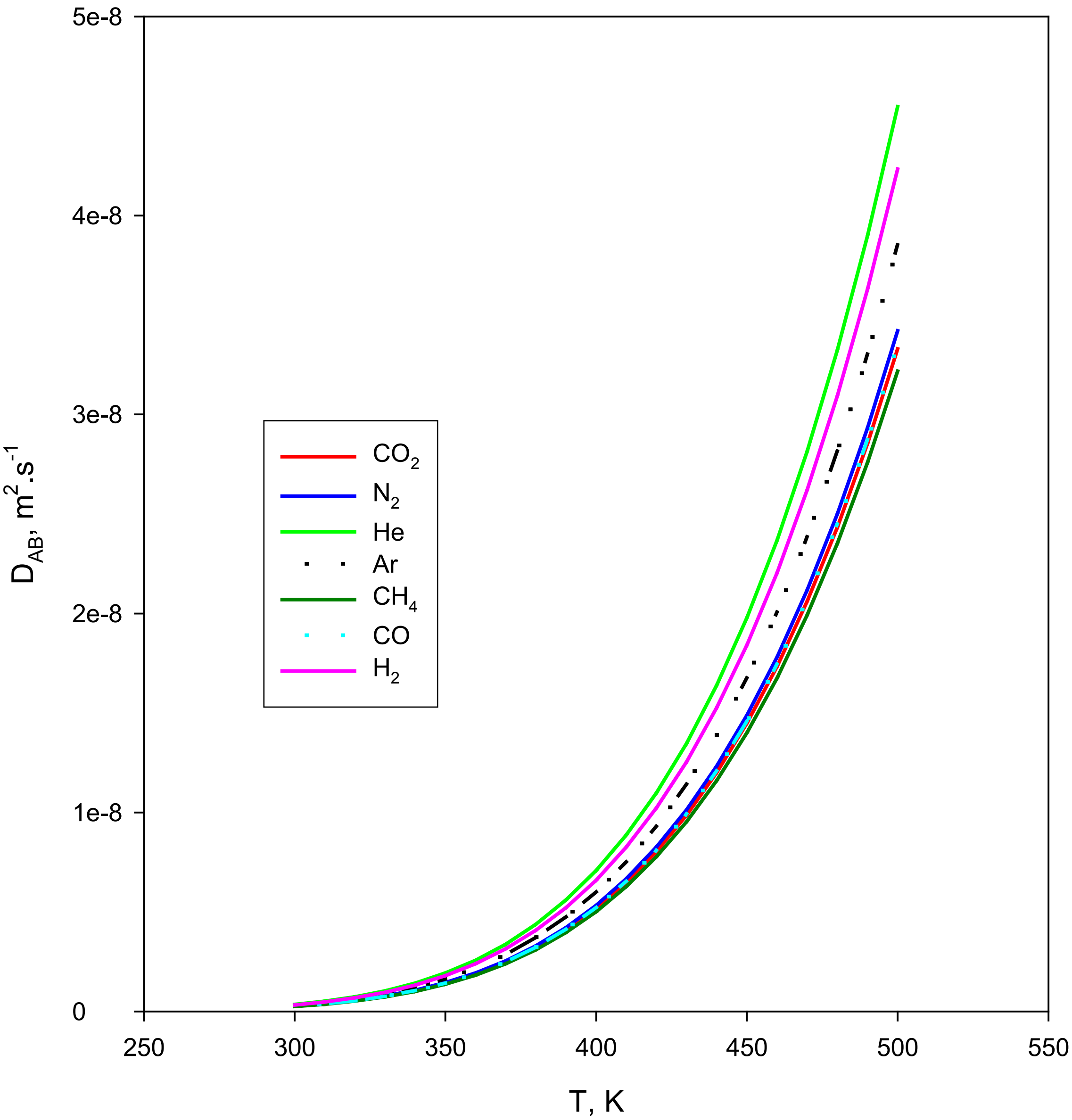

Figure 6.10: Diffusivities of gases in PP11 as a function of temperature

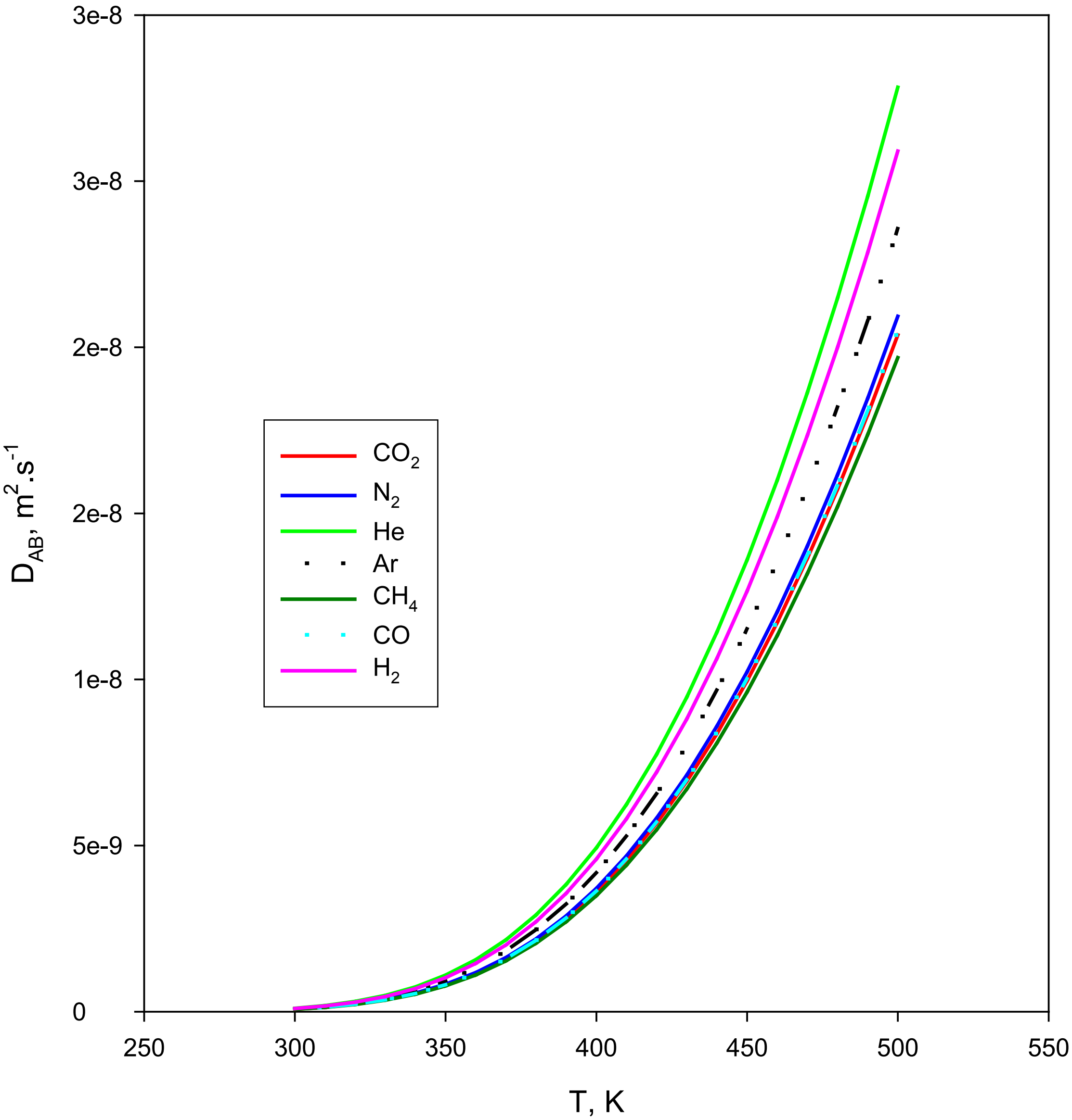

Figure 6.11: Diffusivities of gases in PP25 as a function of temperature

The results for all this physical properties are summarized in Table 6.6.

Table 6.5: Physical properties of the 3 PFCs (Flutec Fluids)[204,205]

	PP10	PP11	PP25
Molecular Formula	$C_{13}F_{22}$	$C_{14}F_{24}$	$C_{17}F_{30}$
Main molecular species	Perfluoroperhydro-fluorene	Perfluoroperhydro-phenanthrene	Perfluoro (cyclohexylmethyldecalin)
Structure	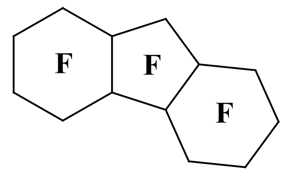	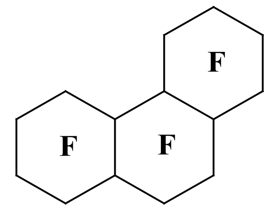	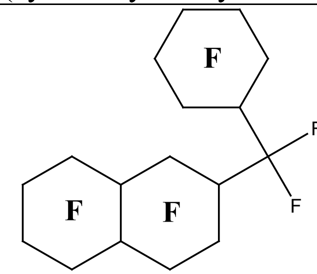
Molecular Weight	574.10	624.11	774.13
Density ($kg.m^{-3}$)	1984	2030	2049
Boiling Point (°C) at 1 atm	194	215	260
Pour Point (°C)	-40	-20	-10
Viscosity (kinematic) ($mm^2.s^{-1}$)	4.84	14.0	56.1
Viscosity (dynamic) (mPa.s)	9.58	28.4	114.5
Surface Tension ($mN.m^{-1}$)	19.7	19	-
Vapor Pressure (mbar)	< 1	< 1	< 1
Heat of Vaporization at Boiling Point ($kJ.kg^{-1}$)	71*	68*	67.9*
Specific Heat ($kJ.kg^{-1}.°C^{-1}$)	0.92*	1.07*	0.957*
Critical Temperature (°C)	357.2*	377*	400.4*
Critical Pressure (bar)	16.2*	14.6*	11.34*
Critical Volume ($L.kg^{-1}$)	1.59*	1.58*	1.574*
Thermal Conductivity ($mW.m^{-1}.°C^{-1}$)	56*	52.6*	63.8*
Coefficient of Expansion at 0°C	0.00078	0.00075	0.00084
Refractive Index n^{20}_D	1.3289	1.3348	1.3376

*Estimated Value by F2 Chemicals Ltd., UK.[204]

Table 6.6: Density, viscosity, surface tension and vapor pressure of the three PFCs

		Equations	Constants	PP10	PP11	PP25
Density	$kg.m^{-3}$	Rackett-type equation:[168,208,210] $\rho_L = A \cdot B^{\left[-\left(1-\frac{T}{T_c}\right)\right]^n}$	A ($kg.m^{-3}$) B (-) T_c (K) n (-)	628.931 0.2655 630.2 0.2532	632.911 0.2666 650.0 0.2192	635.324 0.2667 673.6 0.2136
Viscosity	Pa.s	$\ln(\eta) = A + \frac{B}{T} + \frac{C}{T^2}$	A (-) B (K^{-1}) C (K^{-2})	-13.702 2700.14 0	-14.533 3270.95 0	-8.620 -1350.47 959746
Surface Tension	$N.m^{-1}$	$\sigma_L = \sigma_1 \left(\frac{T_c - T}{T_c - 298.15} \right)^{11/9}$ [168,208]	σ_1 ($N.m^{-1}$) T_c (K)	0.0197 630.2	0.0190 650.0	0.0194 673.6
Vapor Pressure	bar	Wagner-type correlation: $\ln\left(\frac{P_s}{P_c}\right) = \left(\frac{1}{1-X}\right) \times \left(a \cdot X + b \cdot X^{1.5} + c \cdot X^3 + d \cdot X^6\right)$ where $X = 1 - T_r$ and $T_r = T/T_c$	P_c (bar) T_c (K) a (-) b (-) c (-) d (-)	16.2 630.2 -8.4376 1.7499 -5.9196 0.9399	14.6 650.0 -8.5458 1.7534 -6.0944 0.8828	11.34 673.6 -9.6797 1.8856 -8.1024 1.0326
Diffusivity	$m^2.s^{-1}$	Wilke and Chang's Equation:[208,213] $D_{AB} = 1.1728 \times 10^{-16} \frac{(\psi M_B)^{0.5} T}{\eta_B V_A^{0.6}}$ With the molar volume of the diffusing gas at its normal boiling point, defined by Tyn and Calus:[168,214] $V_A = 0.3971 \cdot (V_c)^{1.048}$ ψ is the association factor of the solvent and has a value of 1.0 for unassociated liquids[168]	M_B ($kg.kmol^{-1}$) V_c ($m^3.kmol^{-1}$)	574.10 2.7696	624.11 2.5316	774.13 2.0333

6.3 STATISTICAL EXPERIMENTAL DESIGN APPROACH

Statistical design and analysis is a powerful tool to study a multi-variable system through a statistically designed number of experiments. The advantages of this tool are reliable observation of variables, minimum number of experiments, and highly accurate statistical correlations.[215] In this study, the Central Composite Statistical Design (CCSD) and analysis technique, similar to that employed by Li et al.[216], Tekie et al.[146] and Fillion and Morsi[147] were used to construct an experimental mapping of the parameters, which insured reliable observations; minimum number of experiments; and highly accurate statistical correlations.[217]

Box and Wilson[218] first introduced this design in the 50's as an alternative to 3^k factorials in order to estimate quadratic response surface equations. In this technique, for *k* independent variables at five levels, the total number of experiments is 2^k factorial points augmented by $2\times k$ axial points, and with a number of replicates at the central point following Equation (6-10) in order to provide a design with uniform precision:[219]

$$N_{Central} = \gamma \times \left(\sqrt{N_F} + 2\right)^2 - N_F - 2\times k \tag{6-10}$$

$N_{Central}$ is the number of replicates at the central point, N_F is the number of factorial points, and γ is defined by the following equation:

$$\gamma = \frac{(k+3)+\sqrt{9k^2+14k-7}}{4\times(k+2)} \tag{6-11}$$

The factorial and axial points are equidistant from the central point to offer symmetric properties of the design. In fact, this property becomes important in the examination of the response surface since the orientation of the design does not influence anymore the precision of estimated surfaces. The central composite matrix design was made rotatable by setting the axial point values as follows:

$$\alpha = \sqrt[4]{\left(2^k\right)} \tag{6-12}$$

In this study, the effect of pressure (P), temperature (T), mixing speed (N) and liquid height (H) on the measured experimental data were statistically investigated using the CCSD of four variables (k = 4) at 5 levels. For such a design, the number of replications at the central point is ($N_C = 7$), the number of factorial points ($N_F = 16$) and the radius of the hyper-sphere ($\alpha = 2$). Table 6.7 shows the different levels for the four coded variables studied. The coded variables x_i (i=1,2,3,4) as defined by Equation (6-13) were used in the distribution and analysis of the experiments.

$$x_i = \frac{E_i - E_{i,C}}{\Delta_i} = 2\alpha\,[\frac{E_i - \left(\dfrac{E_{i,MAX} + E_{i,MIN}}{2}\right)}{\left(E_{i,MAX} - E_{i,MIN}\right)}] = \alpha\,[\frac{2 \cdot E_i - \left(E_{i,MAX} + E_{i,MIN}\right)}{\left(E_{i,MAX} - E_{i,MIN}\right)}] \tag{6-13}$$

where E_i and $E_{i,c}$ are the value of the i^{-th} variable at any point, and the central point, respectively; and Δ_i is the step size of the i^{-th} variable. $E_{i,MIN}$ and $E_{i,MAX}$ are the values of the i^{-th} variable at the minimum point and maximum point, respectively. The distribution of experiments for k = 4 can be mathematically represented by Equation (6-14):

$$\sum_{i=1}^{4} x_i^2 = \left(\sqrt[4]{N_F}\right)^2 = \alpha^2 = 2^2 \tag{6-14}$$

The coordinates of the experiments with the coded values are: (0,0,0,0) for the central point, (±1,±1,±1,±1) for the factorial points, and (±2,0,0,0), (0,±2,0,0), (0,0,±2,0) and (0,0,0,±2) for the axial points.

Table 6.7: Ranges of the operating variables and coded values in the experimental CCSD

Levels		Coded Variables	-2	-1	0	+1	+2
Temperature	K	x_1	300	350	400	450	500
	°C		26.85	76.85	126.85	176.85	226.85
Mixing Speed	Hz	x_2	10	12.5	15	17.5	20
	rpm		600	750	900	1050	1200
Liquid Height	m	x_3	0.14	0.16	0.18	0.2	0.22
	cm		14	16	18	20	22
Pressure	bar	x_4	6	12	18	24	30
	psi		87.54	175.08	262.62	350.16	437.70

6.4 STATISTICAL DISTRIBUTION OF THE EXPERIMENTS

Table 6.7 shows the range of each variable and its coded value, and Figure 6.12 shows the spatial setting of all the experiments and therefore the sets of experiments which need to be completed in order to study the effect of the 4 variables over the specified range.

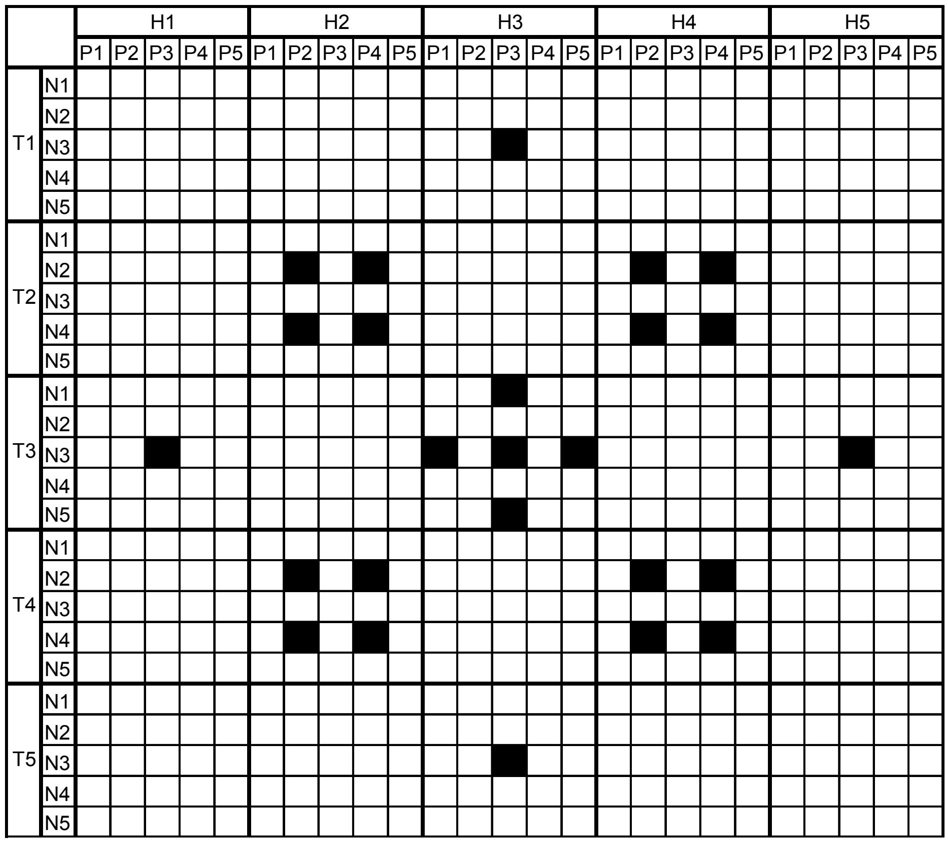

Figure 6.12: Distribution and spatial settings of the experiments according to the central composite statistical design

6.5 EXPERIMENTAL PROCEDURES

6.5.1 Measurement of the Volumetric Mass Transfer Coefficients (k_La) and the Equilibrium Gas Solubility (C^*)

The multi-step physical gas absorption method was used to obtain the equilibrium solubility and the volumetric mass transfer coefficient values of CO_2 and N_2 in the three fluorocarbon liquids used. This experimental procedure used is similar to that reported by Chang;[39] Chang et al.;[116] Chang and Morsi;[117,118] and Tekie et al.[145] It should also be mentioned that one batch of the PFC liquids was used in all experiments and no physical or chemical changes were observed. The experimental procedure followed is given below:

1. A predetermined volume of liquid is charged at room temperature into the reactor.
2. The reactor is closed and the liquid is degassed using the vacuum pump in order to reach the saturation pressure of the liquid.
3. The gas preheater is also vacuumed.
4. The gas is charged into the preheater to an initial pressure.
5. The contents of the reactor and the preheater are heated to a desired temperature.
6. The initial pressure ($P_{I,P}$) and temperature ($T_{I,P}$) in the preheater is recorded.
7. The gas is charged to the reactor at the same temperature and at an initial predetermined pressure (P_I).
8. The final pressure and temperature of the preheater is recorded.
9. The reactor content is stirred at a given mixing speed until the thermodynamic equilibrium, characterized by a constant final pressure in the reactor (P_F), is reached. The pressure decline (P_t) is recorded as a function of time.

10. Steps 6 through 9 were repeated to collect multiple data points at different pressures as shown in Figure 6.13.

The experimental procedure given above was followed at each run with different temperature, mixing speed, superficial gas velocity and liquid height. After each run, C^* and k_La were calculated using a modified Peng-Robinson Equation of State. Detailed calculations of these two values are given in Section 7.1. The computer programs developed by Chang[39] to calculate C^* and k_La were modified for the present gas-liquid systems. The computer programs were designed to:

1. Setup the interfacing channels for data collection.

2. Calibrate the pressure transducers at atmospheric conditions.

3. Record all the operating conditions, including temperature, mixing speed, liquid height, etc. of the system in both phases.

4. Monitor the reactor and the preheater temperatures, induced gas flow rate, superficial gas velocity and pressures on a continuous basis during the experiment.

5. Collect the pressure decline data during the gas absorption on a real time basis.

6. Calculate C^* at equilibrium conditions.

7. Calculate k_La values during the transient period.

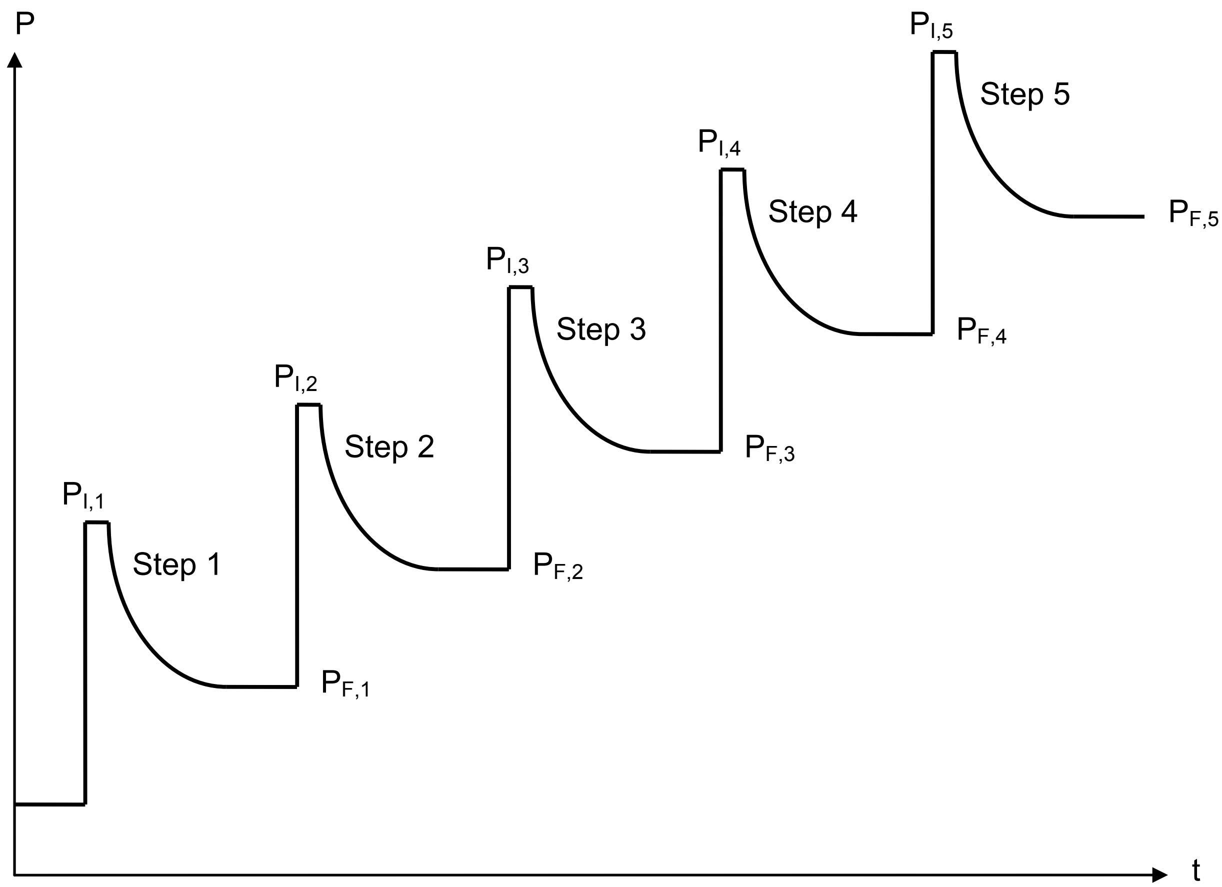

Figure 6.13: Schematic of the multi-step procedure at constant temperature (T), mixing speed (N) and liquid height (H_L)

6.5.2 Measurement of the Gas Bubble Size, d_S

The photographic method, similar to that employed by Fillion and Morsi,[147] was used to measure the bubble size. The bubbles were recorded through the Jerguson sight-window with a digital video camera under the desired operating conditions. The camera was focused on the cooling coil, located above the impeller; and a light source was mounted over the camera in order to provide an optimal lighting. The cooling coil of known outside diameter of 0.00635 m was used to calibrate the bubble size analysis software. The focus of the camera on the cooling coil was essential to avoid and prevent interferences among bubbles, and only discernible bubbles in the focus plan were taken into consideration. The recorded images were then selected and transferred through an image Grabber Software, Snappy 4.0, to a PC. Using Adobe Photoshop CS2 version 9.0 software, the cooling coil and over 200 bubbles were selected. Their contours were then treated and converted in a black and white image, where the selection appeared in white. Particle analysis software, Optimas Version 4.1 from BioScan, was then used to analyze the digitized images. The Sauter mean bubble diameter is then calculated from the bubble sizes measured.

6.5.3 Measurement of the Gas Holdup, ε_G

The dispersion height technique was used to measure the gas holdup under the designed operating conditions. The digital video camera was located in front of the Jerguson glass window of the reactor, and focused at the gas-liquid interface. As a reference, a ruler was placed along the sight-window and the enlarged images on the TV screen were used to precisely measure the dispersion height. Therefore, at any given mixing speed, the gas holdup was determined from the difference between the dispersion height, H_D, and the clear liquid height, H.

7.0 CALCULATION METHODS

7.1 CALCULATION OF THE EQUILIBRIUM GAS SOLUBILITY, C*

The calculation of *C** was carried out under the following assumptions: (1) non-ideal behavior of the liquid and gas phases; and (2) the liquid phase is well mixed. The amount of gas-absorbed prior to the agitation was also accounted which made the calculation of *C** more rigorous and accurate compared with previous studies.[48,51] The Peng-Robinson Equation of State (PR-EOS)[39,208,220] can be written as:

$$P = \frac{RT}{v - b} - \frac{a(T)}{v(v+b) + b(v-b)} \tag{7-1}$$

This equation can be expressed in terms of the compressibility factor, Z as:

$$Z^3 - (1-B)Z^2 + \left(A - 3B^2 - 2B\right)Z - \left(AB - B^2 - B^3\right) = 0 \tag{7-2}$$

where

$$A = \frac{aP}{R^2T^2} \tag{7-3}$$

$$B = \frac{bP}{RT} \tag{7-4}$$

$$Z = \frac{Pv}{RT} \tag{7-5}$$

For a single-component, two-phase system the solution of Equation (7-2) results in three roots with the largest positive root corresponding to the vapor phase and the smallest positive root greater than "*b*" corresponding to the liquid phase. At the critical point:

$$a(T_c) = 0.45724\frac{R^2 T_c^2}{P_c} \tag{7-6}$$

$$b(T_c) = 0.077796\frac{RT_c}{P_c} \tag{7-7}$$

At any temperature:

$$a(T) = a(T_c) \cdot \alpha(T_r, \omega) \tag{7-8}$$

$$b(T) = b(T_c) \tag{7-9}$$

$$\alpha = \left[1 + \kappa\left(1 - \mathrm{T}_\mathrm{R}^{1/2}\right)\right]^2 \tag{7-10}$$

with

$$\kappa = 0.37464 + 1.5422\,\omega - 0.26992\omega^2 \tag{7-11}$$

The fugacity of a pure component is written as:

$$\ln\left(\frac{f}{P}\right) = Z - 1 - \ln(Z - B) - \frac{A}{2\sqrt{2}B}\ln\frac{Z + \left(1 + \sqrt{2}\right)B}{Z + \left(1 - \sqrt{2}\right)B} \tag{7-12}$$

For a binary system, the binary interaction parameter δ_{ij} is required in order to use the PR-EOS. The mixing rules are defined as follows:

$$a = \sum_i \sum_j \; x_i \; x_j \; a_{i,j} \tag{7-13}$$

$$b = \sum_i x_i b_i \tag{7-14}$$

$$a_{ij} = \left(1 - \delta_{ij}\right)\sqrt{a_i a_j} \tag{7-15}$$

The fugacity of each component in the liquid phase is calculated from:

$$\ln\frac{f_k}{x_k P} = \frac{b_k}{b}(Z-1) - \ln(Z-B) - \frac{A}{2\sqrt{2}B}\left(\frac{\sum_i x_i a_{ik}}{a}\right)\ln\frac{Z+\left(1+\sqrt{2}\right)B}{Z+\left(1-\sqrt{2}\right)B} \tag{7-16}$$

If the values of x_i and x_j are replaced by y_i and y_j, Equations (7-13), (7-14) and (7-16) can be used for the vapor phase.

The PR-EOS was selected to calculate the liquid and gas phase densities of the system, as well as the solubility of the gases, C^*, the concentration of the gases in the liquid, C_L, and the total liquid volume, V_L, which was subsequently used in the $k_L a$ calculations. In order to check the accuracy of the PR-EOS, the following steps were followed:

1. The saturated liquid density of the liquid was calculated using the Rackett Equation (6-2).

2. The PR-EOS was used to calculate the saturated liquid density of the liquid, where the pressure of the saturated liquid is the vapor pressure estimated from the Wagner's Equation.

3. These density values were compared, as shown in Figure 7.1, and a significant difference can be observed.

Since the Rackett equation provides accurate estimates of the saturated liquid density of fluorocarbons, two parameters Ψ_1 and Ψ_2 were introduced in the sub-functions of the PR-EOS in order to correct the predicted liquid-phase density of the PR-EOS as previously reported by Enick et al.,[221] Chang[39] and Tekie.[48] The two correction factors, Ψ_1 and Ψ_2, were introduced into the two sub-functions in the PR-EOS as Enick et al.:[221]

$$\alpha^{1/2} = 1 + \Psi_1 \kappa (1 - T_R^{1/2}) \tag{7-17}$$

$$b(T_C) = \Psi_2\, 0.07780 \frac{RT_C}{P_C} \tag{7-18}$$

Ψ_1 and Ψ_2 were then optimized during an iteration process in which the squared error between the saturated liquid densities obtained by the modified PR-EOS and the Rackett Equation (6-2) was minimized. The optimized values of Ψ_1 and Ψ_2 were then correlated as a function of temperature with the following equations:

$$\Psi_1 = A + B\cdot 10^{-3}T + C\cdot 10^{-6}T^2 + D\cdot 10^{-8}T^3 + E\cdot 10^{-11}T^4 \tag{7-19}$$

$$\Psi_2 = A + B\cdot 10^{-3}T + C\cdot 10^{-6}T^2 + D\cdot 10^{-8}T^3 + E\cdot 10^{-11}T^4 \tag{7-20}$$

with T in Equations (7-19) and (7-20) ranging from 300 to 500K. The values of the constants A, B, C, D and E can be found in Table 7.1 for each liquid.

Table 7.1: Constants in Equations (7-19) and (7-20)

Liquid		A	B	C	D	E
PP10	Ψ_1	-0.4648	16.9032	-69.8008	13.1745	-9.3029
	Ψ_2	0.9211	0.9170	-2.8960	0.6602	-0.6885
PP11	Ψ_1	-0.5166	16.9074	-72.1900	13.8568	-10.1224
	Ψ_2	0.9206	0.2387	-0.2900	0.1188	-0.2388
PP25	Ψ_1	0.0538	9.4644	-41.1697	8.0470	-6.0036
	Ψ_2	0.8452	0.3418	-0.7831	0.2187	-0.2745

Figure 7.1 shows the saturated liquid density of the three fluorocarbons from the Rackett equation, the PR-EOS without correction and the modified PR-EOS, and as can be seen in this figure, a very good agreement can be reported between the modified PR-EOS and the Rackett equation.

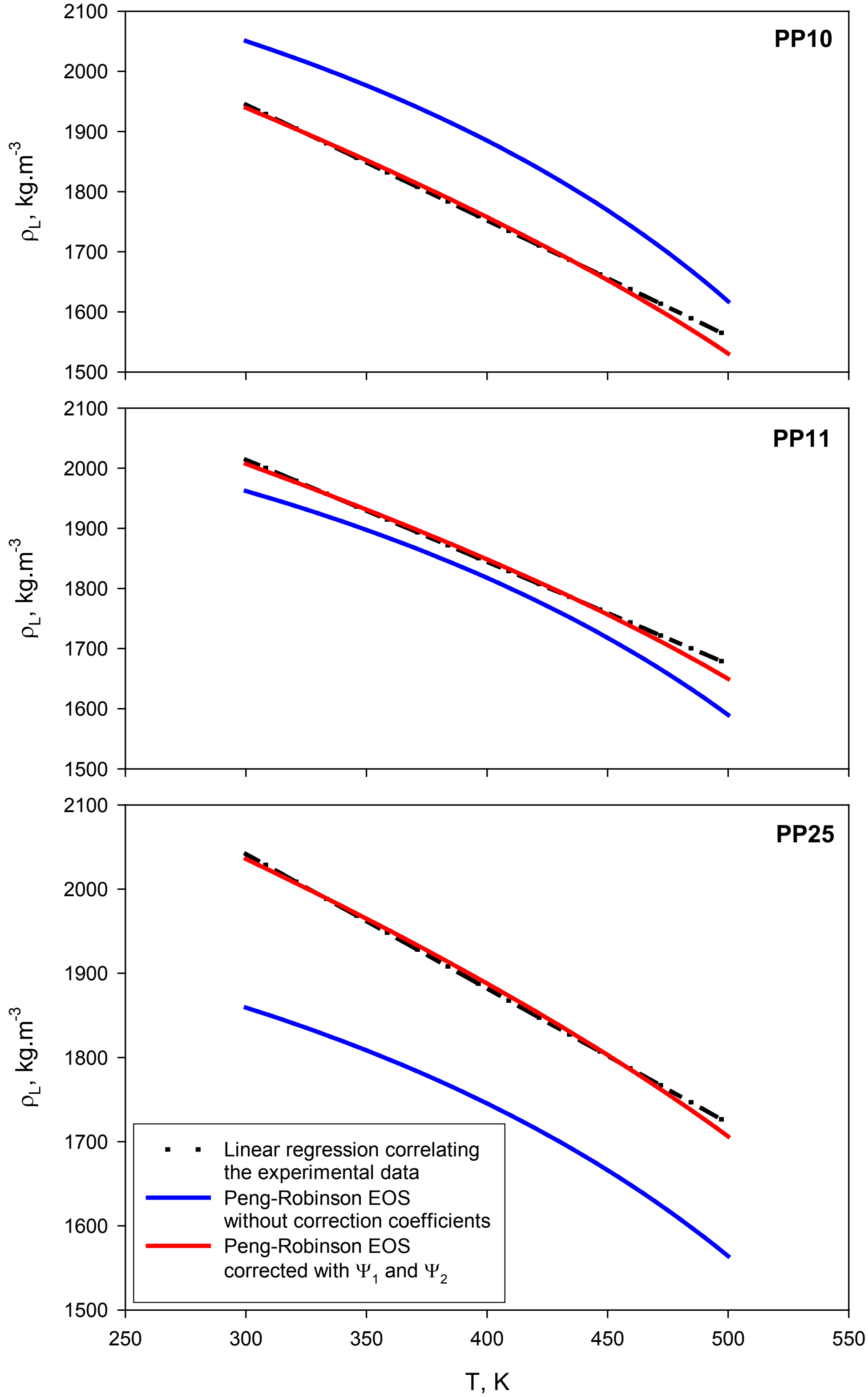

Figure 7.1: Validation of the modified PR-EOS by liquid density calculation

The modified Peng-Robinson Equation of State (PR-EOS), coupled with component mole and volume balances, was used for the calculation of the equilibrium solubility of the gases in the fluorocarbon liquids. For a two-component, two-phase system at equilibrium, the fugacities of each component in each phase are equal:

$$f_i^L = f_i^G \tag{7-21}$$

The fugacities were calculated using Equation (7-16). From the mass balance equation, the total number of moles in the reactor stays the same as:

$$N_T = N_G + N_L \tag{7-22}$$

The component balance could be written as:

$$N_1 = N_G \ y_1 + N_L \ x_1 \tag{7-23}$$

$$N_2 = N_G \ y_2 + N_L \ x_2 \tag{7-24}$$

The overall volume balance is:

$$V_R = V_L + V_G \tag{7-25}$$

V_L and V_G were calculated using the number of moles and the molar volumes (v_G and v_L) obtained from the modified PR-EOS as:

$$V_G = N_G \, v_G \tag{7-26}$$

$$V_L = N_L \, v_L \tag{7-27}$$

In addition to these equations, the number of moles charged to the reactor, N_I, is calculated from the difference between the initial and final conditions in the preheater, using the PR-EOS. The equations used for the calculation of the initial and final molar volumes are:

$$v_G^I = \frac{R T_I Z_G^I}{P_I} \tag{7-28}$$

$$v_G^F = \frac{RT_F Z_G^F}{P_F} \tag{7-29}$$

Subsequently, the number of moles charged becomes:

$$N_1 = V_{preh}\left(\frac{1}{v_G^I} - \frac{1}{v_G^F}\right) \tag{7-30}$$

where V_{preh} is the volume of the preheater. The initial number of moles of liquid in the reactor was determined from the amount of liquid charged and its molar volume at ambient conditions as:

$$N_2 = \frac{V_L}{v_L} \tag{7-31}$$

The liquid molar volume can be calculated from:

$$v_L = \frac{Z_L RT}{P_T} \tag{7-32}$$

Based on the above equations, an iterative algorithm for calculating C^*, initially developed by Chang[39] was modified for the present systems and used. The main steps of this algorithm are depicted in Figure 7.2 and are summarized in the following.

1. The vapor pressure P_S of the fluorocarbon liquid is calculated using Wagner Equation, and the initial values of $y_2 = P_S/P_T$ and $x_1 = 0$ are assumed.
2. A value of the binary interaction parameter, δ_{ij} is assumed.
3. y_1 is calculated as $y_1 = 1\text{-}y_2$.
4. Z_G is calculated using Equations (7-2) to (7-5), (7-13) and (7-14).
5. The molar volume of the gas phase v_G is calculated from:

$$v_G = \frac{Z_G RT}{P_T} \tag{7-33}$$

6. The vapor phase fugacities of both components are calculated using Equation (7-16).

7. x_2 is calculated from $x_2 = 1 - x_1$.

8. Z_L is calculated using Equations (7-2) to (7-5), (7-13) and (7-14).

9. The molar volume of the liquid phase v_L is calculated from:

$$v_L = \frac{Z_L RT}{P_T} \tag{7-34}$$

10. At equilibrium, $f_1^L = f_1^G$, from which a new value of x_1, $\bar{x}_1$ is obtained.

11. If the error calculated from $\Delta x = |\bar{x}_1 - x_1|$ is not less than the specified accuracy (10^{-6}), steps 7 to 11 are repeated with the new value of $x_1 = \bar{x}_1$.

12. f_2^L is obtained from Equation (7-16), since x_1 is fixed.

13. At equilibrium, $f_2^L = f_2^G$ must be true, and a new value of y_2, $\bar{y}_2$ is obtained.

14. If the error calculated from $\Delta y = |\bar{y}_2 - y_2|$ is not less than the specified accuracy (10^{-6}), steps 3 to 13 are repeated with the new value $y_2 = \bar{y}_2$.

15. From Equations (7-23) and (7-24), N_L and N_G are calculated.

16. The gas and liquid phase volumes are determined from $V_G = (v_G \times N_G)$ and $V_L = (v_L \times N_L)$, respectively.

17. A volume balance is confirmed if $V_R = (V_G + V_L)$, otherwise a new value of the interaction parameter δij is assumed and steps 2 through 15 are repeated.

18. If the volume balance is confirmed, the equilibrium values of x_1, y_1, v_L and v_G are obtained at the corresponding pressure and temperature. Finally C^* is calculated from:

$$C^* = \frac{x_1}{v_L} \tag{7-35}$$

Using these data, an expression of the gas solubility C^* as a function of pressure can be developed at a constant temperature as:

$$C^* = E_0 P_{1,F} + E_1 P_{1,F}^2 \qquad (7\text{-}36)$$

with E_1=0 if the gas-liquid system obeys Henry's law.

The density of the three PFC liquids were experimentally measured and then correlated as a function of temperature using a Rackett-type equation[168,208,210] (See Equation (6-2) in Section 6.2.2, page 60)

The Peng-Robinson Equation of State was modified to precisely predict the measured density of the three PFCs using the Rackett-type equation given above.[222] At thermodynamic equilibrium, the modified PR-EOS was employed to calculate the equilibrium solubility, C^*. The values were then correlated as a function of the solute gas partial pressure at constant temperature using Equation (7-36).

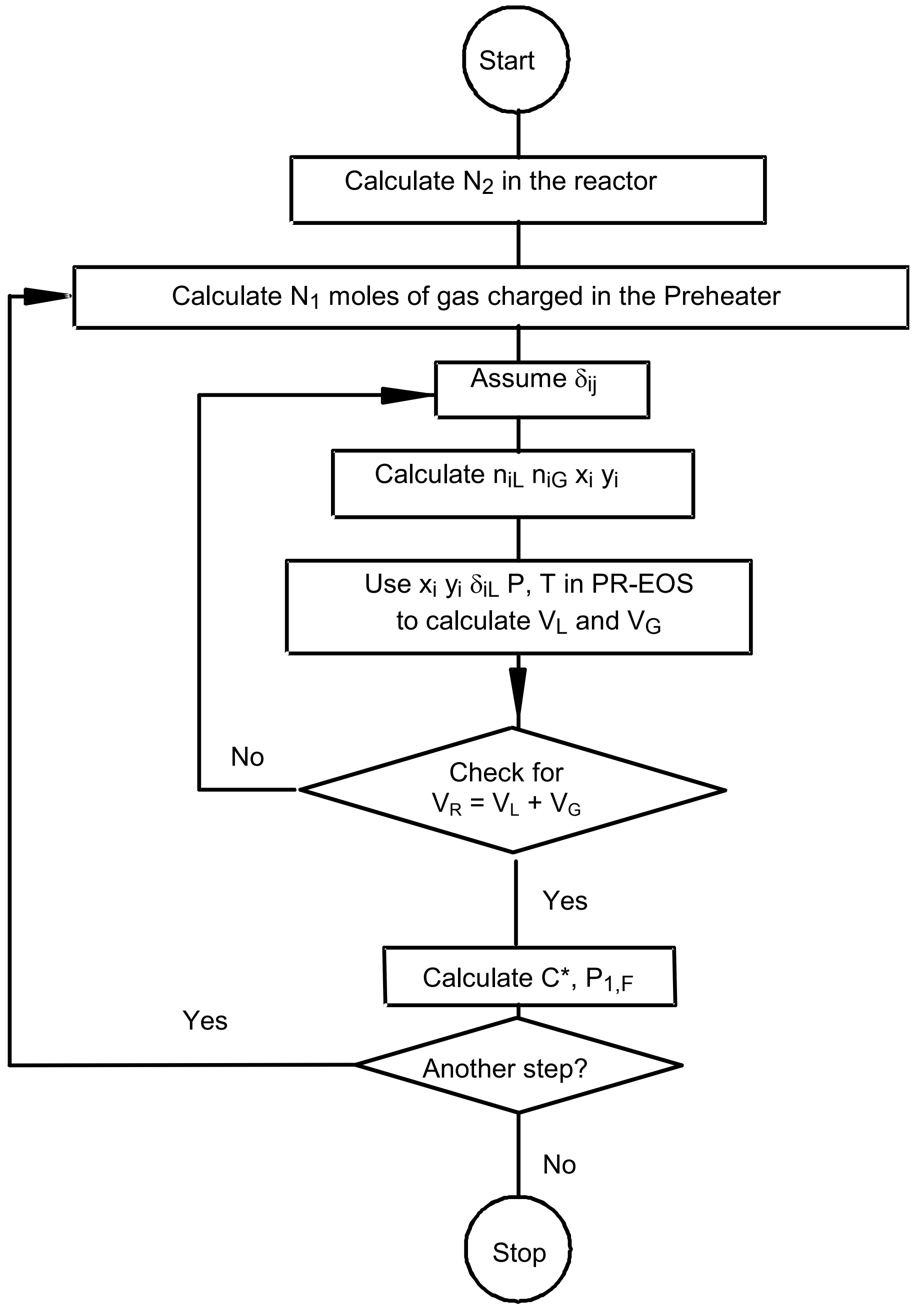

Figure 7.2: Algorithm for C^* calculation in the agitated reactors[39]

7.2 CALCULATION OF THE VOLUMETRIC MASS TRANSFER COEFFICIENT

The calculation of k_La was carried out under the following assumptions: (1) non-ideal behavior of the liquid and gas phases; (2) the liquid phase is well mixed; (3) the mass transfer resistance of the gas phase is negligible compared to the liquid phase. The transient physical gas absorption technique, where the decline of the total pressure of the system with time is recorded, in conjunction with total mole was used to calculate k_La values of CO_2 and N_2 in the three PFC liquids. The rate of mass transfer from the solute gas to the liquid phase is calculated using the two-film model as:

$$\frac{dn_{1L}}{dt} = k_L a\left(C^* - C_L\right) \times V_L \tag{7-37}$$

where n_{1L} is the number of moles of component i transferred from the gas-phase into the liquid-phase, C^* is the concentration of the solute gas at the gas-liquid interface and C_L is the concentration of the gas in liquid bulk. In order to calculate k_La from Equation (7-37), C^*, C_L and n_{1L} were determined as a function of the solute gas partial pressure P_1. From the gas partial pressure P_1 one can calculate the number of moles in the gas phase using the Peng-Robinson equation of state, and knowing the initial number of moles in the gas phase by subtracting the number of mole at any time t, the number of mole in the liquid phase (n_{1L}) can be calculated. Details of a typical pressure versus time experimental data curve can be found in Appendix C. At the gas-liquid interface, the liquid is assumed to be in instantaneous equilibrium with the partial pressure P_1 of the gas phase, hence P_{1F} is replaced by P_1 in Equation (7-36) to obtain C^*.

Since the liquid-phase volume (V_L) is expected to change with time due to the high solubility of CO_2 in the liquid solvent, Equation (7-37) can be written as:

$$\frac{dn_{i,L}}{\left(n_{i,t}^{*} - n_{i,L}\right)} = \left(k_L a\right) dt \tag{7-38}$$

In this equation, $n^{*}_{i,t}$ represents instantaneous equilibrium gas-liquid interface number of moles of component i at any time (t). The corresponding amount of component i within the liquid-phase ($n_{i,L}$) was calculated using the P-R EOS coupled with a reactor volume balance since a batch reactor system was used in all experiments. Assuming k_La constant during the absorption, Equation (7-38) was numerically integrated using Athena Visual Studio Software Package (Version 12.3) from the initial condition (t = 0) to any time (t) near the thermodynamic equilibrium as:

$$\int_0^{n_{i,L}} \frac{dn_{i,L}}{\left(n_{i,t}^{*} - n_{i,L}\right)} = \left(k_L a\right) \int_0^t dt \tag{7-39}$$

The incremental integration of the left-hand-side of the above equation, designated as $F(n_{i,L})$ was plotted as a function of time (t) as:

$$F\left(n_{i,L}\right) = \left(k_L a\right) t \tag{7-40}$$

Then, if the left hand side of the Equation (7-40), plotted versus time, yields a straight line with zero intercept, its slope will correspond to k_La. It should be mentioned that k_La values presented in this study were obtained with a regression coefficient (R^2) greater than 0.98.

7.3 CALCULATION OF GAS HOLDUP AND SAUTER MEAN BUBBLE DIAMETER

In the agitated reactor, the dispersion height technique was used to measure the gas holdup under the designed operating conditions, since the manometric method was reportedly unsuccessful by Tekie[48] due to considerable turbulences created by the impeller, affecting the differential pressure (dP) cells signal. At any given operating conditions, ε_G was determined from the difference between the dispersion height, H_D, and clear liquid height, H, as:

$$\varepsilon_G = \frac{H_D - H}{H_D} \tag{7-41}$$

The Sauter mean Bubble diameter was calculated by measuring the bubble size for about 200 gas bubbles to insure reproducibility of the experimental results. It was then calculated from the bubble volume to area ratio as:[48,51]

$$d_S = \frac{\sum_{i=1}^{k} d_{B\,i}^3}{\sum_{i=1}^{k} d_{B\,i}^2} \tag{7-42}$$

8.0 RESULTS AND DISCUSSION OF PERFLUORINATED SOLVENTS

8.1 EQUILIBRIUM GAS SOLUBILITY OF CO_2 AND N_2 IN THE PFC SOLVENTS

The equilibrium solubilities of CO_2 and N_2 in the three perfluorocarbons used in this study could not be found in the open literature; and the experimental data obtained were with an average deviation of less than 12%. The solubility of CO_2 and N_2, expressed in mole fraction (x^*), in PP10, PP11, and PP25 liquids are presented as a function of the gas partial pressure ($P_{1,F}$) at constant temperatures in Figure 8.1, respectively. As can be seen in these figures, the CO_2 and N_2 solubilities increase with the gas partial pressure at constant temperature in the three solvents. The x^* values of the CO_2 and N_2 in the three PFCs used appeared to vary non-linearly with gas partial pressure at constant temperature and can be modeled by the following equation:

$$x^* = E_0 P_{1,F} + E_1 P_{1,F}^2 \tag{8-1}$$

The values of the coefficients E_0 and E_1 are given in Table 8.1. It should be noted that for N_2 almost a linear relationship can be assumed which is obvious from the small values of E_1. The increase of solubility with pressure can be attributed to the increase of the concentration gradient of the gas species between the two phases, which leads to the increase of the gas amount in the liquid. This solubility behavior is in accordance with a number of findings available in the literature.[48,51,52,85,115]

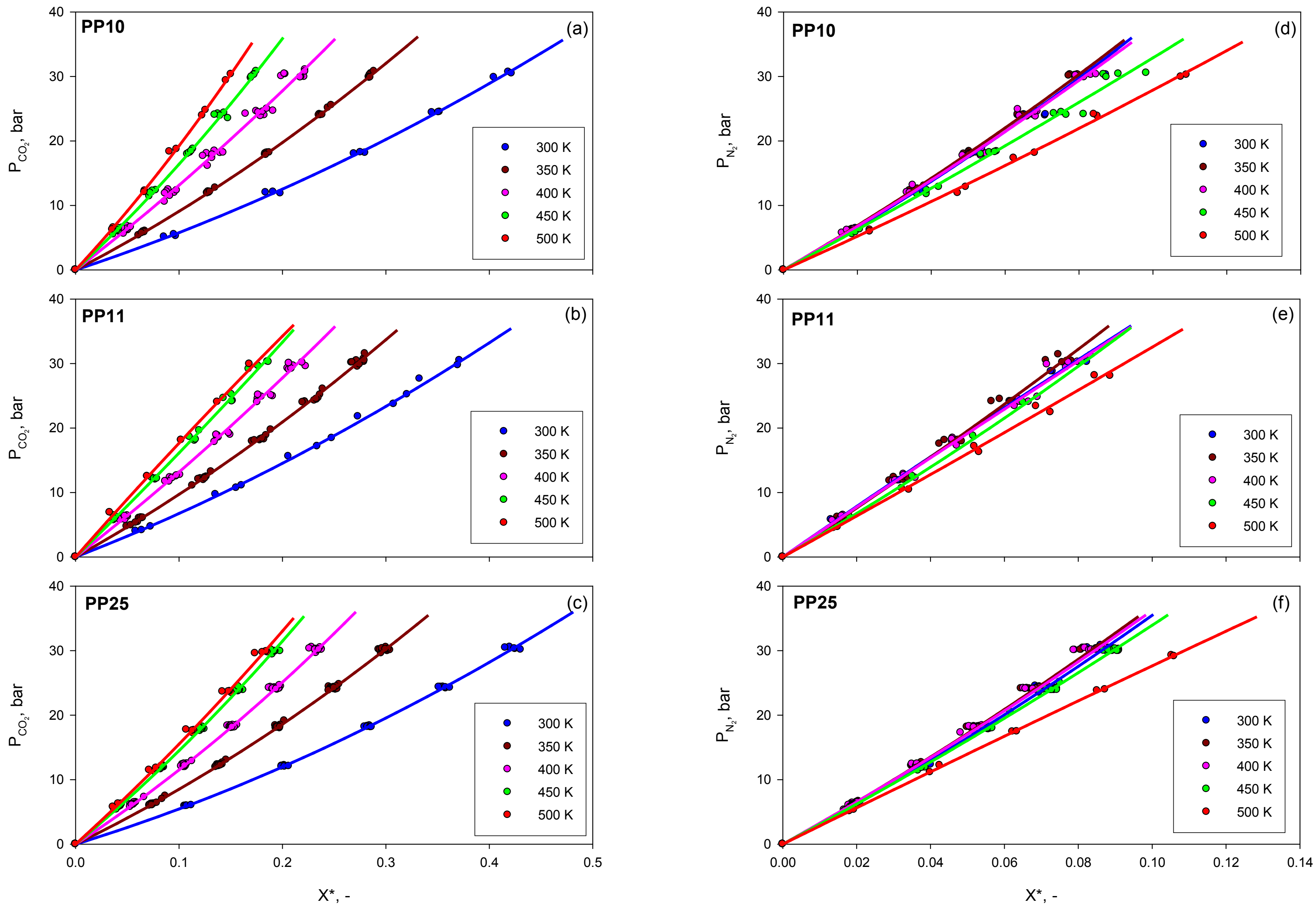

Figure 8.1: Effect of pressure and temperature on the solubility of CO_2 and N_2 in PP10, PP11 and PP25

Table 8.1: Coefficients E_0 and E_1 in Equation (8-1)

Gas	Temperature	PP10		PP11		PP25	
		$E_0\times10^3$	$E_1\times10^5$	$E_0\times10^3$	$E_1\times10^5$	$E_0\times10^3$	$E_1\times10^5$
CO_2	300	17.5302	-12.8406	15.3058	-10.2806	18.4282	-15.0400
	350	11.5405	-6.9523	10.8460	-5.9840	12.2822	-7.9309
	400	8.1781	-3.6591	8.0371	-3.0860	9.2580	-5.0741
	450	6.6328	-3.1160	6.4706	-1.5321	7.4069	-3.4224
	500	5.6870	-2.4788	5.5048	0.9222	6.8706	-2.5957
N_2	300	3.1085	-1.4215	2.5629	0.1346	3.2858	-1.4113
	350	2.9933	-1.1992	2.7310	-0.8385	3.1385	-1.2357
	400	3.0525	-1.1623	2.6343	-0.0707	3.1387	-1.1144
	450	3.3380	-1.0386	3.0609	-1.2516	3.2727	-0.9885
	500	3.8964	-1.1277	3.2224	-0.5467	3.5397	0.2844

At infinite dilution (low gas solubility) and for ideal solutions, the Henry's law can be applied to model the gas solubility. The definition of the Henry's law constant at infinite dilution (He_∞) can be approximately estimated, at constant temperature, using the following equation:

$$He_\infty \cong \lim_{x^* \to 0}\left(\frac{P_i}{x^*}\right) \tag{8-2}$$

The values of the He_∞ were calculated at constant temperature for CO_2 and N_2 in PP10, PP11, and PP25 and the values were correlated as a function of the reciprocal of temperature (*1/T*). This because the effect of temperature on x^* values and has been generally studied through the Henry's law (*He*) constant and the standard heat of solution of a gas (ΔH^o).[223,224] In certain cases (e.g., for relatively small temperature ranges), the standard heat of solution of a gas (ΔH^o) may be treated as a constant and can be related to the Henry's law constant at infinite dilution (He_∞) through Equation (8-3).[224]

$$He_\infty = He_{0,\infty} \times exp\left(\frac{\Delta H^0}{RT}\right) \tag{8-3}$$

However, there are other cases (e.g., for relatively wide temperature ranges) in which ΔH^o is temperature dependent and, therefore, is not a constant. For the latter cases, ΔH^o may be obtained from Equation (8-4).[223,224]

$$\frac{\Delta H^0}{R} = \left[\frac{\partial\left(ln\left(He_\infty\right)\right)}{\partial\left(1/T\right)}\right] \tag{8-4}$$

Figure 8.2 shows that for CO_2 the Henry's law constant (He_∞) can be correlated as a function of the reciprocal of temperature ($1/T$) using an Arrhenius-type equation over the temperature range from 300 to 500 K, which means that the standard heat of solution is constant. Figure 8.2 also illustrates that CO_2 shows higher solubility in the Selexol solvent[224] at relatively low temperature. It should be mentioned, however, that the Selexol solvent cannot be used at temperatures greater than 39°C (312 K), which underlines the thermal stability of the PFCs and underscores their ability to absorb CO_2 at temperatures as high as 500K.

The apparent activation energies of absorption for CO_2 in the three PFCs were obtained using Equation (8-4) within the temperature range of 300-500 K.

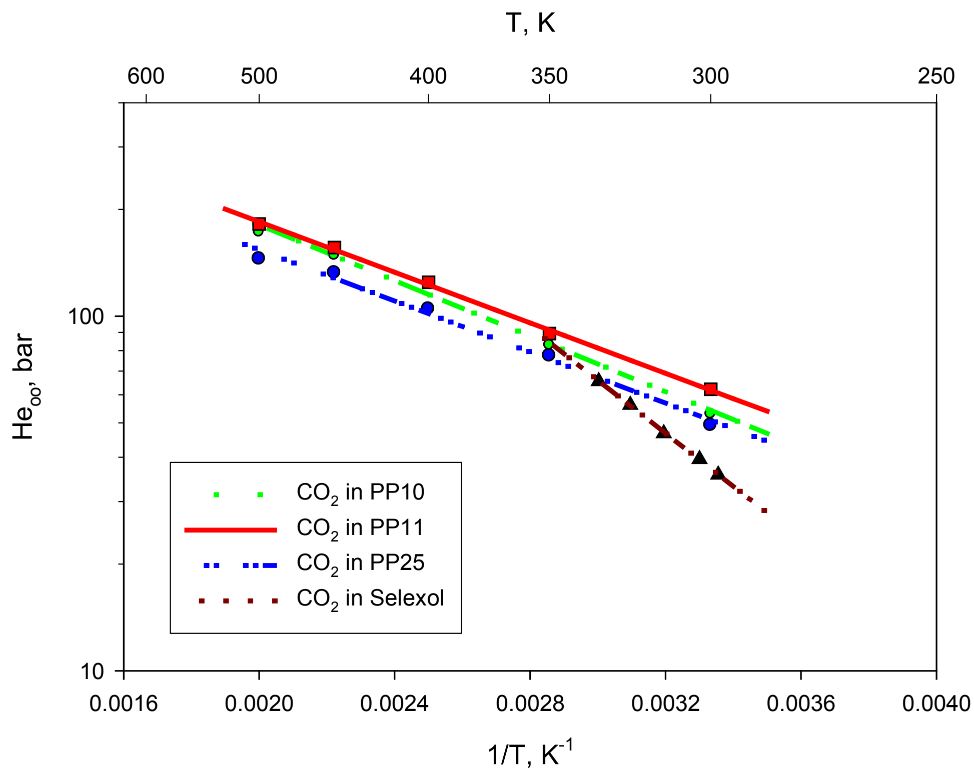

Figure 8.2: Effect of temperature on Henry law constants for CO_2 in the fluorocarbons and Selexol solvent[224]

For numerous gas-liquid systems, on the other hand, Himmelblau,[223] Schulze and Prausnitz[225] and Carroll et al.[226] reported a turn-around point when plotting ln(He_{∞}) versus $1/T$, which means that there are several cases for which the standard heat of solution is dependent on the temperature. In the present study, this behavior was observed when plotting $ln(He_{\infty})$ as a function of ($1/T$) for N_2. Figure 8.3 shows that for N_2 He_{∞} appears to increase with T, until T_{MAX}, the turn-around point, and then decreases with further increase of temperature.

Himmelblau,[223] Schulze and Prausnitz,[225] Battino et al.[227] and Carroll et al.[226] used polynomial functions of temperature or reciprocal of temperature in order to represent the temperature dependency of the gas He_{∞} under these conditions. Following a similar procedure to that developed by Himmelblau,[223] the dependency of He_{∞} on with temperature was described using Equation (8-5), where its coefficients are listed in Table 8.2.

$$ln\left(He_{\infty}\right) = A + \frac{B}{T} + \frac{C}{T^2} \tag{8-5}$$

Table 8.2: Coefficients in He_{∞} correlation, Equations (8-3) and (8-5)

		PP10	PP11	PP25
CO_2	$He_{0,\infty}$ (*bar*)	1099.25	952.76	807.06
	ΔH^0 (*kJ.kmol^{-1}*)	-7,505.68	-6,821.31	-6894.64
N_2	A	2.8590	3.9861	4.2334
	B	2,092.9	1,326.2	1,105.5
	C	-368,333	-223,437	-198,583

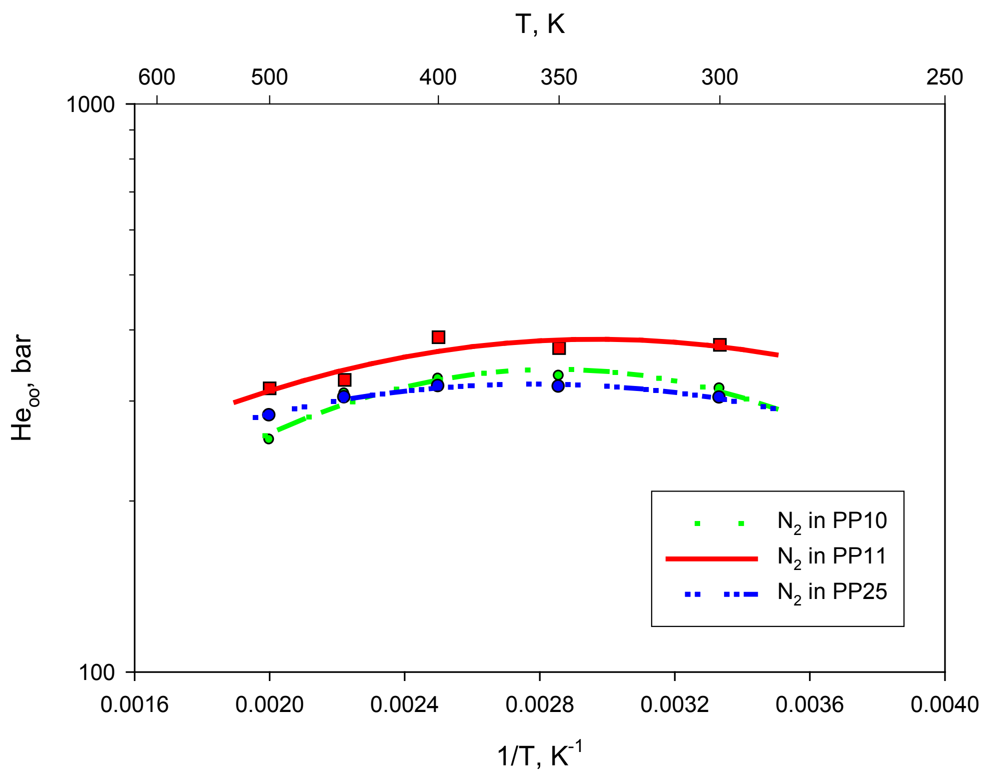

Figure 8.3: Effect of temperature on Henry law constants for N_2 in the fluorocarbons

The values of the standard heat of solution for N_2 were calculated using Equation (8-6), which was derived from Equations (8-4) and (8-5).

$$\Delta H^0 = R\left(B + \frac{2C}{T}\right) \tag{8-6}$$

The values of He_∞ and ΔH^0 calculated using Equations (8-5) and (8-6) are given in Table 8.3. The knowledge of the standard heat of solution in physical absorption processes is important to verify the occurrence of chemical reaction in the range of temperature studied. In fact, Doraiswamy and Sharma[228] reported that ΔE (the apparent activation energy of absorption, which, by definition, equals $-\Delta H^0$),[48,51,115,195,223,225-227,229-232] for mass transfer without chemical reaction should be < 21,000 $kJ.kmol^{-1}$, which is in agreement with the values listed in Tables 8.2 and 8.3.

Table 8.3: He_∞ and ΔH^0 for N_2 in the three PFCs

		300	350	400	450	500
PP10	He_∞ (*bar*)	311.94	341.03	326.76	296.19	262.83
	ΔH^0 ($kJ.kmol^{-1}$)	-3,015.1	-98.5	2,089.0	3,790.4	5,151.5
PP11	He_∞ (*bar*)	373.95	384.24	366.91	340.30	312.55
	ΔH^0 ($kJ.kmol^{-1}$)	-1,358.4	410.9	1,737.8	2,769.9	3,595.6
PP25	He_∞ (*bar*)	302.45	320.82	316.08	301.69	284.31
	ΔH^0 ($kJ.kmol^{-1}$)	-1,815.8	-243.3	936.1	1,853.4	2,587.2

From Figure 8.1, the effect of gas nature on the solubility in the three fluorocarbons used can be deduced. As can be observed at the same pressure and temperature, the solubility values of CO_2 in the three liquids are about 4 times greater than those of N_2. This behavior can be explained using the solubility parameter (δ) concept developed by Hildebrand.[166,233] The solubility parameters can be using Equation (8-7):

$$\delta = \sqrt{\frac{\Delta H_v - RT}{v}} \tag{8-7}$$

The solubility (x_1) of component 1 (gas) in component 2 (liquid) can then be related to the solubility parameters of the two components as follows.

$$x_1 \alpha \exp\left(- \frac{v_1^L \times (\delta_1 - \delta_2)^2 \times \phi_2^2}{RT} \right) \tag{8-8}$$

This relationship indicates that a smaller difference between δ_1 and δ_2 should result in a higher x_1 value.[168,234,235] Table 8.4 shows the solubility parameters for the gases and liquids used.

Table 8.4: Solubility parameter of the gases and liquids used[168,234,235]

Component	δ, $(MPa)^{0.5}$
CO_2	14.6
N_2	10.8
PP10	15.62
PP11	15.52
PP25	15.15

It should be mentioned that the solubility parameters of the three PFCs listed in Table 8.4 were calculated using Hildebrand et al.[166,233] The enthalpy of vaporization, ΔH_v, was determined from Equation (8-9), proposed by Pitzer et al.:[236]

$$\frac{\Delta H_v}{RT_C} = 7.08(1 - T_r)^{0.354} + 10.95\omega(1 - T_r)^{0.456} \tag{8-9}$$

The calculated ΔH_v from Equation (8-9) was then used in Equations (8-10) and (8-11) from Hildebrand et al.[166,168] to obtain the solubility parameters for the PFCs:

$$\Delta U_i \approx \Delta H_{vi} - RT \tag{8-10}$$

$$\delta_i = \left(\frac{\Delta U_i}{V_i^L}\right)^{1/2} \tag{8-11}$$

As can be noticed in Table 8.4 the differences between the solubility parameter of CO_2 and those of the three PFCs are much smaller than those of N_2, which means that less energy is needed for mixing (dissolving) CO_2 in the three PFCs than that for N_2.

Figure 8.1 also shows both CO_2 and N_2 exhibit greater solubilities in the PP25 ($C_{17}F_{30}$) than in the P11 ($C_{14}F_{24}$) and PP10 ($C_{13}F_{22}$), which can be attributed to the fact that the size of PP25 molecule is larger than those of PP11 and PP10, allowing large molecular spaces for accommodating more dissolved gas molecules. It is also apparent that CO_2 solubility increases with the number of fluorine atoms in the solvent molecules.

8.2 GAS HOLDUP, SAUTER MEAN BUBBLE DIAMETER AND VOLUMETRIC MASS TRANSFER COEFFICIENTS OF CO_2 AND N_2 IN PP10, PP11, AND PP25

An extensive literature search revealed that data on the gas holdup, Sauter mean bubble size and volumetric mass transfer coefficients of CO_2 and N_2 in gas-inducing reactors using PFCs as liquid solvent do not exit.[222] In the following the effect of the main operating variables, pressure, temperature, mixing speed, and liquid height above the impeller as well as gas and liquid nature on the holdup, ε_G, Sauter mean bubble diameter, d_S and volumetric mass transfer coefficient, k_La are discussed.

8.2.1 Effect of Pressure on the Gas Holdup, ε_G, Sauter Mean Bubble Diameter, d_S and Volumetric Mass Transfer Coefficient, k_La

Figures 8.4, 8.7 and 8.10 depict the effect of pressure on the gas holdup, and, as can be seen, ε_G values decrease with increasing pressure. In a few cases the gas holdup values remarkably decrease up to pressures of ≤ 20 bar and then the values almost level off with increasing pressures up to 30 bar. This behavior of the gas holdup can be explained by the effect of pressure on the induced gas flow rate. In fact, the induced gas flow rate was observed to decrease with pressure, which can be related to the change of gas-phase and liquid-phase densities. Increasing pressure increases the local density of the gas-liquid system, and, consequently, the hydrostatic head above the impeller, as well as the pressure drop across the orifices, increase, leading to a decrease of the induced gas flow rate and the corresponding gas holdup. This effect of pressure on the gas holdup is in accordance with the findings by Fillion,[51] who found that the induced gas flow rate values decrease with increasing gas density.

Figures 8.5, 8.8 and 8.11 show the effect of pressure on the Sauter mean bubble diameter for CO_2 and N_2 in the three PFCs. As can be observed, d_S values slightly decrease with increasing pressure. Actually, increasing pressure alters the gas-liquid physical properties, such as gas density, liquid viscosity and liquid surface tension, and it was reported to enhance the formation of small rigid spherical gas bubbles.[237,238] This slight decrease of the gas bubbles size, however, implies that at the lowest pressure used (about 6 bar), the gas bubbles are already small and could shrink very slightly with increasing pressure.[48,51] These findings are similar to those previously reported by Chang and Morsi,[239] Li et al.[216] and Inga and Morsi[237] for different gas-liquid systems.

Figures 8.6, 8.9 and 8.12 demonstrate the effect of pressure on the volumetric mass transfer coefficient for CO_2 and N_2 in the three PFCs. In general, k_La tends to increase with increasing pressure, but in some cases k_La for both gases appears to increase up to pressures ≤ 17 bar, and then the values seem to increase very slightly or almost level off. As a matter of fact, increasing pressure increases the gas solubility, which alters the physicochemical properties of the gas-liquid system, such as liquid viscosity and surface tension, which could increase k_La values. Numerous investigators[85,126,128,139,144,146,151,240] reported that k_La values were strongly dependent on the gas-liquid system and the range of pressures used. In this study, it appears that increasing pressure resulted in the formation of small gas bubbles with large gas-liquid interfacial area (a) in the GIR, which resulted in the increase of the volumetric mass transfer coefficient, k_La. Sometimes at pressures greater than 17 bar, however, the negligible increase of k_La values can be attributed to the fact that Sauter mean bubble diameter decreases very slightly with increasing pressure above 17 bar. Thus, the gas-liquid interfacial area sometimes has a strong impact on the volumetric mass transfer coefficient within the operating conditions used.

8.2.2 Effect of Temperature on the Gas Holdup, ε_G, Sauter Mean Bubble Diameter, d_S and Volumetric Mass Transfer Coefficient, k_La

Figure 8.4 shows the effect of temperature on the gas holdup for CO_2 and N_2 in the three PFCs. As can be observed, the gas holdups for both gases increase with increasing temperature. Increasing the temperature decreases the liquid density, and, therefore, increases the induced gas flow rate and, subsequently, the gas holdup, which is in agreement with the results reported by Aldrich and van Deventer.[28] Also, Bruijn et al.[241] showed that the impeller suction efficiency increases with decreasing liquid viscosity (i.e. increasing the temperature) due to the formation of less stable cavities around the impeller under such high temperatures. Thus, increasing the temperature led to the decrease of the density and viscosity of the PFCs, which increased the pumping capacity of the impeller (the induced gas flow rate) and, subsequently, the gas holdup. These results are in agreement with the previous findings by He et al.[40] and Aldrich and van Deventer[28] in GIRs.

Figure 8.5 illustrates the effect of temperature on the Sauter mean bubble diameter for CO_2 and N_2 in PP10, PP11, and PP25. As can be seen in this figure, increasing the temperature from 350 to 450 K appears to slightly decrease d_S by about 20 to 30% for N_2. This behavior can be attributed to the decrease of the liquid viscosity[89,93] and surface tension[51,69,89,91-95] with temperature, and is in accordance with several findings in the literature.[58,90-94,242] In the case of CO_2, d_S appears to be independent of temperature for PP10 and PP11 and is only slightly dependent on the temperature for PP25. It is important to mention that the effect of temperature on the Sauter mean bubble diameter is weaker than its effect on the gas holdup.

The temperature effect on k_La is usually related to the changes of the physicochemical properties of the gas-liquid system used.[39,48,51,96,115] In this study, as shown in Figure 8.6, k_La

values increase with increasing temperature for CO_2 and N_2 in PP10, PP11, and PP25. Several authors[121,129,139,143,146,150,151,240] reported similar trends for k_La values in different gas-liquid systems. In Figures 8.6(a) and 8.6(d), k_La values for CO_2 and N_2 in PP10 increase by about a factor of 2 to 3 when the temperature increases from 350 to 450 K. This effect of temperature on k_La can be explained by its effect on a and k_L. For instance, increasing temperature decreases the liquid viscosity and surface tension, resulting in an increase of the gas holdup and a decrease of the Sauter mean bubble diameter, which lead to an increase of the gas-liquid interfacial area, a, with increasing temperature, as can be deduced from Equation (8-12).

$$a = \frac{6\varepsilon_G}{d_S(1-\varepsilon_G)} \tag{8-12}$$

Also, increasing temperature is expected to increase the gas diffusivity, D_{AB}, according to the Wilke and Chang's Equation,[213] and, subsequently, the mass transfer coefficient, k_L, since k_L is proportional to D_{AB} to a power n as given in Equation (8-13), where n equals 0.5 for penetration theory and 1.0 for the two-film model.[243]

$$k_L \propto D_{AB}^n \tag{8-13}$$

Thus, increasing temperature increases both k_L and a and, subsequently, k_La for both CO_2 and N_2 in the three PFCs under the operating conditions used.

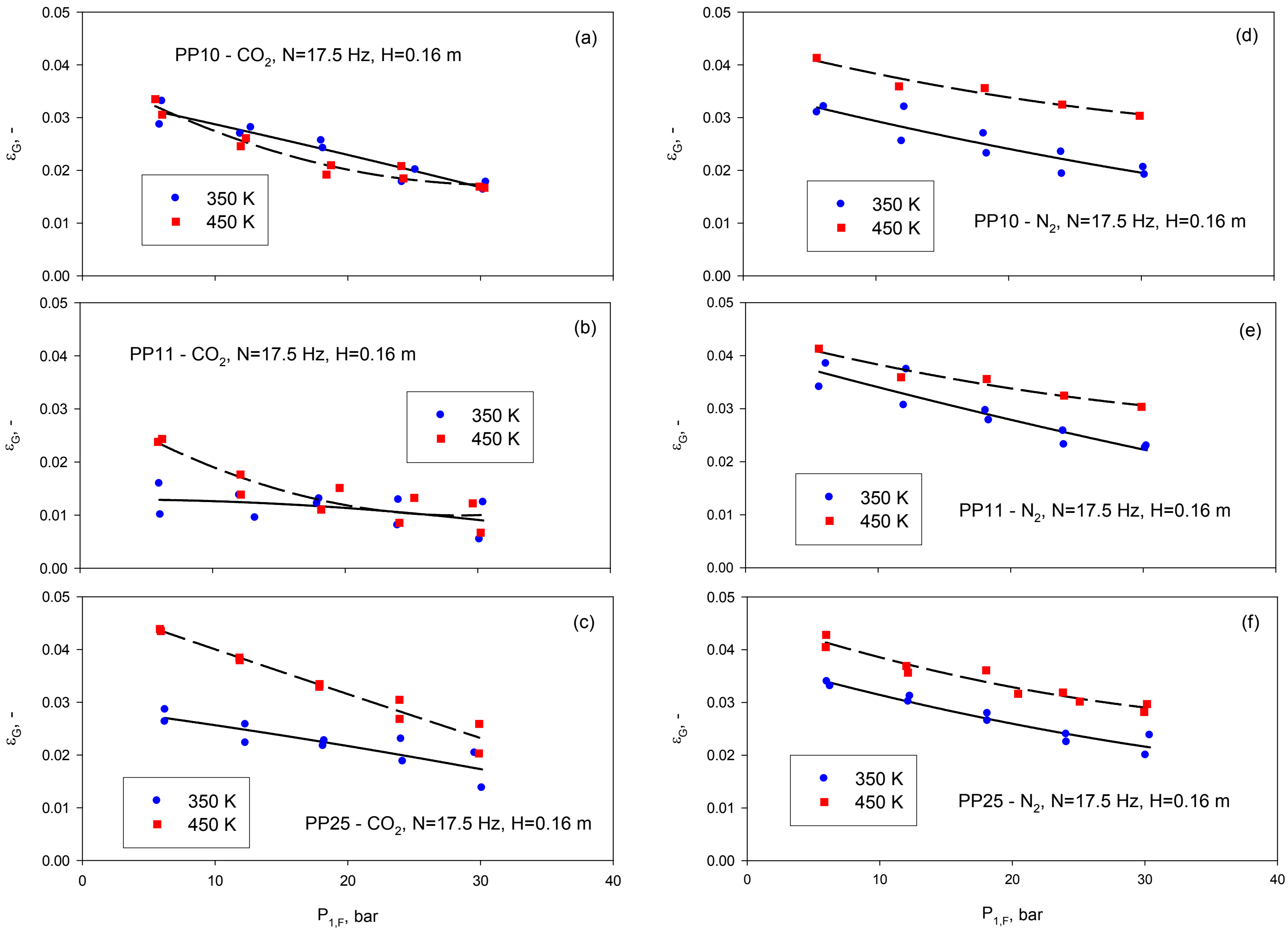

Figure 8.4: Effect of pressure and temperature on ε_G for CO_2 and N_2 in PP10, PP11 and PP25

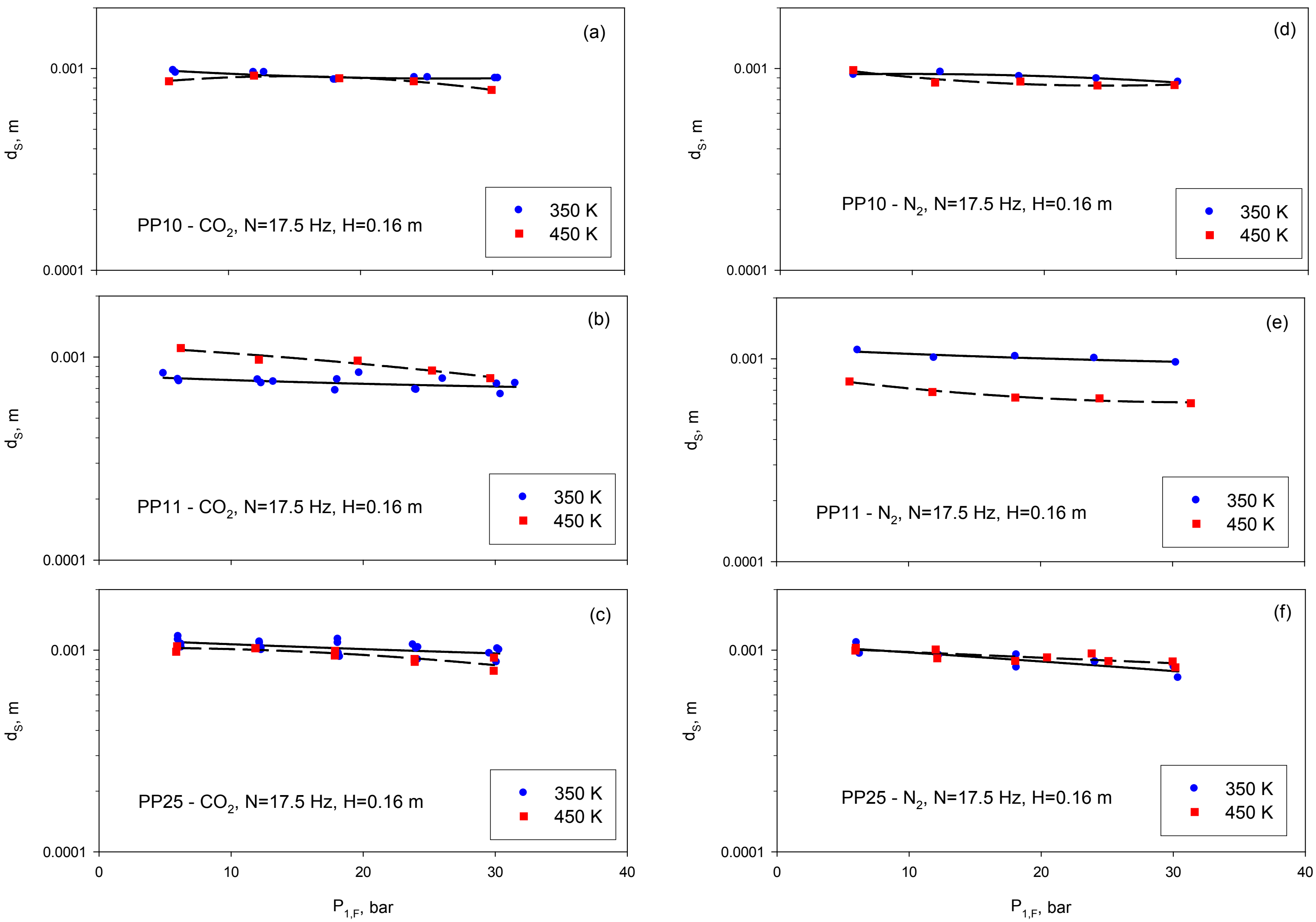

Figure 8.5: Effect of pressure and temperature on d_S for CO_2 and N_2 in PP10, PP11 and PP25

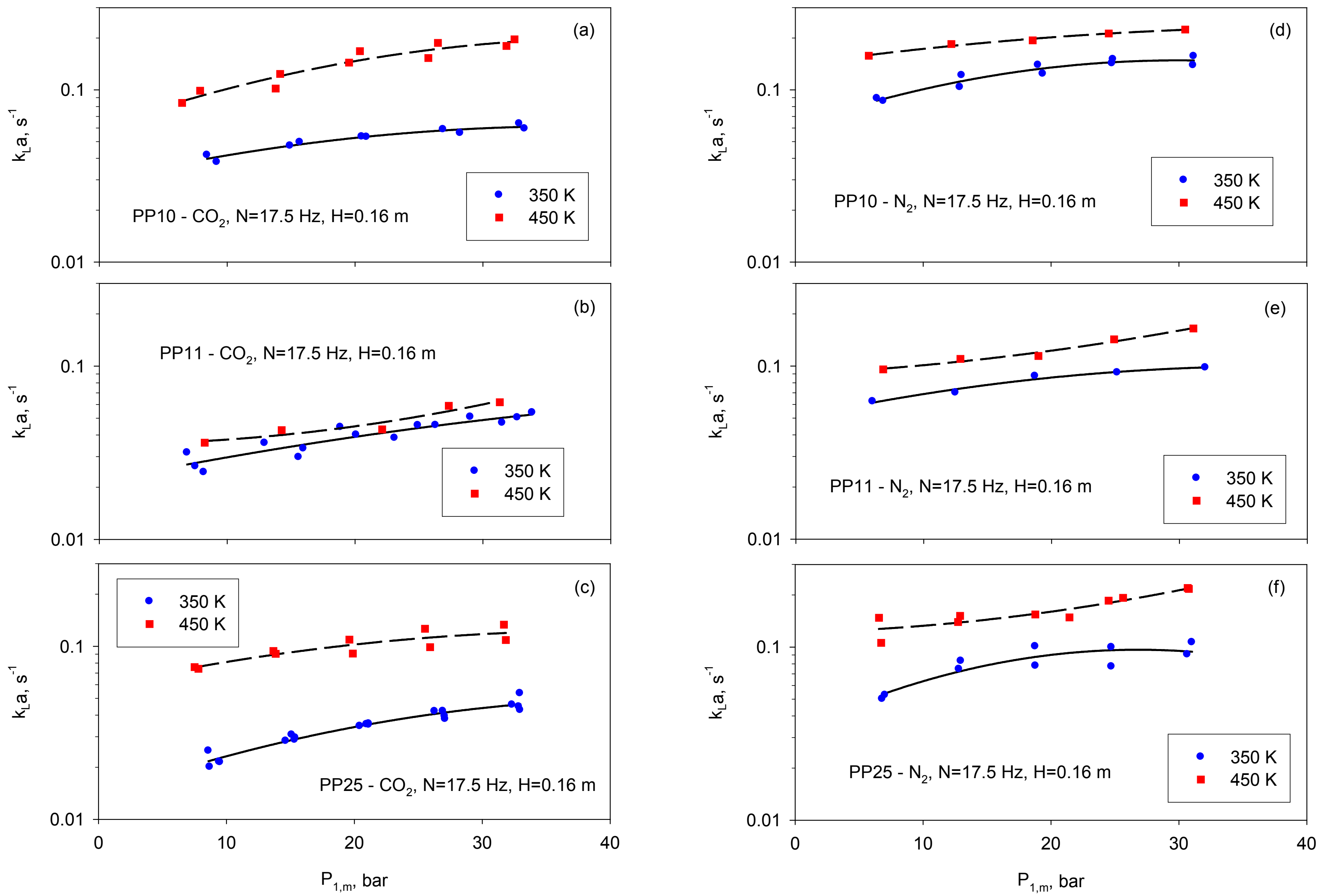

Figure 8.6: Effect of pressure and temperature on k_La for CO_2 and N_2 in PP10, PP11 and PP25

8.2.3 Effect of Mixing Speed on the Gas Holdup, ε_G, Sauter Mean Bubble Diameter, d_S and Volumetric Mass Transfer Coefficient, k_La

Figure 8.7 represents the effect of mixing speed on ε_G in the PP10, PP11, and PP25. As can be seen, the ε_G increases with increasing mixing speed for both gases studied. For the lowest mixing speed, which is close to the critical mixing speed for gas induction, a very small amount of gas is induced in the reactor and therefore small ε_G values are obtained as can be observed in Figure 8.7(b) at 10.0 Hz. Figure 8.7 indicates that increasing mixing speed from 10.0 to 20.0 Hz increases, the gas induction rate in the gas inducing reactor and thus ε_G increases by 3 to 5 times. This behavior is due to the increase of the pumping capacity of the impeller in the reactor,[19,23,29,30] and is in agreement with several literature findings.[46,89,104-106,110,111,244] It is also important to emphasize that under all the conditions studied, ε_G values level off at high mixing speeds due to the establishment of a fully developed hydrodynamic regime in the reactor.

The Sauter mean bubble diameters, d_S, for both gases are found to slightly increase with increasing mixing speed as illustrated in Figure 8.8. Increasing mixing speed increases the induced gas flow rate and the bubble size population in GIRs,[26,41] which could cause an enhancement of the gas bubble coalescence, leading to high values of the Sauter mean bubble diameter. These results are similar to those reported earlier by Fillion and Morsi,[147] Hsu and Huang[25] and Lemoine[52] for different gas-liquid systems in GIRs.

Figure 8.9 shows the effect of mixing speed on the volumetric liquid-side mass transfer coefficient at the central point (400 K, 0.18 m) for CO_2 and N_2 in the three PFCs studied. As can be seen in these figures, increasing mixing speed strongly increases the volumetric liquid-side mass transfer coefficient, k_La, which is in agreement with numerous investigations.[26,51,52,120,126,128,129,139,143,144,148-150,237,240,245-247] The increase of the volumetric liquid-side mass transfer coefficient with mixing speed can be attributed to the increase of the liquid-side mass transfer coefficient k_L and/or the gas-liquid interfacial area, a. Increasing mixing speed increases the turbulence and shear rate in the reactor,[145,146] which reduces the gas-liquid film thickness (Δ), leading to the increase of the mass transfer coefficient; hence, $k_L = D_{AB}/\Delta$. Also, increasing mixing speed increases the pumping capacity of the impeller, and, consequently, more gas bubbles are induced into the liquid through the hollow shaft, which increase the gas holdup. The increase of the number of gas bubbles in the reactor could lead to a slight increase of the Sauter mean bubble diameter due to bubble coalescence. An increase of the gas holdup could lead to an increase of the gas-liquid interfacial area and, hence, to a small increase of the Sauter mean bubble diameter. Since Calderbank and Moo-Young[75] reported that k_L is directly proportional to d_S, k_L increase with mixing speed. Thus, the combined effects of increasing mixing speed on the mass transfer coefficient and the gas-liquid interfacial area led to the increase of k_La values as shown in Figure 8.9. It is also important to mention that the increase of k_L with mixing speed in gas-inducing reactors was reported to be stronger than that in surface aeration reactors[52] due to the higher d_S values exhibited in GIRs. Figure 8.9(b) shows that when increasing mixing speed from 10.8 to 15.0 Hz, k_La values appear to increase by almost 10 times for CO_2, whereas when increasing mixing speed from 15.0 to 20.0 Hz, a smaller increase (2 times) of k_La can be observed. The smaller increase of k_La values at higher mixing speeds can be related to the effect of mixing speed on the induced gas flow rate (Q_{GI}) through the hollow shaft. As reported by Fillion[51] and Lemoine et al.,[206] at mixing speeds greater than the critical mixing speed for gas induction, Q_{GI} increases with mixing speed until a fully developed hydrodynamic regime is reached, and afterward Q_{GI} becomes independent of the mixing speed. Thus, increasing mixing speed after reaching the fully developed hydrodynamic did not significantly increase Q_{GI} and subsequently k_La values were not significantly increased.

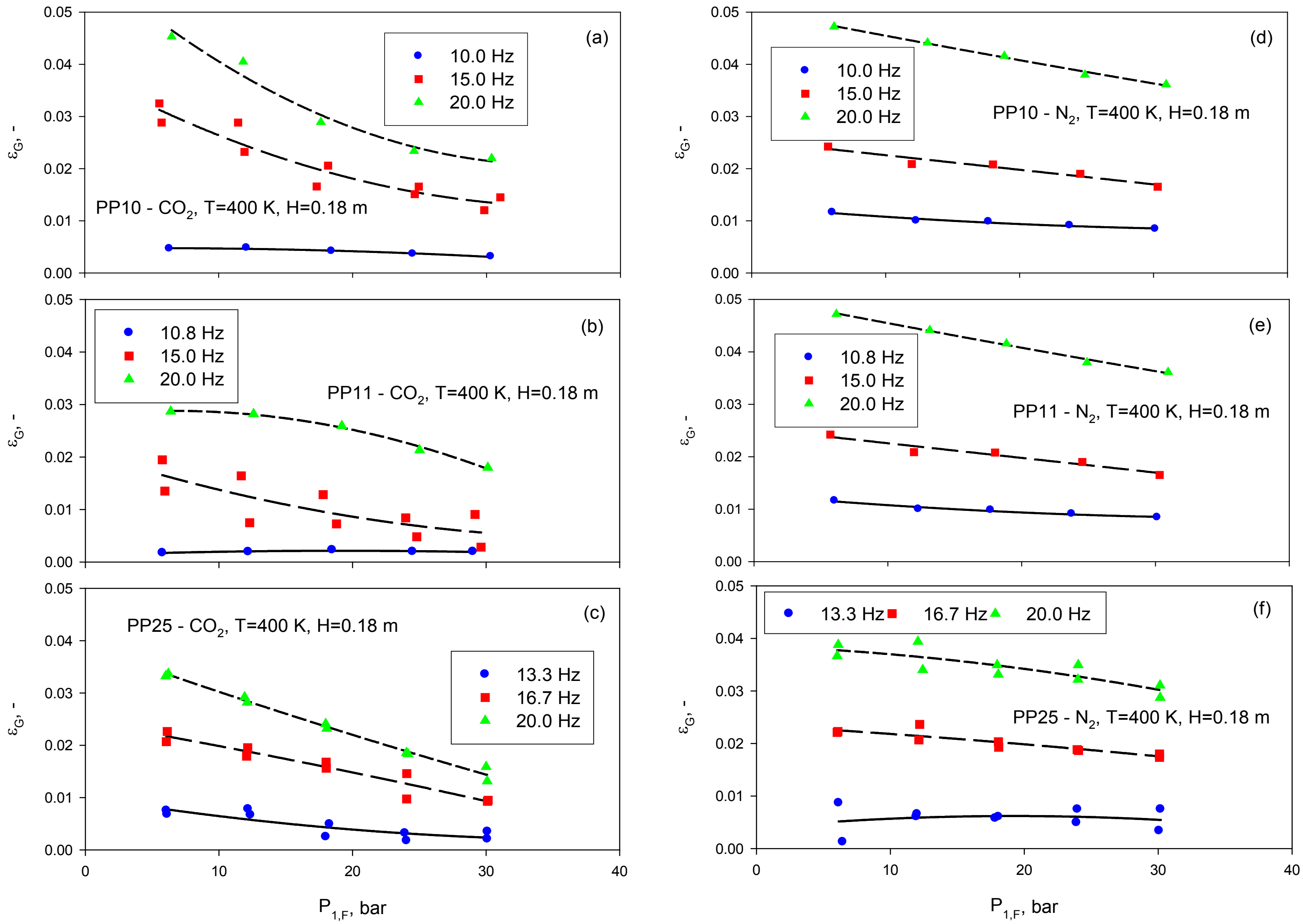

Figure 8.7: Effect of pressure and mixing speed on ε_G for CO_2 and N_2 in PP10, PP11 and PP25

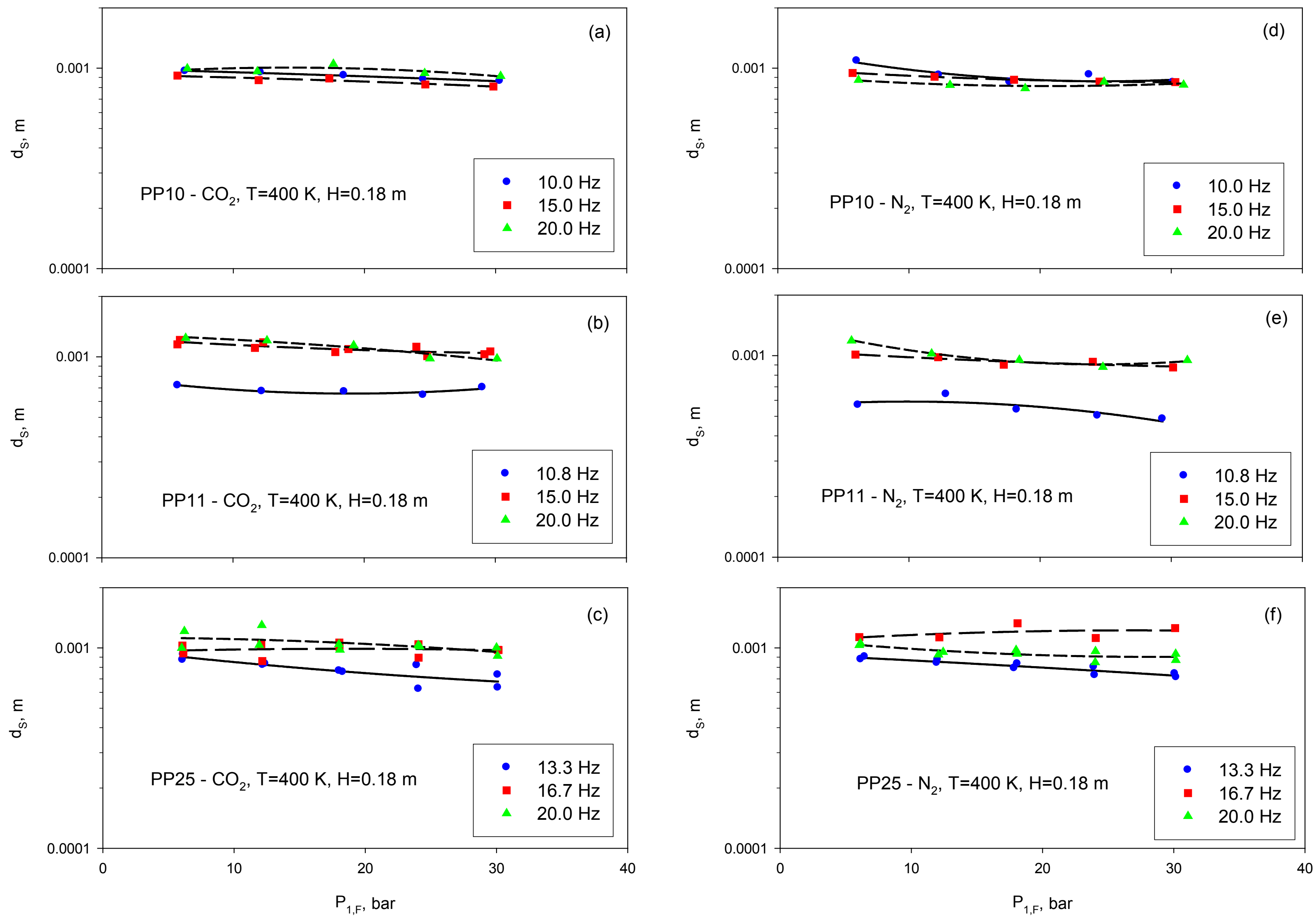

Figure 8.8: Effect of pressure and mixing speed on d_S for CO_2 and N_2 in PP10, PP11 and PP25

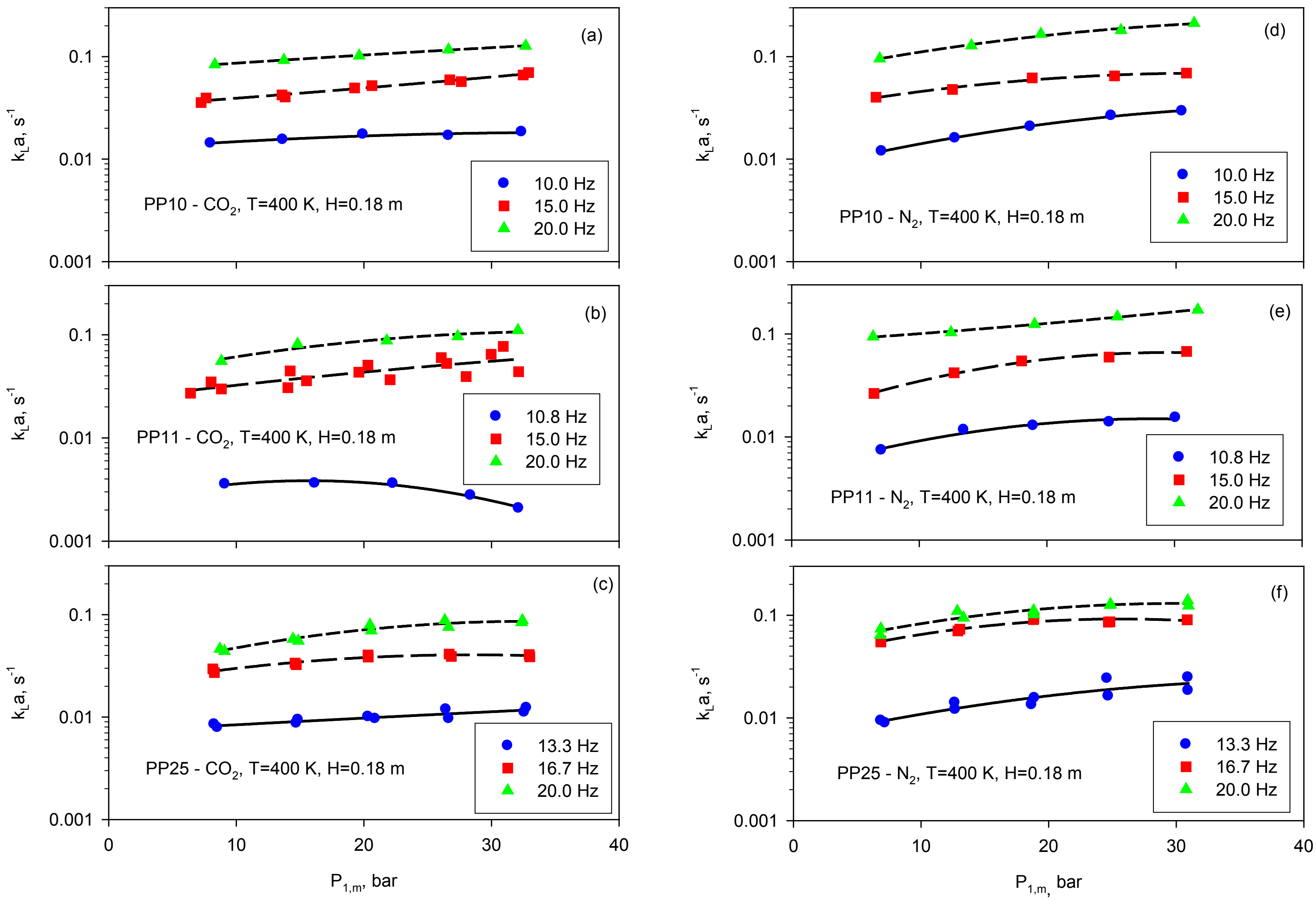

Figure 8.9: Effect of pressure and mixing speed on k_La for CO_2 and N_2 in PP10, PP11 and PP25

8.2.4 Effect of Liquid Height on the Gas Holdup, ε_G, Sauter Mean Bubble Diameter, d_S and Volumetric Mass Transfer Coefficient, k_La

The effect of liquid height above the impeller on the gas holdup is presented in Figure 8.10. As can be seen, the gas holdup decreases with increasing liquid height. For instance, Figure 8.10(a) shows that increasing liquid height from 0.14 to 0.18 m decreases the ε_G by 30% for CO_2 in PP10 and by more than 100% for CO_2 in PP25 (See Figure 8.10(c)). The reason for this gas holdup behavior can be related to the fact that increasing liquid height above the impeller increases the hydrostatic head (pressure drop) needed to induce the gas into the liquid. This increase of pressure drop increases the critical mixing speed for gas induction[19,21,30,51,52] and reduces the pumping capacity of the impeller,[21,23,51] which lead to the decrease of the gas holdup. This behavior of the gas holdup is similar to that reported in numerous literature studies.[24,26,29,35,36,40,145,146] It should be mentioned that the gas holdup for CO_2 at the liquid height 0.22 m was not presented in Figure 8.10 due to the difficulty of seeing the expanded liquid height through the reactor sight-window due to the high solubility of CO_2 in the three PFCs used.

Figure 8.11 illustrates the effect of liquid height on the Sauter mean bubble diameter. As can be seen, d_S values increase from 20 to 30% as the liquid height increases from 0.14 to 0.22 m. Increasing the liquid height decreases the pumping capacity of the impeller, which leads to a decrease in the population of entrained gas bubbles. Also, increasing the liquid height decreases the turbulence in the reactor, which decreases the probability of gas bubbles breakup. Thus, increasing liquid height decreases the number and minimizes the breakup of the induced gas bubbles, and, subsequently, the Sauter mean bubble diameter increases.

Figure 8.12 shows that the volumetric liquid-side mass transfer coefficient, k_La, decreases with increasing liquid height. In Figures 8.12(a) and 8.12(d) for instance, increasing liquid height from 0.14 to 0.22 m decreases the k_La values by a factor of 5 for both CO_2 and N_2 in PP10. The same behavior of k_La for both gases in PP11 and PP25 can be observed in Figures 8.12(b), 8.12(e), 8.12(c) and 8.12(f), where k_La values appear to decrease by one order of magnitude with increasing liquid height from 0.14 to 0.22 m. This behavior of k_La can be related to the effect of liquid height on the mass transfer coefficient (k_L) and the gas-liquid interfacial area (a). As mentioned above, increasing the liquid height decreases the turbulence in the reactor, which results in a decrease of k_L. Also, increasing liquid height decrease the pumping capacity of the impeller, as well as the gas holdup, and increases the Sauter mean bubble diameter, which lead to the decrease of a. Thus, the decrease of the both k_L and a values led to the decrease of k_La with increasing liquid height.

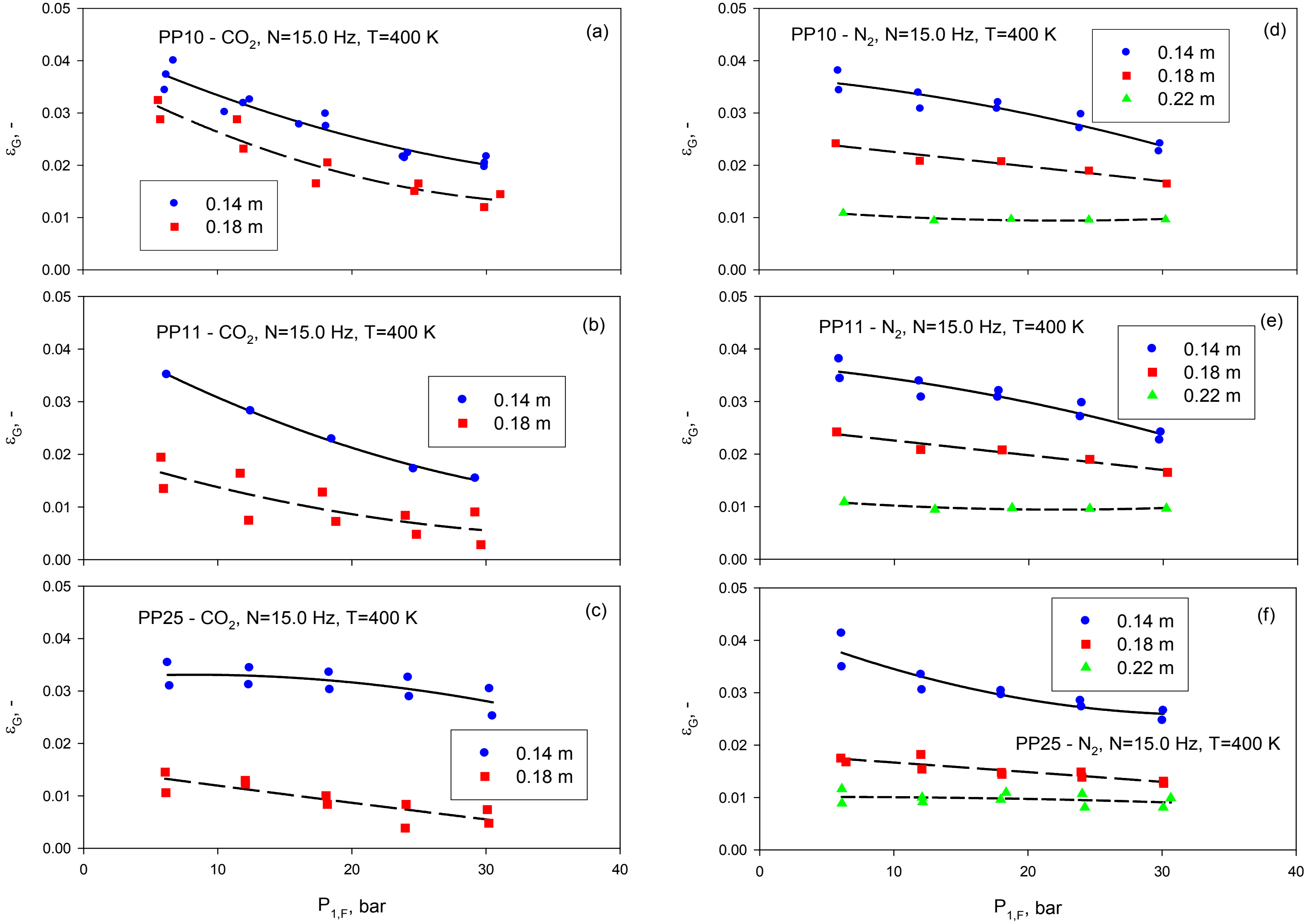

Figure 8.10: Effect of pressure and liquid height on ε_G for CO_2 and N_2 in PP10, PP11 and PP25

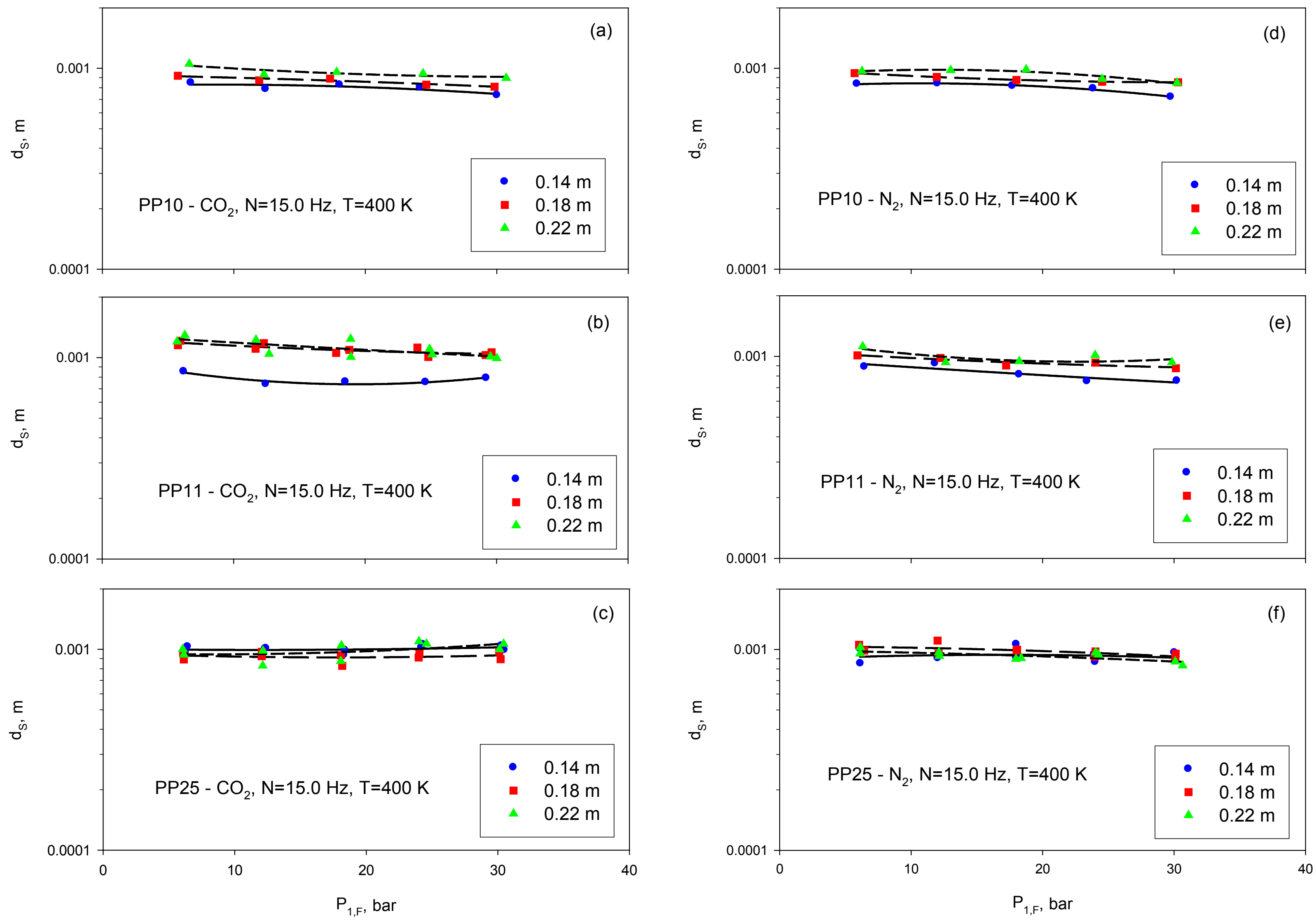

Figure 8.11: Effect of pressure and liquid height on d_S for CO_2 and N_2 in PP10, PP11 and PP25

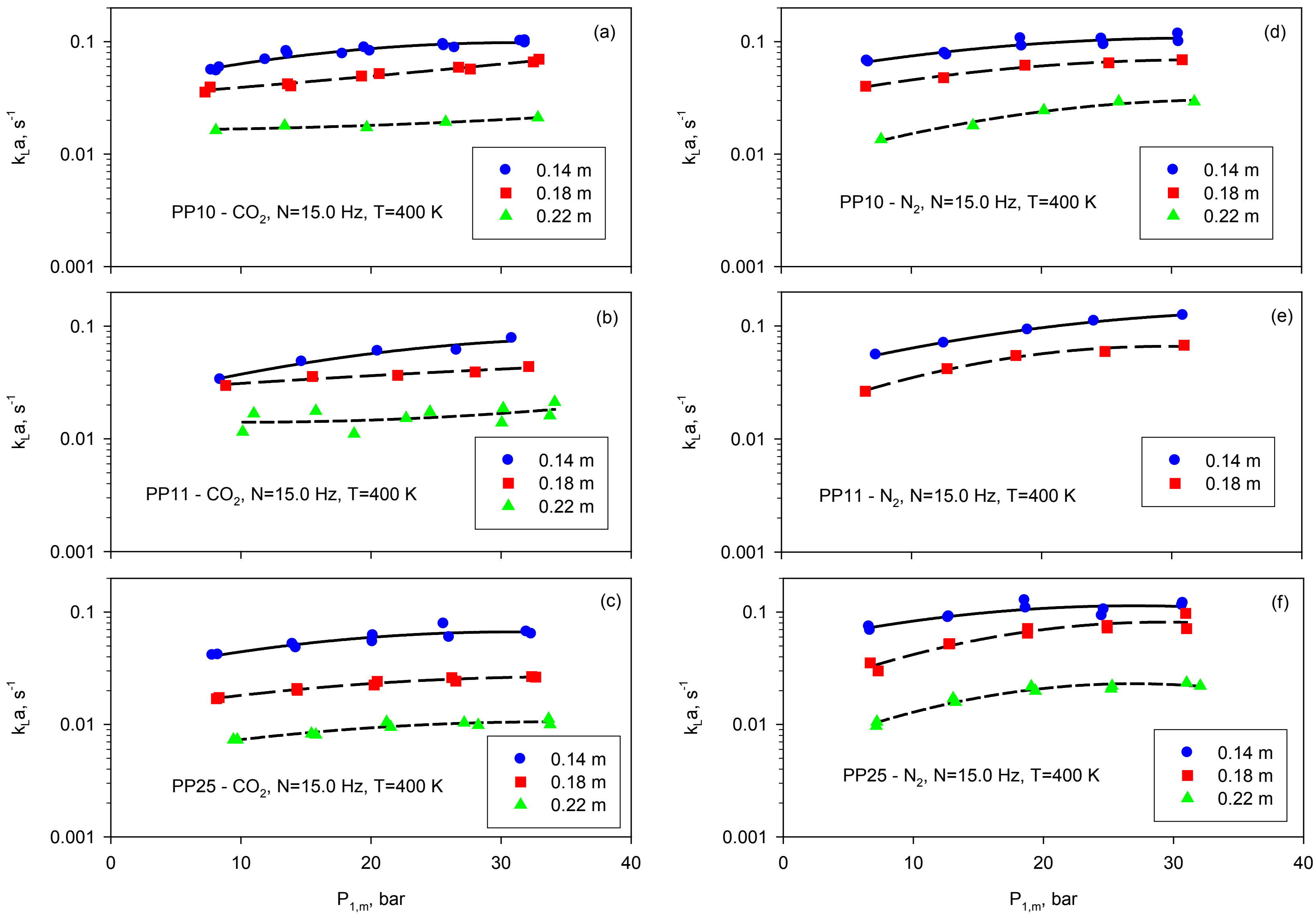

Figure 8.12: effect of pressure and liquid height on k_La for CO_2 and N_2 in PP10, PP11 and PP25

8.2.5 Effect of Gas Nature on the Gas Holdup, ε_G, Sauter Mean Bubble Diameter, d_S and Volumetric Mass Transfer Coefficient, k_La

As can be seen in Figures 8.4, 8.7 and 8.10, the gas holdup values for CO_2 appear to be consistently smaller than those for N_2 under similar operating conditions. This means that the gas bubble population for CO_2 is much larger than that of N_2, and, accordingly, the probability of gas bubble coalescence (formation of large gas bubbles) is higher for CO_2 than for N_2. It should be emphasized that the gas solubility is the amount of dissolved gas, not the mobile or moving gas bubbles which represent the gas holdup. Hence, even though CO_2 has higher solubility values than N_2 in the three PFCs used, it exhibited lower gas holdup values in these liquids as compared with those of N_2.

As can be observed in Figures 8.5, 8.8 and 8.11, the Sauter mean bubble diameter values of CO_2 are always greater than those of N_2 in the three PFCs. Again, this behavior can be attributed to the wider gas bubble population for CO_2 than that of N_2, which resulted in higher probability of gas bubbles coalescence, leading to a larger Sauter mean bubble diameter for CO_2 than those of N_2.

Figure 8.9 depicts the effect of gas nature on the volumetric mass transfer coefficients in PP10, PP11 and PP25. As can be observed in this figure, k_La values for CO_2 in the three PFCs are always smaller than those of N_2 under similar operating condition. This k_La behavior can be attributed to the smaller gas holdup and larger Sauter mean bubble diameter for CO_2 and subsequently its resulting smaller gas-liquid interfacial area when compared with that of N_2 in the three PFCs as shown in Figures 8.7 and 8.8. These data indicate that the gas-liquid interfacial area (a) is controlling the behavior of k_La, since the mass transfer coefficients (k_L) for CO_2 and

N_2 are expected to be the same, given that the diffusivities of CO_2 and N_2 in each liquid used are very close, and the difference of the Sauter mean bubble diameter is not significant. These results are in agreement with the findings by Tekie[48] for k_La values of O_2 and N_2 in cyclohexane.

8.2.6 Effect of Liquid Nature on the Gas Holdup, ε_G, Sauter Mean Bubble Diameter, d_S and Volumetric Mass Transfer Coefficient, k_La

The gas holdup values of CO_2 and N_2 appear to decrease with increasing the molecular weight of the PFCs used as it can be seen in Figure 8.10. Presumably, the increase of the density and viscosity of the liquids with increasing molecular weight under identical operating conditions decreased the pumping capacity of the impeller, which led to the decrease of the gas holdup of CO_2. It should be mentioned that during the physical absorption of CO_2 and N_2 in the three PFCs, no froth was observed under all the operating conditions used, indicating that these solvents are coalescing (non-foaming) liquids.

As can be observed from Figures 8.5, 8.8 and 8.11, the d_S values for CO_2 and N_2 in the three PFCs are very close, and no particular trend can be reported. It was expected that the gas holdup for both gases in PP25 would be greater than that in PP11 and PP10; however, the difference between the values appears to be within the margin of error.

As can be seen in Figure 8.12, the k_La values for CO_2 and N_2 follow the order $(k_La)^{PP25} < (k_La)^{PP11} < (k_La)^{PP10}$, indicating that the volumetric liquid-side mass transfer coefficients decrease with increasing molecular weight (or the viscosity) of the PFCs. This behavior of k_La values is reasonable since the diffusivities in the PFCs were found to follow the order $(D_{AB})^{PP25} < (D_{AB})^{PP11} < (D_{AB})^{PP10}$. Also, the gas-liquid interfacial area (a) of CO_2 and N_2 should follow the order $(a)^{PP25} < (a)^{PP11} < (a)^{PP10}$ since the gas holdup and the Sauter mean bubble diameter appeared to follow the orders $(\varepsilon_G)^{PP25} < (\varepsilon_G)^{PP11} < (\varepsilon_G)^{PP10}$ and $(d_S)^{PP25} \approx (d_S)^{PP11} \approx (d_S)^{PP10}$, respectively. Thus, the combined decrease of the gas-liquid interfacial area (a) and the mass transfer coefficient (k_L) led to the obvious decrease of the volumetric mass transfer coefficients (k_La) with the molecular weight of the PFCs used. These results are in agreement with the findings by Albal et al.,[245] who reported that volumetric liquid-side mass transfer coefficient decreases with increasing liquid phase viscosity.

9.0 STATISTICAL CORRELATION OF K_LA DATA

Different statistical correlations were developed for each gas-liquid system investigated, using the statistical software packages Minitab 15 and SigmaPlot 11.0. Although these statistical correlations are limited to the systems used, they enjoy higher confidence levels (95%) and much better regression coefficients than conventional dimensionless correlations. The following general statistical correlation was found for $\varepsilon_{G,}$ d_S, and k_La:

$$\ln(Y) = \beta_0 + \sum_{i=1}^{4} \beta_i x_i + \sum_{i=1}^{4} \sum_{j \geq i}^{4} \beta_{ij} x_i x_j + \sum_{i=1}^{4} \alpha_i \exp(\gamma_i x_i) \tag{9-1}$$

The coefficients in Equation (9-1) (i.e., the α, β, and γ values) are given Tables 9.2 through 9.7 for CO_2 and N_2, and the parity plot between the experimental and predicted ε_G, d_S, and k_La values are illustrated in Figures 9.1 through 9.3. As can be noticed in these figures, the predictions using the statistical correlations are with average regression coefficients of 91, 88, and 96% for Figures 9.1, 9.2 and 9.3, respectively. It should be mentioned that the coded variables, x_1, x_2, x_3 and x_4, in Equation (9-1) were calculated based on the gas-liquid system used as follows, and more details can be found in Section 6.3 and Equation (6-13):

$$x_1 = 2\left[\frac{2\,T - (500 + 300)}{(500 - 300)}\right] \tag{9-2}$$

$$x_2 = 2\left[\frac{2\,N - (1200 + 600)}{(1200 - 600)}\right] \tag{9-3}$$

$$x_3 = 2\left[\frac{2\,H - (0.22 + 0.14)}{(0.22 - 0.14)}\right] \tag{9-4}$$

$$x_4 = 2\left[\frac{2\,P - (P_{MAX} + P_{MIN})}{(P_{MAX} - P_{MIN})}\right] \tag{9-5}$$

Table 9.1: Values for P_{MAX} and P_{MIN} in Equation (9-5)

		PP10		PP11		PP25	
		CO_2	N_2	CO_2	N_2	CO_2	N_2
Final Pressure	P_{MIN}	4.075	5.539	2.889	4.478	4.663	5.090
	P_{MAX}	31.039	30.949	31.536	31.391	30.531	30.805
Mean Pressure	P_{MIN}	6.473	5.749	5.650	5.226	6.711	5.818
	P_{MAX}	37.149	31.756	35.128	32.035	37.248	32.059

Table 9.2: Coefficients of statistical correlations for ε_G for CO_2

	PP10	PP11	PP25
β_0	-2.870E+00	-3.979E+00	-3.696E+00
β_1	-2.525E-01	-7.118E-02	1.381E-01
β_2	5.241E-01	-4.717E-02	5.132E-01
β_3	1.123E+00	1.320E+00	-3.177E-01
β_4	-3.964E-01	-2.161E-01	-3.553E-01
β_{11}	-2.759E-01	1.902E-01	5.925E-02
β_{12}	4.299E-02	1.143E-01	-3.895E-03
β_{13}	-2.066E-03	8.856E-02	-1.393E-02
β_{14}	-8.470E-03	-4.207E-02	-2.339E-02
β_{22}	-1.455E-01	-3.764E-01	-3.892E-01
β_{23}	1.035E-01	1.816E-01	8.416E-02
β_{24}	-8.345E-05	1.767E-02	-4.726E-03
β_{33}	3.516E-01	6.277E-01	6.401E-02
β_{34}	-1.378E-02	5.267E-03	-4.479E-02
β_{44}	-4.712E-02	2.715E-03	-5.242E-02
α_1	7.500E-02	-3.090E-03	-6.650E-04
α_2	5.068E-02	5.332E-01	1.747E-01
α_3	-1.411E+00	-1.173E+00	-1.317E+00
α_4	2.370E-01	-3.102E-02	2.025E-01
γ_1	1.629E+00	-2.872E+00	3.278E+00
γ_2	-3.439E-01	9.015E-01	1.100E+00
γ_3	8.427E-01	1.039E+00	1.364E-01
γ_4	6.387E-01	1.547E-01	6.430E-01

Table 9.3: Coefficients of the statistical correlations for ε_G for N_2

	PP10	PP11	PP25
β_0	-3.852E+00	1.594E+01	-3.121E+00
β_1	-5.039E-02	7.702E+00	8.881E-01
β_2	3.403E-01	3.627E-01	6.690E-01
β_3	-1.992E-01	-9.745E+00	-1.095E+00
β_4	-1.178E-01	3.182E+00	-1.571E-01
β_{11}	-6.289E-02	1.193E+00	2.120E-01
β_{12}	8.431E-02	2.525E-01	-1.532E-02
β_{13}	-2.593E-01	1.335E-01	-1.513E-01
β_{14}	1.816E-02	-1.883E-02	-4.211E-02
β_{22}	6.161E-02	4.871E-02	-2.919E-01
β_{23}	-2.841E-01	-7.144E-02	2.120E-02
β_{24}	-6.878E-03	3.502E-02	2.880E-02
β_{33}	4.170E-02	1.411E+00	2.522E-01
β_{34}	-1.382E-03	1.052E-03	-5.961E-03
β_{44}	4.080E-03	-3.189E-01	-4.618E-03
α_1	6.033E-04	-2.613E+01	-1.430E+00
α_2	-1.741E-01	1.926E+01	7.315E-02
α_3	-4.369E-01	-3.149E+01	-1.167E+00
α_4	1.450E-01	1.727E+01	1.060E+00
γ_1	3.743E+00	2.768E-01	5.138E-01
γ_2	4.552E-03	7.957E-03	1.363E+00
γ_3	1.970E-01	-2.837E-01	-5.345E-01
γ_4	4.161E-02	-1.876E-01	8.574E-03

Table 9.4: Coefficients of the statistical correlations for d_S for CO_2

	PP10	PP11	PP25
β_0	-5.632E+00	-5.857E+00	-6.240E+00
β_1	1.023E+00	6.399E-01	9.775E-02
β_2	8.757E-01	1.162E-01	1.839E-01
β_3	9.312E-01	-7.677E-02	4.130E-02
β_4	-3.264E-02	-3.749E-02	2.677E-02
β_{11}	4.128E-01	2.022E-01	8.322E-03
β_{12}	3.479E-01	3.518E-02	-4.197E-02
β_{13}	7.661E-01	6.703E-03	9.394E-03
β_{14}	-8.163E-04	-6.163E-03	1.484E-02
β_{22}	4.145E-01	-6.451E-02	-5.853E-02
β_{23}	4.714E-01	-1.189E-02	-7.633E-04
β_{24}	1.134E-03	-1.017E-02	-7.217E-03
β_{33}	3.526E-01	1.510E-02	3.299E-02
β_{34}	-4.697E-03	-5.325E-03	4.479E-03
β_{44}	3.691E-03	9.302E-03	-1.714E-02
α_1	-4.940E-01	-6.613E-01	-3.459E-01
α_2	-1.613E-01	-1.893E-01	-1.563E-01
α_3	-4.287E-01	-2.686E-01	-3.285E-01
α_4	-3.538E-01	-3.460E-04	3.437E-02
γ_1	1.074E+00	6.941E-01	1.956E-01
γ_2	1.531E+00	7.134E-03	9.029E-03
γ_3	1.064E+00	-5.215E-01	7.211E-02
γ_4	5.401E-03	2.856E+00	-9.136E-01

Table 9.5: Coefficients of the statistical correlations for d_S for N_2

	PP10	PP11	PP25
β_0	-5.839E+00	1.209E+01	-5.749E+00
β_1	1.158E+00	6.310E+00	5.835E-01
β_2	6.100E-01	-2.925E+00	8.150E-02
β_3	1.077E+00	-2.028E+00	-2.946E-01
β_4	-8.022E-03	-2.821E-02	-4.274E-02
β_{11}	4.835E-01	9.795E-01	6.654E-02
β_{12}	1.363E-01	-2.180E-02	-2.456E-02
β_{13}	6.093E-01	5.378E-03	-2.363E-03
β_{14}	-6.347E-03	-7.769E-03	1.936E-03
β_{22}	2.711E-01	4.008E-01	-4.513E-02
β_{23}	1.387E-01	1.204E-02	-2.003E-03
β_{24}	5.904E-03	3.882E-03	-2.903E-03
β_{33}	4.082E-01	-2.054E-01	7.278E-02
β_{34}	-1.050E-03	6.649E-03	7.577E-04
β_{44}	8.778E-03	4.490E-03	-1.343E-03
α_1	-5.167E-01	-1.959E+01	-1.011E+00
α_2	-1.910E-01	-9.392E+00	7.719E-02
α_3	-4.684E-01	9.802E+00	-5.813E-01
α_4	-1.343E-02	-3.072E-09	2.641E-01
γ_1	1.122E+00	3.054E-01	4.672E-01
γ_2	1.296E+00	-3.146E-01	2.492E-03
γ_3	1.097E+00	2.059E-01	-4.575E-01
γ_4	1.025E+00	8.636E+00	1.955E-02

Table 9.6: Coefficients of the statistical correlations for k_La for CO_2

	PP10	PP11	PP25
β_0	1.339E+01	-3.527E+00	-3.584E+00
β_1	2.999E-01	4.326E-01	7.667E-01
β_2	4.224E+00	1.972E-01	7.097E-01
β_3	2.665E+00	-1.228E-04	-2.647E-01
β_4	1.428E-01	1.166E-01	2.530E-01
β_{11}	-2.169E-01	-7.230E-03	4.711E-02
β_{12}	1.603E-01	2.721E-02	-1.101E-01
β_{13}	-1.078E-01	6.235E-02	-9.256E-04
β_{14}	2.909E-02	-8.847E-03	-6.772E-02
β_{22}	6.419E-01	-6.289E-01	-3.648E-01
β_{23}	-1.217E-01	1.430E-01	7.060E-02
β_{24}	2.157E-02	3.152E-02	2.064E-02
β_{33}	4.880E-01	7.545E-02	8.854E-02
β_{34}	-5.892E-03	-2.534E-02	-5.263E-03
β_{44}	-2.777E-02	-7.898E-03	-2.297E-03
α_1	1.189E-08	-2.663E-01	-5.653E-02
α_2	-8.824E+00	3.318E-01	1.614E-01
α_3	-7.675E+00	-6.805E-02	-1.434E-01
α_4	1.469E-06	1.251E-01	-1.376E-01
γ_1	9.021E+00	5.539E-01	1.626E+00
γ_2	3.845E-01	1.190E+00	1.056E+00
γ_3	3.642E-01	1.269E+00	8.332E-01
γ_4	6.082E+00	1.963E-02	7.608E-01

Table 9.7: Coefficients of the statistical correlations for k_La for N_2

	PP10	PP11	PP25
β_0	-1.734E+00	-5.759E-01	-3.332E+00
β_1	5.387E-03	1.469E+00	6.481E-01
β_2	2.006E+00	1.210E+00	1.133E+00
β_3	1.889E-01	-1.471E+00	-4.764E-01
β_4	5.513E-02	-3.815E-01	1.855E-02
β_{11}	-1.891E-01	2.684E-01	-1.179E-01
β_{12}	5.828E-02	2.586E-02	-2.112E-01
β_{13}	-2.880E-01	8.733E-02	-5.246E-02
β_{14}	-2.400E-02	3.728E-03	-2.840E-02
β_{22}	4.376E-01	-4.474E-01	-5.453E-01
β_{23}	-2.764E-01	2.166E-01	1.486E-01
β_{24}	-2.087E-02	2.284E-02	-1.930E-02
β_{33}	1.026E-01	2.548E-01	-2.495E-02
β_{34}	2.217E-02	4.031E-03	1.789E-02
β_{44}	-3.745E-02	-1.060E-01	-9.415E-02
α_1	4.637E-04	-2.174E+00	-4.386E-02
α_2	-1.777E+00	1.727E-04	2.331E-01
α_3	-8.331E-01	-2.057E+00	3.636E-02
α_4	1.373E+00	1.668E+00	1.680E-01
γ_1	4.059E+00	4.998E-01	1.599E+00
γ_2	6.436E-01	-5.607E+00	6.996E-01
γ_3	5.452E-01	-4.785E-01	5.788E-01
γ_4	8.843E-02	3.033E-01	7.436E-01

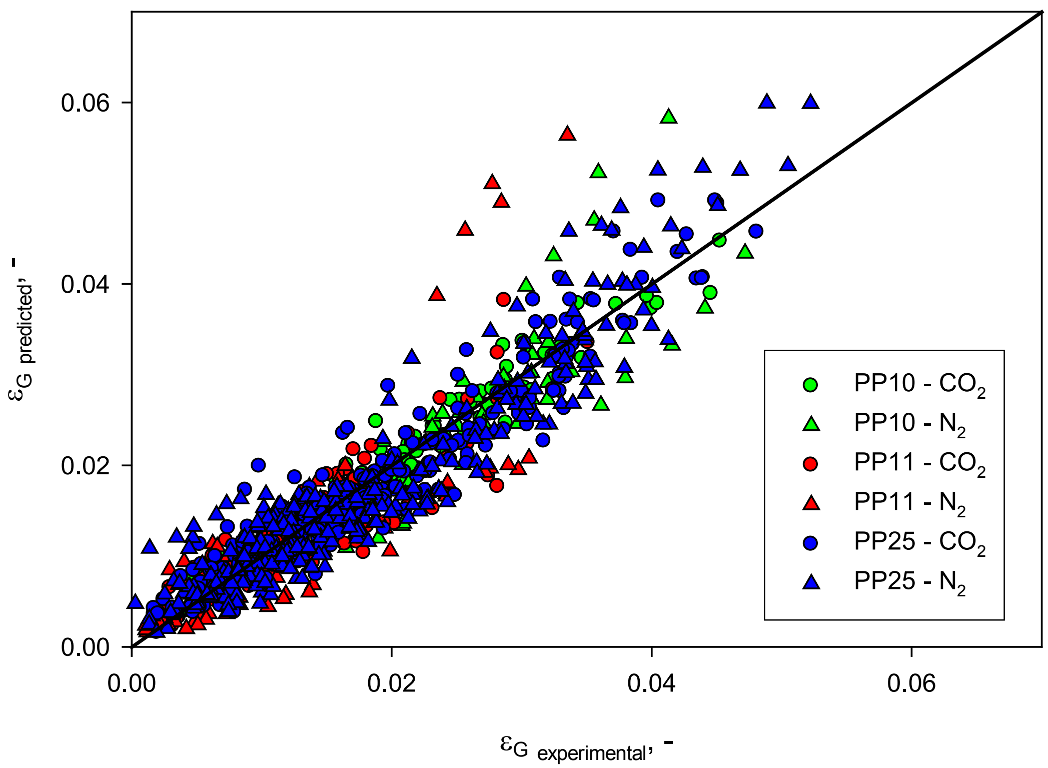

Figure 9.1: Comparison between experimental and predicted ε_G values using the statistical correlation

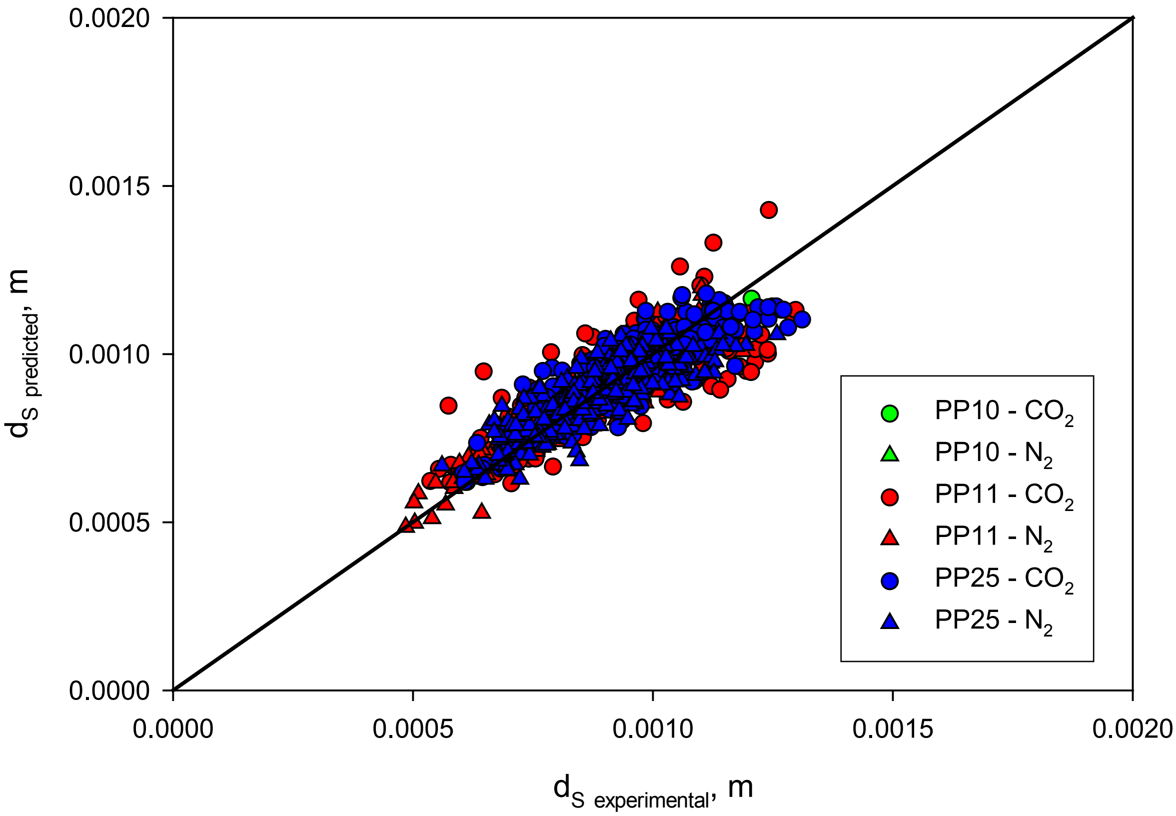

Figure 9.2: Comparison between experimental and predicted d_S values using the statistical correlation

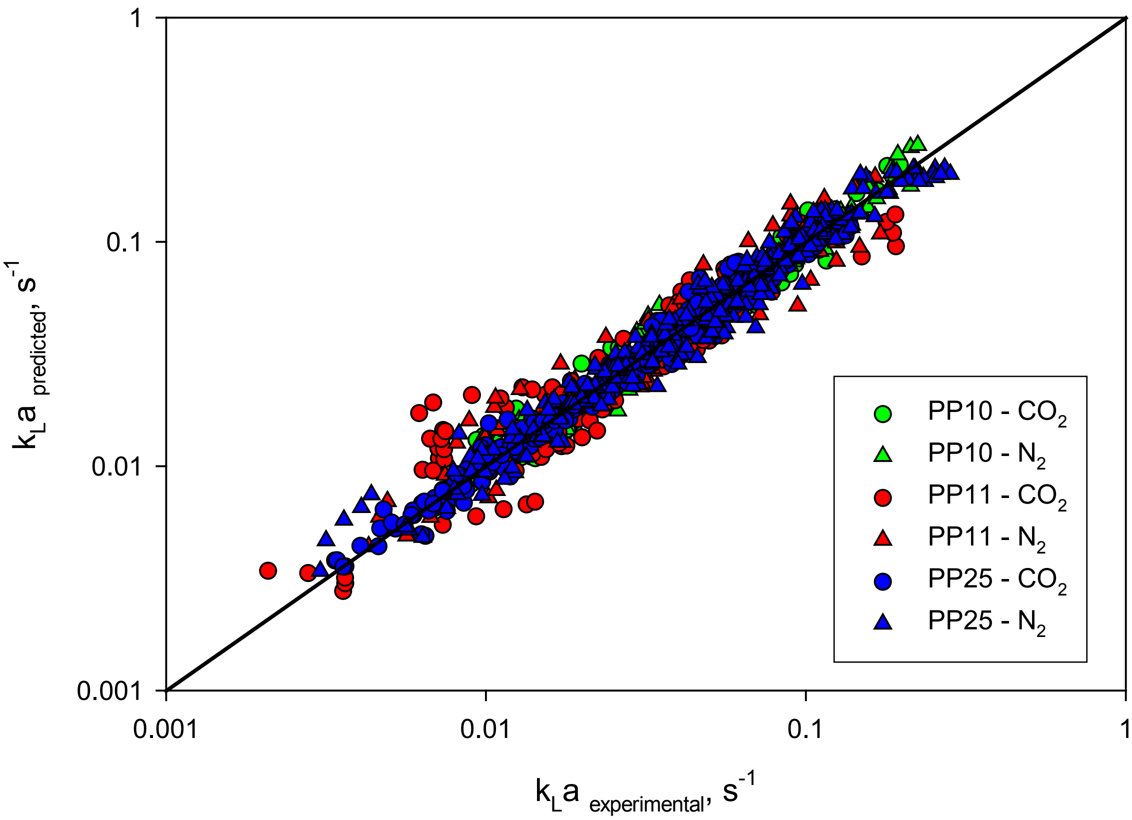

Figure 9.3: Comparison between experimental and predicted k_La values using the statistical correlation

10.0 CONCEPTUAL PROCESS DESIGN USING PP25 SOLVENT

10.1 ASPEN PLUS SIMULATOR

Since CO_2 appears to have higher solubility in PP25 than the other two PFCs, Aspen Plus (version 24.0) was used for the simulation of a conceptual PP25 physical solvent process for selective CO_2 capture from a syngas generated from an E-Gas gasifier using Pittsburgh #8 coal and shifted to a pressure and temperature of 381 psia (26.27 bar) and 857 °F (731.48 K), respectively. The composition of this shifted gas, given in Table 10.1, is taken from "Capital and Operating Cost of Hydrogen Production from Coal Gasification", Final Report, April 2003, by Parsons.[248] After CO_2 capture from the shifted gas stream, CO_2 and H_2 gases were recovered, and PP25 solvent was regenerated using two options, namely Pressure-Swing (P-Swing) and combined Pressure-Temperature-Swing (P-T-Swing).

For the shifted gas shown in Table 10.1, the solubilities of CO_2, N_2 and H_2 in PP25 were measured, whereas those of the other components were calculated using Aspen Plus (version 24.0), which employs the PR-EOS. The solubilities of the gaseous components in PP25 expressed in mole fraction (x^*) are presented as a function of the partial pressure of each gas at different temperatures in Figures Figure D.1 and Figure D.2 in the Appendix D.

In the simulation, the shifted gas flow rate into the conceptual PP25 process was 102.517 kg/s (5.380 kmol/s), and the PP25 solvent flow rate was 11,831.2 kg/s. The CO_2 capture process was carried out at 500 K and 30 bar using an absorber (**ABSORBER**) and the outlet streams were one vapor-phase (**ABS-VAP**) and one liquid-phase (**ABS-LIQ)**. It should be mentioned that when CO_2 capture was carried out at 312 K (similar to Selexol), two immiscible liquid phases, namely an aqueous phase (mainly water) and an organic phase (mainly PP25 containing dissolved gases, including CO_2) were found.

Table 10.1: Composition of the Shifted Gas Used in This Study

Component	Mole fraction
Ar	0.0048
CH_4	0.0024
H_2	0.3750
N_2	0.0033
CO	0.0627
CO_2	0.2387
H_2O	0.3068
NH_3	0.0016
COS	0.0000
H_2S	0.0047
Total	1.0000

In order to allow a comparison between the two PP25 solvent regeneration options, the following constraints were considered: (1) the H_2 recovered from the gas stream enters the turbines at arbitrarily designated 20 bar and 1000 K; and (2) the CO_2 to be delivered for sequestration was arbitrarily available at 20 bar and 310 K.

Figure 10.1 shows a schematic of the conceptual PP25 process with the following main units:

- Absorber (**ABSORBER**): to capture CO_2 from the shifted gas using PP25 solvent.

- 3 flash drums (**FLASH1, FLASH2,** and **FLASH3**): to decrease the pressure (Table 10.2).

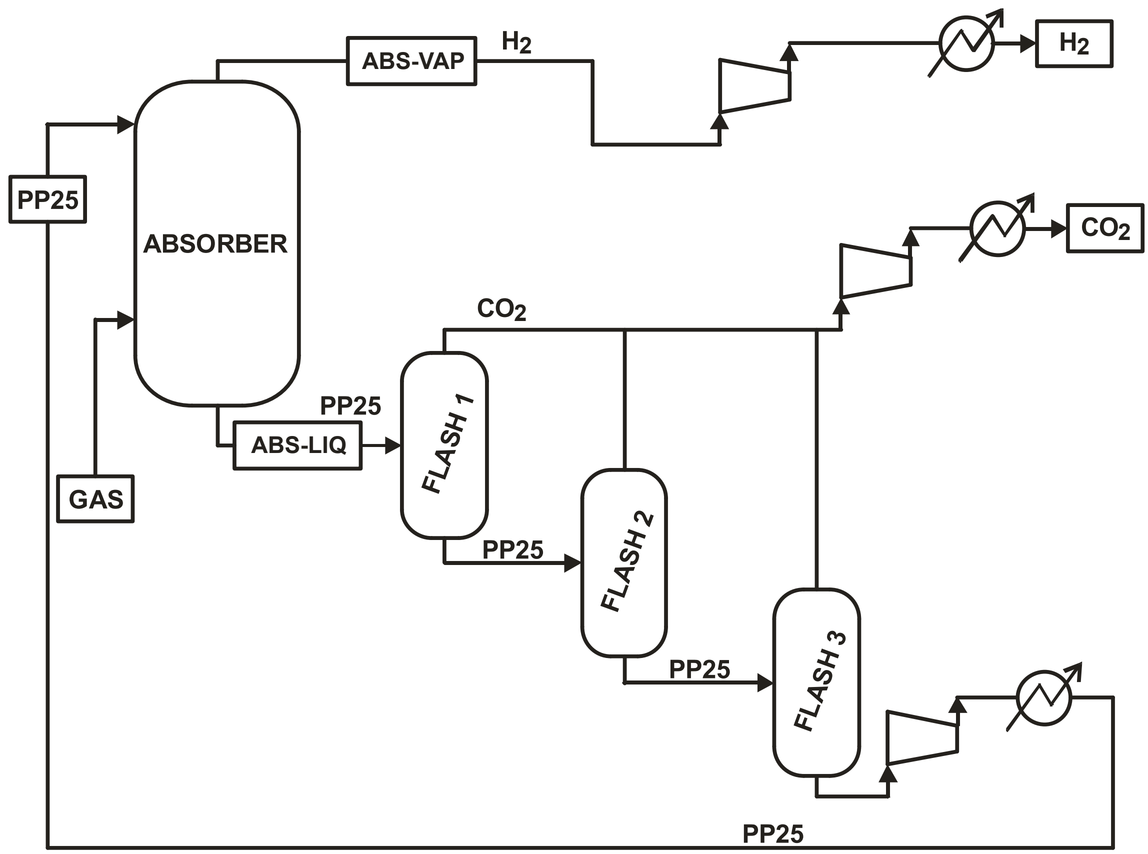

Figure 10.1: P-swing and P-T-swing PP25 Solvent Regeneration Options with 3 Flash Drums

Table 10.2 indicates that the pressure in the third Flash drum **FLASH3** of the P-T-Swing is set at 4 bar and not at 1 bar as in the P-Swing. This is because the temperature in this flash drum is 590 K which is greater than the normal boiling point of PP25 (533 K). Thus, if the pressure in the third flash drum for the P-T-swing option were maintained at 1 bar as in the P-Swing option, all PP25 would be vaporized and lost into the vapor phase.

Table 10.2: Conditions of flash drums for P-Swing and P-T-Swing

PP25 solvent regeneration options

	P-Swing		Combined P-T-Swing	
	P	T	P	T
	bar	*K*	*bar*	*K*
FLASH DRUM - 1	20	500	20	530
FLASH DRUM - 2	10	500	10	560
FLASH DRUM - 3	1	500	4	590

Table 10.3 shows that at the absorber conditions of 500 K and 30 bar, 56.1 % of CO_2 and 79.6% of water in the shifted gas are captured by PP25; and 67.5 % of H_2 in the shifted gas is separated into the vapor-phase from the top of the absorber. Also, 0.36% of the PP25 fed to the absorber is lost in the vapor-phase from the top of the absorber and has to be recovered.

Table 10.3: Composition of the liquid-phase (ABS-LIQ) and vapor-phase (ABS-VAP) from the absorber (500 K and 30 bar)

	Feed to absorber	**Liquid phase (ABS-LIQ)**		**Vapor-phase (ABS-VAP)**	
	kmol/s	*kmol/s*	*Mole Fraction*	*kmol/s*	*Mole Fraction*
Ar	0.0258	0.0118	6.525×10^{-4}	0.0140	5.472×10^{-3}
CH_4	0.0129	6.578×10^{-3}	3.634×10^{-4}	6.333×10^{-3}	2.473×10^{-3}
H_2	2.0174	0.6553	0.0362	1.3621	0.5320
N_2	0.0178	7.346×10^{-3}	4.058×10^{-4}	0.0104	4.064×10^{-3}
CO	0.3373	0.1370	7.568×10^{-3}	0.2003	0.0782
CO_2	1.2841	0.7203	0.0398	0.5639	0.2202
H_2O	1.6505	1.3140	0.0726	0.3365	0.1314
NH_3	8.608×10^{-3}	5.767×10^{-3}	3.186×10^{-4}	2.840×10^{-3}	1.109×10^{-3}
COS	0	0	0	0	0
H_2S	0.0256	0.0172	9.482×10^{-4}	8.399×10^{-3}	3.280×10^{-3}
PP25	15.283	15.2275	0.8412	0.0557	0.0218
Total	**20.6632**	**18.1027**	**1.0000**	**2.5605**	**1.0000**

In the P-Swing option, the absorber and the 3 flash drums were configured to operate adiabatically (no heat exchange with the surroundings), and consequently the heat duties of these units were null. In addition, throughout this regeneration option, the temperature was kept almost constant (~ 500 K) while the pressure was decreased from 30 to 1 bar in 3 steps: 20, 10, and 1 bar. Tables 10.4, 10.5 and 10.6 show a comparison between the compositions of the CO_2 stream to be sent to sequestration, the H_2 streams to be sent to turbines, and the composition of the regenerated PP25 streams to be recycled to the absorber for the P-Swing and P-T-Swing regeneration options. Table 10.4 indicates that the PP25 losses in the CO_2 stream to be sent to sequestration based on the total amount of solvent fed to the absorber in the P-T-Swing option are greater (2.59%) than those found in the case of the P-Swing option (0.82%) despite the fact that the amounts of CO_2 to be sent to sequestration are almost the same, and the amount of H_2 to be sent to turbines (Table 10.5) are almost identical in the two regeneration options. These solvent losses are coming from the absorber (**ABSORBER)**, 1st flash drum **(FLASH1)**, and the 2nd flash drum **(FLASH2**), since a solvent "separator" was used after the 3rd flash drum in order to recover PP25 from the vapor-phase and redirect it to the solvent steam. Table 10.6 confirms the decrease of the amount of PP25 solvent in the stream to be sent to the absorber for the P-T-Swing when compared with the P-Swing as in Table 10.4. It should be emphasized that these relatively elevated PP25 losses, which could be economically prohibitive, can be attributed to the fact that the absorption and regeneration temperatures in both regeneration options are close to the solvent boiling point (533 K), as mentioned above.

Table 10.4: Composition of the CO_2 stream to be sent to sequestration

Component	Original feed to absorber	Feed to flash drums	P-Swing	P-T-Swing
	kmol/s	*kmol/s*	*kmol/s*	*kmol/s*
Ar	0.0258	0.011812	0.0257	0.0257
CH_4	0.0129	6.578×10^{-3}	0.0128	0.0128
H_2	2.0174	0.6553	0	0
N_2	0.0178	7.346×10^{-3}	0.0177	0.0177
CO	0.3373	0.1370	0.3366	0.3362
CO_2	1.2841	0.7203	1.2720	1.2712
H_2O	1.6505	1.3140	1.5387	1.5750
NH_3	8.608×10^{-3}	5.767×10^{-3}	8.405×10^{-3}	8.434×10^{-3}
COS	0	0	0	0
H_2S	0.0256	0.0172	0.0250	0.0250
PP25	15.283	15.2275	0.1248	0.3953
Total	20.6632	18.1027	3.3617	3.6674

Table 10.5: Hydrogen stream to be sent to turbines

Component	Original feed to absorber	Feed to flash drums	P-Swing	P-T-Swing
	kmol/s	*kmol/s*	*kmol/s*	*kmol/s*
H_2	2.01739	0.65527	2.01575	2.01418

Table 10.6: Composition of the regenerated PP25 stream to be sent to the absorber

Component	Original feed to absorber	Feed to flash drums	P-Swing	P-T-Swing
	kmol/s	*kmol/s*	*kmol/s*	*kmol/s*
Ar	0.0258	0.011812	9.326×10^{-5}	1.298×10^{-4}
CH_4	0.0129	6.578×10^{-3}	7.662×10^{-5}	9.524×10^{-5}
H_2	2.0174	0.6553	1.633×10^{-3}	3.209×10^{-3}
N_2	0.0178	7.346×10^{-3}	4.109×10^{-5}	6.273×10^{-5}
CO	0.3373	0.1370	7.197×10^{-4}	1.105×10^{-3}
CO_2	1.2841	0.7203	0.0121	0.0129
H_2O	1.6505	1.3140	0.1118	0.0755
NH_3	8.608×10^{-3}	5.767×10^{-3}	2.025×10^{-4}	1.740×10^{-4}
COS	0	0	0	0
H_2S	0.0256	0.0172	6.081×10^{-4}	5.397×10^{-4}
PP25	15.2832	15.2275	15.1585	14.8879
Total	20.6632	18.1027	15.2857	14.9816

Table 10.6 also shows that for the P-T-Swing, the amount of H_2 in the regenerated PP25 stream to be sent to the absorber is 0.16% based on the total amount of H_2 in the shifted gas fed to the absorber, which is greater than that found for the P-Swing (0.08%). This is explained by the increase in solubility of H_2 in PP25 as a function of temperature.

Table 10.7 shows that even though a large amount of heat is involved in the heating and cooling of the PP25 solvent, the net enthalpy for the P-T-Swing regeneration option is smaller than that for the P-Swing option. This net enthalpy could be utilized for generating steam or in other process applications. It should be pointed out that heating PP25 solvent at large flow rate (11,831.2 kg/s) for only 90 K (from 500 to 590 K) requires a significant amount of power, totaling 1,615.22 MW, which can be related to the high specific heat of the solvent.

Table 10.7: Thermal comparison between the two PP25 solvent regeneration options

	P-Swing	P-T-Swing
	MW	MW
Heating Flash Drums	*0*	*1,615.22*
Heating or Cooling PP25	*24.82*	*-1,396.00*
Total Heat Duty	-28.85	5.83
Work Required	106.74	110.15
Heating H_2	8.36	4.58
Cooling CO_2	-162.44	-213.38
Net Enthalpy	-76.20	-92.82

10.2 IS PP25 SOLVENT AN "IDEAL" SOLVENT?

The PP25 physical solvent used in this conceptual process design for CO_2 capture showed high CO_2 solubilities, has relatively low viscosity at 500 K, possesses very good thermal and chemical stabilities, and has a solubility parameter close to that of CO_2 and hence it could be considered as an *"ideal" solvent*. Unfortunately, the relatively high vapor pressure of PP25 at 500 K appeared to be major drawback of this solvent. This was obvious in the conceptual process design, particularly during the pressure-temperature swing regeneration option, where the solvent loss was significant. This is because the boiling point of PP25 is 533 K, which is close to the absorber temperature, which was set at 500 K. It is therefore imperative to seek different physical solvents, which have negligible vapor pressure, in addition to the other desirable properties of the *"ideal" solvent*.

Ionic liquids are known to have negligible vapor pressure due to their chemical structure and accordingly our research emphasis has been focused on using ionic liquid for CO_2 capture from fuel gas streams at relatively high temperatures.

11.0 IONIC LIQUIDS

Ionic liquids (ILs) are salts having two ions which are poorly coordinated to the extent that these salts can be present as liquids below 373 K, or even at room temperature. In these ILs, at least one ion has a delocalized charge and one component is organic, which prevents the formation of a stable crystal lattice. ILs are different from typical salts such as alkali halides, which have very high melting points due to their extremely strong Columbic forces. ILs offer virtually an infinite number of possible structures that allows them to be tuned towards desirable properties and applications. They have been used as catalysts[249] while combining their power as solvents. They have been used for azeotropic[250] and extractive[251] distillations. Also, due to their thermal stability, ILs have been used as lubricants at relatively high temperatures.[252] ILs are known as "designer" or "tailor-made" solvents because their physical properties, such as melting point, viscosity, and gas solubilization, can be controlled by altering the substituents of the cation or the anion.[249] They are considered "green" or "environmentally-friendly" solvents due to their non-volatility and minimal impact on the environment.[252-254] Some ILs can be easily disposed of, e.g., using ultrasound to degrade solutions of imidazolium-based ionic liquids with hydrogen peroxide and acetic acid to relatively harmless compounds.[255] In addition, the negligible vapor pressure[249] of ILs allows them to be employed in numerous reactions or separation processes.[251,252,256,257]

It should be mentioned that certain ILs have some inherent drawbacks such as: (1) various ILs have been found to be combustible and require careful handling;[258] (2) a brief exposure (5 to 7 seconds) to a flame torch will ignite some ILs, and some of them can be completely consumed by combustion;[258] (3) ILs tend to have a higher viscosity than conventional solvents, which could increase pumping costs; and (4) some ILs are hydroscopic as well as potentially toxic to aquatic environments.[259] This aquatic toxicity should not be ignored as it was reported to be equal to or greater than that of many conventional solvents.[253,254]

11.1 PROPERTIES OF THE GASES AND IONIC LIQUIDS USED

In this study, gaseous CO_2 with 99.99% purity (Grade 4.0), H_2 with 99.99% purity (Grade 4.0), industrial grade N_2 (99.7%) and a gaseous mixture consisting of 9.47/90.53 mole ratio of H_2S/N_2 were obtained from Valley National Gases, LLC, USA.[207] The use of H_2S/N_2 mixture was necessary to allow high pressure in the gas cylinder (137 bar) recommended for applying the physical gas absorption technique and to avoid any exposure to pure H_2S due to its high toxicity at 15 ppm level for a short exposure time. The liquids used as potential solvents for CO_2 capture are the ionic liquids TEGO IL K5, TEGO IL P51P and TEGO IL P9 manufactured by Evonik Goldschmidt Chemical Corporation[260]. The compositions of these solvents and their scientific name as reported by the Company are given in Table 11.1. The selection process for this IL was also guided by the recently developed definition of an "ideal" physical solvent for CO_2 capture.[261,262] Table 11.2 shows the critical properties of the ILs as well as the gases used in this study.

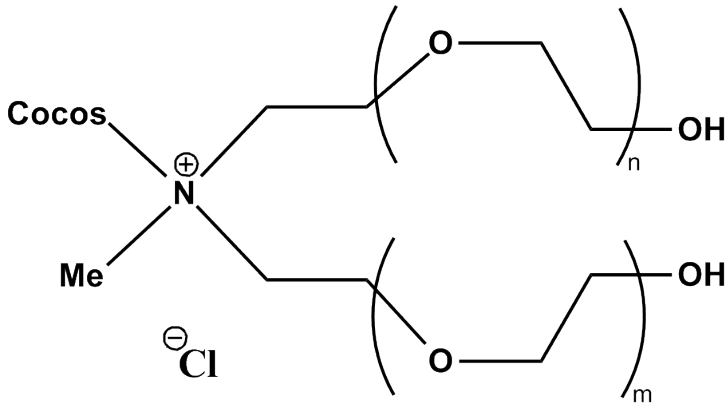

Cocos: mixture of Alkyl chains, $C_{14}H_{29}$

TEGO IL K5 (m+n = 14-25)

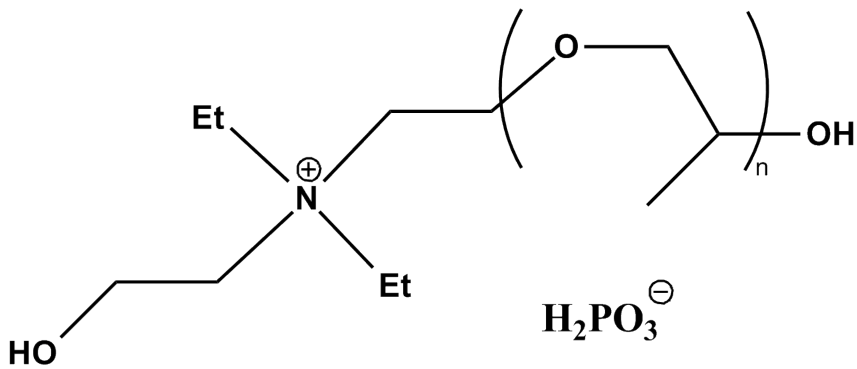

TEGO IL P51P (n = 50-60)

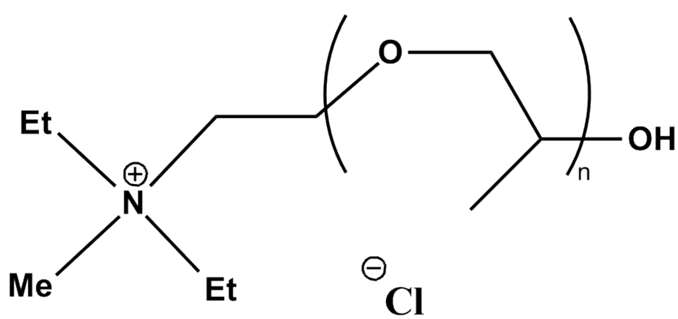

TEGO IL P9 (n = 5-15)

Figure 11.1: ILs used as physical solvent for CO_2 capture

Table 11.1: Composition of the ionic liquids TEGO IL K5, TEGO IL P51P and TEGO IL P9 from the MSDS provided by Evonik Goldschmidt chemical corporation

Ionic Liquid	Components	CAS Number	Concentration (%)
TEGO IL K5	Quaternary Ammonium Compounds, Coco Alkylbis (hydroxyethyl)methyl, Ethoxylated, Chlorides	61791-10-4	100
	Methyl Chloride	74-87-3	< 0.03
TEGO IL P51P	1,2-Ethanediol	107-21-1	1-10
	Alkoxylated Ammonium Phosphate	P-89-783	90-99
TEGO IL P9	Polyoxypropylene methyl diethyl ammonium chloride	68132-96-7	85-95
	Water	7732-18-5	5-15
	Methyl Chloride	74-87-3	< 0.03

Table 11.2: Critical properties of the gases and ILs used

Component	MW kg.kmol^{-1}	T_b K	T_c K	P_c bar	V_c m^3.kmol^{-1}	ω -	Reference
CO_2	44.010	194.70	304.19	73.82	0.0941	0.228	[168,209]
H_2	2.016	20.39	33.18	13.13	0.0642	-0.22	
N_2	28.013	77.35	126.10	33.94	0.0901	0.040	
H_2S	34.082	212.80	373.53	89.63	0.0985	0.083	
IL K5	924.68	626.56	848.46	7.138	2.9486	0.0302	Section 12.3 (See page 182)
IL P51P	3205.27	717.98	824.22	1.857	10.1607	0.0512	
IL P9	690.39	NA	NA	NA	NA	NA	

NA: Not Available

11.2 EXPERIMENTAL SETUP

The same 4-liter ZipperClave agitated reactor as for the perfluorocarbons experiments was employed in ILS experiments. The experimental setup used to obtain the solubilities and volumetric liquid-side mass transfer coefficients for CO_2, N_2 and H_2S in the IL K5 physical solvent is identical to that previously described.

11.3 SECOND GAS-LIQUID SYSTEMS USED

11.3.1 Density of the ionic liquids

In order to maintain a constant volume of liquid in the 4L Zipper Clave reactor, it is important to know the density of the ionic liquids, so that at room temperature the correct amount of solvent can be charged in the reactor. We decided to measure the density in our 4L Zipper Clave reactor by charging a known mass of solvent in the glass liner placed in the reactor. Since the reactor was calibrated with an external ruler, the increase in liquid height as a function of temperature was related to the increase in liquid volume and let to the density of the liquid.

Since the density of the 3 different ionic liquid appeared to decrease linearly with increasing temperatures, instead of a complex Racket equation used for the density correlation of the perfluorocarbon density, we chose a simple linear regression to correlate their density as a function of temperature:

$$\rho_{\mathrm{L}} = A + B \cdot T \qquad (11\text{-}1)$$

Table 11.3: Coefficient for Equation (11-1) for the three ILs

Liquid	A	B
	$kg.m^{-3}$	$kg.m^{-3}.K^{-1}$
TEGO IL K5	1262.9772	-0.590133
TEGO IL P51P	1256.4542	-0.773155
TEGO IL P9	1209.6301	-0.535747

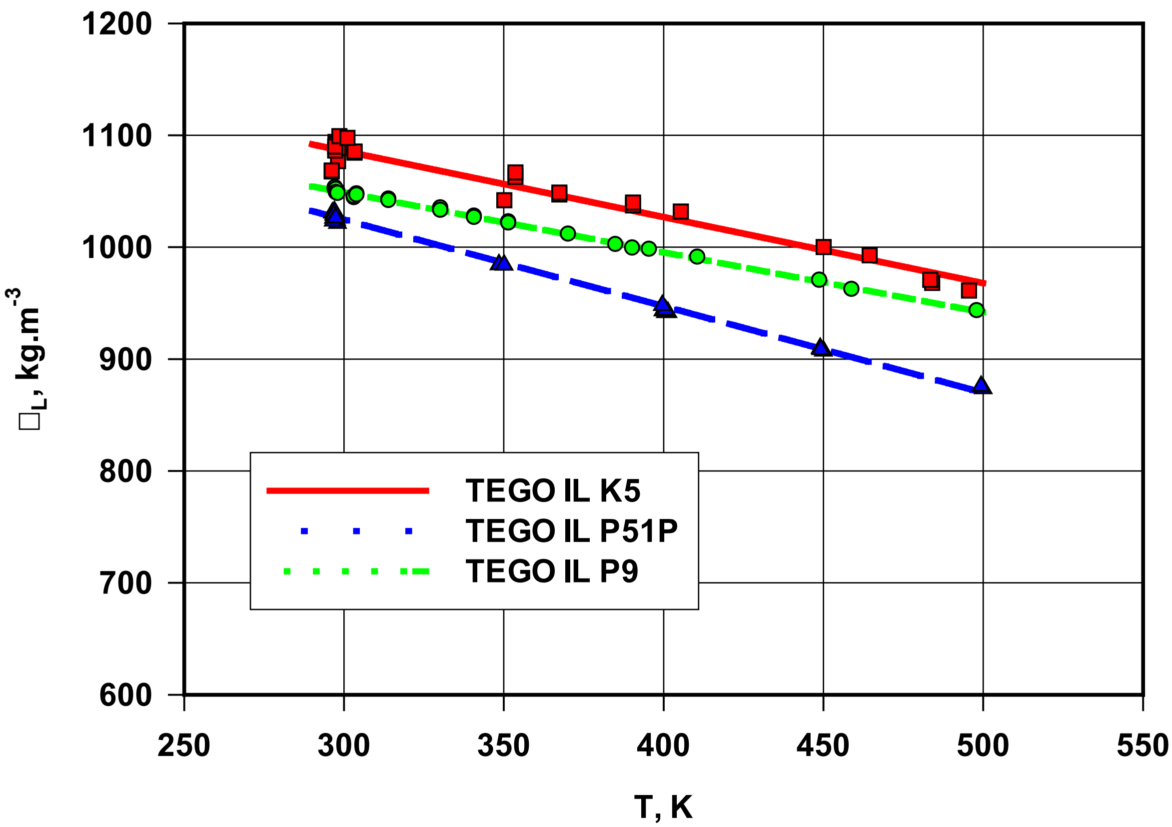

Figure 11.2: Density of the selected ionic liquids as a function of temperature

As it can be seen in Figure 11.3 the data obtained from the experimental density measurement of TEGO IL K5 in the 4L reactor and the data measured using the pcynometer are similar, there is less than 1 % difference between the 2 methods. It should be noted that the pycnometer are designed for measurements at room temperatures, but we were able to extend the measurements up to 400 K after which the glassware became too hot to handle safely and all the accuracy of the measurements could not be guaranteed.

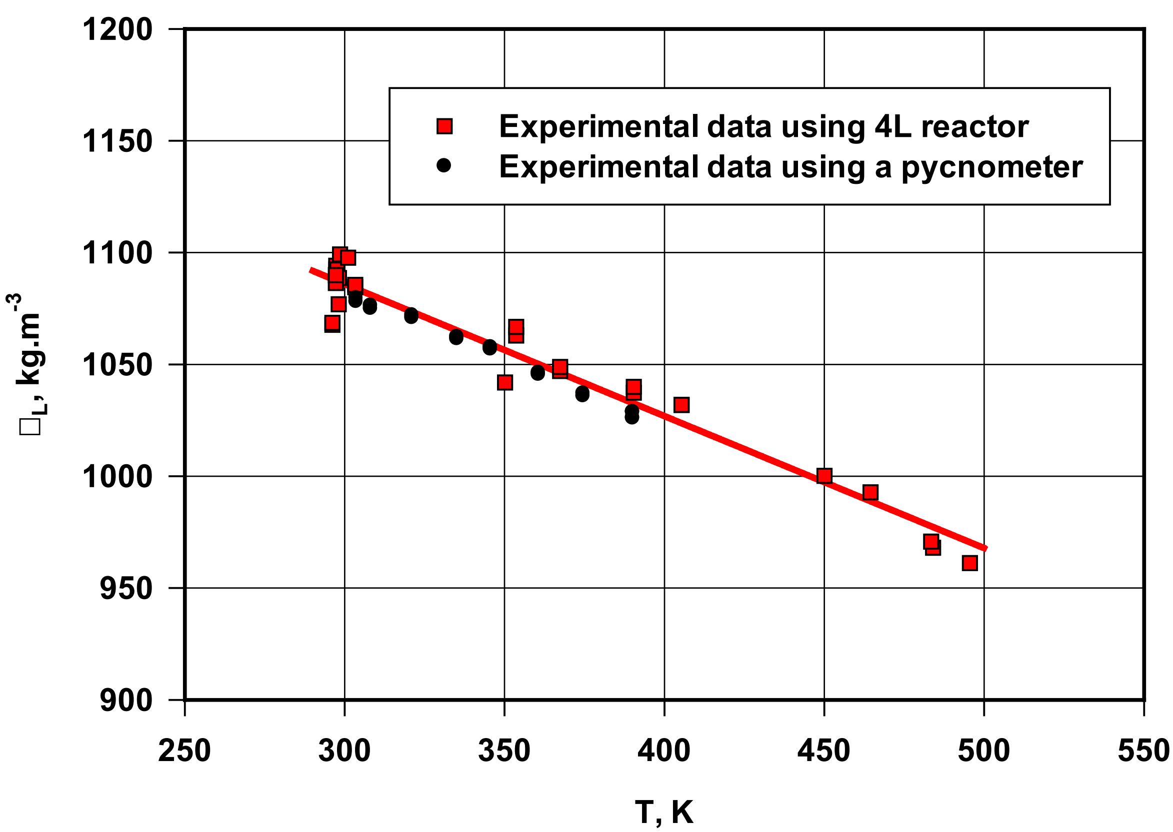

Figure 11.3: Comparison of density data for TEGO IL K5 obtained using the 4L reactor and a pycnometer as a function of temperature

11.3.2 Viscosity of the ionic liquids

Figure 11.4 shows the viscosities of the 3 ILs which were measured using a Cannon-Fenske viscometer in the temperature range of 300 to 450 K. The TEGO IL P9 has the highest viscosity at room temperature, whereas at temperature above 350 K the TEGO IL P51P presents the highest viscosity. The values were correlated using the Vogel-Tamman-Fulcher Equation (11-2) with a regression coefficient (R^2) > 0.99, and the coefficient for the equation can be found in Table 11.4:

$$\mu_L = \mu_O \cdot \exp\left(\frac{B_0}{T - T_O}\right) \tag{11-2}$$

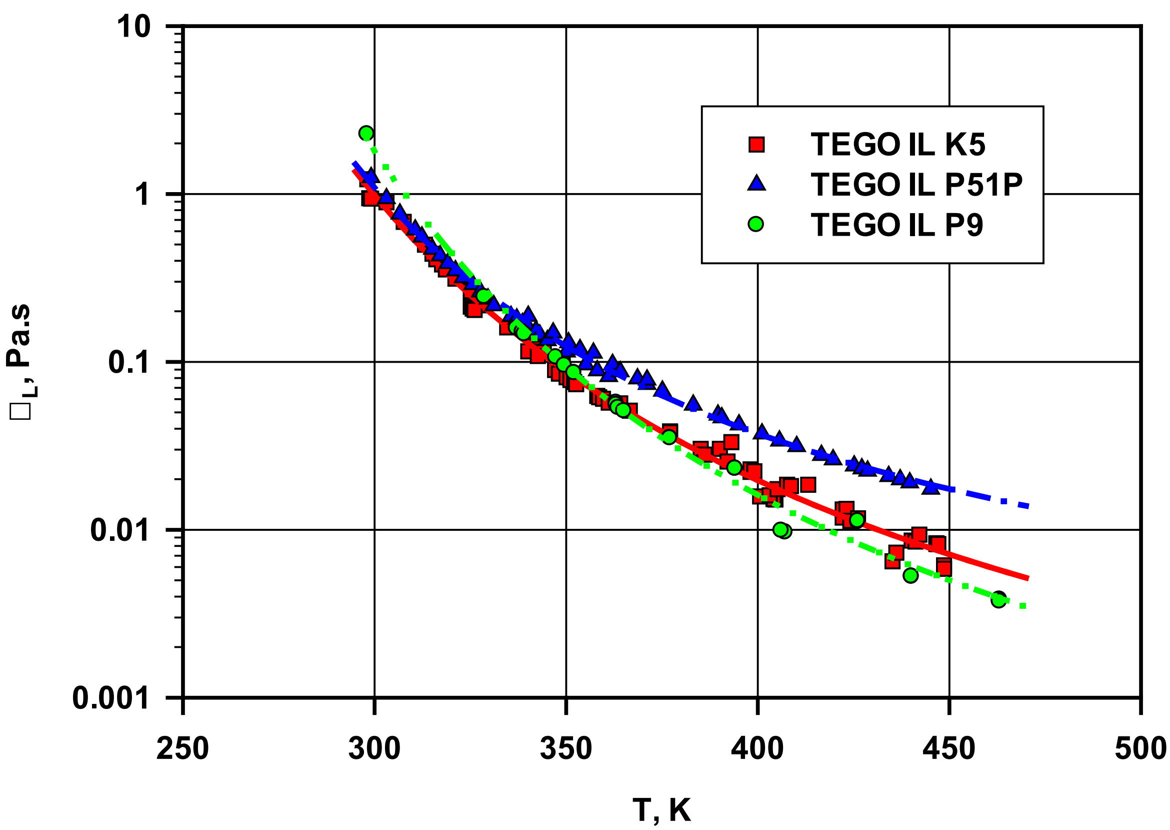

Figure 11.4: Viscosity of the three ionic liquids as a function of temperature

Table 11.4: Coefficient for Equation (11-2) for the three ILs

Liquid	μ_0	B_0	T_0
	Pa.s $\times 10^3$	K	K
TEGO IL K5	0.0343	1667.3	137.5
TEGO IL P51P	0.5974	918.9	177.7
TEGO IL P9	0.0155	1715.2	152.9

11.3.3 Surface tension of the ionic liquids

The Ethoquad C/25 Cocoalkylmethyl[polyoxyethylene (15)] ammonium chloride, CAS# 61791-10-4)[263] from Azko Nobel has a coconut fatty alkyl chain and 15 ethylene oxide units, which is identical to TEGO IL K5. Azko Nobel reported two values for the surface tension of TEGO IL K5 in a water solution at 298 K, 43.4 mN/m at 0.1% and 41.5 mN/m at 1%, which are the only surface tension data found in the literature for the three studied ionic liquids.

To measure the surface tension of the ionic liquids in our laboratory, we used the Fisher Surface Tensiomat, Model 21, which can be used to determine the apparent surface tension and interfacial tension of liquids.

The ring method also known as the Lecomte du Nouy ring method is the technique most often used by researchers for static surface tension measurement. The surface tension can be determined directly from the force required to pull the ring from a liquid. This method does not require any calibration with other methods or known solutions. The surface tension for the du Nouy method is the mechanical force necessary to lift a platinum-iridium ring of precisely known dimensions wire radius (r) and ring radius (R) from the solution surface via a counter-balanced lever-arm. The arm is held horizontal by torsion applied to a taut stainless steel wire to which it is clamped. Increasing the torsion in the wire raises the arm and the ring, which carries with it a film of the liquid in which it is immersed. The force necessary to pull the test ring free from this surface film is measured. The Surface Tensiomat shows this "apparent" surface on a calibrated dial, which can be converted to "absolute" values by multiplying by a correction factor.

The equation describing this process is:

$$\eta = \frac{P \cdot F}{4\pi \cdot R} \tag{11-3}$$

η = surface tension

P = force or pull necessary to detach ring from solution surface

V = volume of solution displaced by the pull of ring

F = Harkins-Jordan correction factor, f(R/r,R^3/V)

Harkins and Jordan[264] also presented some possible sources of error associated with the ring method:

1. The plane of the ring must be horizontal to the liquid surface.
2. The diameter of the vessel holding the liquid should be greater than 8 cm.
3. The ring should lie in a plane.

The surface tensiomat measures apparent surface tension, in order to obtain the absolute surface tension, the following relationship is used:

$$S = P \times F \tag{11-4}$$

where S is the absolute value, P is the apparent value as indicated by the dial reading, and F a correction factor. The correction factor is dependent on the size of the ring and the size of wire used in the ring, the apparent surface tension, and the densities of the two phases. Equation (11-5) shows the relationship for the correction factor:

$$(F - a)^2 = \frac{4b}{(\pi R)^2} \times \frac{P}{D - d} + K \tag{11-5}$$

with

$$K = 0.04534 - 1.679\frac{r}{R} \tag{11-6}$$

By replacing πR=C/2, and Equation (11-6)

$$F = a + \sqrt{\frac{16bP}{C^2(D-d)} + 0.04534 - 1.679\frac{r}{R}} \qquad (11\text{-}7)$$

where

F = correction factor

R = radius of the ring

r = radius of the wire of the ring

P = apparent value or dial reading of surface tension

D = density of the lower phase

d = density of the upper phase

K = 0.04534 – 1.679 r/R

C = circumference of the ring

a = 0.725

b = 0.0009075

K, a and b are universal constants for all rings, for the instrument in our laboratory, C = 6.005 cm and R/r = 53.7936868.

Figure 11.5 represents the surface tension of the TEGO IL K5 and the TEGO IL P51P as a function of temperature in the range from 296 to 369 K. The data for the TEGO IL K5 were correlated with R^2=0.936 and the data for TEGO IL P51P was correlated with R^2=0.848. Since the surface tension of a liquid is related to its critical temperature (T_c) through the Guggenheim's empirical correlation, Equation (11-8), according to Rebelo et al.,[265] this equation was used to model the measured surface tensions of the two ILs values as a function of temperature and the calculated values of σ_0 and T_c for each IL are listed in Table 11.5.

$$\sigma_L = \sigma_0 \left(1 - \frac{T}{T_c}\right)^{11/9} \tag{11-8}$$

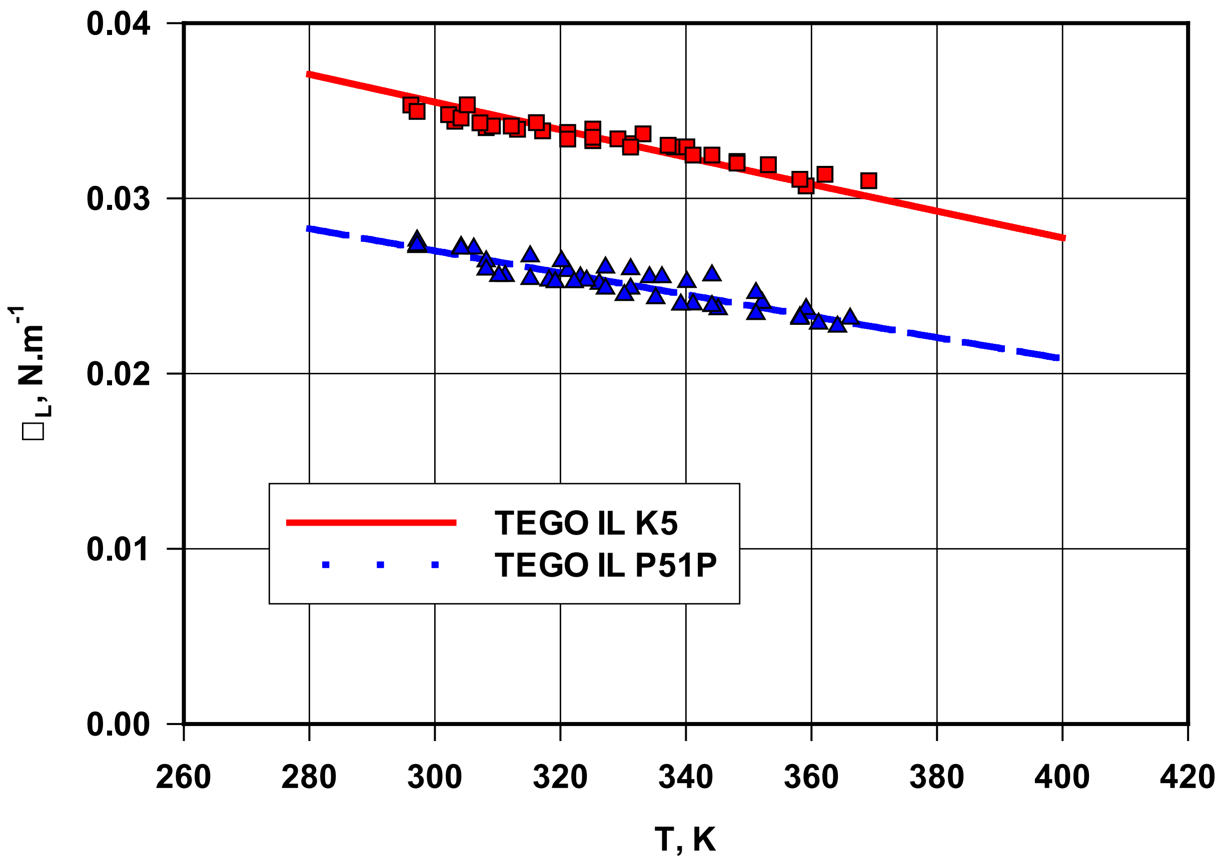

Figure 11.5: Surface tension of TEGO IL K5 and TEGO IL P51P as a function of temperature

Table 11.5: Calculated values of coefficients in Equation (11-8)

	σ_0	T_c
	$N.m^{-1}$	K
TEGO IL K5	0.06050	848.46
TEGO IL P51P	0.04695	824.22

11.4 CALCULATION OF THE SOLUBILITY AND VOLUMETRIC MASS TRANSFER COEFFICIENT OF GASES IN THE ILS

11.4.1 Gas Solubility, C^*

The calculation of the gas solubility in the IL was conducted assuming non-ideal behavior of the liquid and gas phases under the experimental conditions used. Knowing the total pressure and temperature of gas-liquid system inside the reactor, the Peng-Robinson Equation-of –State (P-R EOS) was used to calculate the liquid-phase and gas-phase compositions at thermodynamic equilibrium using the steady-state portion of the P–t profile, where the reactor volume balance was taken into account. The amount of gas absorbed prior to mixing in the reactor was accounted for by building a mass balance on the preheater, which made the calculation of the gas solubility in the liquid more rigorous when compared with previous studies. The solubilities of N_2 and CO_2, as individual gases, in the IL solvent were obtained using the same experimental setup and calculation method. The solubility of N_2, mixed with H_2S, in the IL solvent was subsequently compared with that of N_2 as single gas in the same solvent at identical pressure and temperature conditions. This comparison allowed the validation of the solubility values of N_2 and consequently those of H_2S in the IL solvent.

11.4.2 Volumetric Liquid-Side Mass Transfer Coefficient, k_La

For pure CO_2, H_2 and N_2 the calculation of k_La was carried out using a transient physical absorption technique under the following assumptions: (1) non-ideal behavior of the liquid and gas phases, (2) the liquid phase is well mixed, (3) the mass transfer resistance on the gas-side is negligible when compared with that in the liquid-side, and (4) the double-film theory is applicable. The rate of mass transfer of the solute gas from the gas-phase into the liquid-phase ($n_{i,L}$) during the transient portion of the P–t profile can be expressed using Equation (7-37) (See page 89); and the calculation scheme used for calculating k_La can be found in Section 7.2.

For the N_2/H_2S gaseous mixture, the Mass Spectrometer was used to obtain N_2 and H_2S mole fractions as a function of time by monitoring the intensity at the atomic mass units 28 and 34, corresponding to the 100% peaks for N_2 and H_2S, respectively. The pressure transducer in the reactor was also used to record the total pressure decline as a function of time. The knowledge of these data allowed the calculation of the partial pressures corresponding to N_2 and H_2S as a function of time, which, in turn, were substituted into Equations (7-38) and (7-39) in order to obtain k_La values for each gas in the mixture.

11.5 RESULTS AND DISCUSSIONS OF IONIC LIQUIDS

11.5.1 Solubility of CO_2 in the ILs

As can be seen in Figure 11.6, the equilibrium solubility of CO_2 in the IL, expressed as mole fraction (x^*), appears to increase nonlinearly with CO_2 partial pressure (P_{CO2}) for all 5 temperatures used and Equation (11-9) can be used to model the experimental x^* values in this IL with a correlation coefficient (R^2) > 0.992. It is also important to note that the solubility decreases with increasing temperature. The solubility of CO_2 in the IL at 300 K is about 2.4 to 4.6 times greater than that at 500 K over the pressure range investigated (0-30 bar). This decrease of CO_2 solubility with increasing temperature was previously reported by a number of investigators, including Anthony et al.[266,267], Kumelan et al.[268] and Shin et al.[269]

Figure 11.7 shows the equilibrium solubility of CO_2 in the TEGO IL P51P, and as can also be observed, the solubility values increase nonlinearly with CO_2 partial pressure for all temperatures used, and Equation (11-9) can be employed to model the solubility data for this IL with $R^2 > 0.98.5$.

$$P_{CO2} = a_1 \cdot X^{*2} + b_1 \cdot X^* \tag{11-9}$$

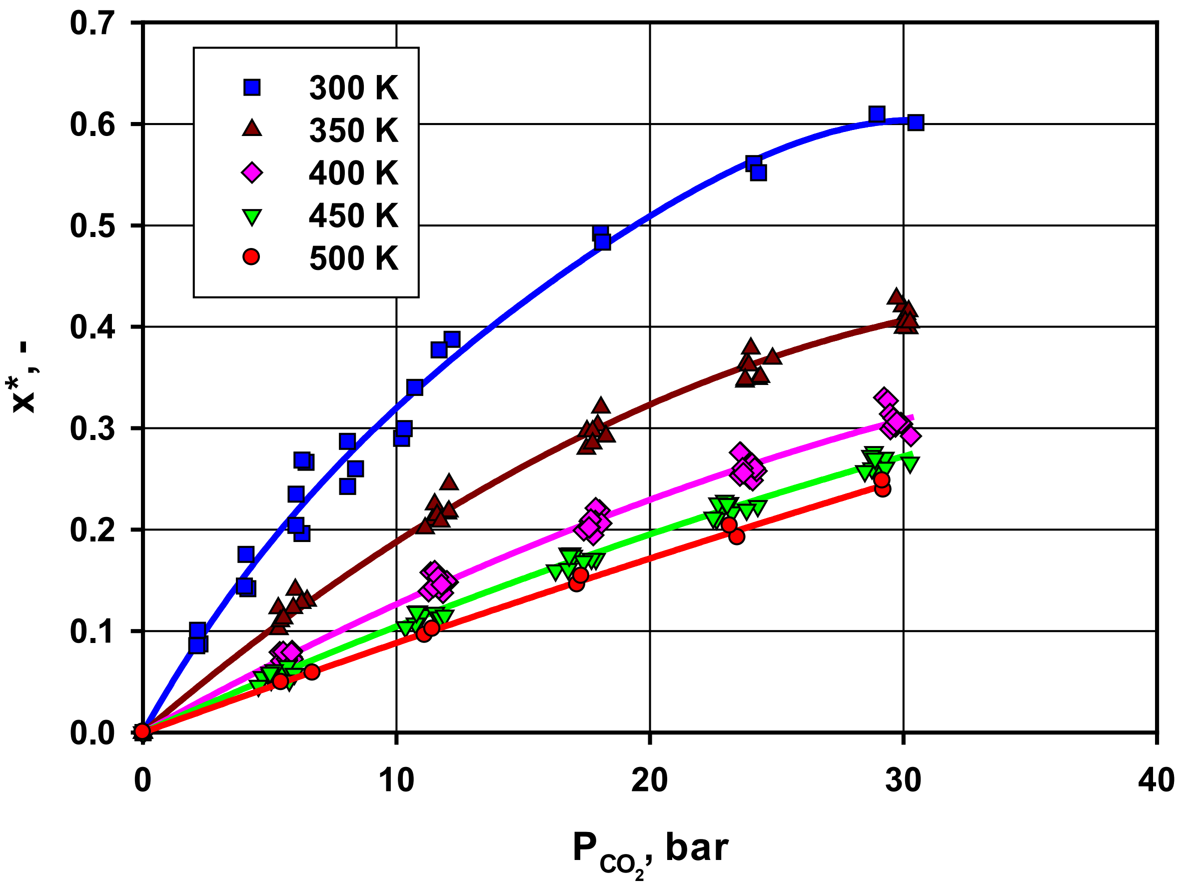

Figure 11.6: Solubility of CO_2 in the TEGO IL K5 as a function of temperature and CO_2 partial pressure

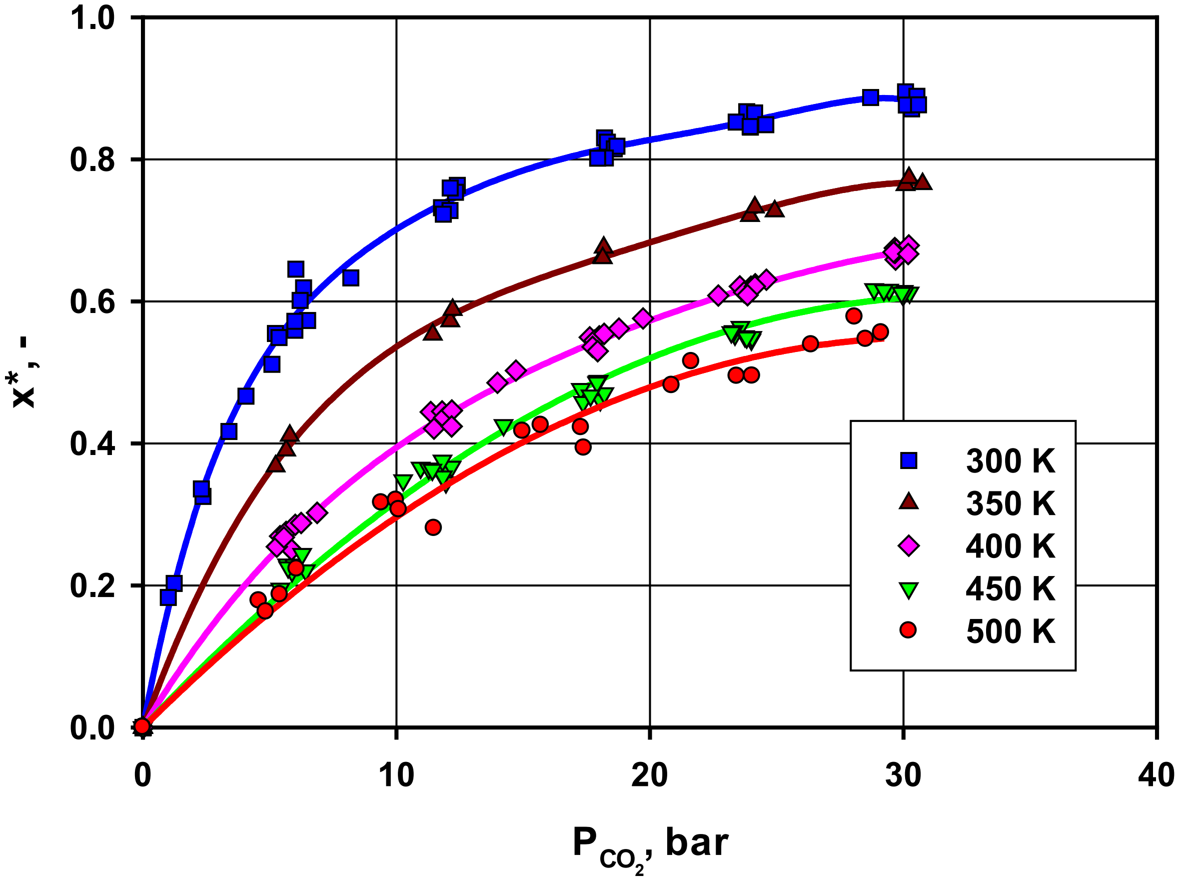

Figure 11.7: Solubility of CO_2 in the TEGO IL P51P as a function of temperature and CO_2 partial pressure

The TEGO IL P9 was not investigated in details since preliminary solubility measurements at 300 and 500 K show lower solubility than the other 2 ionic liquids investigated (TEGO IL K5 and TEGO IL P51P). Figure 11.8 shows a value of x* = 0.14 at 30 bar and 500 K for the TEGO IL P9, furthermore when comparing the 3 ionic liquids and Selexol at 300 K, there is a clear advantage to use the TEGO IL K5 or even better the TEGO IL P51P which display larger solubilities as shown in Figure 11.9.

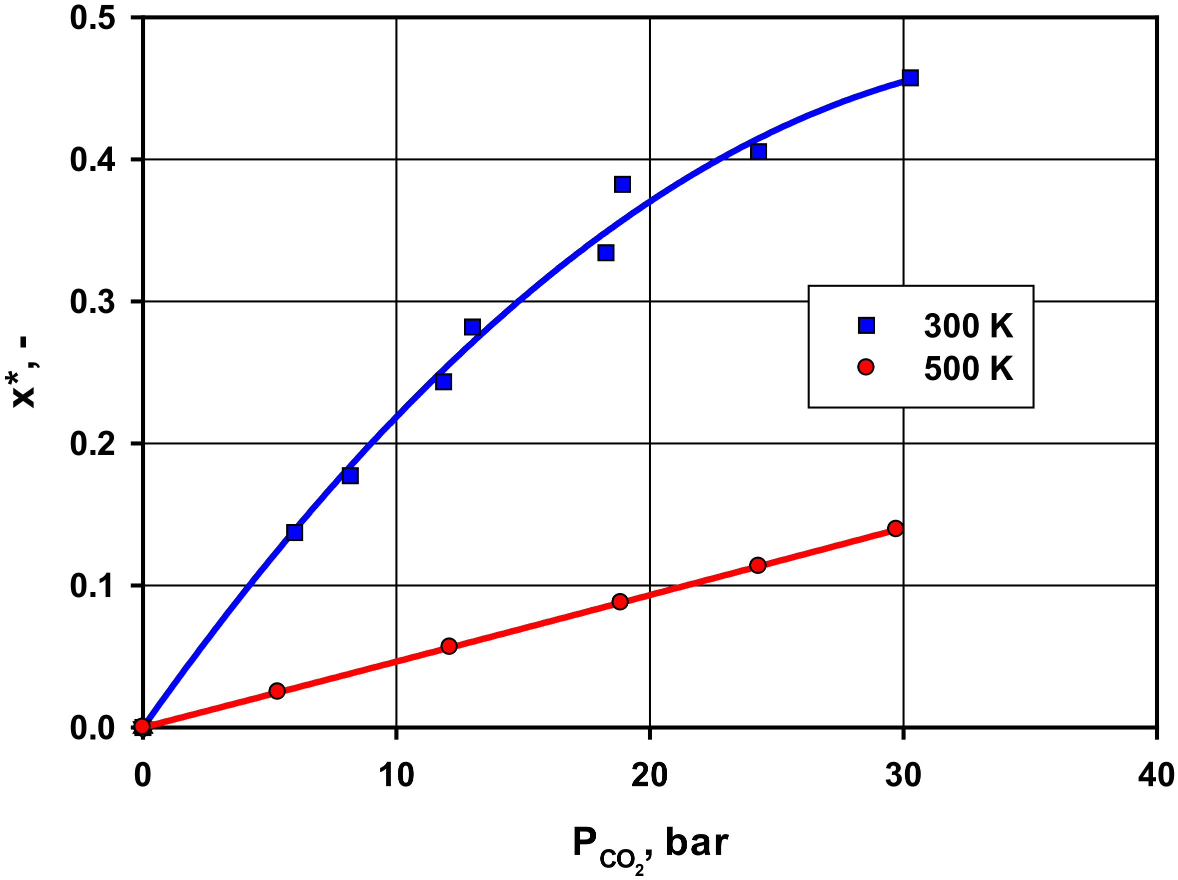

Figure 11.8: Solubility of CO_2 in the TEGO IL P9 as a function of temperature and CO_2 partial pressure

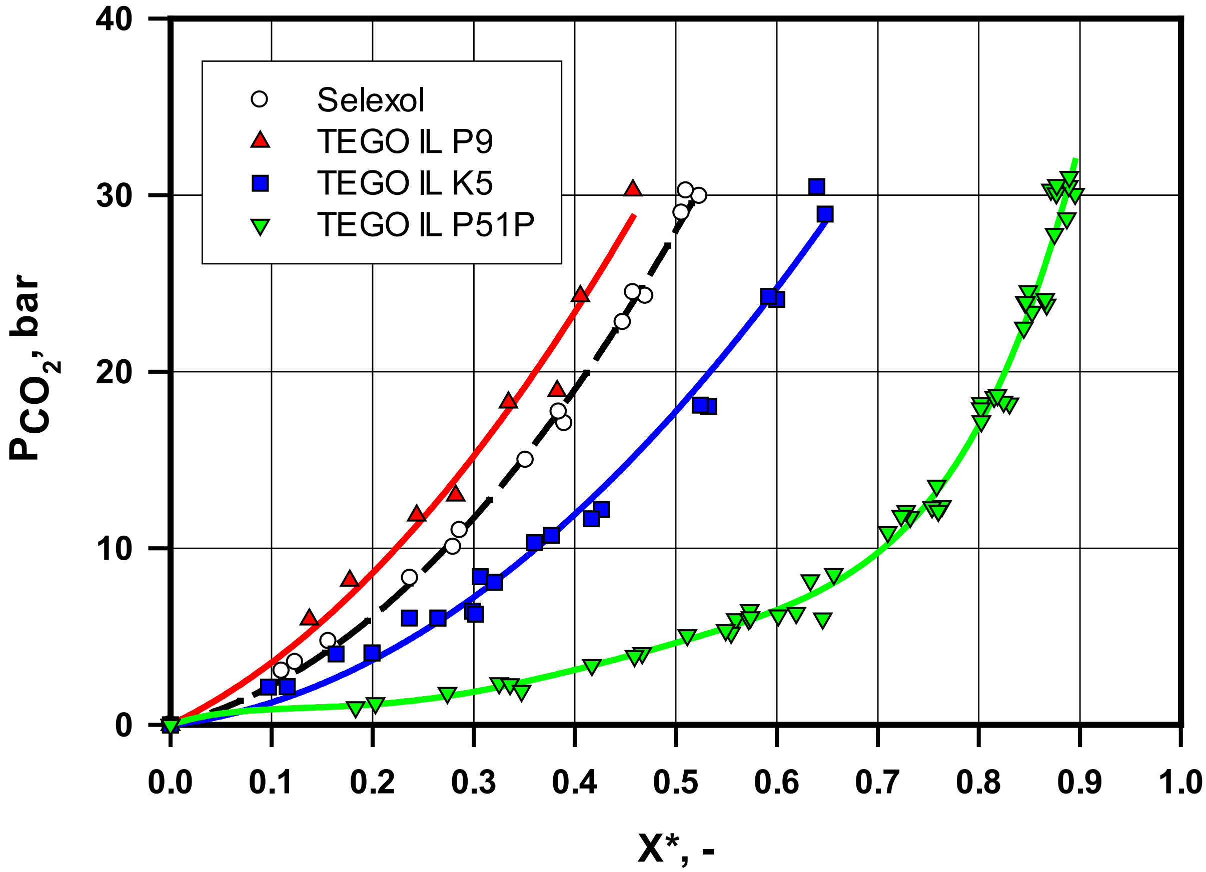

Figure 11.9: CO_2 Solubility comparison between Selexol, TEGO IL K5, TEGO IL P51P and TEGO IL P9 as a function of CO_2 partial pressure at 300 K

Figure 11.10 indicates that at 500 K which is more likely to be the temperature of the fuel gas streams, the CO_2 solubility in the TEGO IL P51P is more than twice that in the TEGO IL K5, and, hence, the TEGO IL P51P would be a better physical solvent for CO_2 capture from IGCC facilities. Figure 11.10 shows that at 500 K and similar CO_2 partial pressure, the solubility of CO_2 in the TEGO P51P is greater than that in the TEGO IL K5. This might be attributed to the greater number of ethylene oxide groups present in the TEGO IL P51P when compared with those in the other two ILs.

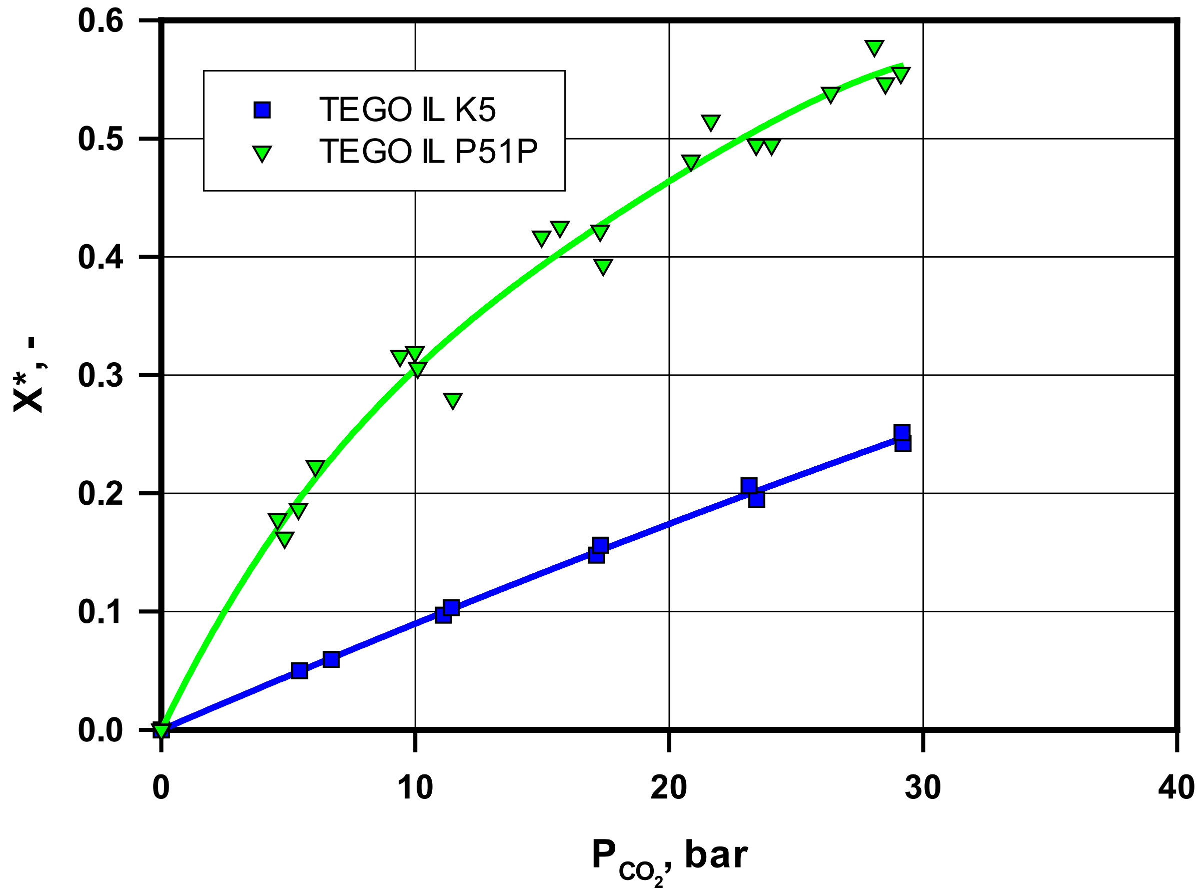

Figure 11.10: CO_2 Solubility comparison between TEGO IL K5 and TEGO IL P51P as a function of CO_2 partial pressure at 500 K

11.5.2 Henry's Law constants at infinite dilution for CO_2

The Henry's Law constants at infinite dilution (He_{∞}), calculated using Equation (11-10) for CO_2 in the TEGO IL K5 and TEGO IL P51P, are given in Table 11.7. Again, the Henry's Law constants at infinite dilution for the TEGO IL P51P are smaller than those of the TEGO IL K5 indicating that CO_2 is more soluble in the TEGO IL P51P than in the other IL. Table 11.7 shows that the value of the Henry's law constant at infinite dilution for the TEGO IL K5 at 500 K is 7.5 times that at 300 K.

$$He_{\infty} = \lim_{X^* \to 0} \left(\frac{P_{CO2}}{X^*} \right) = b_1 \tag{11-10}$$

In certain cases (e.g., for relatively small temperature ranges), the standard heat of solution of a gas (ΔH^o) may be treated as a constant and can be related to the Henry's law constant at infinite dilution (He_{∞}) through Equation (11-11).[224]

$$\ln(He_{\infty}) = \ln(He_o) + \frac{\Delta H^o}{RT} \tag{11-11}$$

However, there are other cases (e.g., for relatively wide temperature ranges) in which ΔH^o is temperature dependent and, therefore, is not a constant. For the latter cases, ΔH^o may be obtained from Equation (11-12).[223,224,270]

$$\frac{\Delta H^o}{R} = \left[\frac{\partial \ln(He_{\infty})}{\partial(1/T)} \right] \tag{11-12}$$

Figure 11.11 depicts $\ln(He_{\infty})$ as a function of the reciprocal of absolute temperature (1/T) and shows that the Henry's law constants at infinite dilution (He_{∞}) for the two ILs are not a linear function of the reciprocal of temperature; accordingly the standard heat of solution of CO_2 (ΔH^o) is temperature-dependent. Therefore, the Henry's law constants at infinite dilution (He_{∞}) were modeled as a function of the reciprocal of absolute temperature using Equation (11-13), where the constants in this equation are given in Table 11.6.

$$\ln(He_{\infty}) = A + \frac{B}{T} + \frac{C}{T^2} \tag{11-13}$$

Table 11.6: Coefficients in Equation (11-13)

	TEGO IL K5	TEGO IL P51P
A	4.569	-10.912
B	1032.61	11069.1
C	-479,608.6	-2,127,077

The combination of Equations (11-12) and (11-13) yields the following expression:

$$\Delta H^o = R\left(B + \frac{2C}{T}\right) \tag{11-14}$$

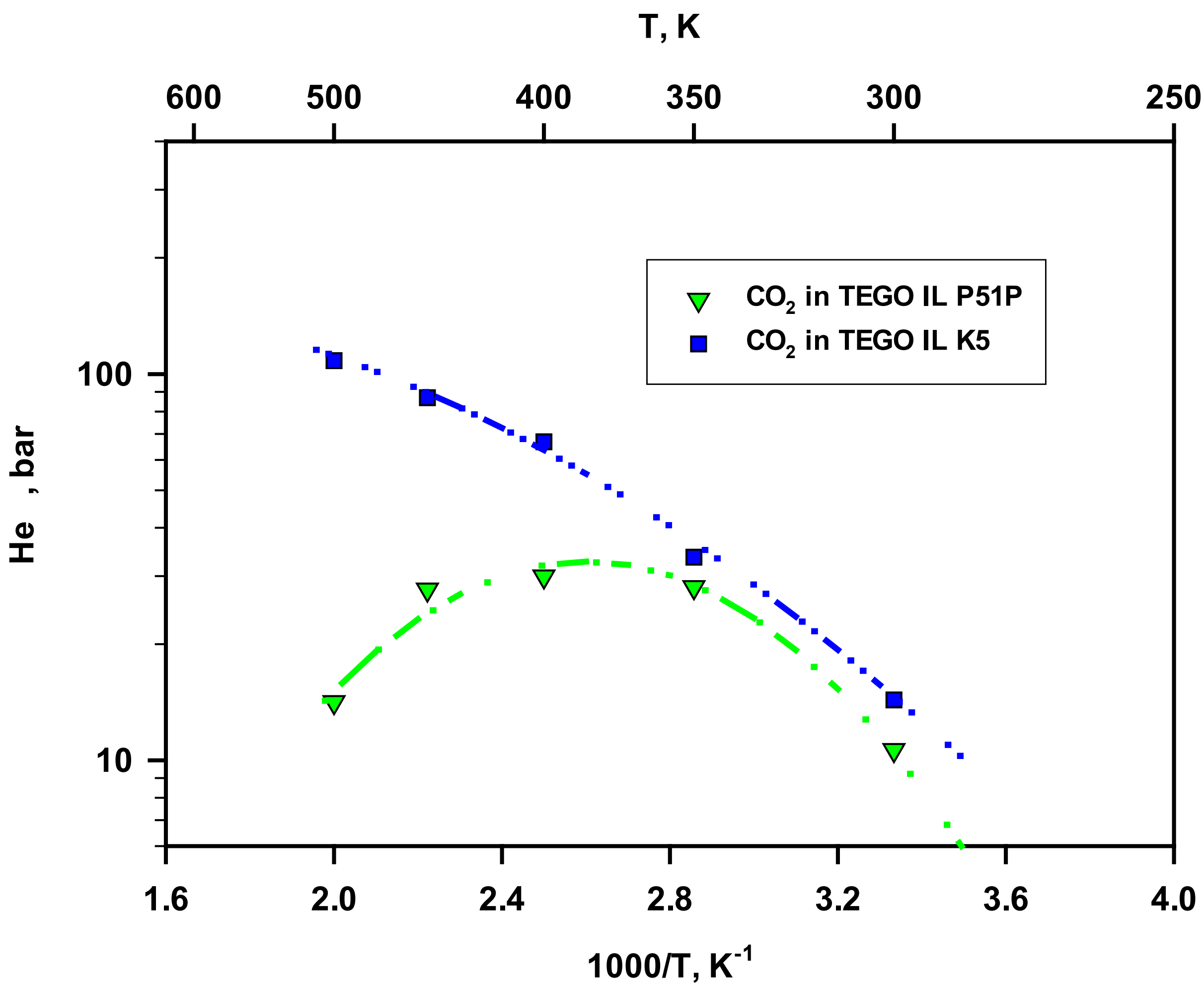

Figure 11.11: Henry's law constant as a function of temperature for CO_2

in the TEGO IL K5 and TEGO IL P51P

The values of ΔH^o for CO_2 in both ILs are given in Table 11.7. The negative values of ΔH^o indicate that CO_2 dissolves in the ionic liquids in the specified temperature range, even though the magnitude of ΔH^o decreases from that for relatively strong acid-base bonds at 300 K to that for either very weak acid-base bonds or van der Waals associations at 500 K.[262]

Table 11.7: Henry's law constant at infinite dilution and standard heat of solution for CO_2 dissolved in the TEGO IL K5 and TEGO IL P51P

	T (K)	He_∞ (bar)	ΔH^o (kJ.mol^{-1})
TEGO IL K5	300	14.35	-18.00
	350	33.57	-14.20
	400	66.80	-11.35
	450	86.93	-9.14
	500	108.39	-7.37
TEGO IL P51P	300	10.62	-25.87
	350	28.10	-9.03
	400	29.94	3.61
	450	27.70	13.43
	500	14.16	21.29

11.5.3 Solubility of H_2 in the TEGO IL P51P

Figure 11.12 shows the solubility of H_2 (expressed in mole fraction) in the TEGO IL P51P, and, as can be observed from Figure 11.12, the solubility of H_2 increases with temperature from 350 to 500 K, which is similar to that reported for other ILs by Kumelan et al.[271] The comparison between Figures 11.7 and 11.12 reveals that the solubility of CO_2 in the TEGO IL P51P is about 4 times that of H_2 at 350 K; and this ratio decreases to about 1.5 at 500 K. This behavior is similar to that reported for the solubilities of CO_2 and H_2 in other ionic liquids.[268,271]

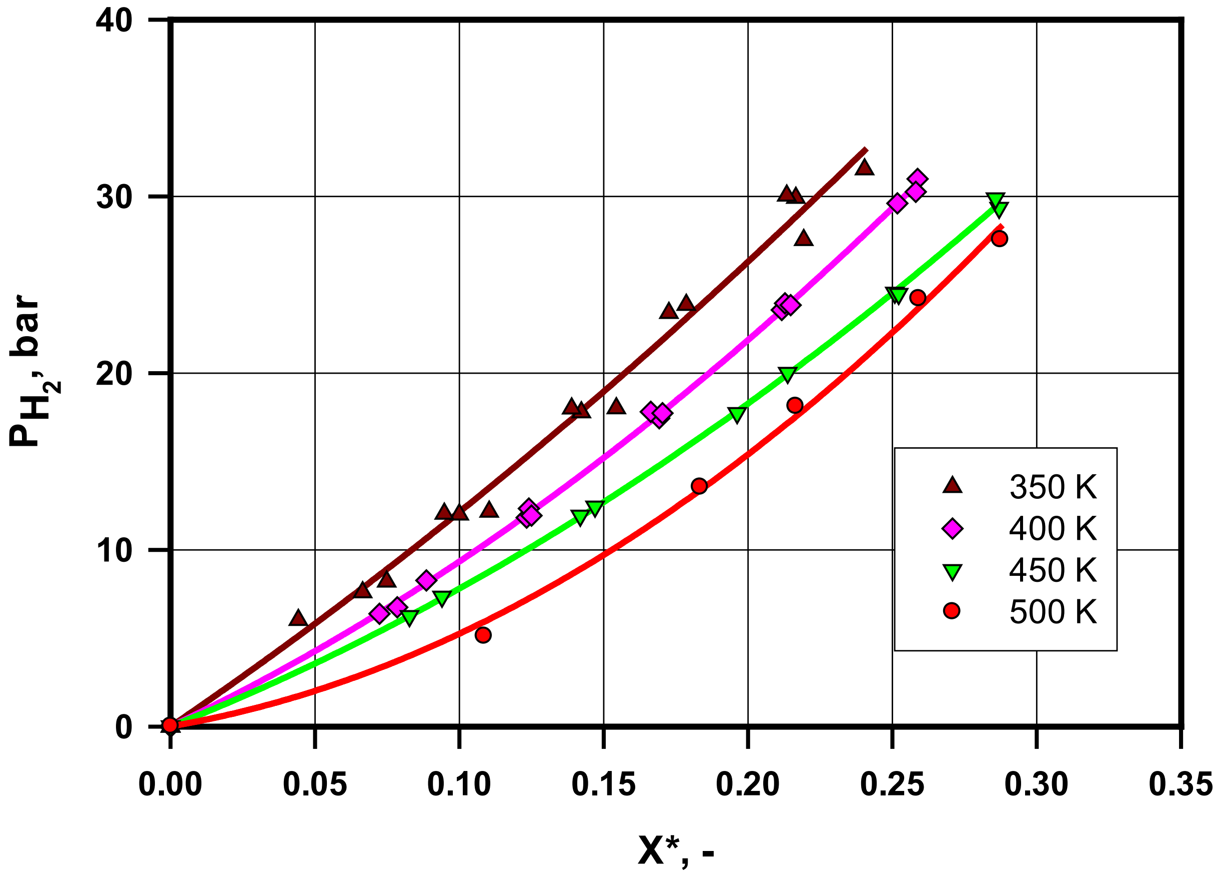

Figure 11.12: Solubility of H_2 in the TEGO IL P51P as a function of pressure and temperature

11.5.4 Solubility of H_2S in the TEGO IL K5

As mentioned above, the solubilities of N_2 and H_2S (as a gas mixture) in the IL physical solvent were simultaneously calculated using the P-R EOS. Thus, in order to validate the solubility values of H_2S in the solvent, the N_2 solubility data calculated using the gaseous mixture were compared with those measured with N_2 as single gas in the same solvent under similar pressure and temperature conditions as shown in Figure 11.13. As can be seen in this figure, all data points for N_2 lie on the same line, indicating that the solubility values calculated for N_2 using the H_2S/N_2 mixture are in perfect agreement with those measured for N_2 as single gas and consequently the solubility data for H_2S in the IL physical solvent using the gas mixture should also be reliable. It should be mentioned that the partial pressures of H_2S used in the experiments were < 2.5 bar because the original gas mixture contained 9.47 mole% of H_2S, and the highest total pressure used in the experiments was 30 bar. The H_2S solubility data obtained within this small pressure range, however, are useful since the H_2S mole fraction in a typical shifted gas stream using Pittsburgh No. 8 Coal was reported to be 0.48 mole % which corresponds to 0.13 bar, considering the fuel gas pressure is available at 26.3 bar.[248]

Figure 11.14 shows that the solubility of H_2S in the IL physical solvent non-linearly increases with pressure within the range investigated. This behavior is not surprising since similar behavior of CO_2 solubility can be observed in Figure 11.6. It is also important to note that the H_2S solubility in the IL decreased with increasing temperature, which is also similar to the behavior of the CO_2 solubility in the same ionic liquid.

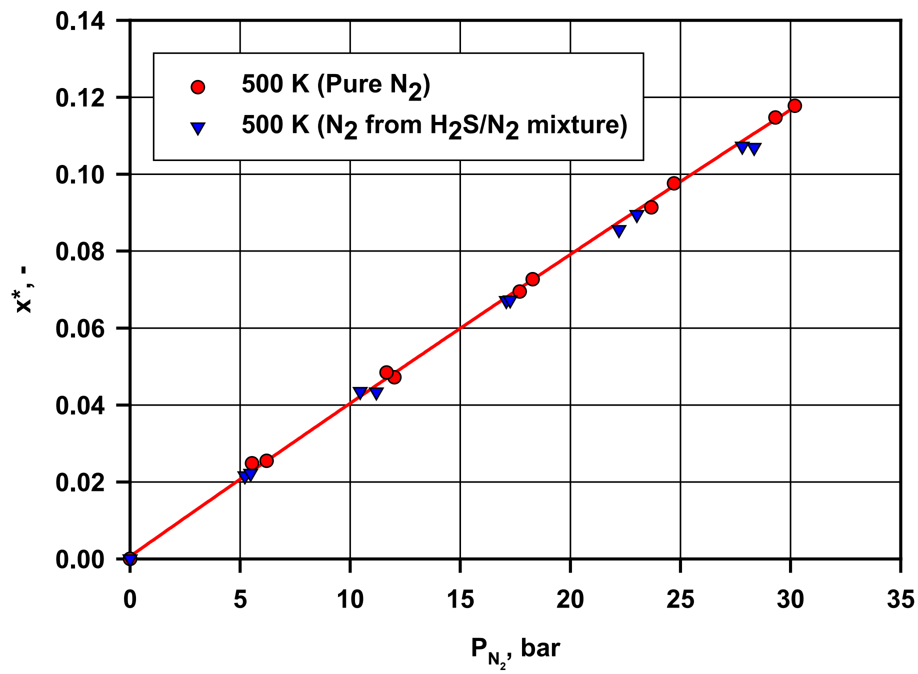

Figure 11.13: Comparison between the solubilities in the IL of

N_2 as single gas and N_2 within the binary H_2S/N_2 mixture

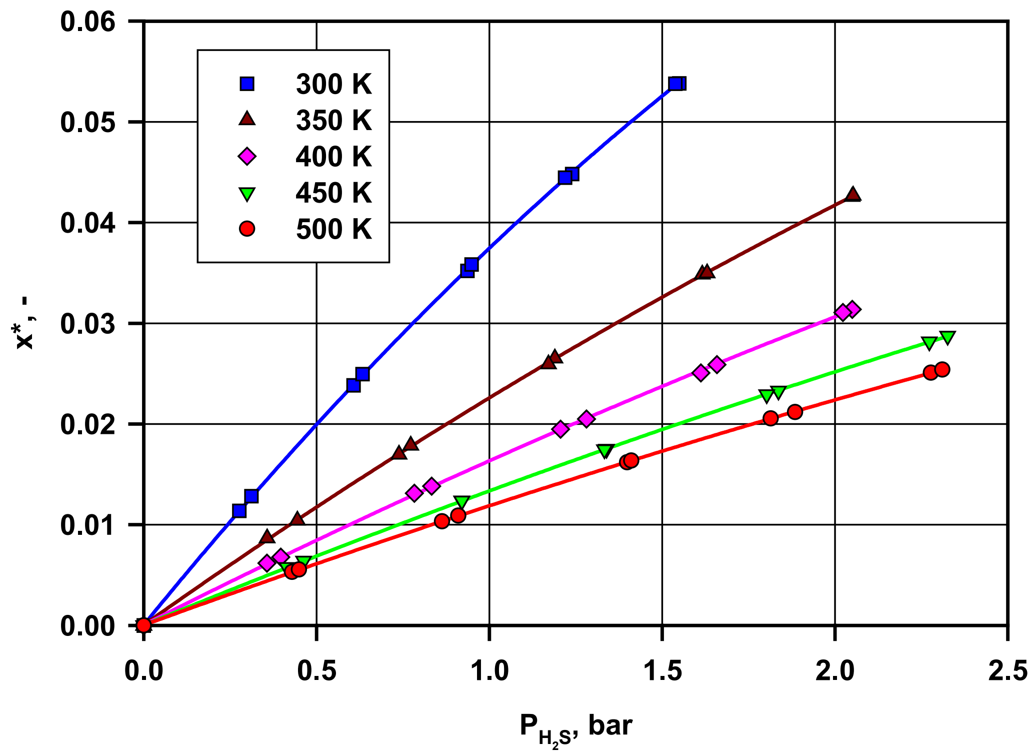

Figure 11.14: Solubility of H_2S in the IL as a function of temperature and H_2S partial pressure

11.5.5 Comparison between H_2S and CO_2 solubilities in the TEGO IL K5

Table 11.8 shows a comparison between the solubilities of H_2S and CO_2 in the IL physical solvent under similar pressures and temperatures. The solubility values of CO_2 were predicted by fitting the data measured at pressures varying from 2 to 30 bar. As can be deduced from this table, the solubilities of H_2S in the IL are lower than those predicted for CO_2 at 300 K. At the other temperatures used (350, 400, 450 and 500 K), however, H_2S solubilities appear to be greater than those of CO_2. Thus, the IL can be used to remove H_2S and CO_2 from a relatively dry hot gas stream within a temperature range from 350 to 500 K under pressures up to 30 bar.

11.5.6 k_La of CO_2 and H_2 in the TEGO IL K5 and TEGO P51P

In order to design a CO_2 capture process using ILs, one must know the solubility and the volumetric liquid-side mass transfer coefficients (k_La) which will determine the size of the absorber, such as a packed-bed reactor.[272] These mass transfer coefficients should be measured under the pressure and temperature of the CO_2 capture process in order to properly design and scaleup the absorber.

11.5.6.1 Effect of Pressure on k_La

Figures 11.15, 11.16 and 11.17 show the effect of pressure on k_La values for CO_2 in the TEGO IL K5 and TEGO IL P51P at various temperatures, mixing speeds, and liquid heights. In general, k_La values increase with pressure, and in some cases, k_La values increase up to a pressure of about 25 bar and then slightly increase or level off. The reason for increasing k_La with pressure can be attributed to the increase of the CO_2 solubility, which alters the physicochemical properties of the liquid phase, such as liquid viscosity and surface tension, which are supposed to increase k_La. Numerous investigators[85,126,128,139,144,146,151,240] reported that k_La is strongly dependent on the gas-liquid system and the range of pressures used. In this study, it appears that increasing pressure resulted in shrinkage of the gas bubbles into small ones with large gas-liquid interfacial area (a), leading to the increase of k_La.

11.5.6.2 Effect of Temperature on k_La

Figure 11.15 illustrates that k_La values increase with increasing temperature for CO_2 in the TEGO IL K5 and TEGO IL P51P within the temperature range used. Similarly, several authors reported an increase of k_La values with temperature in different gas-liquid systems.[121,129,139,143,146,150,151,240] The effect of temperature on k_La can be explained by its effect on the gas-liquid interfacial area (a) and the liquid-side mass transfer coefficient (k_L). For instance, increasing temperature decreases the liquid viscosity and surface tension, resulting in an increase of the gas holdup (ε_G) and a decrease of the Sauter mean bubble diameter (d_S), resulting in increasing the gas-liquid interfacial area (a), as can be deduced from Equation (8-12). Also, increasing temperature results in increasing the gas diffusivity and, consequently, the liquid-side mass transfer coefficient (k_L) since it is directly proportional to the gas diffusivity to power 1 (film-theory) or 0.5 (penetration theory).[261] Thus, the combined effect of temperature on both a and k_L led to the observed increase of k_La, as indicated in Figure 11.15.

$$a = \frac{6\varepsilon_G}{d_S(1-\varepsilon_G)} \tag{11-15}$$

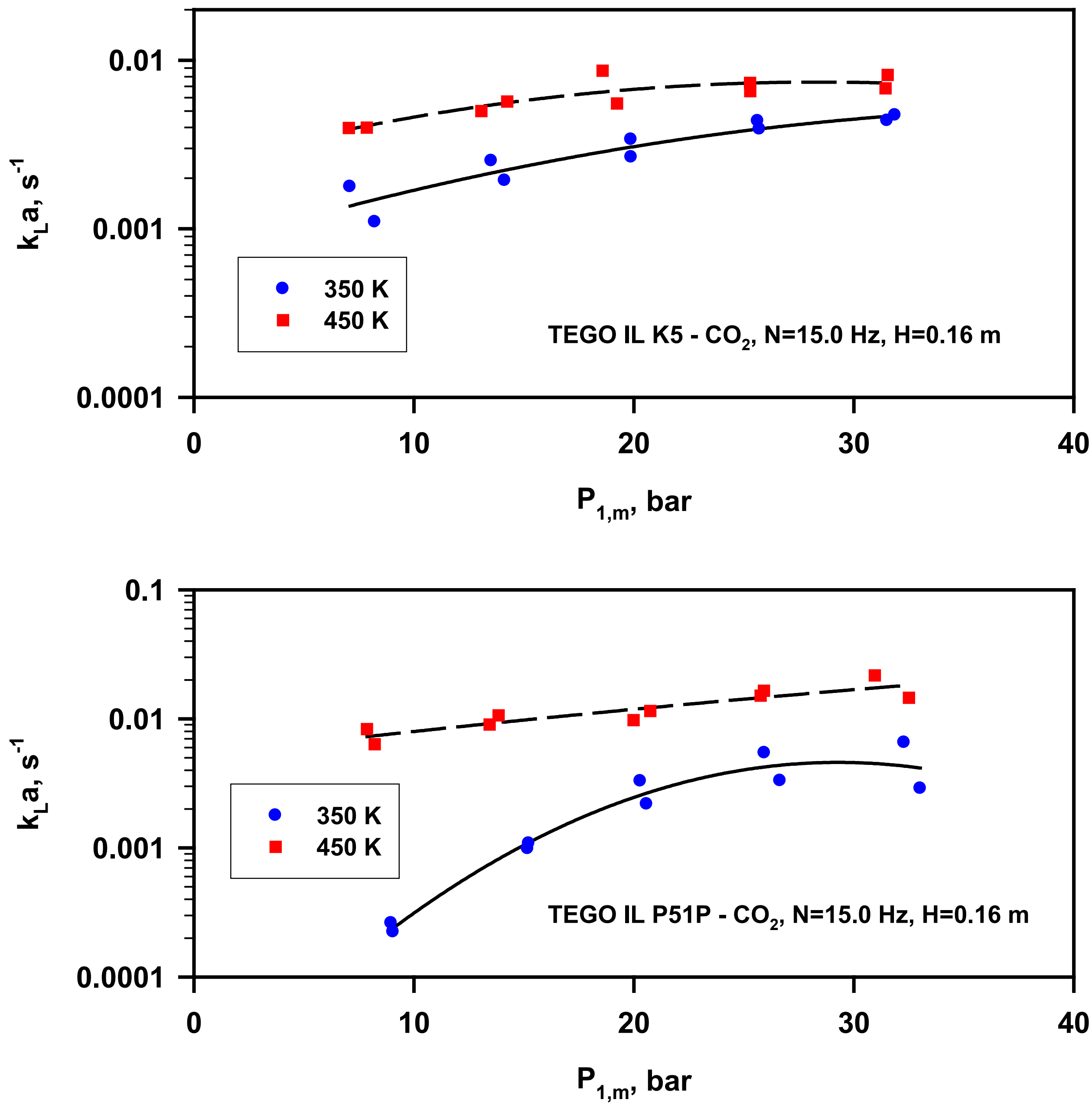

Figure 11.15: Effect of temperature on k_La for CO_2 in the TEGO IL K5 and TEGO IL P51P

11.5.6.3 Effect of Mixing Speed on k_La

Figure 11.16 shows the effect of mixing speed on k_La for CO_2 in the TEGO IL K5 and TEGO IL P51P and, as can be observed, increasing mixing speed increases k_La, which is in agreement with numerous investigations.[26,51,52,120,126,128,129,139,143,144,148-150,237,240,245-247] The increase of k_La with mixing speed can be attributed to the effect on the liquid-side mass transfer coefficient k_L and the gas-liquid interfacial area (a). Increasing mixing speed increases the turbulence and shear rate in the reactor,[145,146] which reduces the gas-liquid film thickness (Δ), leading to the increase of the mass transfer coefficient, since $k_L = D_{AB}/\Delta$. Also, increasing mixing speed increases the pumping capacity of the impeller, and, consequently, more gas bubbles are induced into the liquid through the hollow shaft, which increases the gas holdup. This increase of the gas holdup (ε_G) should increase the gas-liquid interfacial area (a) according to Equation (8-12). It is important to note that the increase in k_La from 13.3 to 16.7 Hz is about 20 times, whereas the increase in k_La from 16.7 to 20 Hz is about 2-3 times. This smaller increase of k_La values at higher mixing speeds can be related to the effect of mixing speed on the induced gas flow rate (Q_{GI}) through the hollow shaft. As reported by Fillion[51] and Lemoine et al.,[206] at mixing speeds greater than the critical mixing speed for gas induction, Q_{GI} increases with mixing speed until a fully developed hydrodynamic regime is reached, and then Q_{GI} becomes independent of the mixing speed. Thus, it appears that a fully developed hydrodynamic regime is reached at 16.7 Hz and, accordingly, further increase of mixing speed up to 20 Hz did not significantly increase Q_{GI} and subsequently, k_La values were not significantly increased.

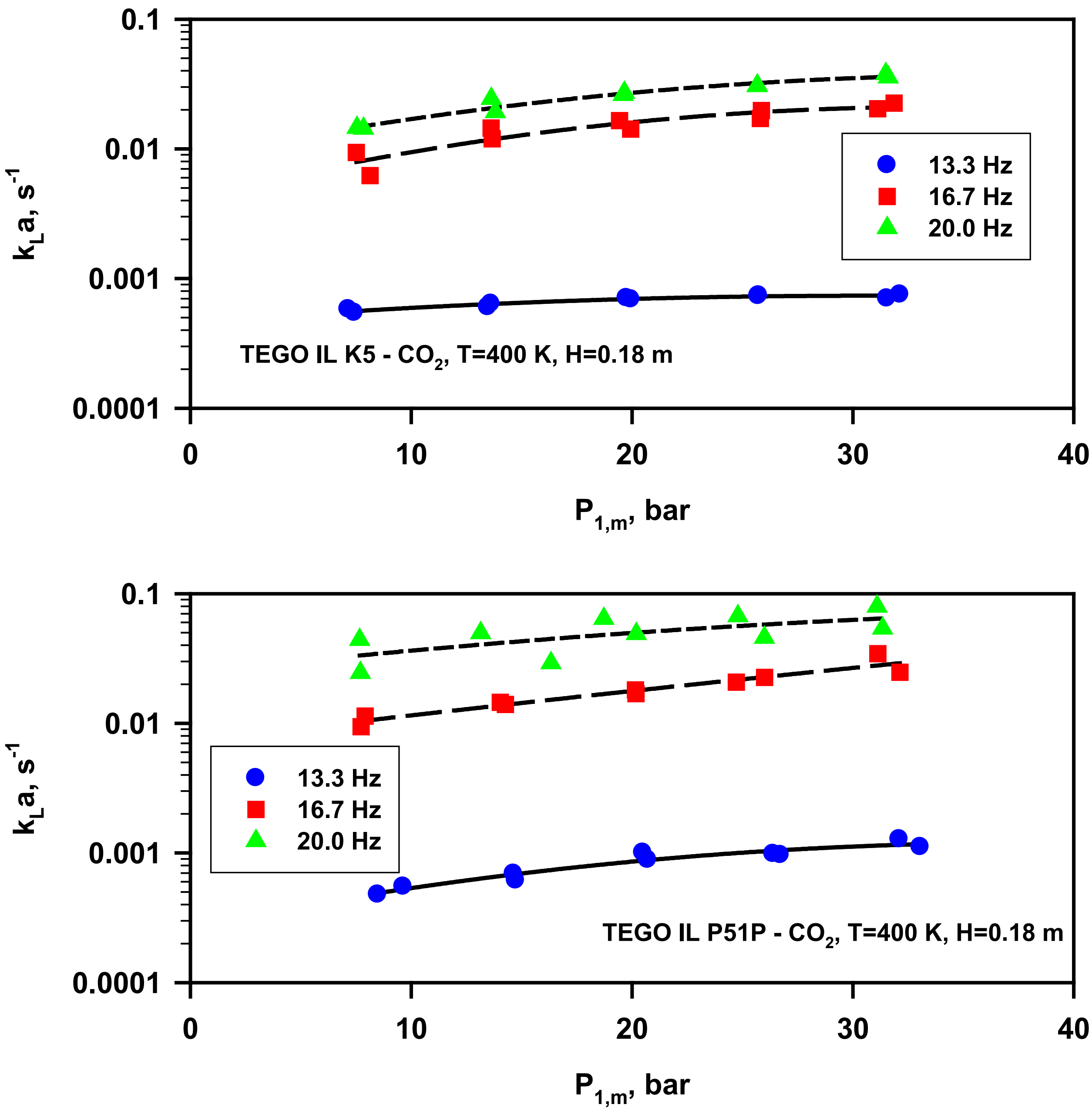

Figure 11.16: Effect of mixing speed on k_La for CO_2 in the TEGO IL K5 and TEGO IL P51P

11.5.6.4 Effect of Liquid Height on k_La

Figure 11.17 shows the effect of liquid height on k_La for CO_2 in the TEGO IL K5 and TEGO IL P51P and as can be seen k_La values decrease with increasing liquid height. For instance, increasing liquid height from 0.14 to 0.22 m decreases the k_La values by an order of magnitude for CO_2 in the TEGO IL P51P and about 8 times in the TEGO IL K5. This behavior of k_La can be related to the effect of liquid height on both the mass transfer coefficient (k_L) and the gas-liquid interfacial area (a). Increasing liquid height decreases the turbulence in the reactor, which results in a decrease of k_L. Also, increasing liquid height decreases the pumping capacity of the impeller, as well as the gas holdup, and increases the Sauter mean bubble diameter, which leads to the decrease of a. Thus, the decrease of both the k_L and a values led to the decrease of k_La with increasing liquid height.

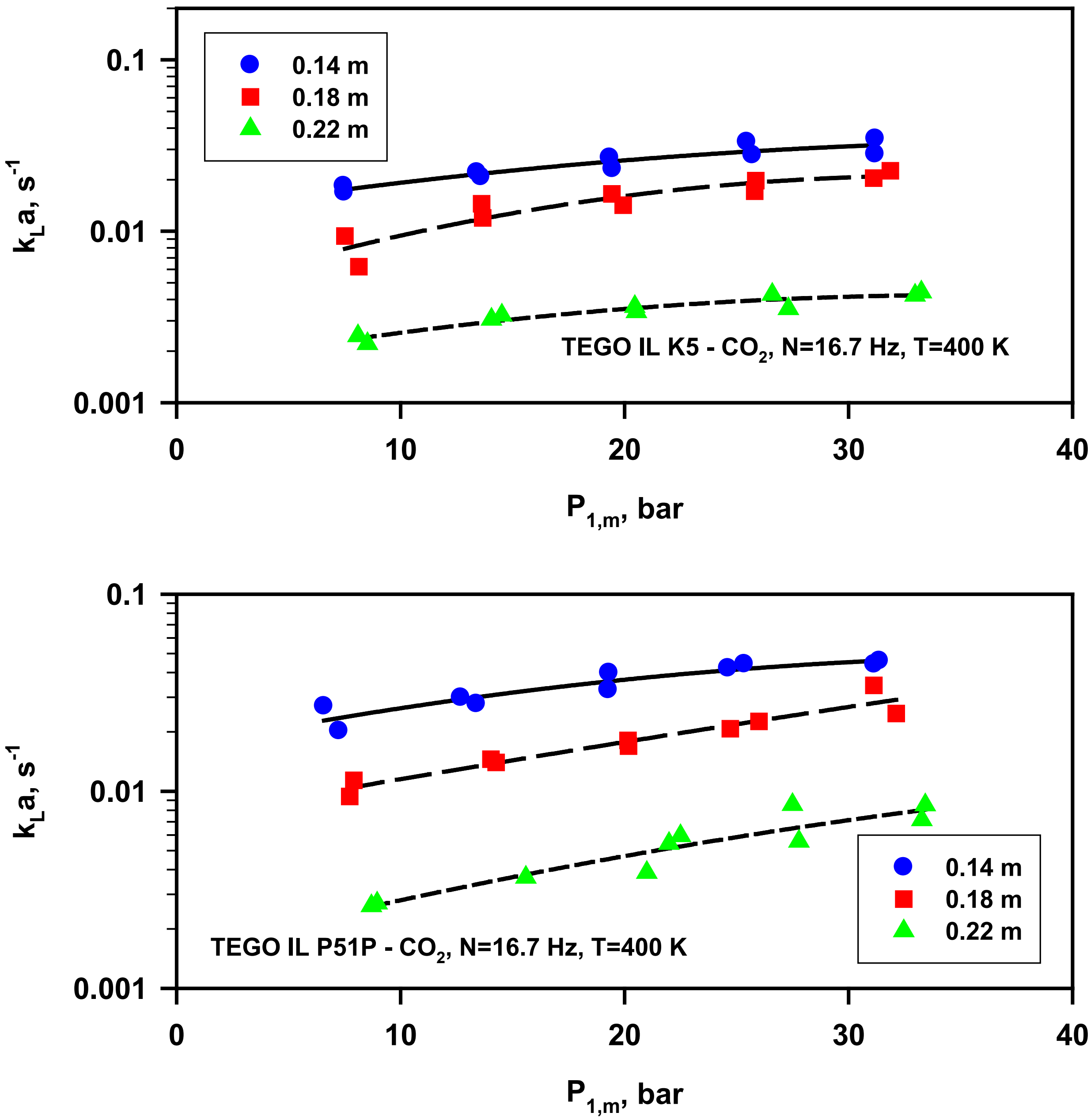

Figure 11.17: Effect of liquid height on k_La for CO_2 in the TEGO IL K5 and TEGO IL P51P

11.5.6.5 Effect of Gas Nature on k_La

Figure 11.18 depicts the effect of gas nature at 400 K, 16.7 Hz, 0.18 and 0.22 m on k_La values for CO_2 and H_2 in the TEGO IL P51P. As can be observed in this figure, k_La values for CO_2 are smaller than those of H_2 under similar operating conditions. This k_La behavior can be attributed to the smaller gas holdup and larger Sauter mean bubble diameter for CO_2 which led to a smaller gas-liquid interfacial area for CO_2 than that of H_2.. These data indicate that the gas-liquid interfacial area (a) is controlling the behavior of k_La in the gas-inducing reactor (GIR), since the mass transfer coefficients (k_L) for CO_2 is supposed to be larger than that of H_2, given the fact that the diffusivity of CO_2 is about four times that of H_2 according to the Wilke-Chang Equation.[168]

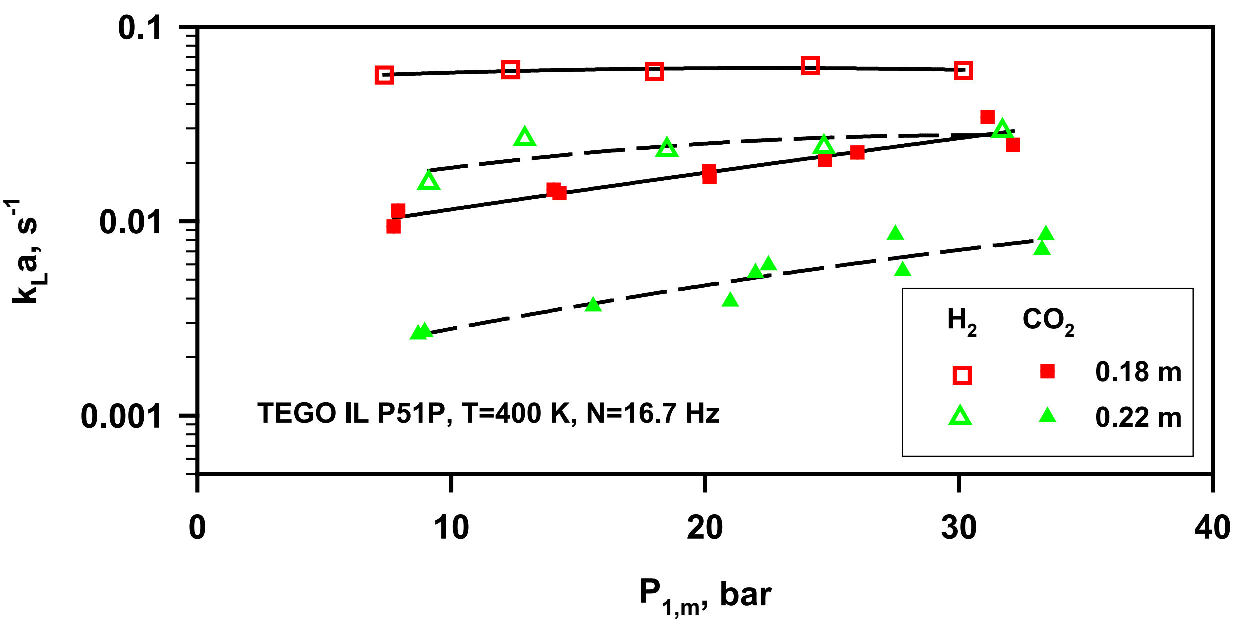

Figure 11.18: Effect of gas nature on k_La in the TEGO IL P51P

11.5.6.6 Effect of Liquid Nature on k_La

As can be deduced from Figures 11.15, 11.16 and 11.17, under similar operating conditions, k_La values for CO_2 in the TEGO IL K5 are smaller than those in the TEGO IL P51P. Figure 11.19, however, shows that the difference between k_La values in both ILs is minimal, which could be due to the small differences between the viscosities and densities of the two ILs under the operating conditions used in this study.

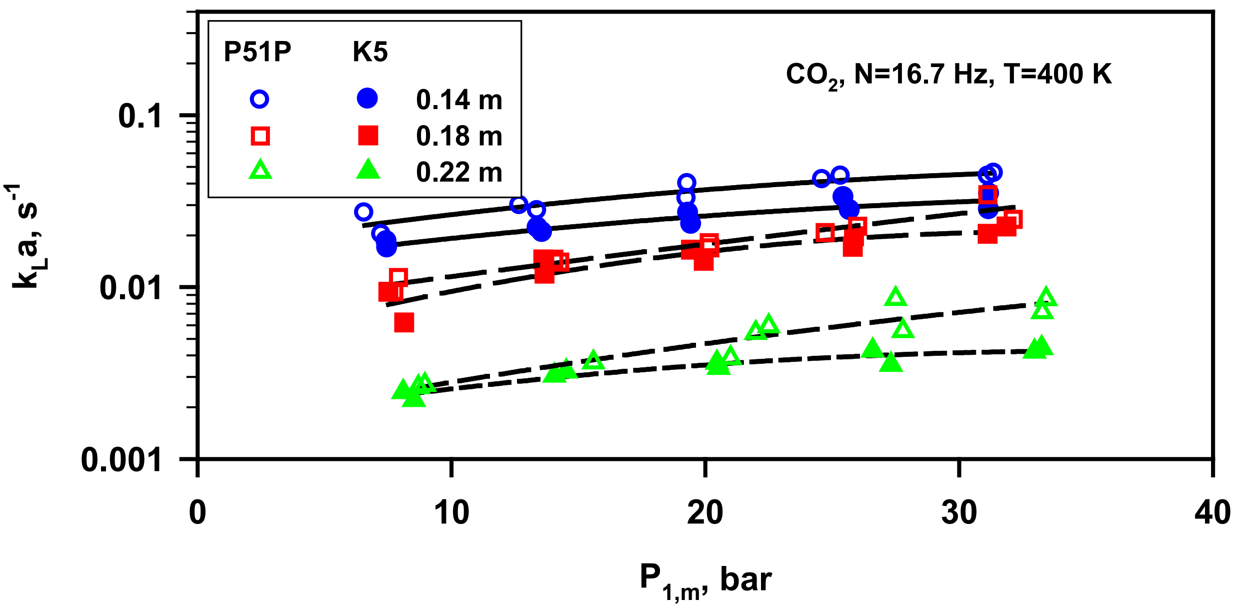

Figure 11.19: Effect of liquid nature on k_La in the TEGO IL K5 and TEGO IL P51P

11.5.7 Comparison among k_La of gases in the TEGO IL K5

Figures 11.20 and 11.21 illustrate a comparison among k_La for CO_2, H_2S and N_2 in the IL at 350 and 500 K, respectively. As can be seen in these figures k_La values of each gas increase with increasing pressure, which is in agreement with the behavior of k_La for CO_2 and N_2 in perfluorocarbon solvents previously reported by Heintz et al.[261] These figures also show k_La

values for N_2 in the gas mixture with H_2S are lower than those obtained for N_2 as a single gas. This important finding underlines the fact that the presence of H_2S with N_2 in the gaseous mixture creates a resistance to N_2 mass transfer from the gas bubbles into the IL solvent, ($1/k_Ga$) leading to the decrease of its k_La value. The reciprocal of this resistance represents the volumetric gas-side mass transfer coefficient (k_Ga), which can be quantified from the following relationship:

$$\frac{1}{(k_L a)_{N_2,mixture}} = \frac{1}{(k_L a)_{N_2,\sin gle}} + \frac{1}{k_G a} \tag{11-16}$$

The calculated k_Ga from the experimental data at N_2 mean pressure of 5 and 28 bar, respectively was found to vary from 0.0020 to 0.0028 s^{-1} at 350 K and from 0.033 to 0.040 s^{-1} at 500 K. Such resistance may be attributable, in part, to dipolar coupling and/or hydrogen bonding between H_2S and N_2 molecules.

Figures 11.20 and 11.21 show that k_La values for CO_2 in IL are greater than those for N_2 and since CO_2 solubility values in the same solvent are also greater than those of N_2, this combined behavior highlights the stronger selectivity of IL towards CO_2 than towards N_2. Furthermore, even though the mean pressure for H_2S is much lower than that of CO_2 and N_2, Figures 11.20 and 11.21 show that k_La values of H_2S in the IL appear to be greater than those of CO_2 and N_2. It should be mentioned that similar behavior of k_La values was also observed at 400 and 450 K. Thus, this k_La behavior, in addition to the greater solubility of H_2S than that of CO_2 in the IL within the temperature range studied, indicates that H_2S can be more easily captured than CO_2 from the fuel gas stream by the IL physical solvent within this temperature range from 350 to 500 K. Also, due to the greater solubility and mass transfer coefficients of H_2S than those of CO_2 in the IL a shorter absorber can be employed for H_2S capture than that needed for CO_2.

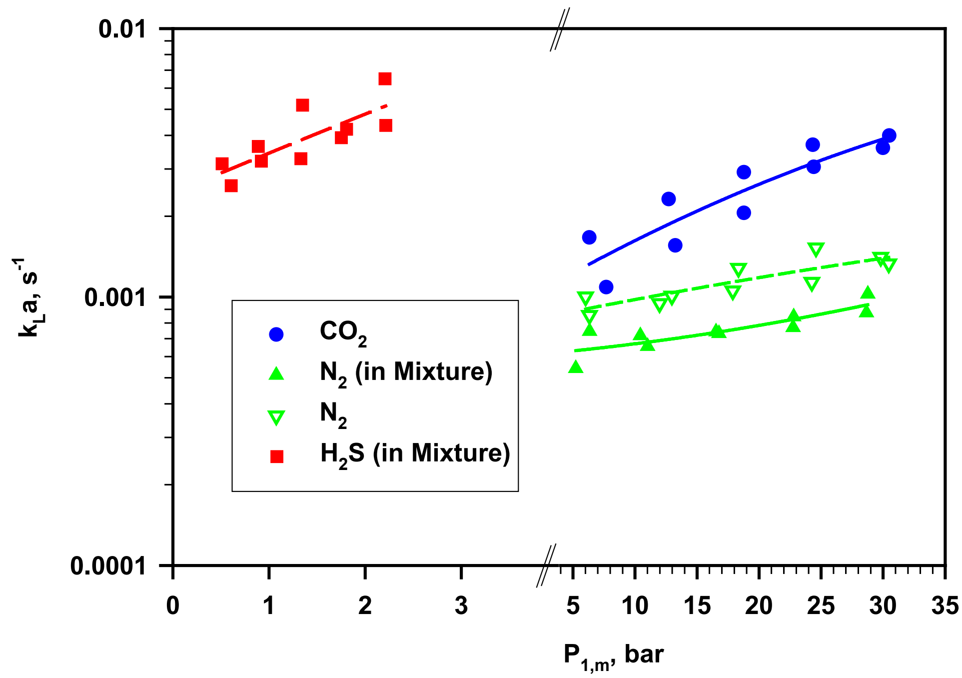

Figure 11.20: Comparison among k_La values for CO_2, H_2S and N_2 in the IL (T = 350 K, N = 15.0 Hz, H = 0.16 m)

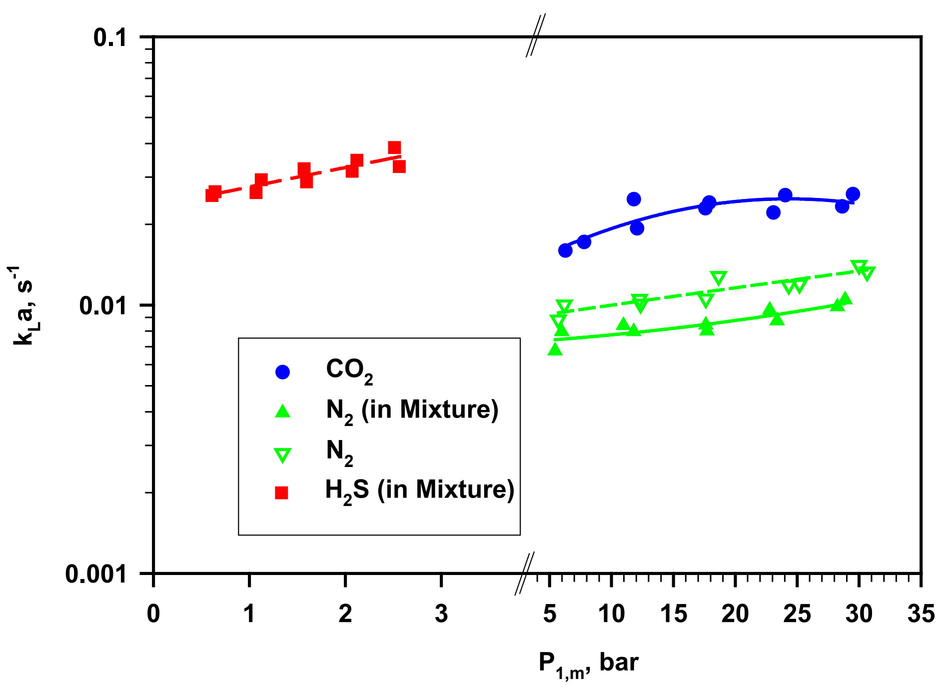

Figure 11.21: Comparison among k_La values for CO_2, H_2S and N_2 in the IL K5

(T = 500 K, N = 16.7 Hz, H = 0.18 m)

Table 11.8: Comparison between the solubility of H_2S and CO_2 in the IL K5 physical solvent

Temperature	Pressure	x^*_{H2S}	x^*_{CO2} (calculated from experimental data)	x^*_{H2S} / x^*_{CO2}
K	bar	%	%	-
300	0	0	0	
	0.277	1.14	1.28	0.89
	0.312	1.28	1.44	0.89
	0.607	2.38	2.77	0.86
	0.633	2.49	2.89	0.86
	0.937	3.52	4.24	0.83
	0.949	3.58	4.30	0.83
	1.219	4.45	5.48	0.81
	1.240	4.48	5.57	0.80
	1.538	5.38	6.85	0.78
	1.550	5.38	6.90	0.78
350	0	0	0	
	0.357	0.87	0.68	1.27
	0.445	1.04	0.85	1.23
	0.739	1.70	1.41	1.20
	0.773	1.79	1.47	1.21
	1.171	2.59	2.23	1.17
	1.190	2.65	2.26	1.17
	1.616	3.49	3.06	1.14
	1.630	3.50	3.09	1.13
	2.050	4.26	3.87	1.10
	2.053	4.27	3.87	1.10
400	0	0	0	
	0.357	0.62	0.46	1.33
	0.397	0.68	0.52	1.31
	0.783	1.31	1.02	1.29
	0.833	1.38	1.08	1.28
	1.206	1.95	1.56	1.25
	1.281	2.05	1.66	1.24
	1.612	2.51	2.09	1.20
	1.659	2.59	2.15	1.21
	2.023	3.11	2.61	1.19
	2.050	3.14	2.65	1.19
450	0	0	0	
	0.415	0.58	0.45	1.29
	0.463	0.64	0.50	1.28
	0.920	1.24	0.99	1.25
	0.921	1.24	0.99	1.25
	1.333	1.75	1.44	1.21
	1.339	1.75	1.44	1.21
	1.803	2.29	1.94	1.18
	1.837	2.33	1.98	1.18
	2.273	2.82	2.44	1.15
	2.326	2.87	2.50	1.15
500	0	0	0	
	0.429	0.53	0.41	1.29
	0.449	0.56	0.43	1.29
	0.863	1.03	0.83	1.25
	0.910	1.09	0.87	1.25
	1.399	1.62	1.34	1.21
	1.411	1.64	1.35	1.21
	1.814	2.05	1.74	1.18
	1.885	2.12	1.81	1.17
	2.278	2.51	2.18	1.15
	2.311	2.54	2.21	1.15

12.0 CONCEPTUAL PROCESS DESIGN USING IONIC LIQUIDS

Compared to coal-powered combustion systems, Integrated Gasification Combined-Cycle (IGCC) is considered the most promising process for power generation due to its high thermal efficiency (~ 40%), low emissions, and the flexibility in using different feedstocks.[4] For the IGCC process to become commercially viable, however, all contaminants, such as Hg, As, Cd, Se, SO_x, NO_x, H_2S and CO_2 in the syngas have to be removed prior to combustion. Cold-, hot- and warm-gas acid gas removal technologies from IGCC syngas streams were discussed by Vidaurri et al.[3,4] and have been recently summarized by Heintz et al.[273] Among the emission control technologies, the warm-gas cleanup process is the most appropriate and efficient technique for IGCC systems. It can remove multi-contaminants from the syngas such as acid gases, sulfur, and heavy metals at high temperatures without the need of expensive alloy equipment or cooling systems, while incurring a lower energy penalty compared to the cold-gas and hot-gas cleanup.[273] The warm-gas cleanup process significantly increases the thermal efficiency and reduces the capital and operating costs of IGCC when compared with other conventional processes.[274] Given the benefits of the warm-gas cleanup process, there is a need to develop novel warm-gas cleanup processes to mitigate the emission of sulfur, chlorides, NH_3, CO_2, Hg, As, Se and Cd, and further reduce the cost of energy production associated IGCC power generation.

Recently, Ionic Liquids (ILs) have been investigated as potential physical solvents for acid gas removal from warm gas streams.[273] ILs consist mainly of a large organic asymmetric cation (i.e., pyridinium, imidazolium, phosphonium, etc.) and either an inorganic (i.e., Cl^-, BF_4^-, PF_6^-, $CF_3SO_3^-$, NTf_2^-) or an organic (i.e., $RCOO^-$) anion,[275] which in combination prevent the formation of a stable crystal lattice.[276,277] The physical properties (melting point, viscosity, gas solubilization, etc.) of ILs are strongly affected by their anion and cation compositions.[275] In general, ILs exist as liquids at a low temperature (< 373 K)[278] and possess many attractive properties for acid gas removal, such as chemical and thermal stability, non-inflammability, high ionic conductivity, and wide electrochemical potential window.[278] Furthermore, ILs exhibit extremely low vapor pressures which allowed them to gain a reputation as 'green' or environmentally-friendly solvents.[252-254,278] ILs offer virtually an infinite number of possible structures that allow them to be tailor-made for desirable applications. They have been used as catalysts[249,279] and lubricants,[252] and used in azeotropic and extractive[251] distillations and in numerous reactions or separation processes.[251,252,256,257] However, ILs have some inherent drawbacks summarized by Heintz et al.,[273] which include combustibility, higher viscosity, higher production cost and potential toxicity to aquatic environments.[259]

Research conducted by Anderson et al.[280] indicated that ILs can selectively capture CO_2 from flue gas streams by showing that CO_2 has greater solubility than other gases (C_2H_4, C_2H_6, CH_4, O_2, N_2) in 1-hexyl-3-methylpyridinium bis(trifluoromethylsulfonyl)imide [hmpy][Tf_2N].[281] Further, Anderson et al.[280] and Muldoon et al.[282] showed that the CO_2 solubility in ILs is strongly dependent on the composition of the anion. Therefore this paper is focused on the development of a conceptual process for CO_2 capture from shifted warm syngas streams using the ILs TEGO IL K5 and TEGO P51P as physical solvents.

12.1 PHYSICAL PROPERTIES OF THE INVESTIGATED IONIC LIQUIDS

The TEGO IL K5 and the TEGO IL P51P solvents are supplied by Evonik-Degussa GmbH Company (Hopewell, VA).[260] The structures of the solvents are illustrated in Figure 11.1 where the exact values of m and n in the TEGO IL K5 were not given by the supplier or the Solvent Innovations GmbH, which manufactures "AMMOENG" as analogues of the TEGO ILs. Therefore, in this study, the values for m and n were assumed in order to obtain an approximate formula for this IL. For instance, the chemical formula of the TEGO IL K5 was represented by (m + n) = 13, resulting in 15 ethylene oxide units (as specified in Evonik Degussa's MSDS). Table 11.1 shows the composition of TEGO IL K5 and TEGO IL P51P and their scientific names. The molecular weight of this IL (924.68 $kg.kmol^{-1}$) was determined from the patent by Jork et al.,[283] which has a representation of the TEGO IL K5 molecule. The molecular weight of the TEGO IL P51P, shown also in Figure 11.1, was calculated assuming n = 51 (as indicated by the "P51" nomenclature and Evonik Degussa's specification that n = 50 – 60) resulting in a value of 3205.27 $kg.kmol^{-1}$. The selection of these ILs for CO_2 capture was guided by the developed definition of an "ideal" physical solvent for CO_2 capture,[261,262] where the presence of multi ether functional groups in these ILs was one of the main motivation for their selection. Multi ether functional groups were used as a required feature for the "ideal" physical solvents because ether functional groups has been reported to selectively absorb CO_2 at near ambient temperature (~39 °C). Inaddition, Selexol,[261] which consists of polyethylene glycol of dimethylethers, ($CH_3O(CH_2CH_2O)_nCH_3$ with $3 \leq n \leq 9$), is widely used as a physical solvent for CO_2 capture.

12.2 EXPERIMENTAL APPROACH

The density, viscosity, and surface tension of TEGO IL K5 and TEGO IL P51P were measured in our laboratory and modeled as a function of temperature within the temperature range of 300 to 500 K. The shifted gas composition used in this study is given in Table 12.1. The solubility of CO_2, H_2, H_2S and N_2 were measured in the TEGO IL K5.The solubility of CO_2 and H_2 were measured in the TEGO IL P51P within the same temperature range. The PR-EOS was selected in the Aspen Plus simulation in order to calculate the solubility of these gases as well as those of the other gases (given in Table 12.1) in the two ILs. In order to use the PR-EOS, the critical properties of ILs are needed. Unfortunately, extensive literature search yielded no values, and therefore, the critical properties of the two ILs used were estimated as described in Section 12.3.

Table 12.1: Shifted gas composition used

Component	mol%
Ar	0.48
CH_4	0.24
H_2	37.50
N_2	0.33
CO	6.27
CO_2	23.87
H_2O	30.68
NH_3	0.16
H_2S	0.47
COS	0.00

12.3 ESTIMATION OF THE CRITICAL PROPERTIES OF THE IONIC LIQUIDS

Valderrama and Rojas[284] applied the group contribution method and proposed Equations (12-1) and (12-2) to calculate the boiling point (T_b) and critical point (T_c), respectively and proposed Equations (12-3), and (12-4) to calculate the critical volume (V_c), and critical pressure (P_c), respectively.

$$T_b = 198.2 + \sum n\Delta T_b \tag{12-1}$$

$$T_c = \frac{T_b}{0.5703 + 1.0121 \cdot \sum n\Delta T_c - \left(\sum n\Delta T_c\right)^2} \tag{12-2}$$

$$V_c = 6.75 + \sum n\Delta V_c \tag{12-3}$$

$$P_c = \frac{MW}{\left(0.2573 + \sum n\Delta P_c\right)^2} \tag{12-4}$$

Valderrama and Robles[285] also coupled the definition of the acentric factor (ω), Equation (12-5)[236,286] and Antoine Equation (12-6) for the vapor pressure (P^s) proposed by Rudkin[287] to calculate ω using Equation (12-7).

$$\omega = -\log_{10}\left(\frac{P^s}{P_c}\right)_{(T/T_c)=0.7} - 1 \tag{12-5}$$

$$\log_{10}\left(P^s\right) = A - \frac{B}{T-43} \tag{12-6}$$

$$\omega = \frac{(T_b-43)(T_c-43)}{(T_c-T_b)(0.7T_c-43)}\log_{10}\left(\frac{P_c}{P_b}\right) - \frac{(T_c-43)}{(T_c-T_b)}\log_{10}\left(\frac{P_c}{P_b}\right) + \log_{10}\left(\frac{P_c}{P_b}\right) - 1 \tag{12-7}$$

When Equations (12-1) and (12-2) were used to calculate T_b and T_c for the two ILs investigated they yielded unrealistic values. Therefore another scientific approach was implemented.

For the TEGO IL K5 T_c was calculated using the experimental surface tension data and Equation (11-8) (see value in Table 11.5), then T_c was utilized to calculate T_b using Equation

(12-2) above. V_c, P_c and ω were also calculated using Equations (12-3), (12-4) and (12-7), respectively. At T_b, the value of P_b = 1.01325 bar.

The calculated values of P_c = 5.884 bar, T_c = 848.46 K, and ω = - 0.0718 were then used in the P-R EOS to calculate the density of the TEGO IL K5 as a function of temperature (Experimental data were correlated by Equation (11-1) and coefficients can be found in Table 11.3). As can be seen in Figure 12.1 the calculated density values are considerably lower than those measured in our laboratory.

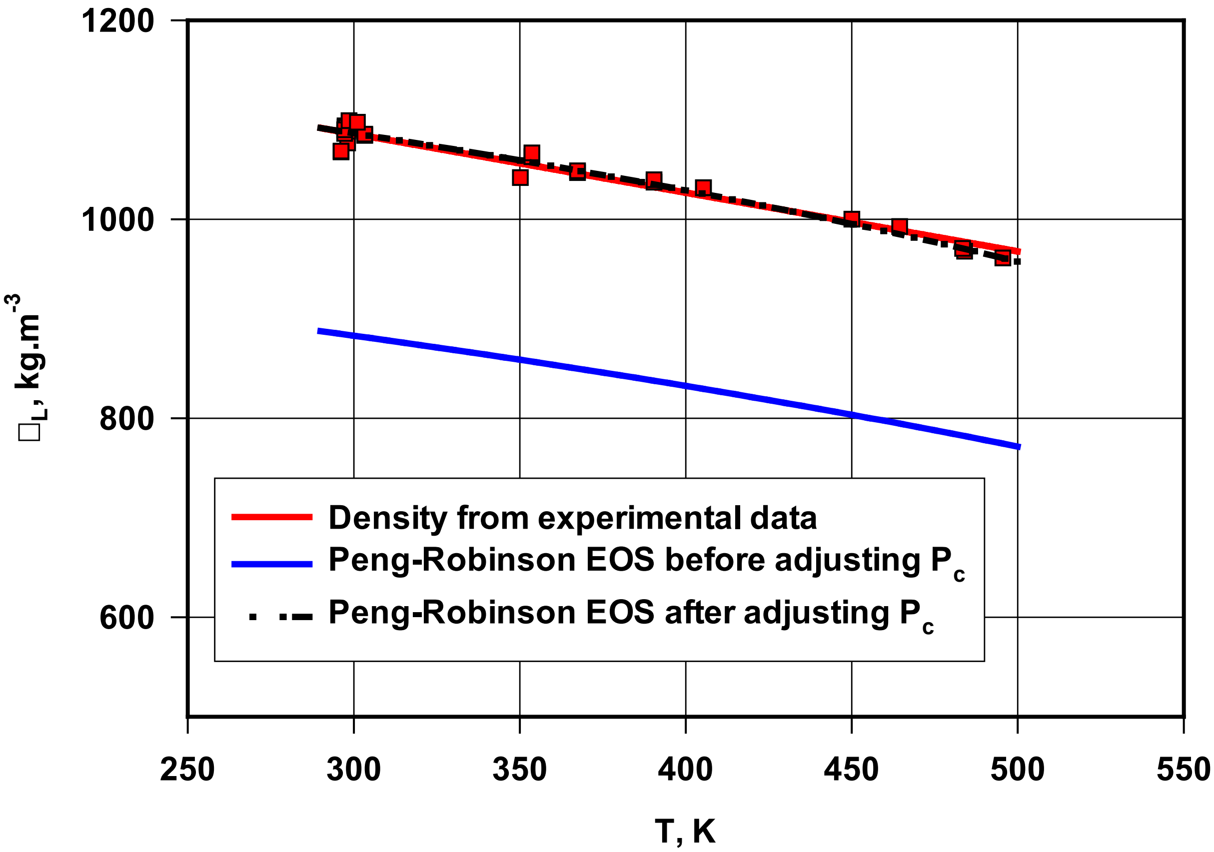

Figure 12.1: Density of the TEGO IL K5 as a function of temperature

This means that the P_c value predicted with Equations (12-4) has to be readjusted so that the P-R EOS can predict the experimental density values with high precision. Therefore, the P_c value is optimized in order to minimize the deviation between the experimental and calculated density values using the P-R EOS. The optimization results led to P_c = 7.138 bar and ω = 0.0302.

For the TEGO IL P51P, after calculating T_b and using its value in Equation (12-2), the T_c value came to be negative due to the large value of the group contribution of this IL. In order to obtain a realistic T_c value, the experimental vapor pressure data of this IL were correlated using Equation (12-8), which is required for Aspen Plus:

$$\ln\left(P^s\right) = D_1 + \frac{D_2}{T + D_3} + D_4 \cdot T + D_5 \cdot \ln\left(T\right) + D_6 \cdot T^{D_7} \tag{12-8}$$

in order to simplify this equation, the coefficients D_3, D_4 and D_6 were set to nil; the coefficients D_1, D_2 and D_5 were regressed in order to fit the experimental values. The regression resulted in D_1 = -15.483, D_2 = -15275.3, and D_5 = 134.62.

The P_c for the TEGO IL P51P was then optimized by minimizing the deviation between experimental and calculated density values using the P-R-EOS. Figure 12.2 indicates that the deviation between the values is less than 2%. The ω for this IL was also calculated using Equation (12-7). Table 12.2 summarizes the critical properties of the TEGO IL K5 and TEGO IL P51P calculated for the P-R EOS which was employed in the Aspen Plus simulation.

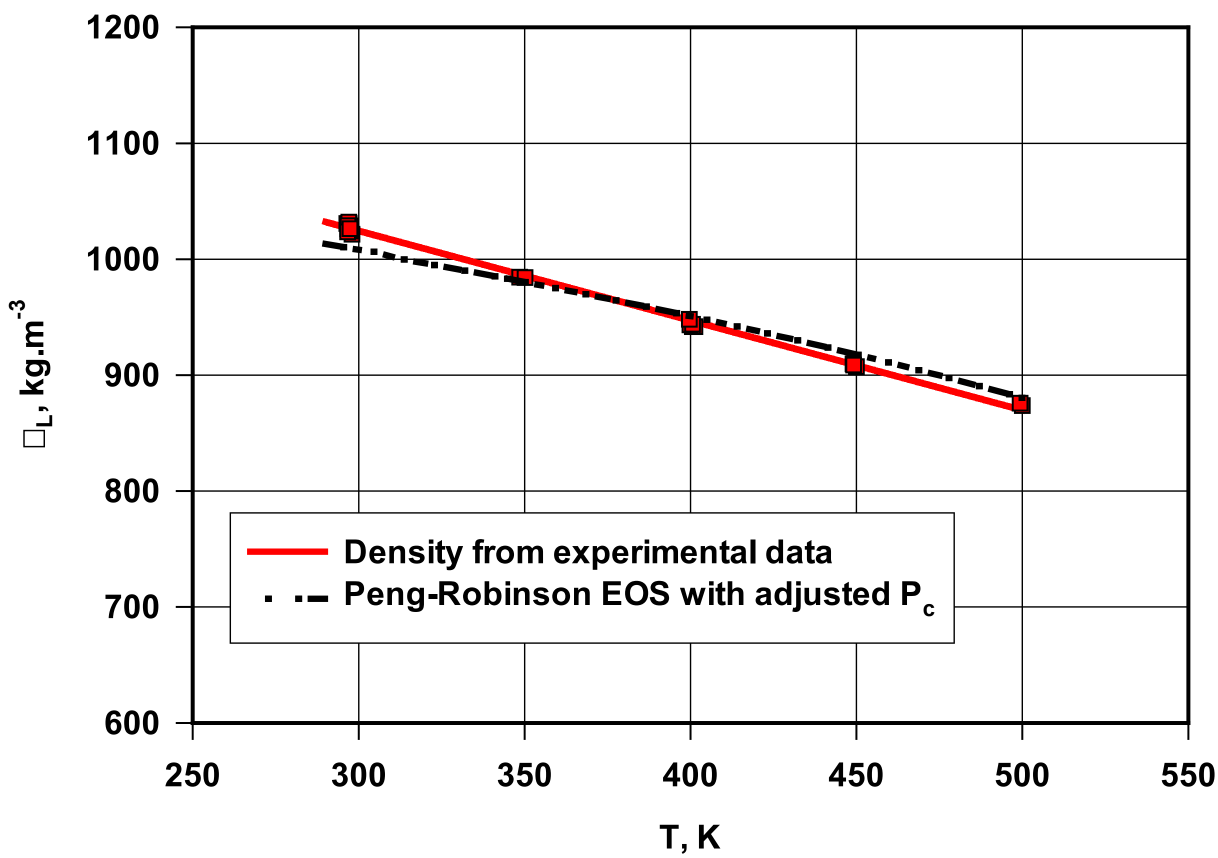

Figure 12.2: Density of the TEGO IL P51P as a function of temperature

Table 12.2: Critical properties of the TEGO IL K5 and the TEGO IL P51P

Critical values	Units	TEGO IL K5	TEGO IL P51P
MW	$kg.kmol^{-1}$	924.68	3205.27
T_c	K	848.46	824.22
T_b	K	626.56	717.98
V_c	$m^3.kmol^{-1}$	2.9486	10.1607
P_c	bar	7.138	1.857
ω	-	0.0302	0.0512
Z_c	-	0.2984	0.2753

The use of the P-R EOS in the Aspen simulation for predicting the solubility of the constituents of the fuel gas in the two ILs requires the knowledge of the binary interaction parameters (δ_{ij}) between each two components in the system. Aspen database include some binary interaction parameters between the gases in the mixture, however, the interaction parameters between the gases and the ILs are not available because these ILs are not in the Aspen database. As mentioned above the solubility of CO_2, H_2, H_2S and N_2 in the TEGO IL K5 and the solubility of CO_2 and H_2 in the TEGO IL P51P were measured at different pressures and temperatures. At each temperature, the critical properties of the gases and the ILs shown in Table 12.2 were used in the P-R EOS to predict the solubility of these gases in the ILs. The binary interaction parameters between the gases and the ILs were optimized so that the difference between the predicted and measured solubility values is minimized. The binary interactions for CO_2, H_2, H_2S and N_2 in the TEGO IL K5 and those for CO_2 and H_2 in the TEGO IL P51P were then correlated as a function of temperature using Equation (12-9). Table 12.3 lists the coefficients in Equation (12-9) for calculating the binary interaction parameters. Also, Figures 12.3 and 12.4 show the experimental and predicted solubility values as a function of pressure and temperature for CO_2 in the TEGO IL K5 and TEGO IL P51P, respectively.

$$\delta_{ij} = A + B \cdot T + \frac{C}{T} \tag{12-9}$$

Table 12.3: Coefficients in Equation (12-9) for calculating the binary interaction parameters

Liquid Solvents	*Gases*	*A*	*B*	*C*
TEGO IL K5	CO_2	0.21	0.00034	-100
	H_2	-71.2	0.1256	11206
	H_2S	-0.28	0.001	0
	N_2	0.1	0.002	0
TEGO IL P51P	CO_2	5.133	-0.00602	-1239.1
	H_2	-122.167	0.16952	23257.6

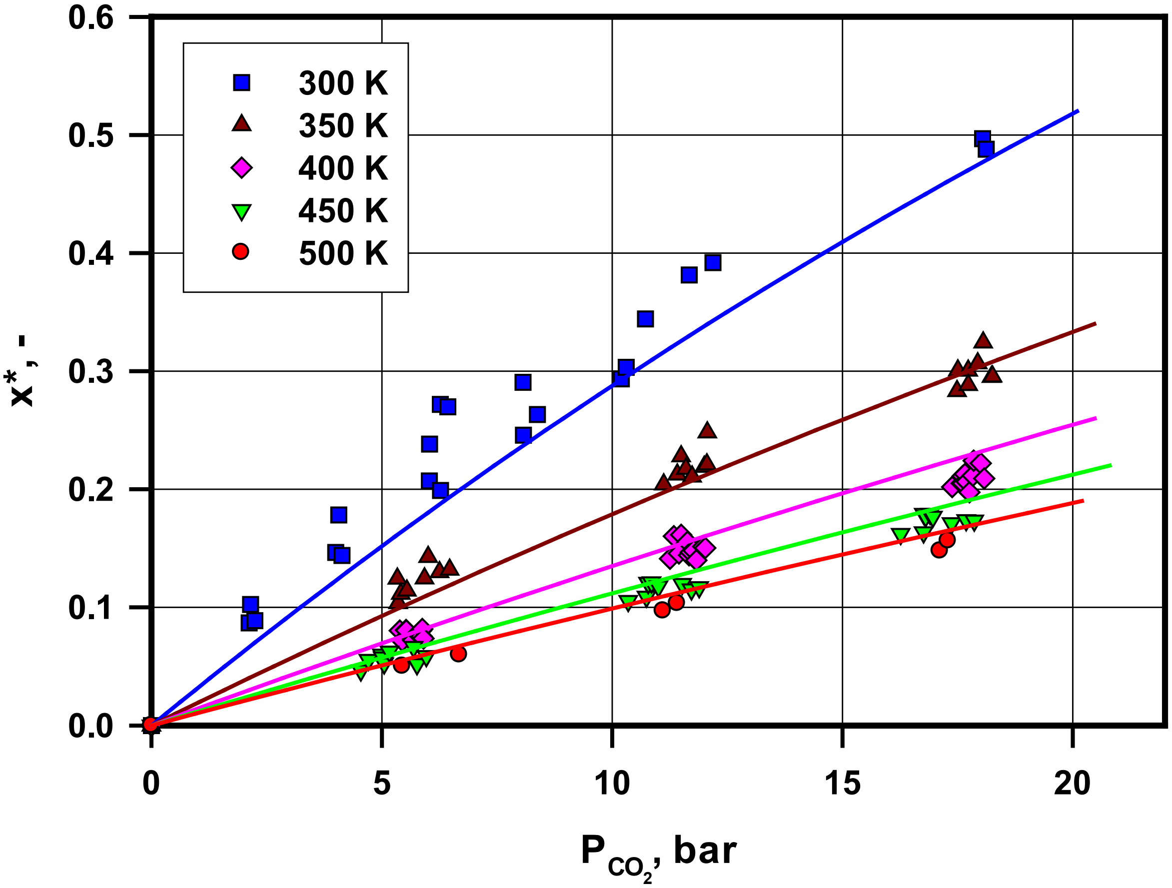

Figure 12.3: Experimental solubility of CO_2 in TEGO IL K5. Solid lines obtained using Aspen Plus with the binary interaction parameter listed in Table 12.3

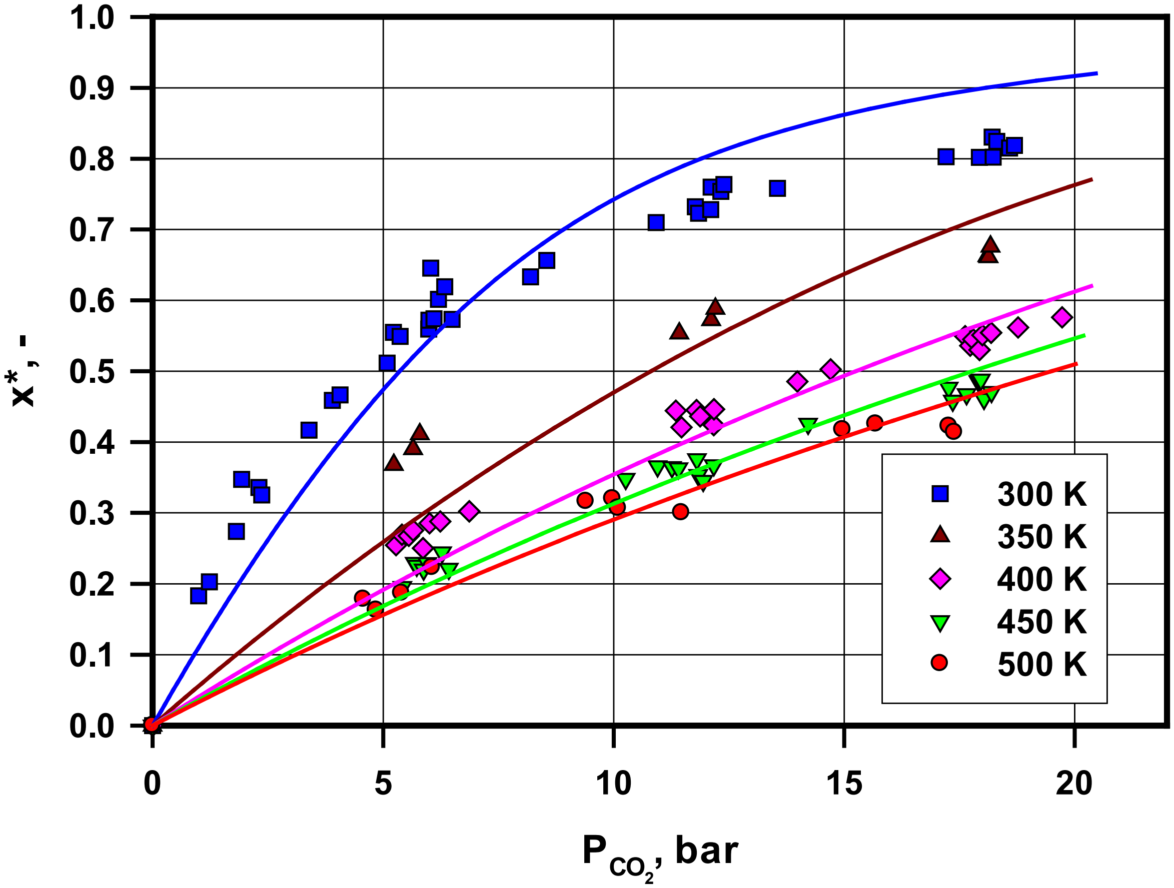

Figure 12.4: Experimental solubility of CO_2 in TEGO IL P51P. Solid lines obtained using Aspen Plus with the binary interaction parameter listed in Table 12.3

12.4 DEVELOPMENT OF THE CO_2 CAPTURE CONCEPTUAL PROCESS USING IONIC LIQUIDS

The conceptual process uses the TEGO IL K5 as a physical solvent to selectively capture CO_2 from a fuel gas stream generated from an E-Gas gasifier using Pittsburgh #8 coal and shifted to a pressure and temperature of 381 psia (26.27 bar) and 857 °F (731.48 K), respectively. The composition of this shifted gas, given in Table 12.1, is taken from “Capital and Operating Cost of Hydrogen Production from Coal Gasification", Final Report, April 2003, by Parsons[248]. The apparent molecular weight of this shifted gas stream is 19.055 kg/kmol. Shuster et al.[288] reported in the Interim Report "Systems Analysis Study on the Development of Fluorinated Solvents for Warm-Temperature/High-Pressure CO_2 Capture of Shifted Syngas" April 19, 2005, that fuel gas stream for a 400-MWe power plant is 813,643 lb/h (102.52 kg/s) or 5.38 kmol/s.

In the Aspen Plus simulation of the conceptual process development, the pressure and temperature of the shifted gas stream was set to 30 bar and 500 K, respectively. The process consists of 4 identical adiabatic packed-bed absorbers arranged in parallel (Figure 12.5) to handle the total shifted gas mass flow rate of 102.52 kg/s. In order to capture CO_2 from this gas stream, 16,000 kg/s of the TEGO IL K5 or 12,000 kg/s of TEGO IL P51P are required. Therefore each packed-bed can support a mass flow rate of 25.63 kg/s (1.345 kmol/s) of the shifted gas and 4,000 kg/s (4.326 kmol/s) of the TEGO IL K5 solvent or 3,000 kg/s (0.936 kmol/s) of the TEGO IL P51P solvent.

The shifted gas enters each packed-bed absorber from the bottom at 500 K and the IL solvent enters each absorber from the top at 298 K in a counter-current scheme. In each absorber, the TEGO IL K5 and the TEGO IL P51P solvents are heated by the sensible heat of the gas to 415.2 K and 467.4 K, respectively. In the continues process, 10.19 kg/s of the TEGO IL K5 or 20.29 kg/s of the TEGO IL P51P were needed to compensate for solvent losses during the CO_2 capture and regeneration steps. Table 12.4 shows the solvent losses in the main process streams. A review of the data suggests that the greater solvent losses measured in the TEGO IL P51P can be correlated to the higher absorber temperature when compared to the TEGO IL K5 solvent.

Table 12.4: Solvent loss streams

Flowrate in kg/s	TEGO IL K5	TEGO P51P
CO_2 stream	7.92	0.34
H_2 stream	2.27	3.42
H_2O stream	0.00	16.53
Total amount of solvent lost	10.19	20.29

The packed-bed absorber characteristics and packing specifications used in the Aspen Plus simulation are given in Table 12.5.

Table 12.5: Packed-bed and packing specifications

Description	Unit	Value
Packed column diameter	m	2.4
Packed bed cross section area	m^2	4.52
Number of stages	-	6
Height of each stage	m	3
Packed bed height	m	18
Packing type	-	Plastic Pall Rings
Packing dimension	m	0.025 (1”)
Packing surface area	m^2/m^3	205
Void fraction	-	0.90
Gas flowrate	kg/s	25.63
Liquid flowrate	kg/s	4002.22

The gas-solvent mass transfer in the packed-bed, was accounted for using the Billet and Schultes' Correlations (1993),[289] which were implemented to estimate the mass transfer coefficients and the effective gas-liquid interfacial area in packed-beds with random and structured packings. The liquid-phase binary mass transfer coefficient ($K_{i,k}^L$) is defined in Aspen Plus as:

$$k_{i,k}^L = C_L \left(\frac{g\rho_L}{\mu^L} \right)^{0.167} \sqrt{\frac{D_{i,k}^L}{d_h}} \left(\frac{u_s^L}{a_p} \right)^{0.333} \tag{12-10}$$

with a default value of $C_L = 0.905$ (this value is reported by Billet and Schultes[289]).

The total interfacial area for mass transfer (a^I) is defined by:

$$a^I = a_e A_t h_p \tag{12-11}$$

The effective area (a_e) per unit volume of the bed is related to the specific area of packing (a_P) through the following equation:

$$\frac{a_e}{a_p} = \frac{1.5}{\sqrt{a_p d_h}} Re_L^{-0.2} We_L^{0.75} Fr_L^{-0.45} \tag{12-12}$$

The volumetric mass transfer coefficients ($k_L a$) for CO_2 in the solvent were calculated from the liquid-phase binary mass transfer coefficient ($K_{i,k}^L$) obtained from Aspen Plus, where (i) and (k) stand for CO_2 and the solvent, respectively, using the following equation:

$$k_L a = k_{i,k}^L \cdot a_e = \frac{K_{i,k}^L}{\rho_L \cdot a^I} \times a_e \tag{12-13}$$

Figure 12.5 (for more detailed schematics – Aspen Printout – see Appendix E) indicates that subsequent to gas absorption in the packed-beds, the gas streams (solvent-poor) from the top of the 4 absorbers are combined into one stream; and the liquid streams (solvent-rich) from the bottom of the 4 absorbers are also combined into one stream. The solvent-rich stream is regenerated using pressure-swing option with 3 adiabatic flash drums arranged in series at different pressures, 20, 10 and 1 bar, respectively. These flash drums allow the separation of the absorbed gases from the IL into a CO_2-rich gas-stream, containing some H_2 and H_2O vapor at about 414 K for the TEGO IL K5 and about 467 K for the TEGO IL P51P, and an IL solvent-rich stream containing some CO_2, H_2 and other dissolved gaseous constituents.

For both solvents, the gas streams leaving the top of the 3 flash drums are cooled to 288 K to separate any water present prior to being combined into one stream. This stream is then compressed to 80 bar, followed by intercooling to 298 K in order to separate some liquid CO_2. This stream is further compressed to 153 bar (2200 psia) followed by intercooling at 223 K in order to separate any remaining H_2 from liquid CO_2 stream which is sent to sequestration sites.

The IL solvent-rich stream from the bottom of the third flash drum at 1 bar is pumped to 30 bar and recycled back to the packed-bed absorbers where the required make-up solvent is added to it at 298 K before it enters the absorbers.

In addition, the H_2 streams from the entire process are combined, pressurized to 100 bar, and heated to 1500 K before sending to turbines as shown in Figure 12.5.

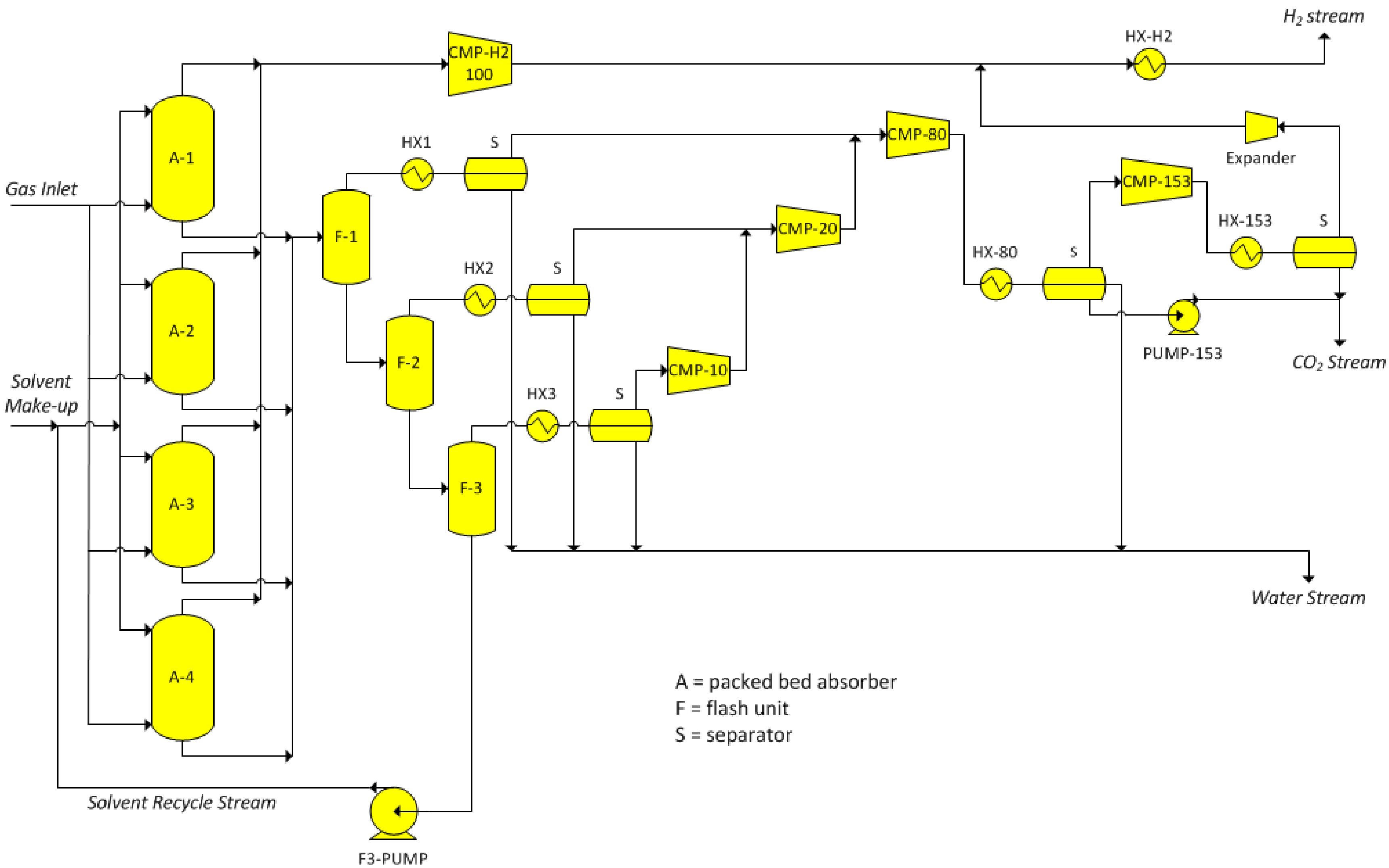

Figure 12.5: Schematic of the conceptual design process for CO_2 capture using ILs

12.5 SIMULATION RESULTS USING IONIC LIQUIDS

The composition of the combined outlet liquid stream from the 4 packed-bed absorbers, for the two ILs, expressed in molar flow rate and percentage of the inlet feed molar flow rates, is presented in Table 12.6. As can be seen 98.51 mol% of the CO_2, 47.67 mol% of H_2, 98.75 mol% of H_2S and 98.99 mol% of H_2O are captured using the TEGO IL K5 solvent and about 0.01 mol% of this solvent is lost in the gas stream. Also, 93.04 mol% of CO_2, 52.67 mol% of H_2, 91.90 mol% of H_2S and 95.64 mol% of H_2O are captured using the TEGO IL P51P and about 0.03 mol% of this solvent is lost.

Table 12.6: Composition of the outlet liquid stream from the packed-bed absorbers

	TEGO IL K5		**TEGO IL P51P**	
Component	**Mole flow rate**	**Percentage of the inlet stream**	**Mole flow rate**	**Percentage of the inlet stream**
	kmol/s	mol%	kmol/s	mol%
Ar	0.0256	96.51	0.0199	76.28
CH_4	0.0131	97.98	0.0107	81.62
H_2	0.9632	47.67	1.0653	52.67
N_2	0.0136	76.25	0.0131	73.17
CO	0.3251	94.41	0.2472	72.67
CO_2	1.3345	98.51	1.2321	93.04
H_2O	1.9350	98.99	1.6661	95.64
NH_3	0.0093	98.91	0.0081	91.08
H_2S	0.0268	98.75	0.0238	91.90
Solvent	17.3008	99.99	3.74288	99.97

Table 12.6 shows that a significant mole flow rate of H_2 is absorbed by both solvents since CO_2 solubility decreases (see Figure 12.3), while the H_2 solubility increases with temperature (see Section 11.5). A series of compression-cooling steps is therefore deemed necessary to separate H_2 from CO_2 liquid at 223 K.

Based on the inlet gas stream composition, the CO_2-rich stream which is being sent to sequestration site at 153 bar and 223 K contains 87.6 mol% of CO_2, 2.3 mol% of H_2 and 89.4 mol% of H_2S, when using the TEGO IL K5 solvent (Table 12.7); and 81.42 mol% of CO_2, 2.1 mol% of H_2 and 82.06 mol% of H_2S when using the TEGO IL P51P solvent (Table 12.8). Also, based on the inlet gas stream composition indicates that the H_2-rich stream which is being sent to turbines at 100 bar and 1500 K contains 97.7 mol% of H_2, 84.6 mol% of CO, 12.4 mol% of CO_2 and 1.2 mol% of H_2O vapor when the TEGO IL K5 solvent (Table 12.7) is used; and 98.86 mol% of H_2, 89.55 mol% of CO, and 17.78 mol% of CO_2 when using the TEGO IL P51P solvent (Table 12.8). This mole percentage of CO_2 is significant since with this solvent cooling to 223 K was not sufficient to separate any remaining H_2 from liquid CO_2 stream to be sent for sequestration.

Based on the inlet gas stream composition, the water-stream is separated from the system at 288.2 K and 1 bar and contains 98.70 mol% of H_2O and 75.70 mol% of NH_3 and 0.1 mol% of H_2S when using the TEGO IL K5 solvent (Table 12.7); and 94.70 mol% of water, 72.37 mol% of NH_3, 0.80 mol% of CO_2, 0.47 mol% H_2S, and other gases with less than 0.20 mol% when using the TEGO IL P51P solvent (Table 12.8). Also, based on the inlet gas stream composition, the recycled solvent-stream contains 15.56 mol% of H_2O, 5.20 mol% of CO_2, and 0.13 mol% of H_2 when using the TEGO IL K5 solvent (Table 12.7); and 5.24 mol% of H_2O, 5.24 mol% of CO_2, and 0.26 mol% of H_2 when using the TEGO IL P51P solvent (Table 12.8).

Table 12.7: Composition of the outlet streams from the conceptual process based on the inlet gas composition for the TEGO IL K5 solvent

	Gas Inlet stream	**CO_2 stream**	**H_2 stream**	**H_2O stream**	**TEGO IL K5 recycle stream**
	kmol/s	mol%	mol%	mol%	mol%
Ar	0.0258	27.49	72.51	0	2.63
CH_4	0.0129	30.57	69.43	0	3.74
H_2	2.0176	2.31	97.69	0	0.13
N_2	0.0178	12.23	87.77	0	0.67
CO	0.3373	15.36	84.64	0	2.05
CO_2	1.2843	87.60	12.40	0	5.20
H_2O	1.6506	0.10	1.20	98.70	15.56
NH_3	0.0086	22.67	1.63	75.70	8.53
H_2S	0.0253	89.35	10.55	0.09	6.98
T (K)	500	219.5	1500	288.2	414.3
P (bar)	30	153	100	1	30

Table 12.8: Composition of the outlet streams from the conceptual process based on the inlet gas composition for the TEGO IL P51P solvent

	Gas Inlet stream	**CO_2 stream**	**H_2 stream**	**H_2O stream**	**TEGO IL P51P recycle stream**
	kmol/s	mol%	mol%	mol%	mol%
Ar	0.0258	19.65	80.18	0.17	0.99
CH_4	0.0129	23.10	76.69	0.20	1.31
H_2	2.0176	2.10	97.86	0.03	0.26
N_2	0.0178	10.46	89.39	0.15	0.84
CO	0.3373	10.30	89.55	0.15	0.82
CO_2	1.2843	81.42	17.78	0.80	3.02
H_2O	1.6506	0.70	4.60	94.70	5.24
NH_3	0.0086	18.19	9.44	72.37	3.37
H_2S	0.0253	82.06	17.47	0.47	2.55
T (K)	500	220.8	1500	286.2	467.0
P (bar)	30	153	100	1	30

Table 12.9 shows details of the power duty and requirements for each unit presented in Figure 12.5. The units which are operated adiabatically exhibit no power requirements as it is the case for the packed-bed absorbers and the flash drums. It should be noted that when the power is negative, it means that work is done by the system on the surroundings; and when the power is positive, such as in all compression and pumping units, it means that the work is applied by the surroundings onto the system.

Table 12.9 shows that the largest power consumptions are for heating and cooling of the CO_2 streams (**HX1**, **HX2**, **HX3**) after the flash units and the intercooling (**HX-80**, **HX-153**) during the CO_2 compression, which represents -228.93 MW and -226.68 MW for the TEGO IL K5 and the TEGO IL P51P, respectively. The intercooling stage (**HX-80**) requires - 43.51 MW when using the TEGO IL K5 and -36.37 MW when using the TEGO IL P51P. This is because as Table 12.4 indicates 77.70 mol% of the TEGO IL K5 solvent is lost in CO_2-stream, whereas 81.53 mol% of the solvent lost is found in the water-stream and only 1.70 mol% in the CO_2-stream with TEGO IL P51P. Heating (**HX-H2**) the H_2 streams to 1500 K before sending to the turbines requires 97.8 MW for the TEGO IL K5 system and 99.91 MW for the TEGO IL P51P.

Also, for the TEGO IL P51P solvent, since after the unit HX-80 there is no liquid in the stream, the units SEPA-80 and PMP-153 are not required.

The pumping power (**F3-PUMP**) required to recycle the IL solvent-stream back to the absorbers at 30 bar is 75.11 MW for the TEGO IL K5 and 63.97 for TEGO IL P51P. This is because the recycled mass flow rate of the former solvent is larger than that of the latter. Also, the distribution of the cooling in the 3 flash drums (**HX1**, **HX2** and **HX3)** was found to be different since decreasing the pressure from 30 to 1 bar in 3 steps changes the flow rates of the vapor and liquid phases exiting the units depending on the IL solvent used. Furthermore, since more CO_2 is reaching the turbines in the case of the TEGO IL P51P, the compressor (**CMP-H2)** requires more power 9.97 MW instead of 8.12 MW in the case of the TEGO IL K5 solvent.

Table 12.9 also indicates that the net power balance is more negative (-26.45 MW) for the TEGO IL K5 than for the TEGO IL P51P, which means that the conceptual process scheme with the former IL provides useful excess power which can be used for steam or other power generation.

Table 12.9: Energy consumption of the process

Units	Description	Power MW TEGO IL K5	Power MW TEGO IL P51P
ABSORB-1	Packed-Bed Absorbers	0.00	0.00
ABSORB-2		0.00	0.00
ABSORB-3		0.00	0.00
ABSORB-4		0.00	0.00
FLASH1	Flash Drums	0.00	0.00
FLASH2		0.00	0.00
FLASH3		0.00	0.00
CMP-H2	Compressor to boost H_2 to 100 bar	8.12	9.97
HX-H2	Heater to heat H_2 to 1500 K	97.80	99.91
HX1	Heat exchanger to cool CO_2 stream to 288 K	-4.99	-32.83
HX2		-9.28	-55.08
HX3		-144.18	-75.68
SEPAR-1	Separator to separate CO_2 gas from IL after cooling to 288 K	-5.54	-0.38
SEPAR-2		-12.04	-0.46
SEPAR-3		-6.80	-1.63
SEPAR-4		0.00	0.00
CMP-10	CO_2 compressor to 10 bar	10.88	6.74
CMP-20	CO_2 compressor to 20 bar	7.08	5.74
CMP-80	CO_2 compressor to 80 bar	23.37	22.28
HX-80	Intercooling to 298 K	-43.51	-36.37
SEPA-80	Separation of Liquid CO_2 from CO_2 stream containing H_2	-0.82	NA
CMP-153	CO_2 compressor to 153 bar	6.00	6.00
HX-153	Intercooling to 223 K	-26.98	-26.73
SEPAR-153	Separation of Liquid CO_2 from CO_2 stream containing H_2	-0.73	-0.19
PMP-153	Pumping of liquid CO_2 to 153 bar	0.06	NA
F3-PUMP	Pump to bring IL back to 30 bar for recycling	75.11	63.97
Net Power		**-26.45**	**-14.72**

NA: Not available

12.5.1 Effect of packed-bed absorber height on CO_2 capture

Figure 12.6 shows the effect of the packed-bed height on CO_2 captured in the packed-bed absorber. As shown in Figure 12.6 CO_2 absorption increases from 97.3 mol% at 6 m to 98.5 mol% for a 30 m bed, whereas the H_2 absorption decreases from 53.6 mol% to 52.0 mol%. A further increase in the absorber height resulted in a negligible effect on the absorption rate, therefore, 18 m was used in the calculations.

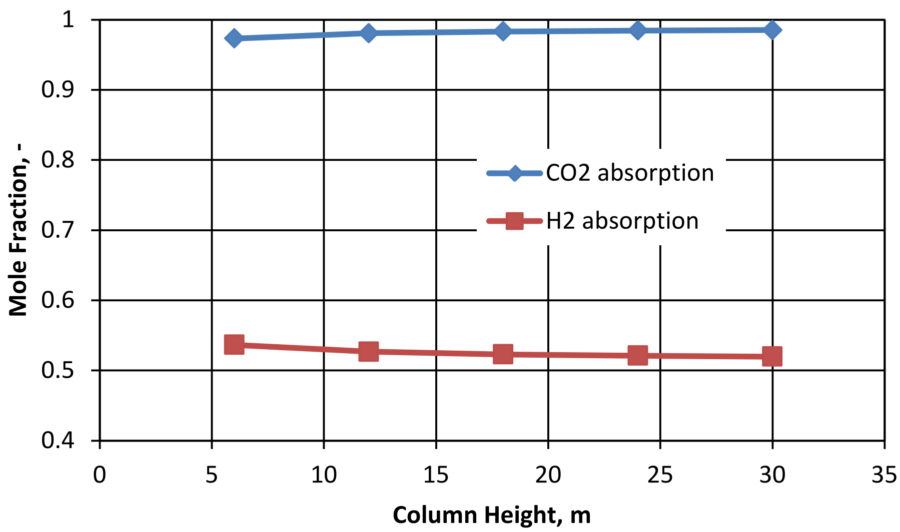

Figure 12.6: Effect of packed-bed height on CO_2 and H_2 absorption

12.5.2 Effect of column height on k_La

The correlation by Billet and Schulte,[289] Equation (12-10), along with the definition of k_La given in Aspen Plus by Equation (12-13) allow the extraction of k_La for each stage, therefore values along the height of the packed-bed column for each stage. Figure 12.7 show that the values of

k_La for the TEGO IL P51P are larger than those for the TEGO IL K5, which can be explained by a larger diffusion coefficient of CO_2 in the TEGO IL P51P affecting directly the binary mass transfer coefficient for the liquid $k^{L}_{CO2,ILP51P}$ as seen from Equation (12-10).

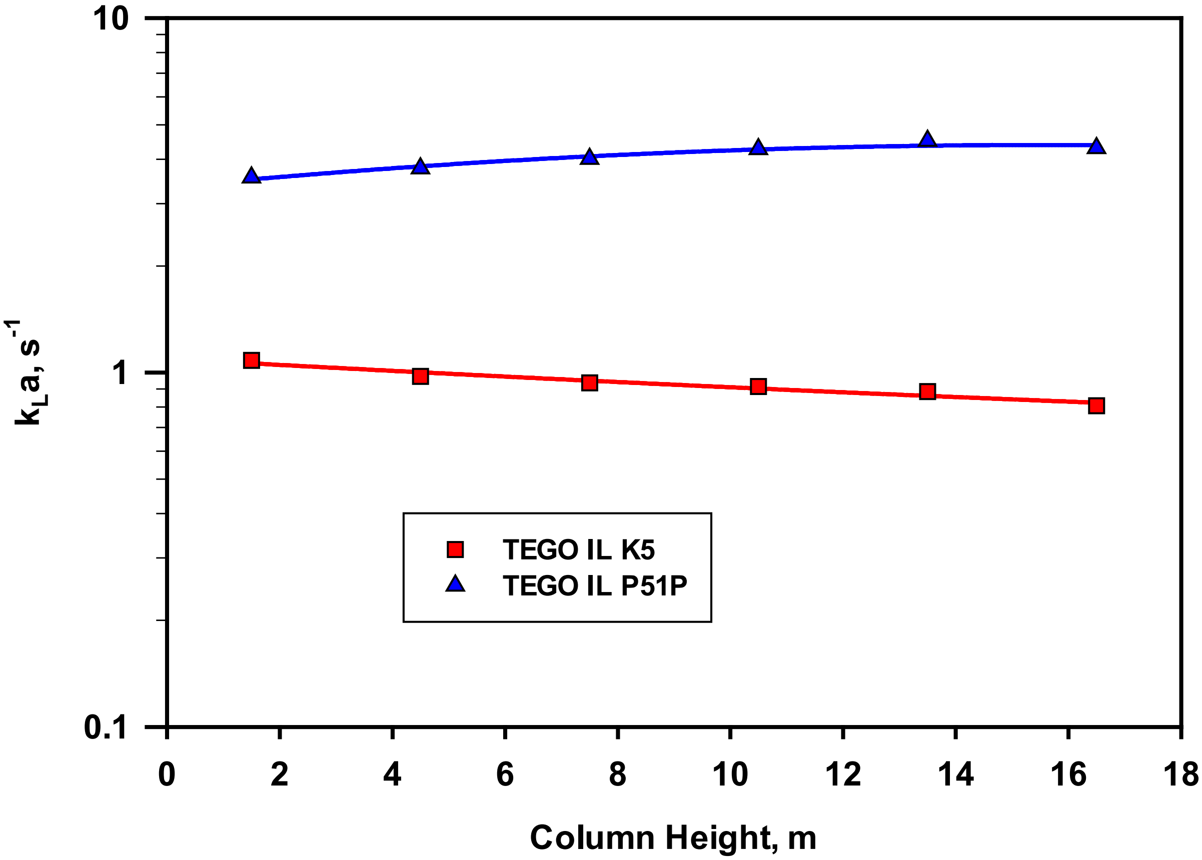

Figure 12.7: Comparison of k_La along the packed-bed column for the TEGO IL K5 and TEGO IL P51P

12.6 DISCUSSION

An Aspen Plus simulator, which employed the Peng-Robinson Equation of State (P-R EOS), was used to develop a conceptual process for CO_2 capture from a shifted hot fuel gas stream produced from Pittsburgh # 8 coal for a 400 MWe power plant using two ILs as physical solvents: TEGO IL K5 and TEGO IL P51P. The compositions of the process streams, CO_2 capture efficiency, and net power were calculated for the two solvents. The compositions of the main four process streams, CO_2-rich, H_2-rich, water, and IL solvent, were expressed as a percentage of the composition of the absorber gas inlet stream.

The mol% values are expressed as a function of the shifted fuel gas stream inlet flowrates to the absorber. The CO_2-rich stream which is being sent to sequestration site at 153 bar and 223 K contained 87.6 mol% of CO_2, 2.3 mol% of H_2, and 89.4 mol% of H_2S, when the TEGO IL K5 solvent is used.; and 81.42 mol% of CO_2, 2.1 mol% of H_2 and 82.06 mol% of H_2S when using the TEGO IL P51P solvent. The H_2-rich stream which is being sent to turbines at 100 bar and 1500 K contained 97.7 mol% of H_2, 84.6 mol% of CO, 12.4 mol% of CO_2, and 1.2 mol% of H_2O vapor when using the TEGO IL K5 solvent and 98.86 mol% of H_2, 89.55 mol% of CO, and 17.78 mol% of CO_2 when using the TEGO IL P51P solvent. The water stream which is separated from the system at 288.2 K and 1 bar contained 98.70 mol% of H_2O and 75.70 mol% of NH_3 and 0.1 mol% of H_2S when the TEGO IL K5 solvent is used; and 94.70 mol% of water, 72.37 mol% of NH_3, 0.80 mol% of CO_2, 0.47 mol% H_2S, and other gases with less than 0.20 mol% when using the TEGO IL P51P solvent. In addition the solvent-stream for the TEGO IL K5 , which is recycled to the absorbers, contained 15.56 mol% of H_2O, 5.20 mol% of CO_2, and 0.13 mol% of $H_{2,}$ In comparison the solvent-stream for the TEGO IL P51P contained 5.24 mol% of H_2O, 5.24 mol% of CO_2, and 0.26 mole% of $H_{2.}$

In addition, the two physical solvents exhibited minimum losses of 0.06 and 0.17 wt% with a net power balance of -26.44 and -14.72 MW for the TEGO IL K5 and the TEGO IL P51P, respectively. Thus, the TEGO IL K5 could be selected as a physical solvent for CO_2 capture from shifted hot fuel gas streams.

13.0 CONCLUSIONS

From the extensive experimental and simulation results obtained in this study so far, the following conclusions can be drawn:

1. These results proved that PFCs are thermally and chemically stable under the operating conditions employed, and CO_2 is consistently more soluble in these solvents than N_2 under similar conditions. Thus, PFCs show a potential for selective CO_2 capture from post-shift fuel gas streams at elevated pressures and temperatures.
2. The equilibrium solubilities (x^*) of CO_2 and N_2 in PP10, PP11, and PP25, expressed in mole fraction, were found to increase with pressure at constant temperatures. The solubilities for both gases were greater in PP25 than in the other two PFCs due to its larger molecular weight when compared with those of the other two PFCs. Under similar operating conditions, the solubility of CO_2 in the three PFCs appeared to be about 4 times that of N_2, which is attributed to the closeness of the solubility parameter of CO_2 to those of the PFCs when compared with that of N_2.
3. CO_2 is more soluble in the Selexol solvent than in the PFCs only at low temperatures ($\leq$ 333 K). The Selexol process, however, is customarily operating at temperatures of about 312 K, indicating that the Selexol solvent would not be effective at high temperatures typifying those at the exit of the gasifier system. This study proved the thermal and chemical

stability and the ability of the PFCs to selectively absorb CO_2 at temperatures up to 500 K and pressures as high as 30 bar.

4. The volumetric mass transfer coefficients (k_La) of CO_2 and N_2 in PP10, PP11, and PP25, increased with increasing mixing speed, pressure, and temperature due to the increase of the gas-liquid interfacial area (a) and the liquid-side mass transfer coefficient (k_L). The increase of the gas-liquid interfacial area with these operating variables was attributed to the increase of the gas holdup (ε_G) and the decrease of the Sauter mean bubble diameters (d_S).
5. The volumetric mass transfer coefficients of CO_2 and N_2 in the three PFCs decreased with increasing liquid height above the impeller due to the decrease of the gas holdup and increase of the Sauter mean bubble diameter, which led to the decrease of the gas-liquid interfacial area.
6. The volumetric mass transfer coefficients of CO_2 in the three PFCs were found to be always smaller than those of N_2 due to the smaller gas-liquid interfacial areas (smaller gas holdup and larger Sauter mean bubble diameter) of CO_2 when compared with those of N_2 under similar operating conditions.
7. The volumetric mass transfer coefficients for CO_2 and N_2 in PP25 were smaller than those in PP11, and both were smaller than those in PP10, indicating that the volumetric mass transfer coefficients decrease with increasing PFC viscosity. Also, under the operating conditions investigated, the gas-liquid interfacial areas of CO_2 and N_2 in the three PFCs appeared to control the behavior of the volumetric mass transfer coefficients in the gas-inducing reactor used.
8. The simulation results using the PP25 physical solvent showed that the P-T-Swing option leads to a greater solvent loss, but a more favorable (more negative) net enthalpy when

compared with the P-Swing option. However, in either regeneration option to be economically viable, the PP25 solvent must be completely recovered from the absorber and all flash drums.

9. The use of the TEGO IL K5 ionic liquid as a solvent for CO_2 capture showed promising results. The solubilities of H_2S and CO_2 were found to increase with pressure and decrease with increasing temperature. The H_2S solubilities in the IL were greater than those of CO_2 within the temperature range investigated (300 - 500 K) up to a H_2S partial pressure of 2.33 bar. Accordingly, the IL can be used to remove H_2S and CO_2 from dry gas mixture within a temperature range from 300 to 500 K under a total pressure up to 30 bar. The CO_2 solubility (x*) in TEGO IL P51P is greater than the solubility in TEGO IL K5 for the temperature range studied. The CO_2 solubility decreased, whereas that of H_2 increased with increasing temperature in the TEGO IL P51P.
10. The volumetric liquid-side mass transfer coefficients (k_La) for CO_2 in the TEGO IL K5 and TEGO IL P51P at 450 K were higher than the ones at 350 K due to the lower viscosity of the two ILs at 450 K than at 350 K. The k_La values for CO_2 and H_2 in both ILs increased with temperature and mixing speed and decreased with liquid height. The k_La for CO_2 and H_2 in both ILs increased with pressure up to 25 bar and then leveled off. Under similar operating conditions, k_La values for H_2 in the TEGO IL P51P were greater than those for CO_2; and k_La values for CO_2 in the TEGO IL K5 were almost the same as those in the TEGO IL P51P.
11. The presence of H_2S in the H_2S/N_2 mixture created mass transfer resistance which decreased k_La values for N_2. The k_La and $x*$ values of CO_2 were found to be greater than those of N_2 in the IL which highlight the stronger selectivity of this physical solvent to CO_2 when compared with that of N_2. Also, in the temperature range from 350 to 500 K, since the solubility and

k_La of H_2S in the IL were greater than those of CO_2, H_2S can be more easily captured than CO_2 from dry fuel gas streams using a shorter absorber than that needed for CO_2.

12. The Aspen Plus simulator, which employed the Peng-Robinson Equation of State (P-R EOS) was used to design a conceptual process for CO_2 capture from a shifted hot fuel gas stream produced from Pittsburgh # 8 coal for a 400 MWe power plant using the TEGO IL K5 and TEGO IL P51P ILs. The simulation results indicated that the TEGO IL K5, with a net power balance of -26.44 MW, had better performance than that of the TEGO IL P51P. This is because the CO_2-rich stream sent to sequestration sites at 153 bar and 223 K contained 87.6 mol% of CO_2, 2.3 mol% of H_2, and 89.4 mol% of H_2S, for TEGO IL K5; and 81.42 mol% of CO_2, 2.1 mol% of H_2, and 82.06 mol% of H_2S for the TEGO IL P51P. Also, TEGO IL K5 exhibited lower losses of 0.06 wt% whereas the TEGO IL P51P exhibited 0.17 wt%. Thus, these results suggested that the TEGO IL K5 IL could be used as a potential physical solvent for CO_2 capture from shifted fuel gas streams at temperatures up to 500 K and pressures up to 30 bar.

APPENDIX A

SELEXOL SOLVENT

This appendix was retrieved from the Dow Chemical website[173] and gives some information on the Selexol solvent, but unfortunately this datasheet was removed since last consulted in 2003.

SELEXOL Solvent
For Gas Treating

Introduction

SELEXOL™ solvent is one of Dow's high-performance gas treating solvents, complementing the UCARSOL™ solvent product line. SELEXOL solvent is a member of The Dow Chemical Company family of physical solvents designed to provide effective and economical bulk CO_2 removal and selective absorption of H_2S, COS, mercaptans, or BTEX from a variety of natural and synthesis gas streams. SELEXOL solvent has been proven effective and economical in a variety of gas treating applications, including:

- Purification of lean natural gas
- Low-energy ammonia/urea production
- Coal gasification
- Heavy oil partial oxidation
- Landfill gas purification
- Light hydrocarbon dew point control

SELEXOL solvent is particularly effective in high-pressure, low-temperature, high-acid gas systems.

Special Advantages

Among the special advantages of using SELEXOL solvent are the following:

- Removes gases by physical absorption rather than by chemical reaction
- High flash point ensures ease and safety in handling
- Nonfouling and inherently nonfoaming
- Can be used as-received—no mixing, formulating, diluting, or activating agents required
- Chemically and thermally stable
- Low vapor pressure results in low solvent loss
- Includes full range of Solvent Services to prevent and correct specific problems through technical assistance and follow-up
- Simultaneously dehydrates process gas streams
- May require little or no heat input, significantly reducing operating costs

Process Evaluation

In order to determine the feasibility of using SELEXOL solvent to treat a gas stream, Dow will evaluate the application using computer simulation based on data supplied by the processor. The results of the evaluation are provided in a written report that displays and interprets the pertinent operating parameters and indicates, in each particular case, the benefits of using SELEXOL solvent.

Gas Treating Services

Dow is the worldwide leader in providing gas processors with specialized technology and services. To aid in both plant design and operation, UCARSOL and SELEXOL solvents are supported by advanced computer capabilities, state-of-the-art laboratories, field test equipment, analytical procedures, and an on-going optimization program. The services Dow provides encompass preliminary assessments, start-up services, on-going monitoring, and follow-up services. Included in this total support program are training for your people in the field, regular sample testing, and performance evaluation. To ensure complete customer protection and satisfaction, Dow is there every step of the way—before, during, and after installation.

Computer Capabilities
With information drawn from the actual operating conditions of over 45 plants, Dow has the experience base to make accurate designs for SELEXOL systems. Dow's sophisticated computer programs provide a powerful tool for process analysis and design. In addition to its use as a grassroots process design tool, the computer is extremely valuable after start-up to make any adjustments necessary to optimize the process. Field representatives have laptop computers that can be taken into a customer's plant, making it possible to predict the performance of SELEXOL solvents under actual plant conditions.

Laboratory and Field Testing
Dow's Analytical Service Laboratories perform regular service analyses of customer solvents to ensure good performance of the treating system, as well as specialized analyses to assist in trouble-free operation. Among the routine analyses performed are ion chromatography, atomic absorption, and solution alkalinity. Specialized analyses include gas chromatography/mass spectroscopy, FTIR (Fourier Transform Infra Red), ICP (Inductively Coupled Plasma Spectro-scopy), NMR (Nuclear Magnetic Resonance Spectroscopy), and x-ray fluorescence. Analyses are normally completed and reported to the customer within a few days. Dow's written report usually includes a technical service interpretation of the analytical results and their impact on the customer's operation.

Sample Kits
Dow offers a unique sample kit. Completely self-contained, the kit provides everything necessary—from containers to labels—to obtain solvent samples, seal them, and safely ship them for routine analysis.

Other Services
Dow's engineering expertise is also available to provide information on process and equipment requirements, and the corrosion group can assist in field inspections or set up corrosion-monitoring programs for customers. Also, Dow trains customer personnel prior to and during installation, and follows up with them to ensure optimum performance.

Physical Properties

Odor	Very mild
Freezing Point, °C (°F)	-22 to -29 (-8 to -20)
Flash Point, °C (°F)	151 (304)
Vapor Pressure at 25°C, mm Hg (Pa)	0.0007 (0.093)
Specific Heat at 25°C, BTU/lb•°F (J/kg•°K)	0.49 (2090)
Density at 25°C, lb/gal (kg/m^3)	8.57 (1030)
Viscosity at 25°C, cP	5.9
Thermal Conductivity at 25°C, BTU/ft•hr•°F (W/m•°K)	0.10 (0.19)

Performance Properties

Comparative Solubilities of Gases in SELEXOL Solvent Relative to Methane

Component	Index$^{(1)}$
H_2	0.2
CH_4	1.0
CO_2	15.0
COS	35.0
H_2S	134.0
CH_3SH	340.0
C_6H_6	3800.0
H_2O	11,000.0

(1) $\frac{K' \; CH_4}{K' \; \textit{Component}}$

Product Safety

When considering the use of any Dow products in a particular application, you should review Dow's latest Material Safety Data Sheets and ensure that the use you intend can be accomplished safely. For Material Safety Data Sheets and other product safety information, contact a Dow representative or the nearest sales office at the numbers listed on the back of this brochure. Before handling any other products mentioned in the text, you should obtain available product safety information and take necessary steps to ensure safety of use.

No chemical should be used as or in a food, drug, medical device, or cosmetic, or in a product or process in which it may contact a food, drug, medical device, or cosmetic until the user has determined the suitability and legality of the use. Since government regulations and use conditions are subject to change, it is the user's responsibility to determine that this information is appropriate and suitable under current, applicable laws and regulations.

Dow requests that the customer read, understand, and comply with the information contained in this publication and the current Material Safety Data Sheet(s). The customer should furnish the information in this publication to its employees, contractors, and customers, or any other users of the product(s), and request that they do the same.

The Dow Chemical Company
Midland, Michigan 48674 U.S.A.

In the United States and Canada: call 1-800-UCARSOL • 1-800-447-4369 • fax 1-989-832-1465
In Europe: call toll-free +800 3 694 6367 • +32 3 450 2240 • fax +32 3 450 2815
In the Pacific: call +852 2879 7260 • fax +852 2827 5881
In Other Global Areas: call 1-989-832-1560 • fax 1-989-832-1465
Or visit us at www.dow.com

Published October 2001.

Printed in the U.S.A.

Form No. 111-01363-1001 AMS

APPENDIX B

LITERATURE REVIEW ON PERFLUOROCARBON COMPOUND

B.1 ABSTRACT

A comprehensive literature search was conducted in order to delineate the electrochemical, physical and thermodynamic properties, manufacture, and existing industrial applications of perfluorinated compounds (PFCs). The potential use of PFCs in acid gas removal (AGR) processes has been also investigated. The two main processes currently used for the manufacture of PFCs are electrochemical fluorination (ECF) and cobalt fluoride processes. The ECF process enjoys lower cost when compared with cobalt fluoride, but suffers from producing lower yields and selectivity, as well as extensive molecular rearrangement.

The numerous industrial applications of PFCs underscore their unique and important properties. For instance, owing to their good heat transfer capacity, PFCs are extensively used in energy-dissipating devices and refrigeration applications. Their low toxicity, non-flammability and inert properties made them useful as fire-extinguishing agents. Their low volatility and high boiling point along with reasonable viscosity and density allowed their employment as lubricants and greases. Also, their high electrical resistivity and dielectric strength are currently attracting attention for their potential use as insulators in capacitors.

The PFCs have low reactivity and high chemical stability due to the high energy of their C-F bonds. The PFCs have high boiling point and low vapor pressure because of the strength of the C-F bond and their high molecular weights, which minimize PFCs losses under high temperature applications. PFCs have also no dipole and very low molecular interactions due to the repulsive tendency of fluorine atoms, which lead to high gas solubility and decrease of the forces required to expel gas molecules upon decreasing pressure or increasing temperature. These unique properties make PFCs strong good candidates for AGR from fuel or flue gas under high pressures and temperatures.

B.2 INTRODUCTION

Fluorine is predominantly found in the salts of halide ions $^{19}_{9}F^{-}$, such as fluorite (CaF_2) and cryolite (Na_3AlF_6), or in a gaseous state as (F_2), which is highly toxic and colorless. It is placed 13th in the order of abundance of elements on the earth, and thus outranks the other four halogens (Cl, Br, I, At), which are the elements in Group VIIA, the next-to-last column of the Periodic Table.[290,291] Fluorine is the most electronegative among common elements (Pauling values: F: 4.0; O: 3.4; Cl: 3.2; C: 2.6; H: 2.2) and is the most reactive element known.[184] Fluorine it highly difficult to handle, hence asbestos, water, and silicon burst into flame in its presence, and it reacts with Kr, Xe, and Rn, elements which were once thought to be inert.[292] Fluorine is a powerful oxidizing agent, which can force other elements into unusually high oxidation numbers, such as in AgF_2, PtF_6, and IF_7. Also, fluorine forms the strongest single bond to carbon and requires a very small space when compared with other halogens,[182] as it is the second smallest atom after hydrogen.[292,293]

Fluorine is primarily used in the manufacture of teflon or polytetrafluoroethylene (PTFE), $(C_2F_4)_n$, and other low and high molecular weight fluoro-polymers, which are utilized as oils and thermoplastics in many applications, including gaskets, valve packings, and linings for storage vessels, pans, rectors, and pipes that need to be inert during chemical reactions. Large amounts of fluorine are also consumed each year in the manufacture of freons, such as CCl_2F_2 which is used in refrigerators and cars.

Perfluorocarbon (PFC) liquids represent a growing market as they possess unique properties, which have led to their extensive use as inert fluids in: (1) testing electronics, (2) cooling electronic devices, and (3) vapor-phase soldering. The quantities of PFCs required for each of these three applications are approximately in the ratio of 3:1:1, with a total world market in excess of 1000 tons in 1990.[205] The use of Latin prefix (Perfluoro-) to indicate the highest substitution possible of hydrogen atoms attached to carbon by fluorine atoms in organic compounds without affecting the nature of the functional groups present in the molecule is widely used for the denomination of many fluoro-compounds. It has been acceptable to directly state the number of fluorine atoms for simple molecules, such as C_1–C_4 aliphatics [e.g., tetrafluoroethene (CF_2=CF_2), pentafluoropropionic acid ($C_2F_5CO_2H$), and octafluoropropane (C_3F_8)] or monocyclic aromatics e.g., hexafluorobenzene (C_6F_6), pentafluoropyridine (C_5F_5N)]. For large molecules, however, such names become cumbersome and do not reveal immediately that the compounds are fully perfluorinated [e.g., dodecafluorocyclohexane (c-C_6F_{12}) or pentadecafluorooctanoic acid (n-$C_7F_{15}CO_2H$)]. In such cases, it is advantageous to use the prefix "Perfluoro-" in conjunction with the standard hydrocarbon nomenclature [e.g., Perfluoro-cyclohexane and Perfluoro-octanoic acid]. Actually, this has been a common practice for over 40 years, where many authors use Perfluoro- even for quite simple molecules, [e.g., Perfluoropropene ($CF_3CF{=}CF_2$)[185,294]]. In the following, a literature review is presented in order to assess, identify and better understand the behavior of PFCs and their potential for AGR applications under high pressures and temperatures.

B.3 ELECTROCHEMICAL PROPERTIES OF PFCS

The physical properties and chemical reactivities of organic molecules can be dramatically affected by fluorination. The numerous commercial applications of organo-fluorine materials clearly reflect the beneficial effects of fluorination. This is because over the past two decades advances in both experimental and theoretical aspects of organofluorine chemistry have made the "unusual" behavior of perfluorinated compounds much more understandable and predictable, which is important for the design of commercial products.[182]

Most of the effects of fluorination can be anticipated by comparing the physical properties of fluorine atom with those of other common atoms as shown in Table B.1. As can be seen in this table, the high ionization potential[295] and relatively low polarizability[296] of fluorine atom imply very weak intermolecular interactions, low surface energies, and low refractive indices for perfluorocarbons.[184] Also, the extreme electronegativity of fluorine atom as shown in the table insures that it will always be inductively electron-withdrawing when bonded to carbon, and that the bond will be strongly polarized (δ+)C–F(δ-), since the bond polarity can be derived from electronegativity differences.[297] Consequently, the C–F bond has relatively higher ionic strength and is stronger than the corresponding C–X bond, where X could be H, Cl, Br, I, C, N, and O atoms as listed in Table B.1. The consequence of the C–F bond dipole is that partially perfluorinated compounds have a strong polar character, and accordingly their physical properties are often different from those of either their hydrocarbon or perfluorocarbon counterparts. Thus, the resulting electronic effects of fluorination on molecular properties can be attributed to the unique combination of the fluorine atom properties: its high electronegativity and small size,[298] its three tightly bound, nonbonding electron pairs, and the excellent match between its 2s or 2p orbital with the corresponding orbital of carbon atom.

Table B.1: Atomic Physical Properties[295,296,298]

Atom	Ionization potential (IP)	Electron affinity (EA)	Atom polarizability (α_v)	Van der Waals' radius (r_v)	Electronegativity Pauling (χ_p)
	kcal.mol^{-1}	*kcal.mol^{-1}*	*Å^3*	*Å*	-
H	313.6	17.7	0.667	1.20	2.20
F	401.8	79.5	0.557	1.47	3.98
Cl	299.0	83.3	2.18	1.75	3.16
Br	272.4	72.6	3.05	1.85	2.96
I	241.2	70.6	4.7	1.98	2.66
C	240.5	29.0	1.76	1.70	2.55
N	335.1	-6.2	1.10	1.55	3.04
O	314.0	33.8	0.82	1.52	3.44

B.4 PHYSICAL PROPERTIES OF PFCS

Perfluorocarbons (PFCs) are characterized by an unusual physical properties when compared with their analogous hydrocarbons (HCs).[178-181] A comparison among some physical properties of saturated perfluoro-hexane (n-C_6F_{14}), saturated n-hexane (n-C_6H_{14}) and partially perfluorinated alkanes (n-$CF_3(CF_2)_2(CH_2)_2CH_3$) is given in Table B.2. In general, PFCs have significantly greater compressibilities and viscosities than those of HCs; and their densities are typically about 2.5 times those of the latter. The saturated PFCs have the lowest dielectric constants, refractive indices, and surface tensions of any liquids at room temperature, which reflect their nonpolar character and low polarizability.[182] These physical properties, coupled with their outstanding chemical and thermal stabilities, make perfluorinated compounds ideal candidates for several commercial applications.[299-301] For instance, their high densities, viscosities, and expansion coefficients make them excellent convective coolants. Also, their chemical inertness combined with low dielectric constants, low dielectric losses, and high dielectric strengths and resistance makes them good insulating materials, especially for electronics applications.[205,302]

Table B.2: Comparison Among Physical Properties of Different Hexanes[178]

Property	n-C_6F_{14}	n-$CF_3(CF_2)_2(CH_2)_2CH_3$	n-C_6H_{14}
Molecular weight, kg.kmol^{-1}	338.0	212.1	86.2
Boiling Point, bp (°C)	57	64	69
Heat of Vaporization, ΔH_v (kcal.mol^{-1})	6.7	7.9	6.9
Critical Temperature, T_c (°C)	174	200	235
Density at 25 °C, d (g.cm^{-3})	1.672	1.265	0.655
Viscosity at 25 °C, η (cP)	0.66	0.48	0.29
Surface Tension at 25 °C, σ (dyn.cm^{-1})	11.4	14.3	17.9
Compressibility at 1 atm, β (10^{-6} atm^{-1})	254	198	150
Refractive index, n^{25}_D (-)	1.252	1.290	1.372
Dielectric constant, ε_I (-)	1.69	5.99	1.89

Although several physical properties of partially perfluorinated alkanes (HFCs) lie between those of PFCs and HCs, differences and exceptions still exist. For example, the dielectric constant of n-$CF_3(CF_2)_2(CH_2)_2CH_3$ is much greater than those of n-C_6F_{14} and n-C_6H_{14}. Also, n-$C_6H_{13}F$ has a greater boiling point (91.5°C) and a considerably higher surface tension (19.8 dyn.cm^{-1}) than those of n-C_6F_{14} and n-C_6H_{14}, whereas the boiling point and surface tension of n-$CF_3(CF_2)_2(CH_2)_2CH_3$ lie in between those of HC and PFC. These "anomalies" point to the importance of polar effects in HFCs owing to the net C–F or C–C dipoles which are absent in PFCs and HCs.[182] Table B.2 also shows that the molecular weights of the PFCs are greater than those of HCs, however, the boiling points of homologous linear PFCs and HCs are similar, indicating that the molecular weights have little influence on the boiling points.

Table B.3 indicates that branching has a negligible effect on the boiling points of perfluorinated compounds, which is in contrast with the behavior of the corresponding HCs.[179-181,183] The trends of the boiling points shown in Table B.3 reflect extremely low intermolecular interactions in PFCs, which make them behave as ideal liquids.[179-181]

Table B.3: Boiling Points of Homologous Perfluoroalkanes and Alkanes[182]

	Boiling point (°C)									
	n = 1	2	3	4	5	6	7	8	9	10
n-C_nF_{2n+2}	-128	-78	-38	-1	29	57	82	104	125	144
n-C_nH_{2n+2}	-161	-88	-42	-0.5	36	69	98	126	151	174
c-C_nF_{2n}			-32	-6	23	53	81	102		
c-C_nH_{2n}			-34	13	50	81	118	151		

The surface tension (σ) of a liquid is a measure of the molecular energy acting on its surface (dyn.cm^{-1} = mN.m^{-1}) in order to oppose its expansion. Table B.4 shows that the PFCs have the lowest surface tension values of any organic liquid, which mean that the PFCs will wet practically any solid surface. Table B.2 also indicates that the surface tension of PFC is greater than that of the corresponding HFC, and both are smaller than that of their HC counterpart. It should be mentioned that perfluorinated ethers and amines have low surface tensions, typically 15-16 dyn.cm^{-1}, indicating their PFC-like character.[182]

Table B.4: Surface Tensions of Perfluorocarbons and Hydrocarbons[179,303,304]

	Surface Tension ($dyn.cm^{-1}$)[(a)]	
	PFC	HC
n-Pentane	9.4	15.2
n-Hexane	11.4	17.9
n-Octane	13.6	21.1
Methyl-c-hexane	15.4	23.3
Decalin	17.6	29.9[(b,c)]
Benzene	22.6[(d)]	28.9[(b)]

(a) at 25 °C, (b) at 20 °C, (c) trans isomer, (d) at 23 °C

B.5 THERMODYNAMIC PROPERTIES OF PFCS

In the following section, the thermal stability of PFCs and the solubility of different fuel gases, including CO_2, in PFCs and HCs as well as other perfluorinated solvents are presented.

B.5.1 Stability: Bond Strengths and Reactivity of PFCs

The C–F bonds in fluoro-alkenes (and fluoro-benzenes) are quite strong, 116 $kcal.mol^{-1}$ in C_2H_3F and 125 $kcal.mol^{-1}$ in C_6H_5F,[305] but their C=C π-bond strengths vary considerably with the degree of fluorination. The π-bond dissociation energies (D_π) for CH_2=CH_2 and CH_2=CF_2 are 64–65 $kcal.mol^{-1}$,[306] and 62.8±2 $kcal.mol^{-1}$,[307] respectively, while D_π for CF_2=CF_2 is only 53 $kcal.mol^{-1}$. The Experimental D_π values for other fluoro-ethylenes are not known, but available thermodynamic data indicate that monofluorination stabilizes double bonds, whereas neighboring difluorination and trifluorination are destabilizing.[308] Also, fluorination of acetylenes is highly destabilizing,[309] as both HC≡CH and FC≡CF are dangerously explosive and

$CF_3C{\equiv}CCF_3$ is an extraordinarily reactive dienophile (possibility to react with a diene) and enophile.[310,311]

In the case of saturated compounds, fluorine forms the strongest single bond with carbon. In monohaloalkanes, the C–F bond is about 25 kcal.mol^{-1} stronger than the C–Cl bond[308,312] and the difference between the heterolytic bond dissociation energies (breaking of a chemical bond in a compound) is even greater with values close to 30 kcal.mol^{-1}.[313] As a consequence of the relatively strong C–F bond and the poor departure group ability of fluoride ion,[314-316] alkyl fluorides are 10^2–10^6 times less reactive than the corresponding chlorides in typical S_N1 solvolysis or S_N2 displacement reactions.[317,318] The alkyl fluorides displacement reactions, however, can be catalyzed by acid when H-bonding assists the departure of fluoride.[319,320] For instance, $C_6H_5CH_2X$ solvolysis in 10% aqueous acetone has k_F to k_{Cl} ratio (k_F/k_{Cl}) of 3.2×10^{-2}, but with 6 M $HClO_4$, the k_F to k_{Cl} ratio is 2.6×10^3.[320] Also, the decomposition of benzyl fluoride catalyzed by HF can be violent, leading to storage problems.[321]

Tables B.5 and B.6 show the bond dissociation energies (heats of formation of simple alkyl radicals,[305,322] D^0) for different ethanes; and as can be seen while α-fluorination increases the C–F bond dissociation energies, it does not significantly affect those of C–H, C–Cl, or C–Br bonds. The increase of C–F bond dissociation energies from 107.9 kcal.mol^{-1} in CH_3CH_2–F to 124.8 kcal.mol^{-1} in CH_3CF_2–F shows the strong impact of the α-fluorination. On the other hand, β-fluorination significantly increases the C–H bond dissociation energies, but has little effect on those of C–F bonds, as can be seen for CH_3CH_2–X and CF_3CH_2–X in Table B.5.

Table B.5: Bond Dissociation Energies of Ethanes[308,323]

	D^0 (C–X) (kcal.mol^{-1})			
X	CH_3CH_2–X	CH_3CF_2–X	CF_3CH_2–X	CF_3CF_2–X
H	100.1	99.5	106.7	102.7
F	107.9	124.8	109.4	126.8
Cl	83.7	-	-	82.7
Br	69.5	68.6	-	68.7
I	55.3	52.1	56.3	52.3

Table B.6: C–C and C–O Bond dissociation Energies[308]

Ethane	D^0 (C–C) (kcal.mol^{-1})	Ether	D^0 (C–O) (kcal.mol^{-1})
CH_3CH_3	88.8	CH_3OCH_3	83.2
CH_3CF_3	101.2	-	-
CF_3CF_3	98.7	CF_3OCF_3	105.2

The α- and β-fluorination appear to decrease the reactivity of saturated compounds towards nucleophilic reactions. Compared with CH_3CH_2Br, the reaction between CF_3CH_2Br and NaI in acetone is about one fold slower,[324] and RCF_2Br compounds are inert to halide exchange under identical conditions. The strong C–F bonds appear to diminish the reactivities of alkyl CF_3 and CF_2H groups towards F^- displacement or hydrolysis, which can be attributed to the shielding of the carbon center by the F and inductive effects. The polyfluorohaloalkanes can resist direct attack on carbon, but their reaction with nucleophiles involve initial attack on halogen by either one- or two-electron transfer processes.[325,326]

Aliphatic C–C bonds are usually strengthened by fluorination.[308,327] The CF_3–CF_3 bond is 10 kcal.mol^{-1} stronger than the CH_3–CH_3 bond, and the C–C bonds in poly(CF_2CF_2) are about 8 kcal.mol^{-1} stronger than those in poly(CH_2CH_2).[293] Fluorination also increases the C–C bond strength in four and larger ring cyclo-alkanes, and is believed to reduce the strain energy of cyclobutane.[308,327,328] Partially perfluorinated alkanes, however, can have stronger C–C bonds than those in perfluorinated alkanes. For instance, the CF_3–CH_3 bond is 2.5 kcal.mol^{-1} stronger than the CF3–CF_3 bond.

The high strength of C–F and C–C bonds in PFCs contributes to their outstanding thermal and chemical stabilities.[184] The PFCs thermal stabilities are limited only by the strengths of their C–C bonds, which decrease with increasing the chain length or chain branching.[185] The most robust PFC is CF_4, whose C–F bonds can measurably dissociate only above 2000 °C. Temperatures approaching 1000 °C are required to pyrolyze n-C_2F_6 or n-C_3F_8,[185] but poly(CF_2CF_2) rapidly decomposes above 500 °C and its copolymers with perfluoroalkenes are significantly less stable.[329] The PFCs with tertiary C–C bonds thermolyze (decomposition of an organic compound into a solid phase then gas phase with thermal treatment without oxygen) around 300 °C and highly branched systems can undergo more chemical changes than their HC analogs.[182] Perfluorocyclopropanes, on the other hand, are different, since c-C_4F_8 undergoes homolysis at a rate of <5% h^{-1} at 500 °C[330] whereas c-C_3F_6 extrudes CF_2 at about 170 °C.[331] Perfluoroethers often are more thermally stable than PFCs owing to their especially strong C–O bonds, as at 585 °C poly(CF_2CF_2O) decomposes about 10 times slower than poly(CF_2CF_2).[329]

Partially perfluorinated hydrocarbons (HFCs) are thermally less stable than their PFC counterparts, but they decompose primarily by HF elimination rather than by C–C bond rupture.[184] Even though poly(CH_2CF_2) has stronger C–C bonds than poly(CF_2CF_2), it is unstable above 350 °C and starts to lose HF rapidly with further increase of temperature.[329] Similarly, CF_3CF_2H loses HF only at 925 °C and C–C bond split becomes significant only about 1125 °C.[332] The eliminations of HF from HFCs are greatly accelerated by the presence of bases, which provide means to treat partially perfluorinated elastomers[333] and functionalize the surfaces of hydrofluorinated plastics.[334,335] The chemical unreactivity associated with saturated PFCs has also its exceptions, as PFCs are susceptible to defluorination by reducing agents and fusion with alkali metals, which has been exploited to convert most PFCs to carbon and metal fluorides[336,337] for elemental analysis.

B.5.2 Solubility of Gases in PFCs

Perfluorinated compounds are nonpolar and are poor solvents for all materials except those with very low cohesive energies, such as gases. Saturated PFCs are practically insoluble in water and HF, but slightly soluble in HCs, and dissolve relatively well in low-molecular weight HCs.[170,179] The cohesive pressures of PFCs are only about half those of their corresponding HCs;[170] the heats of solution of PFCs are much different from those of HCs;[170,186,187] and the enthalpies of interaction between PFCs and HCs are smaller than those between HCs.[186,187] In terms of solvent-solute interactions, PFCs are more like Ar and Kr than HCs.[178] The distinct difference between interaction energies of PFCs and those of HCs is related to their boiling-point trends, and is manifested by the non-ideal behavior of their mixtures.[166,188-193]

Among several empirical solvent polarity scales,[338] the one introduced by Middleton and co-workers[190-192] based on the analysis of the solvent polarity, is particularly useful in ranking perfluorinated solvents. The PFCs solvent spectral polarity indices shown in Table B.7 underline the nonpolar character of PFCs, reveal higher polarity of HFCs when compared with those of HCs (P_S = 7.52 for C_6H_5F versus 6.95 for C_6H_6), and indicate high polarity of perfluorinated alcohols. The polarity values for CF_3CH_2OH and $(CF_3)_2CHOH$ are 10.2 and 11.08, respectively, when compared with 10.64 and 12.1 for 50% aqueous HCO_2H and H_2O, which reflect the strong hydrogen-bonding character of PFC-alcohols.[182]

A useful property of PFCs is their ability to dissolve oxygen and other gases.[194,195] PFCs dissolve about two to three times more oxygen than their analogous HCs, and about ten times more than water, which explain their use as oxygen carriers in artificial blood and organ perfusion applications.[196] The high solubility of O_2 in PFCs is not due to any specific attractive interaction between these two compounds,[197-200] but rather results from the existence of large cavities (free volume) in PFC liquids which can accommodate the gas molecules.

Table B.7: Solvent spectral Polarity Index[339]

Solvent	Polarity Index	Solvent	Polarity Index
n-C_6F_{14}	0.00	n-C_6H_{14}	2.56
c-$C_6F_{11}CF_3$	0.46	c-$C_6H_{11}CH_3$	3.34
n-C_8F_{18}	0.55	n-C_8H_{18}	2.86
(n-$C_4F_9)_3N$	0.68	(n-$C_4H_9)_3N$	3.93
c-$C_{10}F_{18}$ (Perfluorodecalin)	0.99	c-$C_{10}H_{18}$ (Decalin)	4.07
$CFCl_2CFCl_2$	3.22	$CHCl_2CHCl_2$	9.23
$CFCl_3$	3.72	CCl_4	4.64
C_6F_6	4.53	C_6H_6	6.95
CF_3CO_2Et	6.00	CH_3CO_2Et	6.96
C_6H_5F	7.52	C_6H_5Cl	8.30
o-$C_6H_4F_2$	7.86	o-$C_6H_4Cl_2$	8.94
CF_3CH_2OH	10.2	CH_3CH_2OH	8.05
$(CF_3)_2CHOH$	11.08	$(CH_3)_2CHOH$	7.85

c: cyclo, o: ortho

Table B.8 compares the solubility of oxygen in hexane and perfluorohexane; and as can be noticed the solubility of O_2 in perfluorohexane is twice as that in hexane and increasing temperature decreases the oxygen solubility in both liquid.

Table B.8: Experimental data on mole fraction solubilities and Henry's law coefficient for O_2 in hexane and perfluorohexane[201]

T	x_1, $1\times10^{3(a)}$	$H_{1,2}{}^{(b)}$
K	-	*MPa*
	n-C_6H_{14}	
288.89	2.17	46.7
293.20	2.10	48.2
298.10	1.99	51.0
298.51	1.99	50.9
298.86	1.99	51.0
303.43	1.83	55.5
307.84	1.69	60.1
312.44	1.55	65.6
	n-C_6F_{14}	
288.69	4.94	20.5
293.38	4.68	21.6
299.36	4.23	23.9
303.36	3.75	26.9
303.37	3.79	26.6
303.41	3.75	27.0
303.47	3.76	26.9
307.83	3.42	29.6
312.58	2.94	34.5

(*a*) at a solute partial pressure of 101325 Pa

(*b*) Henry's law coefficients at the saturation pressure of the pure solvent

The tabulated experimental values for Henry's law were fitted as a function of 1/T[201] using Equations (B-1) and (B-2) as:

For n-C_6H_{14}:

$$\ln H_{1,2} = 3.8310\times10^{6} - \frac{2.6901\times10^{4}}{T} + \frac{6.4874\times10^{1}}{T^{2}} \tag{B-1}$$

For n-C_6F_{14}:

$$\ln H_{1,2} = 3.9986\times10^{6} - \frac{2.8629\times10^{4}}{T} + \frac{6.8020\times10^{1}}{T^{2}} \tag{B-2}$$

Costa Gomes et al.[202] investigated the solubilities of O_2 and CO_2 in the same liquids and found an improvement of almost 100% for the solubility of O_2 in perfluorohexane when compared with that in n-hexane. In the case of CO_2, as shown in Table B.9, the increase is not as significant, but it is important to notice that perfluorohexane dissolves between 2-20 times more CO_2 than O_2 depending on the temperature.

Table B.9: Solubility (x_1, 1×10^3) of O_2 and CO_2 in n-Hexane and in Perfluoro-n-hexane[202]

T	O_2		CO_2		CO_2 (no electrostatics)	
K	n-C_6H_{14}	n-C_6F_{14}	n-C_6H_{14}	n-C_6F_{14}	n-C_6H_{14}	n-C_6F_{14}
200	5.9±0.4	10±1	174±30	231±39	171±29	196±34
300	3.0±0.1	5.4±0.1	16.6±0.4	24.3±0.8	16.6±0.4	22.4±0.7
400	3.1±0.1	5.1±0.1	7.9±0.1	11.2±0.2	8.0±0.1	10.7±0.2

Table B.10 compares the solubility of O_2, CO_2 and CO in different liquids; and as can be observed the solubility of CO_2 is once again greater than that of O_2 in both solvents, and CO behaves like O_2. The difference between gas solubilities in hydrocarbon and fluorocarbon solvents, however, is not as substantial for CO_2 as for CO and O_2 which can be explained by comparing their dipoles. Costa Gomes et al.[202] explained the solute-solvent interactions by the dispersion forces rather than the electrostatic terms, a hypothesis that could be supported by the polarizability values: CO, α_V = 1.60 Å^3; O_2, α_V = 1.95 Å^3; CO_2, α_V = 2.65 Å^3.

Table B.10: Experimental solubility (x_1, 1×10^3) of Gases at 298 K in various hydrocarbon and fluorocarbon solvents[202]

	O_2	**CO_2**	**CO**
n-C_6H_{14}	1.99	-	-
n-C_7H_{16}	2.04	-	-
n-C_8H_{18}	2.05	12.6	1.71
C_6H_6	0.815	9.70	0.663
n-C_6F_{14}	4.23	-	-
n-C_7F_{16}	5.22	-	-
n-C_8F_{18}	5.34	-	-
C_6F_6	2.41	22.0	2.12
$x(C_6F_{14})/x(C_6H_{14})$	2.13	-	-
$x(C_7F_{16})/x(C_7H_{16})$	2.56	1.73	2.24
$x(C_8F_{18})/x(C_8H_{18})$	2.60	-	-
$x(C_6F_6)/x(C_6H_6)$	2.96	2.27	3.20

In Table B.11, the solubility of CO_2 in different fluorocarbon liquids is again higher than those of all the other gases listed, and when compared with H_2 or N_2, at the temperature used, it differs by more than one order of magnitude. Thus, perfluorinated compounds are expected to have higher selectivity toward CO_2 than other gases present in the flue or fuel gas.

Table B.11: Solubility (x_1, 1×10^4) of gases in TFE and HFIP at 101.33 kPa gas partial pressure[340]

	TFE, 2,2,2-trifluoroethanol		HFIP, 1,1,1,3,3,3-hexafluoropropan-2-ol	
Gas	268.15 K	283.15 K	273.15 K	283.15 K
He	1.13	1.41	2.24	2.38
Ne	1.73	1.99	3.66	3.79
Ar	9.21	8.87	16.26	15.51
Kr	20.88	18.81	31.61	29.91
Xe	49.48	42.59	69.16	61.28
H_2	2.13	2.43	3.50	3.84
N_2	6.02	6.23	11.61	11.68
O_2	9.36	9.29	16.60	16.37
CH_4	13.20	12.32	19.71	19.37
C_2H_4	73.61	60.42	127.0	117.2
C_2H_6	61.44	50.51	79.75	71.84
CO_2	209.7	152.2	264.8	221.9
CF_4	16.87	14.99	38.76	35.57
SF_6	89.88	68.45	230.7	186.4

In Table B.12 and Figure B.1, it can be seen that the solubility of CO_2 in 1-N-butyl-3-methylimidazolium hexafluorophosphate increases linearly with pressure, and accordingly the data follow Henry's law over the pressure and temperature ranges used. Figure B.2 shows Henry's law constant plot as a function of the reciprocal of temperature (1/T); and even though the solubility of CO_2 appears to decreases with temperature, large amounts of CO_2 can still be dissolved in 1 kg of solvent, which underlines the potential use of PFCs as physical solvent in AGR processes.

Table B.12: Solubility of CO_2 in 1-N-butyl-3-methylimidazolium hexafluorophosphate[341]

T=293.15 K		T=313.15 K		T=333.15 K		T=353.15 K		T=373.15 K		T=393.15 K	
m_{CO2}	p	m_{CO2}	p	m_{CO2}	p	m_{CO2}	p	m_{CO2}	p	m_{CO2}	p
mol/kg	MPa	mol/kg	MPa	mol/kg	MPa	mol/kg	MPa	mol/kg	MPa	mol/kg	MPa
1.199	1.533	0.0557	0.105	0.1554	0.424	0.0734	0.266	0.0510	0.229	0.2179	1.199
1.809	1.967	0.6674	1.292	0.6344	1.746	0.3710	1.329	0.3286	1.486	0.6023	3.416
2.244	2.755	1.478	2.893	1.043	2.885	0.7914	2.915	0.6153	2.827	0.7959	4.571
3.497	4.190	2.187	4.242	1.350	3.730	1.234	4.592	0.9427	4.467	0.9649	5.513
3.985	4.752	3.018	5.844	1.614	4.492	1.641	6.194	1.221	5.830	1.132	6.526
		3.656	7.293	2.073	5.807	2.088	8.025	1.459	7.055	1.307	7.597
		4.391	9.480	2.488	7.091	2.453	9.685	1.867	9.191	1.430	8.324
				2.719	7.822						
				2.917	8.562						
				3.116	9.184						

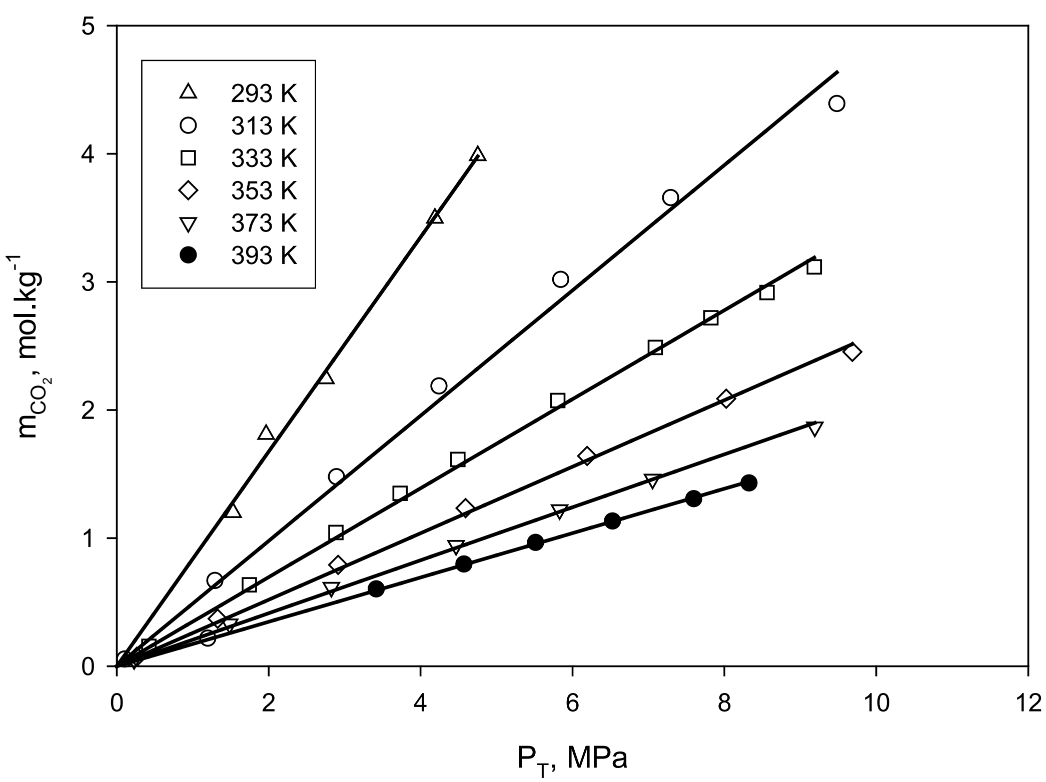

Figure B.1: Solubility of CO_2 in 1-N-butyl-3-methylimidazolium hexafluorophosphate [PF_6] as a function of temperature and total pressure[341]

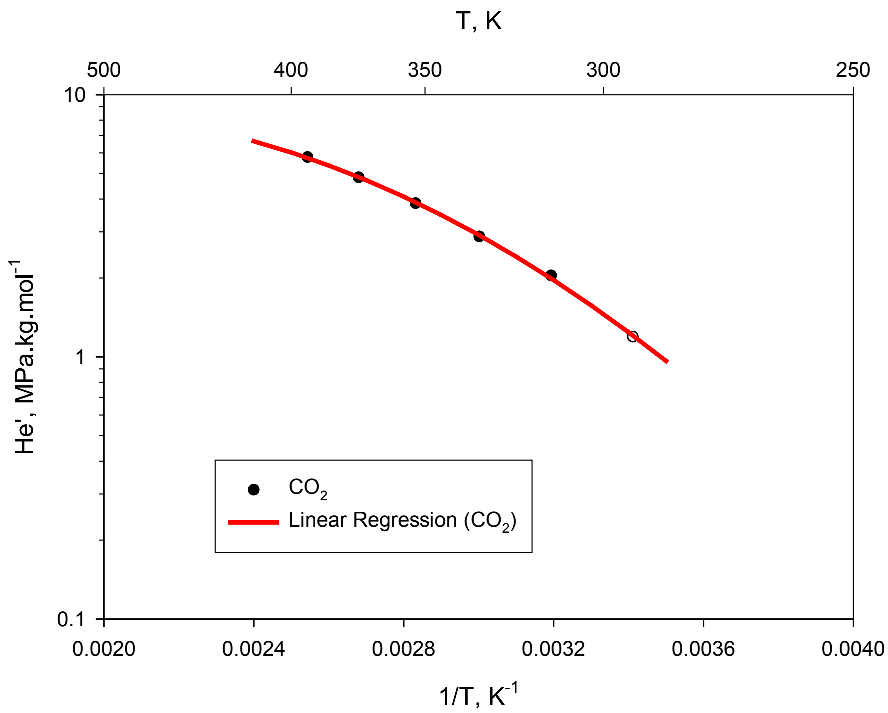

Figure B.2: Henry's law constant of CO_2 in 1-N-butyl-3-methylimidazolium hexafluorophosphate $[PF_6]$[341]

Table B.13 compares the solubility of N_2 in water, acetone, cyclohexane and perfluorohexane; and as can be seen the solubility of CO_2 follows the order: perfluohexane > cyclohexane > acetone > water. In water, the molecules are held tightly together by hydrogen-bonding, and consequently the gas is expected to dissolve poorly as few spaces are available for gas molecules. In acetone, the molecules interactions are weaker, and therefore more CO_2 is dissolved. Cyclohexane has an induced dipole, which contributes to higher solubility than in acetone. Perfluorocarbons, however, have no dipole, and induced dipoles are prevented to appear due to the presence of fluorine atoms. Thus, the fluorine atoms have a tendency to repel each other, which lead to very low molecular interactions between perfluorocarbon molecules.[342] Increasing pressure forces the gas molecules into the liquid, however, a perfluorocarbon will not exert a large force to squeeze the gas molecules out due to the low degree of molecular interactions, and consequently, the gas will dissolve in a large quantity in such solvent[342]

Table B.13: Solubilities of nitrogen in various solvents at 298 K and 1 atm[342]

Expressed as mL of gas per 100g of liquid at 25 °C, 1 atm	
Liquid	Solubility
Perfluorohexane	44.2
Cyclohexane	18.5
Acetone	17.7
Water	1.6

Some gases, however, can contribute to the intermolecular forces existing in the solvent. In fact, gases with high boiling points have greater attractions towards the liquid molecules, as indicated in Table B.14.

Table B.14: Solubilities of various gases in a perfluorohexane (PP1) at 298 K and 1 atm[342]

Expressed as mL of gas per 100g of liquid at 25 °C, 1 atm		
Gas	Solubility	Gas Boiling Point (°C)
He	6.6	-272
H_2	10.7	-259
N_2	26.3	-210
CO	26.3	-192
Ar	39.8	-186
O_2	41.0	-183
CO_2	156.0	-78
SF_6	167.0	-64
C_2H_6	263.0	-89
Cl_2	781.0	-35

Table B.15 shows the solubilities of different gases in one of the perfluorocarbon liquids (PP5) made by FLUTEC INC., and again this perfluorocarbon shows a large selectivity toward CO_2 when compared with other gases, such as H_2, CO, and N_2.

Table B.15: Solubilities of various gases in a typical FLUTEC™ (Perfluorodecalin (PP5)) liquid at 298 K and 1 atm[343]

Expressed as mL of gas per 100g of liquid at 25°C, 1 atm	
Gas	Solubility
He	3.9
H_2	6.3
N_2	15.6
CO	17.1
Ar	23.7
O_2	24.4
CO_2	93
SF_6	99
C_2H_6	156
Cl_2	463

* Ozone figures were for 6 wt% in oxygen in the gas phase; the actual solubility is likely to be significantly higher

Table B.16 compares the solubility of different gases in different perfluorocarbon liquids. The solubility of each gas decreases as the molecular weight, liquid viscosity and density increase (see Table B.19). Increasing such physical properties decreases the space between the fluorine atoms and thus fewer gaps are available to accommodate CO_2, leading to lower solubility as shown in Table B.16.

Table B.16: Solubility of different gases in perfluorocarbon liquids at 298 K and 1 atm[204]

Gas solubility, mL(gas)/100 g (liquid) at 25 °C and 1 atm					
Gas	FLUTEC Liquid				
	Perfluoro hexane	Perfluoromethyl -cyclohexane	Perfluoro-1,3-dimethyl-cyclohexane	Perfluoro decalin	Perfluoro methyldecalin
	C_6F_{14}	C_7F_{14}	C_8F_{16}	$C_{10}F_{18}$	$C_{11}F_{20}$
	PP1	PP2	PP3	PP6	PP9
He	6.6	5.5	4.6	3.9	3.4
H_2	10.7	9.0	7.4	6.3	5.6
N_2	26.3	22.0	18.3	15.6	13.8
CO	26.3	24.2	20.0	17.1	15.0
Ar	39.8	33.5	27.7	23.7	20.0
O_2	41.0	34.6	28.6	24.4	22.0
CO_2	156.0	132.0	109.0	93.0	82.0
SF_6	167	140	116	99	87
C_2H_6	263	221	183	156	138
C_3H_8	5.9	-	-	-	-
Cl_2	781	657	542	463	408
F_2	44	-	-	-	-
O_3*	7.8	7.4	-	6.3	6.3

* Ozone figures were for 6 wt.% in oxygen in the gas phase; the actual solubility is likely to be significantly higher

In Table B.17, the solubilities of several gases in fluorocarbons at 1 atm are listed; and it is important to mention that the solubility of CO_2 is almost one order of magnitude greater than those of the other listed gases in fluorocarbons.

Table B.17: Solubility of gases in fluorocarbons at 1 atm gas pressure[344]

1 atm, 25 °C		
Solvent	Gas	$10^4 \times x_2$
$n\text{-}C_7F_{16}$	He	8.90
	H_2	14.2
	Ar	53.0
	N_2	39.1
	O_2	55.3
	CO	38.8
	CO_2	208.8
	C_2H_6	0.203
$C_6F_{11}\text{-}CF_3$	N_2	31.8
	Ar	45.9
$C_6F_{10}\text{-}CF_3\text{-}(CF_3)$	N_2	33.0
$(C_4F_9)_3N$	Ar	50.0
Cyclic $C_8F_{16}O$	Air	46.0
	Ar	50.0

In addition, Table B.18 shows that CO_2 has a greater solubility than those of N_2 or O_2 which suggests that perfluorocarbons will selectively absorb CO_2 in larger quantities relative to other gases.

Table B.18: Solubility of Gases in Perfluorocarbon Solvents[344]

Solubility in g/kg						
Liquids	Temperature	Air		O_2	N_2	CO_2
		O_2	N_2			
$n\text{-}C_7F_{16}$	25°C	-	-	0.457	0.283	2.42
FC-80		0.093	0.181	0.361	0.216	1.95
L-1822[345]		0.072	0.158	0.285	0.184	1.55
FC-47		0.072	0.134	0.272	0.174	1.46
$n\text{-}C_7F_{16}$	37°C	-	-	-	-	-
FC-80		0.086	0.171	0.354	0.217	1.61
L-1822		0.065	0.121	0.271	0.162	1.31
FC-47		0.071	0.129	0.276	0.171	1.34

B.6 MANUFACTURE OF PFCS

In recent years, the continuing quest for economical processes aimed at producing high boiling point fluids has achieved considerable success. In fact, high-purity perfluorocarbon liquids are now available, such as Flutec Fluids produced by Rhône-Poulenc Chemicals Ltd., and Multifluor Inert Fluids by Air Products and Chemicals Inc.[205] The Flutec Fluids are produced with large ranges of boiling points which can exceed 260 °C, as shown in Table B.19. It is also important to mention that the availability of Flutec Fluids with various boiling points, has led to the development of new applications of perfluorinated liquids.[346]

The higher-boiling perfluoro-alkanes and cycloalkanes are manufactured either by electrochemical fluorination or by cobalt trifluoride fluorination[347,348] of the corresponding alkanes, alkenes, or aromatic hydrocarbons (C_5–C_{18}). Inherently, electrochemical fluorination (ECF) should be the lower-cost process for the production of the low molecular-weight perfluorocarbon liquids, since it avoids the cost of generating elemental fluorine. The ECF route, on the other hand, has some disadvantages since high reactants purity is required despite the fact that low yield and selectivity, and extensive molecular rearrangement are often obtained. With few recycle steps, however, higher yield and selectivity can be achieved. The cobalt fluoride (CoF_3) process leads to rearrangement of the parent hydrocarbon,[205] but with proper control of the process conditions and careful selection of feed stocks, it is possible to manufacture some perfluorocarbons at the high 99% or even 99.9% purity level (e.g., tracer applications). Owing to the recycle capability of the cobalt fluoride process, it is also economically feasible to reduce trace impurities, such as CH-containing material to extremely low levels (<0.1 ppm w/w).

When comparing C_7 perfluorocarbon samples manufactured by these two industrial processes, perfluoroheptane synthesized by ECF contains generally 70% of C_7F_{14}, whereas 90%

of C_7F_{14} is produced by CoF_3 fluorination. The technical-grade perfluoromethylcyclohexane produced by CoF_3 process for industrial use contains approximately 90% of $C_6F_{11}CF_3$, which can be enhanced to 99% $C_6F_{11}CF_3$ for tracer applications. The manufacture of perfluoroperhydrophenanthrene (Flutec PP11), shown below, is typical of the production of high molecular-weight cyclic perfluorocarbons:

$$C_{14}H_{10} + 17F_2 \xrightarrow{CoF_3, 350^{\circ}C} C_{14}F_{24} + 10HF \tag{B-3}$$

In the finished product, about 85% of the material possesses the phenanthrene skeleton, while the remaining substance contains perfluorobicycloalkanes.

The cobalt trifluoride process used at Rhône-Poulenc Chemicals Ltd. was pioneered in the US by Fowler in the 1940s,[347] developed further in the U.K.,[349] and is now commonly operated in a continuous stirred reactor, as described in the patent literature.[205] Vaporized phenanthrene and fluorine are fed simultaneously to a reactor containing a CoF_2/CoF_3 mixture to produce a perfluorocarbon product which is condensed and separated from the HF byproduct. Physical separation techniques are used to recycle perfluorinated material to the reactor, followed by chemical stabilization steps and drying of the highly perfluorinated material. A similar sequence is used in the ECF process, and the specification of the perfluorocarbon may be modified to meet the physical or chemical requirements of the intended application. It should be emphasized that often physical, thermal, or electrical properties of a final product are more important than its precise chemical composition.

In Table B.19, several physical and thermodynamic properties of Flutec Fluids are summarized. The composition of these fluids may vary during their production; however, this does not constitute a major issue as pure compounds are not required in most of PFCs applications.

Table B.19: Typical Properties of Flutec Fluids[204,205]

	PP50	PP1C	PP1	PP2	PP3	PP5/6	PP7/9	PP10	PP11	PP24	PP25
Molecular Formula	C_5F_{12}	C_6F_{12}	C_6F_{14}	C_7F_{14}	C_7F_{14}/ C_8F_{16}	$C_{10}F_{18}$	$C_{10}F_{18}$/ $C_{11}F_{20}$	$C_{13}F_{22}$	$C_{14}F_{24}$	$C_{16}F_{26}$	$C_{17}F_{30}$
Main molecular species	Perfluoropentanes	Perfluoro (methylcyclopentanes)	Perfluorohexanes	Perfluoro (methylcyclohexane)	Perfluoro(methyl/dimethylcyclohexanes)	Perfluorodecalin (*cis*- and *trans*- isomers)	Perfluoro(decalin/methyldecalin) (*cis*- and *trans*- isomers)	Perfluoroperhydrofluorene	Perfluoroperhydro phenanthrene	Perfluoroperhydro fluoranthene	Perfluoro (cyclohexylmethyldecalin)
Molecular Weight	288	300	338	350	400	462	512	574	624	686	774
Density (kg.m^{-3})	1604	1707	1682	1788	1828	1917	1972	1984	2030	2052	2049
Boiling Point (°C) at 1 atm	29	48	5	76	102	142	160	194	215	244	260
Pour Point (°C)	-120	-70	-90	-30	-70	-8	-70	-40	-20	0	-10
Viscosity (kinematic) (mm^2.s^{-1})	0.29	0.615	0.39	0.873	1.06	2.66	3.25	4.84	14.0	15.3	56.1
Viscosity (dynamic) (mPa.s)	0.465	1.049	0.656	1.561	1.919	5.10	6.41	9.58	28.4	31.5	114.5
Surface Tension (mN.m^{-1})	9.4	12.6	11.1	15.4	16.6	17.6	18.5	19.7	19	22.2	-
Vapor Pressure (mbar)	862	368	294	141	48	8.8	2.9	<1	<1	<1	<1
Heat of Vaporization at Boiling Point (kJ.kg^{-1})	90.8	75.8*	85.5	85.9	82.9	78.7	75.5	71*	68*	65.8*	67.9*
Specific Heat (kJ.kg^{-1}.°C^{-1})	1.05	0.878*	1.09	0.963	0.963	1.05	1.09	0.92*	1.07*	0.93*	0.957*
Critical Temperature (°C)	148.7	180.8*	177.9	212.8	241.5	292.0	313.4	357.2*	377*	388.7*	400.4*
Critical Pressure (bar)	20.48	22.64*	18.34	20.19	18.81	17.52	16.60	16.2*	14.6*	15.1*	11.34*
Critical Volume (L.kg^{-1})	1.626	1.567*	1.582	1.522	1.520	1.521	1.500	1.59*	1.58*	1.606*	1.574*
Thermal Conductivity (mW.m^{-1}.°C^{-1})	64.0	66.4*	65.3	59.9	60.4	57.0	57.5	56*	52.6*	64.6*	63.8*
Coefficient of Expansion at 0 °C	0.00189	0.00167	0.00159	0.00138	0.00123	0.00104	0.00095	0.00078	0.00075	0.00078	0.00084
Coefficient of Expansion at bp	0.00213	-	0.00205	0.00190	0.00178	0.00170	0.00167	-	-	-	-
Refractive Index n^{20}_D	1.2383	1.2650	1.2509	1.2781	1.2895	1.3130	1.3195	1.3289	1.3348	1.3462	1.3376

*Estimated Value

B.7 APPLICATIONS OF PFCS

The perfluorocarbon liquids are predominantly used as an alternative to chlorofluorocarbons (CFC). The continuing trend for size/cost reduction in electronics and electrical industries leads to higher packing densities of energy-dissipating devices, and therefore more effective heat removal systems are required. This has been successfully achieved in many cases by direct liquid cooling, where l,1,2-trichloro-1,2,2-trifluoroethane (CFC-113) has been used extensively.[303] This situation, however, is beginning to change since CFC-113 is implicated in stratospheric ozone depletion. Thus, perfluorocarbons are now being studied and used for larger volume applications, e.g., in distribution transformers and large voltage regulators. Since the heat transfer during boiling increases with pressure, in a hermetically sealed system the vapor pressure and temperature of CFC-113 (boiling point 47.6 °C at 1 atm) minimize the possibility of thermal damage and provide good heat transfer. This particular characteristic is being investigated for the prospect of using perfluorocarbons as alternative coolants. More specifically, the following two important parameters which are required to efficiently optimize the heat removal, are being studied: (1) the critical heat flux as a function of saturated boiling temperature (this affects the size and cost of a device), and (2) the temperature difference between the heat emitting surface and the liquid coolant.

Refrigeration applications operating in the -20 to -40°C temperature range have increasingly used R-502, which is an azeotropic mixture of R-22 (CF_2HCl) and R-115 (C_2F_5Cl), rather than R-22 alone. The high halogen content of R-115 results in extra thermal capacity benefits, which decrease the temperature of compression and improve the energy efficiency.

Unfortunately, R-115 is being banned because of its ozone-depleting effects, and finding a substitute for R-502 has been so far difficult. It is, however, possible to use perfluoropropane (R-218) instead of R-115 and obtain similar temperature-reduction benefits, without the ozone-depletion problem. Nonetheless, some loss of efficiency occurs, which can usually be overcome by adding a minor proportion of propane as a third ingredient.[350] The ternary mixture has better properties than R-502 and is being commercialized as Isceon 69-L by Rhône-Poulenc Chemicals Ltd., as an interim solution. Although this mixture has a much reduced ozone-depletion potential, R-22 is not yet regarded as an acceptable refrigerant for a long term.

From a technical viewpoint, perfluorocarbons are ideal candidates for all types of fluid cooled transformers, but such applications have been limited to those which justify the high cost of the fluid, like mobile radar. In the past, non-flammability in transformers for the general distribution of electrical power has been achieved using liquids such as polychlorinated biphenyl/trichlorobenzene blends (PCB), perchloroethylene, and 1,1,2-trichloro-l,2,2-trifluoroethane (CFC-113). PCBs and CFC-113 have become environmentally unacceptable, and perchloroethylene is receiving increasingly adverse comments regarding its possible carcinogenicity and accumulation in various natural lipids.[205]

The capacitors have inevitably been included in the modern electronics trend to reduce component size, preferably without compromising performance. Liquid impregnated capacitors play a significant role in achieving such objectives, and perfluorocarbons are particularly effective because they have all the desirable properties, except low permittivity (1.8–2) when compared with that of other organic capacitor impregnants (3–5.5). Hence, a low relative permittivity would be expected to give a low energy storage for an equivalent potential on the capacitor surfaces.[205] The properties of perfluorocarbons, however, allowed to overcome this defect, since the capacitors made at Sandia Laboratories have considerably improved energy density and reliability when compared with those impregnated with hydrocarbon or silicone.[205] The devices were operated at near-atmospheric pressures, where perfluorocarbon vapors have high enough dielectric strength to reduce the likelihood of electrical breakdown caused by gas bubbles formed during ebullition. Other properties of the perfluorocarbons, such as low liquid surface tension and viscosity, are critical in efficiently wetting and impregnating the capacitor windings. A typical performance improvement is the increase of pulses before failure from about 10^6 to 10^8 at electrical stress levels, which corresponds to about three times those possible with silicone or hydrocarbon impregnants.[184] The fluids used were based on perfluorotributylamine and perfluorohexanes. Other perfluorocarbons are also obvious candidates, such as perfluoro(methylcyclohexane) and perfluoro(1,3-dimethylcyclohexane), as they have some of the highest vapor dielectric strengths known.[351]

The effectiveness of perfluorocarbons as fire-extinguishing agents has also been known,[352] but they were historically dismissed in favor of Halon-1211 (CF_2ClBr) and Halon-1301 (CF_3Br) for efficiency/cost ratio purposes. Halon-1301 is exceptional in being the only material usable in enclosed spaces where humans are present, as it is used on oil platforms, in aircraft, etc. Finding an alternative to Halon-1301 has been difficult, however, the very low toxicities of perfluorocarbons will allow their use in human-occupied enclosed situations, and work is in progress to assess their suitability.[353] One major drawback, which is being thoroughly studied, is the tendency of some perfluorocarbons to form toxic perfluoroisobutene under extremely high temperatures.[184]

Perfluorocarbon ethers combine the usual inert, nonflammable characteristics of perfluorocarbons with exceptionally low vapor pressures. Consequently, these fluids have become extensively used as lubricants, both in high vacuum and oxygen handling technologies.[354] Examples of such applications include handling of corrosive halogen compounds and lubrication of high-temperature heat pumps. In certain other applications, however, limitations occur due to the formation of Lewis acids, causing a chemical degradation at the C–O–C linkage, and in order to overcome such limitations, the use of compounds containing only carbon and fluorine (i.e. perfluorocarbons) is being considered.

Because of the volatility of perfluorocarbon lubricants, the low boiling point compounds can only be used under hermetically sealed conditions. It should be mentioned; however, those lubricants with boiling points of ≥ 250 °C should have sufficiently low vapor pressures for open lubrication of glands, valves, etc. Perfluorocarbon ethers could also be suitable for greases which incorporate low molecular-weight fluorocarbon polymers as thickening agents.

Three Flutec perfluorocarbons containing no additives were tested for boundary lubrication properties and compared with those of an ISO 10 mineral oil (contains performance-enhancing additives). Although both fluids have approximately equivalent viscosity,[205] the perfluorocarbons required a greater load than the mineral oil to cause both initial seizure and weld. At equivalent loads, the temperatures reached with the perfluorocarbons were higher those with mineral oil, indicating an increased tendency for mild wear, however, this disadvantage can be overcome by including additives or modifying the viscosity of the perfluorocarbons.[205]

B.8 PERFLUOROCARBONS SUMMARY

The attractive properties of the perfluorocarbons (PFCs) make them a potential alternative to current physical solvents being used to capture CO_2 in commercial acid gas removal (AGR) processes, such as methanol (Rectisol) and dimethylethers of polyethylene glycol (Selexol). The perfluorinated liquids can be selected for potentially capturing CO_2, at elevated temperatures and pressures, from fuel gas based on the following properties: (1) CO_2 displays much higher solubility in perfluorinated compounds than in the corresponding hydrocarbons, about twice as much;[203] (2) Perfluorinated liquids are extremely chemically and thermally stable, due to the high energy of C–F bond; (3) Perfluorinated liquids vapor pressure is extremely low, and therefore solvent losses are minimum; (4) Perfluorinated liquids have typically a relatively low viscosity, which could minimize the pumping and re-circulation costs of solvents; and (5) Perfluorinated liquids are non-toxic and completely safe under high pressure and temperature conditions. Some of the drawbacks of perfluorinated liquids include, high cost, and physical absorption of other gases (light hydrocarbons) along with CO_2.

APPENDIX C

EXPERIMENTAL PRESSURE VERSUS TIME PLOT FOR CO_2 ABSORPTION IN PP25

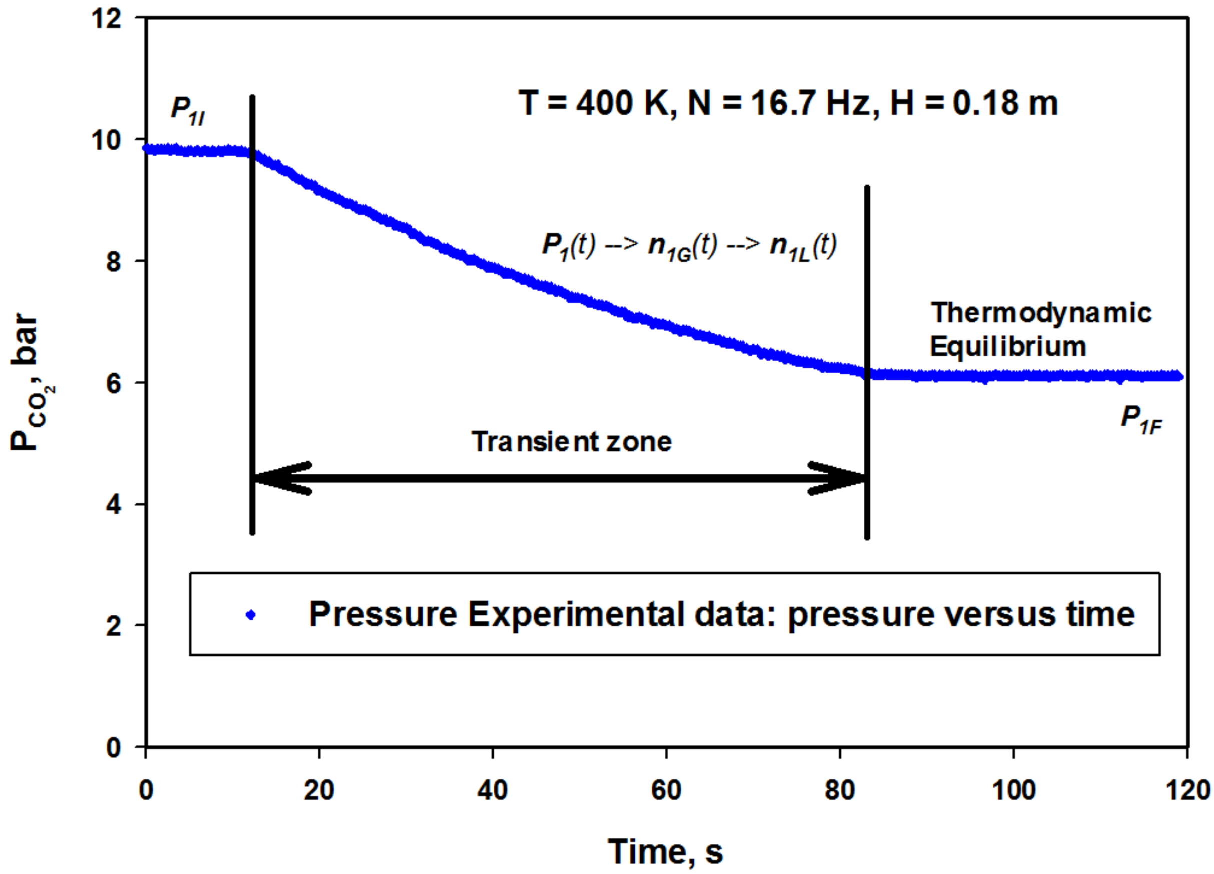

Figure C.1: Typical pressure versus time data plot

APPENDIX D

PREDICTED SOLUBILITIES OF GASES IN PP25 AS A FUNCTION OF PRESSURE AND TEMPERATURE USING ASPEN PLUS, EMPLOYING P-R EOS

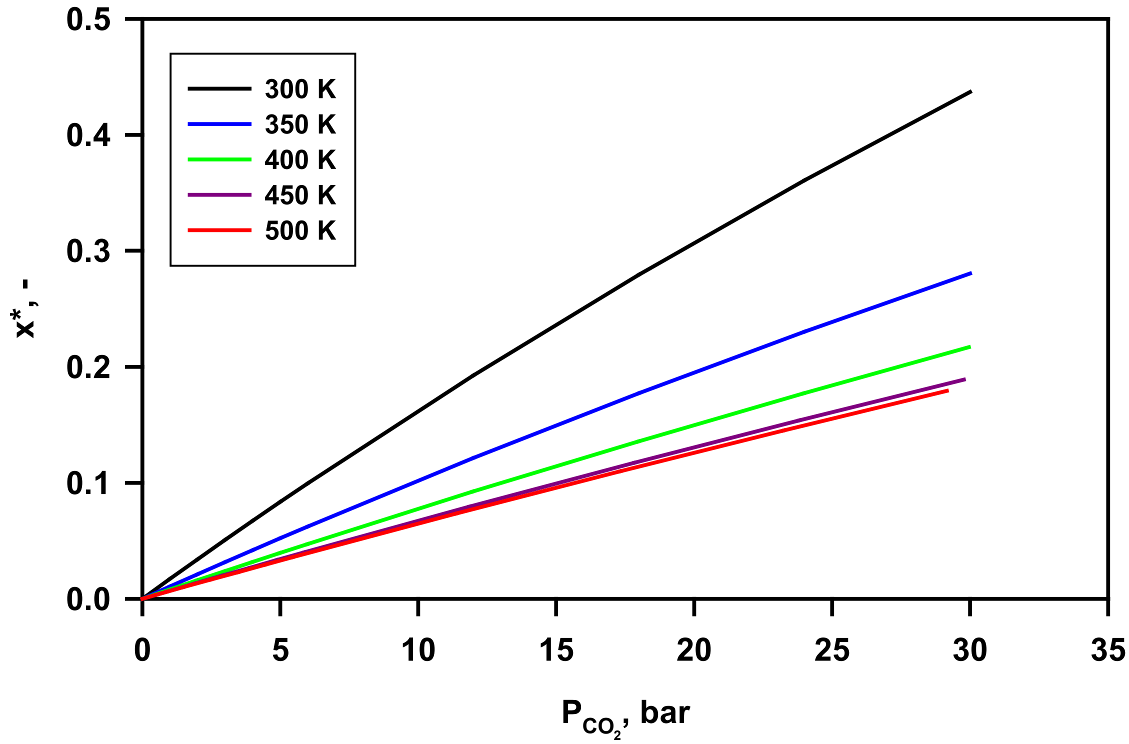

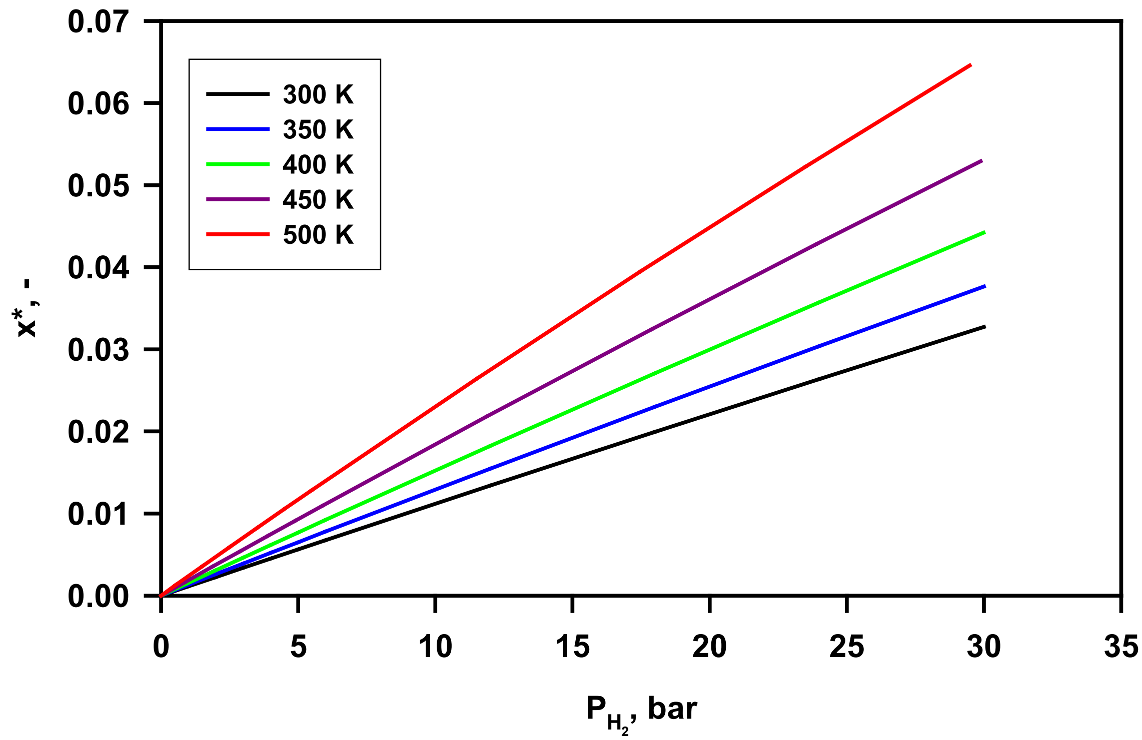

Figure D.1: Solubilities of CO_2 and H_2 in PP25 (Predicted using Aspen Plus version 24.0)

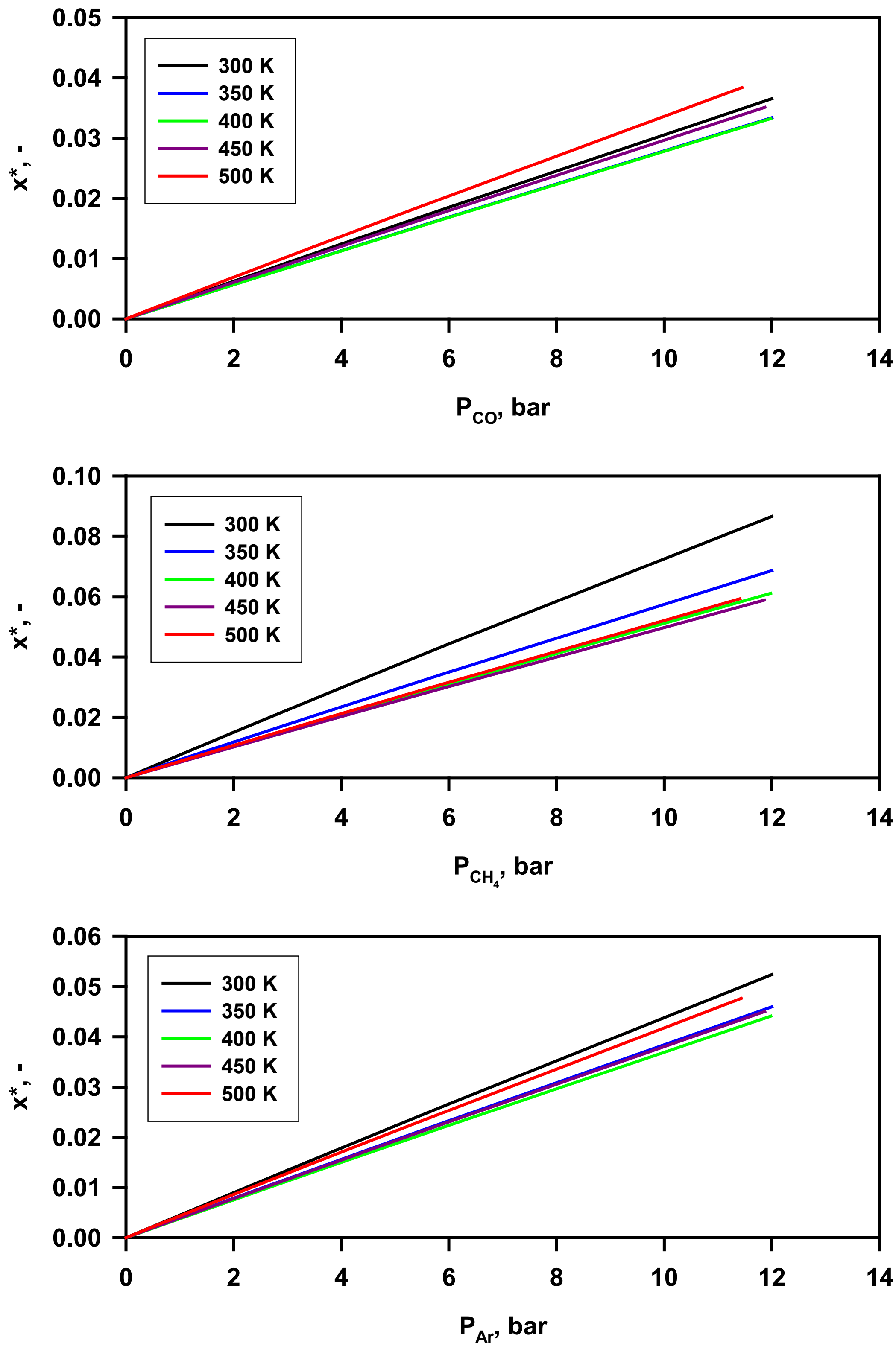

Figure D.2: Solubilities of CO, CH_4, Ar in PP25 (Predicted using Aspen Plus version 24.0)

APPENDIX E

ASPEN PLUS DETAILED SCHEMATIC OF THE CONCEPTUAL DESIGN PROCESS FOR CO_2 CAPTURE USING IONIC LIQUIDS

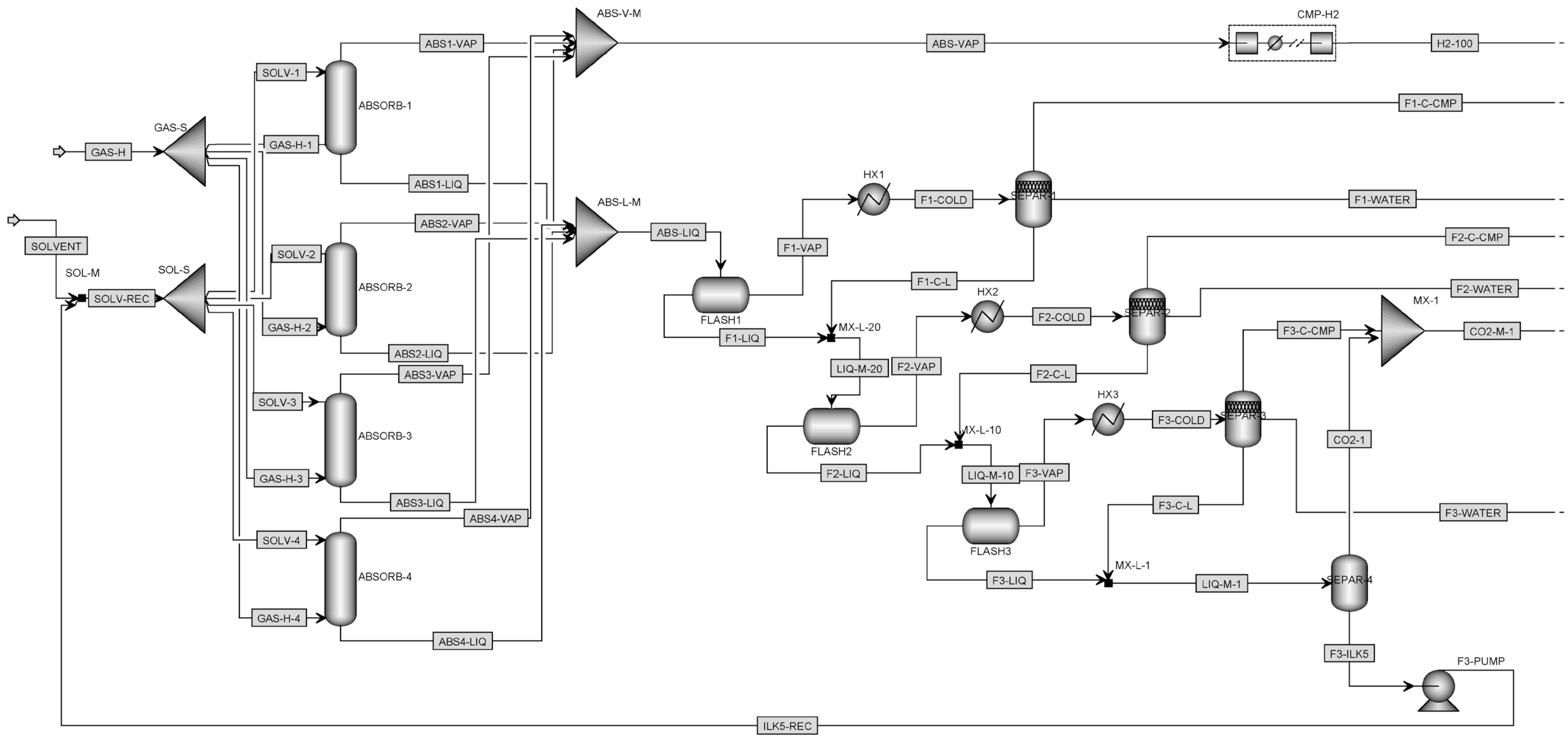

Figure E.1: Conceptual design schematic (part 1: absorber and flash units)

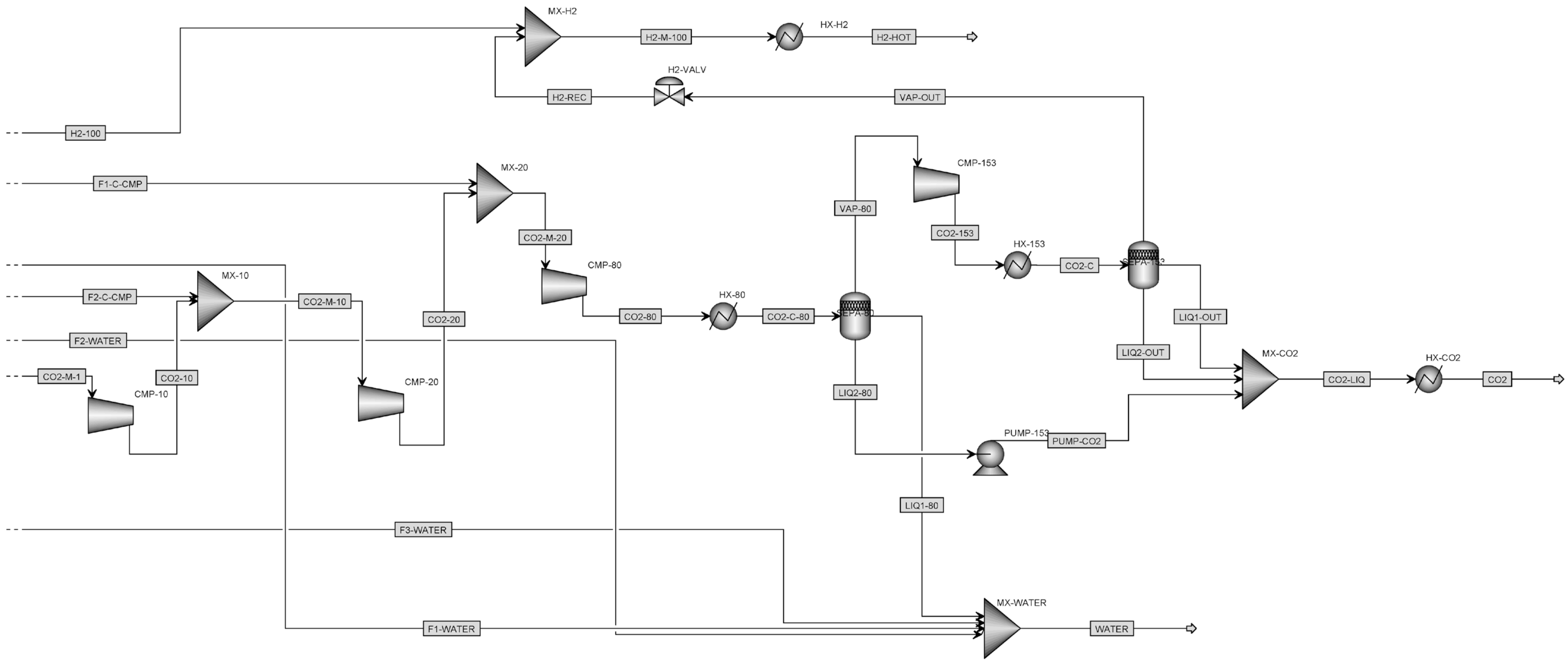

Figure E.2: Conceptual design schematic (part 2: CO_2 compression and CO_2/H_2 separation)

BIBLIOGRAPHY

1. Ratafia-Brown, J. A.; Manfredo, L. M.; Hoffmann, J. W.; Ramezan, M.; Stiegel, G. J. In *An Environmental Assessment of IGCC Power Systems*, Proceedings - 19th Annual International Pittsburgh Coal Conference, Pittsburgh, PA, September 23 - 27, 2002; Pittsburgh, PA, 2002; pp 235-250.

2. White, C. M.; Strazisar, B. R.; Granite, E. J.; Hoffman, J. S.; Pennline, H. W., Separation and capture of CO_2 from large stationary sources and sequestration in geological formations-coalbeds and deep saline aquifers. *Journal of the Air and Waste Management Association* **2003,** 53 (6), 645-715.

3. Vidaurri, J.; Larsen, R.; Martin, J.; Looker, M.; Gebhard, S.; Srinivas, G. In *Multicontaminant Warm Gas Cleanup*, Proceedings - 24th Annual International Pittsburgh Coal Conference, Johannesburg, South Africa, September 10 – 14, 2007; Johannesburg, South Africa, 2007; pp 194/1-194/14.

4. Korens, N.; Simbeck, D. R.; Wilhelm, D. J.; Longanbach, J. R.; Stiegel, G. J. *Process Screening Analysis of Alternative Gas Treating and Sulfur Removal for Gasification: Revised Final Report*; SFA Pacific, Inc., Mountain View, CA, U.S. Department of Energy, National Energy Technology Laboratory, Pittsburgh, PA, Task Order No. 739656-00100: December 2002.

5. Gielen, D. In *The Energy Policy Consequences of Future CO_2 Capture and Sequestration Technologies*, Paper prepared for the 2nd Annual Conference on Carbon Sequestration: Developing & Validating the Technology Base to Reduce Carbon Intensity, Alexandria, VA, May 5-8, 2003; Alexandria, VA, 2003.

6. Klara, J. M.; Woods, M. C.; Capicotto, P. J.; Haslbeck, J. L.; Kuehn, N. J.; Matuszewski, M.; Pinkerton, L. L.; Rutkowski, M. D.; Schoff, R. L.; Vaysman, V. *Cost and Performance Baseline for Fossil Energy Plants, Volume 1: Bituminous Coal and Natural Gas to Electricity*; National Energy Technology Laboratory, US Department of Energy, Research and Development Solutions, LLC (RDS): Revision 1, August 2007.

7. Stiegel, G. J. *Gasification - Versatile Solutions*; National Energy Technology Laboratory, US Department of Energy: Version O, October 10, 2007.

8. Hochgesand, G., Rectisol and Purisol. *Industrial and Engineering Chemistry* **1970,** 62 (7), 37-43.

9. Raney, D. R., Remove Carbon Dioxide with Selexol. *Hydrocarbon Processing, International Edition* **1976,** 55 (4), 73-75.

10. McKetta, J. J.; Executive Editor; Weismantel, G. E.; Associate Editor, Solvent Selection. In *Encyclopedia of Chemical Processing and Design, Volume 52*, Marcel Dekker Inc.: New York, 1995; Vol. 52, pp 458-472.

11. Kolbe, B.; Menzel, J., Modelling phase equilibria and related physical properties for the Morphysorb process. *Proceedings, Annual Convention - Gas Processors Association* **2000,** 79th, 103-112.

12. Kolbe, B.; Menzel, J.; Gross, M., Acid gas removal. *Hydrocarbon Engineering* **2000,** 5 (5), 71-72,74.

13. Bendall, E.; Aiken, R. C.; Mandas, F., Selective Absorption of H_2S from Larger Quantities of CO_2 by Absorption and Reaction in Fine Sprays. *AIChE Journal* **1983,** 29 (1), 66-72.

14. Bucklin, R. W.; Schendel, R. L., Comparison of Physical Solvents Used for Gas Processing. In *Acid and Sour Gas Treating Processes*, Newman, S. A., Ed. 1985; pp 42-79.

15. Isaacs, E. E.; Otto, F. D.; Mather, A. E., Solubility of hydrogen sulfide and carbon dioxide in propylene carbonate solvent. *The Canadian Journal of Chemical Engineering* **1977,** 55 (6), 751-752.

16. Shah, V. A., Carbon dioxide removal from ammonia synthesis gas with Selexol solvent process. *Energy Progress* **1988,** 8 (2), 67-70.

17. Itoh, J.; Dow Chemical Japan Ltd. In *Chemical & Physical Absorption of CO_2*, RITE International Seminar, January 14, 2005, 2005; 2005.

18. Tatterson, G. B., *Scaleup and Design of Industrial Mixing Processes*. McGraw-Hill Inc.: New York, 1994.

19. Martin, G. Q., Gas-Inducing Agitator. *Industrial and Engineering Chemistry Process Design and Development* **1972,** 11 (3), 397-404.

20. Joshi, J. B.; Sharma, M. M., Mass Transfer and Hydrodynamic Characteristics of Gas Inducing Type of Agitated Contactors. *The Canadian Journal of Chemical Engineering* **1977,** 55 (6), 683-695.

21. Sawant, S. B.; Joshi, J. B., Critical Impeller Speed for the Onset of Gas Induction in Gas-Inducing Types of Agitated Contactors. *The Chemical Engineering Journal* **1979,** 18 (1), 87-91.

22. Zundelevich, Y., Power Consumption and Gas Capacity of Self-Inducting Turbo Aerators. *AIChE Journal* **1979,** 25 (5), 763-773.

23. Aldrich, C.; van Deventer, J. S. J., Modeling of Induced Aeration in Turbine Aerators by Use of Radial Basis Function Neural Networks. *The Canadian Journal of Chemical Engineering* **1995,** 73 (6), 808-816.

24. Heim, A.; Kraslawski, A.; Rzyski, E.; Stelmach, J., Aeration of Bioreactors by Self-Aspirating Impellers. *Chemical Engineering Journal* **1995,** 58 (1), 59-63.

25. Hsu, Y.-C.; Huang, K.-F., Effects of Geometrical Factors on Liquid Mixing in a Gas-Induced Agitated Tank. *Journal of Chemical Technology and Biotechnology* **1997,** 68 (2), 222-228.

26. Hsu, Y.-C.; Huang, C.-J.; Peng, R. Y., Onset of Gas Induction, Power Consumption Gas Holdup and Mass Transfer in a New Gas-Induced Reactor. *Chemical Engineering Science* **1997,** 52 (21-22), 3883-3891.

27. Hsu, Y.-C.; Huang, C.-J.; Yen, W.-H.; Peng, R. Y., Onset of Gas Induction and Power Consumption in an Agitated Tank having Shortened Narrower Baffles. *Journal of Chemical Technology and Biotechnology* **1998,** 71 (3), 187-196.

28. Aldrich, C.; van Deventer, J. S. J., Observations on the Effect of Medium Density and Viscosity on the Rate of Induced Aeration in Agitated Vessels. *Metallurgical Transactions. B, Process Metallurgy* **1994,** 25 (2), 303-306.

29. Patwardhan, A. W.; Joshi, J. B., Design of Gas-Inducing Reactors. *Industrial and Engineering Chemistry Research* **1999,** 38 (1), 49-80.

30. Forrester, S. E.; Rielly, C. D.; Carpenter, K. J., Gas-Inducing Impeller Design and Performance Characteristics. *Chemical Engineering Science* **1998,** 53 (4), 603-615.

31. Zlokarnik, M., Hollow stirrers for gassing of liquids. Determination of gas diffusion and wave performance. *Chemie Ingenieur Technik* **1966,** 38 (3), 357-366.

32. Zlokarnik, M.; Judat, H., Tube- and Disk-Stirrers. Two Efficient Stirrers for the Gassing of Liquids. *Chemie Ingenieur Technik* **1967,** 39 (20), 1163-1168.

33. Topiwala, H. H.; Hamer, G., Mass transfer and dispersion properties in a fermenter with a gas-inducing impeller. *Transactions of the Institution of Chemical Engineers* **1974,** 52 (2), 113-120.

34. White, D. A.; de Villiers, J. U., Rates of induced aeration in agitated vessels. *The Chemical Engineering Journal* **1977,** 14 (2), 113-117.

35. Sawant, S. B.; Joshi, J. B.; Pangarkar, V. G., Mass Transfer and Hydrodynamic Characteristics of the Wemco Type Flotation Cell. *Indian Chemical Engineer* **1980,** 22 (4), 3-10.

36. Sawant, S. B.; Joshi, J. B.; Pangarkar, V. G.; Mhaskar, R. D., Mass Transfer Transfer and Hydrodynamic Characteristics of the Denver Type of Flotation Cells. *The Chemical Engineering Journal (Amsterdam, Netherlands)* **1981,** 21 (1), 11-19.

37. Joshi, J. B.; Pandit, A. B.; Sharma, M. M., Mechanically Agitated Gas-Liquid Reactors. *Chemical Engineering Science* **1982,** 37 (6), 813-844.

38. Raidoo, A. D.; Rao, K. S. M. S. R.; Sawant, S. B.; Joshi, J. B., Improvements in gas inducing impeller design. *Chemical Engineering Communications* **1987,** 54 (1-6), 241-264.

39. Chang, M.-Y. Mass Transfer Characteristics of Gases in Aqueous and Organic Liquids at Elevated Pressures and Temperatures in Agitated Reactors. Unpublished Ph.D Dissertation, University of Pittsburgh, Pittsburgh, 1991.

40. He, D.-X.; Chiang, S.-H.; Klinzing, G. E., Operating Characteristics of a Gas/Liquid Contactor using Gas-Inducing Turbine. *Journal of the Chinese Institute of Chemical Engineers* **1991,** 22 (6), 321-328.

41. Rielly, C. D.; Evans, G. M.; Davidson, J. F.; Carpenter, K. J., Effect of vessel scaleup on the hydrodynamics of a self-aerating concave blade impeller. *Chemical Engineering Science* **1992,** 47 (13-14), 3395-3402.

42. Aldrich, C.; van Deventer, J. S. J., Observations on Induced Aeration in Agitated Slurries. *The Chemical Engineering Journal* **1994,** 54 (3), 199-205.

43. Saravanan, K.; Mundale, V. D.; Joshi, J. B., Gas Inducing Type Mechanically Agitated Contactors. *Industrial and Engineering Chemistry Research* **1994,** 33 (9), 2226-2241.

44. Al Taweel, A. M.; Cheng, Y. H., Effect of Surface Tension on Gas/Liquid Contacting in a Mechanically-Agitated Tank with Stator. *Chemical Engineering Research and Design* **1995,** 73 (A6), 654-660.

45. Hsu, Y.-C.; Huang, C.-J., Characteristics of a New Gas-Induced Reactor. *AIChE Journal* **1996,** 42 (11), 3146-3152.

46. Saravanan, K.; Joshi, J. B., Fractional Gas Hold-up in Gas Inducing Type of Mechanically Agitated Contactors. *The Canadian Journal of Chemical Engineering* **1996,** 74 (1), 16-30.

47. Patwardhan, A. W.; Joshi, J. B., Hydrodynamics of a Stirred Vessel Equipped with a Gas-Inducing Impeller. *Industrial and Engineering Chemistry Research* **1997,** 36 (9), 3904-3914.

48. Tekie, Z. Mass Transfer and Modeling of Liquid-phase Cyclohexane Oxidation Process in Agitated Reactors. Unpublished Ph.D. Dissertation, University of Pittsburgh, Pittsburgh, 1997.

49. Patwardhan, A. W.; Joshi, J. B., Design of Stirred Vessels with Gas Entrained from Free Liquid Surface. *The Canadian Journal of Chemical Engineering* **1998,** 76 (3), 339-364.

50. Patil, S. S.; Joshi, J., Stability of gas-inducing type impellers. *The Canadian Journal of Chemical Engineering* **1999,** 77 (5), 793-803.

51. Fillion, B. Modeling of Soybean Oil Hydrogenation Process. Unpublished Ph.D. Dissertation, University of Pittsburgh, Pittsburgh, 2001.

52. Lemoine, R. Hydrodynamics, Mass Transfer and Modeling of the Toluene Oxidation Process. Unpublished Ph.D. Thesis, University of Pittsburgh, Pittsburgh, 2005.

53. Lemoine, R.; Morsi, B. I., Hydrodynamic and Mass Transfer Parameters in Agitated Reactors Part II: Gas-Holdup, Sauter Mean Bubble Diameters, Volumetric Mass Transfer Coefficients, Gas-Liquid Interfacial Areas, and Liquid-Side Mass Transfer Coefficients. *International Journal of Chemical Reactor Engineering* **2005,** 3 (A20), 1-49.

54. Evans, G. M.; Rielly, C. D.; Davidson, J. F.; Carpenter, K. J., A Fundamental Study of Gas-Inducing Impeller Design. *Institution of Chemical Engineers Symposium Series* **1990,** 121 (Fluid Mixing 4), 137-152.

55. Evans, G. M.; Rielly, C. D.; Davidson, J. F.; Carpenter, K. J. In *Hydrodynamic Characteristics of a Gas-Inducing Impeller*, Proceedings of the 7th European Conference on Mixing, (Kiav, Brugge, Sept. 18-20, Belgium, 1991), 1992; 1992; pp 515-523.

56. Clark, M. W.; Vermeulen, T., Incipient Vortex Formation in Baffled Agitated Vessels. *AIChE Journal* **1964,** 10 (3), 420-422.

57. Barigou, M.; Greaves, M., Bubble-Size Distributions in a Mechanically Agitated Gas-Liquid Contactor. *Chemical Engineering Science* **1992,** 47 (8), 2009-2025.

58. Parthasarathy, R.; Ahmed, N., Sauter Mean and Maximum Bubble Diameters in Aerated Stirred Vessels. *Chemical Engineering Research and Design* **1994,** 72 (A4), 565-572.

59. Parthasarathy, R.; Ahmed, N., Sauter Mean and Maximum Bubble Diameter in Aerated Stirred Vessels (Erratum to Chemical Engineering Research and Design, 1994, Vol. 72(A4), pp. 565-572). *Chemical Engineering Research and Design* **1995,** 73 (A1), 93.

60. Deckwer, W. D.; Louisi, Y.; Zaldi, A.; Ralek, M., Hydrodynamic Properties of the Fischer-Tropsch Slurry Process. *Industrial and Engineering Chemistry Process Design and Development* **1980,** 19 (4), 699-708.

61. Grund, G.; Schumpe, A.; Deckwer, W.-D., Gas-Liquid mass transfer in a bubble column with organic liquids. *Chemical Engineering Science* **1992,** 47 (13-14), 3509-3516.

62. Sarrafi, A.; Müller-Steinhagen, H.; Smith, J. M.; Jamialahmadi, M., Gas holdup in homogeneous and heterogeneous gas-liquid bubble column reactors. *The Canadian Journal of Chemical Engineering* **1999,** 77 (1), 11-21.

63. Bouaifi, M.; Hebrard, G.; Bastoul, D.; Roustan, M., A comparative study of gas hold-up, bubble size, interfacial area and mass transfer coefficients in stirred gas-liquid reactors and bubble columns. *Chemical Engineering and Processing* **2001,** 40 (2), 97-111.

64. Moustiri, S.; Hebrard, G.; Thakre, S. S.; Roustan, M., A unified correlation for predicting liquid axial dispersion coefficient in bubble columns. *Chemical Engineering Science* **2001,** 56 (3), 1041-1047.

65. Pohorecki, R.; Moniuk, W.; Zdrojkowski, A.; Bielski, P., Hydrodynamics of a pilot plant bubble column under elevated temperature and pressure. *Chemical Engineering Science* **2001,** 56 (3), 1167-1174.

66. Jiang, P.; Lin, T.-J.; Luo, X.; Fan, L.-S., Flow visualization of high pressure (21 MPa) bubble column: bubble characteristics. *Chemical Engineering Research and Design* **1995,** 73 (A3), 269-274.

67. Krishna, R.; Urseanu, M. I.; van Baten, J. M.; Ellenberger, J., Rise velocity of a swarm of large gas bubbles in liquids. *Chemical Engineering Science* **1999,** 54 (2), 171-183.

68. Wilkinson, P. M.; Haringa, H.; Van Dierendonck, L. L., Mass transfer and bubble size in a bubble column under pressure. *Chemical Engineering Science* **1994,** 49 (9), 1417-1427.

69. Parthasarathy, R.; Jameson, G. J.; Ahmed, N., Bubble Breakup in Stirred Vessels. Predicting the Sauter Mean Diameter. *Chemical Engineering Research and Design* **1991,** 69 (A4), 295-301.

70. Akita, K.; Yoshida, F., Bubble Size, Interfacial Area, and Liquid-Phase Mass Transfer Coefficient in Bubble Columns. *Industrial and Engineering Chemistry Process Design and Development* **1974,** 13 (1), 84-91.

71. Kasireddy, V. K.; Taweel, A. M. A., Improved Light Attenuation Technique for Measuring Large Interfacial Areas. *The Canadian Journal of Chemical Engineering* **1990,** 68 (4), 690-693.

72. Takahashi, K.; Nienow, A. W., Bubble sizes and coalescence rates in an aerated vessel agitated by a Rushton turbine. *Journal of Chemical Engineering of Japan* **1993,** 26 (5), 536-542.

73. Kawecki, W.; Reith, T.; van Heuven, J. W.; Beek, W. J., Bubble size distribution in the impeller region of a stirred vessel. *Chemical Engineering Science* **1967,** 22 (11), 1519-1523.

74. Lin, T.-J.; Tsuchiya, K.; Fan, L.-S., Bubble Flow Characteristics in Bubble Columns at Elevated Pressure and Temperature. *AIChE Journal* **1998,** 44 (3), 545-560.

75. Calderbank, P. H.; Moo-Young, M. B., The continuous phase heat and mass-transfer properties of dispersions. *Chemical Engineering Science* **1961,** 16 (1-2), 39-54.

76. Calderbank, P. H., Physical Rate Processes in Industrial Fermentation. Part II. Mass Transfer Coefficients in Gas-Liquid Contacting with and without Mechanical Agitation. *Transactions of the Institution of Chemical Engineers* **1959,** 37, 173-185, 186-189.

77. Chang, J.-S.; Harvel, G. D., Determination of gas-liquid bubble column instantaneous interfacial area and void fraction by a real-time neutron radiography method. *Chemical Engineering Science* **1992,** 47 (13-14), 3639-3646.

78. Burgess, J. M.; Calderbank, P. H., The measurement of bubble parameters in two-phase dispersions--I : The development of an improved probe technique. *Chemical Engineering Science* **1975,** 30 (7), 743-750.

79. Soong, Y.; Harke, F. W.; Gamwo, I. K.; Schehl, R. R.; Zarochak, M. F., Hydrodynamic study in a slurry-bubble-column reactor. *Catalysis Today* **1997,** 35 (4), 427-434.

80. Chabot, J.; de Lasa, H. I., Gas holdups and bubble characteristics in a bubble column operated at high temperature. *Industrial and Engineering Chemistry Research* **1993,** 32 (11), 2595-2601.

81. Fukuma, M.; Muroyama, K.; Yasunishi, A., Properties of Bubble Swarm in a Slurry Bubble Column. *Journal of Chemical Engineering of Japan* **1987,** 20 (1), 28-33.

82. Lu, W.-M.; Hsu, R.-C.; Chien, W.-C.; Lin, L.-C., Measurement of local bubble diameters and analysis of gas dispersion in an aerated vessel with disk-turbine impeller. *Journal of Chemical Engineering of Japan* **1993,** 26 (5), 551-557.

83. Pandit, A. B.; Varley, J.; Thorpe, R. B.; Davidson, J. F., Measurement of Bubble Size Distribution: an Acoustic Technique. *Chemical Engineering Science* **1992,** 47 (5), 1079-1089.

84. Sriram, K.; Mann, R., Dynamic gas disengagement: A new technique for assessing the behaviour of bubble columns. *Chemical Engineering Science* **1977,** 32 (6), 571-580.

85. Inga, J. R. Scale Up and Scale Down of Slurry Reactors: a New Methodology. Unpublished Ph.D. Dissertation, University of Pittsburgh, Pittsburgh, 1997.

86. Behkish, A.; Lemoine, R.; Sehabiague, L.; Oukaci, R.; Morsi, B. I., Prediction of the Gas Holdup in Industrial-Scale Bubble Columns and Slurry Bubble Column Reactors Using Back-Propagation Neural Networks. *International Journal of Chemical Reactor Engineering* **2005,** 3 (A53), 1-37.

87. Daly, J. G.; Patel, S. A.; Bukur, D. B., Measurement of gas holdups and sauter mean bubble diameters in bubble column reactors by dynamics gas disengagement method. *Chemical Engineering Science* **1992,** 47 (13-14), 3647-3654.

88. Charpentier, J.-C., Gas-Liquid Reactors. In *ACS Symposium Series*, Washington, D.C., 1978; Vol. 72, pp 223-261.

89. Matsumura, M.; Sakuma, H.; Yamagata, T.; Kobayashi, J., Performance of Oxygen Transfer in a New Gas Entraining Fermentor. *Journal of Fermentation Technology* **1982,** 60 (6), 551-563.

90. Miller, D. N., Scale-Up of Agitated Vessels Gas-Liquid Mass Transfer. *AIChE Journal* **1974,** 20 (3), 445-453.

91. Sridhar, T.; Potter, O. E., Gas Holdup and Bubble Diameters in Pressured Gas-Liquid Stirred Vessels. *Industrial and Engineering Chemistry Fundamentals* **1980,** 19 (1), 21-26.

92. Hughmark, G. A., Power Requirements and Interfacial Area in Gas-Liquid Turbine Agitated Systems. *Industrial and Engineering Chemistry, Process Design and Development* **1980,** 19 (4), 638-641.

93. Vermeulen, T.; Williams, G. M.; Langlois, G. E., Interfacial Area in Liquid-Liquid and Gas-Liquid Agitation. *Chemical Engineering Progress* **1955,** 51, 85F-94F.

94. Calderbank, P. H., Physical Rate Processes in Industrial Fermentation. Part I. The Interfacial Area in Gas-Liquid Contacting with Mechanical Agitation. *Transactions of the Institution of Chemical Engineers* **1958,** 36, 442-459.

95. Fuchs, R.; Ryu, D. D. Y.; Humphrey, A. E., Effect of Surface Aeration on Scale-Up Procedures for Fermentation Processes. *Industrial and Engineering Chemistry Process Design and Development* **1971,** 10 (2), 190-196.

96. Charpentier, J.-C., Mass Transfer Rates in Gas-Liquid Absorbers and Reactors. In *Advances in Chemical Engineering*, Drew, T. B.; Cokelet, G. R.; Hoopes, J. W. J.; Vermeulen, T., Eds. Academic Press: New York, 1981; Vol. 11, pp 1-133.

97. Yoshida, F.; Miura, Y., Gas Absorption in Agitated Gas-Liquid Contactors. Interfacial Area, Gas Holdup, Liquid-Phase Mass Transfer Coefficient, and Reaction Factor. *Industrial and Engineering Chemistry Process Design and Development* **1963,** 2 (4), 263-268.

98. Robinson, C. W.; Wilke, C. R., Simultaneous Measurement of Interfacial Area and Mass Transfer Coefficients for a well-mixed Gas Dispersion in Aqueous Electrolyte Solutions. *AIChE Journal* **1974,** 20 (2), 285-294.

99. Bukur, D. B.; Daly, J. G.; Patel, S. A., Application of ?-ray Attenuation for Measurement of Gas Holdups and Flow Regime Transitions in Bubble Columns. *Industrial and Engineering Chemistry Research* **1996,** 35 (1), 70-80.

100. Kocamustafaogullari, G.; Wang, Z., An experimental study on local interfacial parameters in a horizontal bubbly two-phase flow. *International Journal of Multiphase Flow* **1991,** 17 (5), 553-572.

101. Ram, M. D. Performance of Surface Aerators. Unpublished MS Dissertation, University of Mumbai, Mumbai, India, 1987.

102. Kolte, P. P. Design of Surface Aerators. Unpublished MS Dissertation, University of Mumbai, Mumbai, India, 1988.

103. Matsumura, M.; Masunaga, H.; Haraya, K.; Kobayashi, J., Effect of Gas Entrainment on the Power Requirement and Gas Holdup in an Aerated Stirred Tank. *Journal of Fermentation Technology* **1978,** 56 (2), 128-138.

104. Murugesan, T., Dispersed phase hold-up in mechanically agitated gas-liquid contactors. *Journal of Chemical Technology and Biotechnology* **1998,** 72 (3), 221-226.

105. Loiseau, B.; Midoux, N.; Charpentier, J.-C., Some Hydrodynamics and Power Input Data in Mechanically Agitated Gas-Liquid Contactors. *AIChE Journal* **1977,** 23 (6), 931-935.

106. Rushton, J. H.; Bimbenet, J. J., Holdup and Flooding in Air-Liquid Mixing. *The Canadian Journal of Chemical Engineering* **1968,** 46 (1), 16-21.

107. Reilly, I. G.; Scott, D. S.; De Bruijn, T. J. W.; MacIntyre, D., Role of gas phase momentum is determining gas holdup and hydrodynamic flow regimes in bubble column operations. *The Canadian Journal of Chemical Engineering* **1994,** 72 (1), 3-12.

108. Wichterle, K., Free Level Effect on the Impeller Power Input in Baffled Tanks. *Collection of Czechoslovak Chemical Communications* **1995,** 60 (8), 1274.

109. de Figueiredo, M. M. L.; Calderbank, P. H., The Scale-Up of Aerated Mixing Vessels for Specified Oxygen Dissolution Rates. *Chemical Engineering Science* **1979,** 34 (11), 1333-1338.

110. Westerterp, K. R., Design of Agitators for Gas-Liquid Contacting. *Chemical Engineering Science* **1963,** 18 (8), 495-502.

111. Westerterp, K. R.; van Dierendonck, L. L.; de Kraa, J. A., Interfacial Areas in Agitated Gas-Liquid Contactors. *Chemical Engineering Science* **1963,** 18 (3), 157-176.

112. Takahashi, K.; Nienow, A. W., Effect of gas density on power consumption in aerated vessel agitated by a Rushton turbine. *Journal of Chemical Engineering of Japan* **1992,** 25 (4), 432-434.

113. Van't Riet, K., Review of measuring methods and results in nonviscous gas-liquid mass transfer in stirred vessels. *Industrial and Engineering Chemistry Process Design and Development* **1979,** 18 (3), 357-364.

114. Mann, R., *Gas-Liquid Contacting in Mixing Vessels*. Institution of Chemical Engineers (Great Britain): Rugby, Warwickshire, 1983.

115. Mohammad, A. Gas-Liquid Mass Transfer Parameters in Benzoic Acid Oxidation Process. Unpublished Ph.D. Dissertation, University of Pittsburgh, Pittsburgh, 1999.

116. Chang, M.-Y.; Morsi, B. I., Mass Transfer in a Three-Phase Reactor Operating at Elevated Pressures and Temperatures. *Chemical Engineering Science* **1992,** 47 (7), 1779-1790.

117. Chang, M.-Y.; Eiras, J. G.; Morsi, B. I., Mass Transfer Characteristics of Gases in n-Hexane at Elevated Pressures and Temperatures in Agitated Reactors. *Chemical Engineering and Processing* **1991,** 29 (1), 49-60.

118. Chang, M.-Y.; Morsi, B. I., Mass Transfer Characteristics of Gases in n-Decane at Elevated Pressures and Temperatures in Agitated Reactors. *Chemical Engineering Journal* **1991,** 47 (1), 33-45.

119. Danckwerts, P. V., *Gas-Liquid Reactions*. McGraw-Hill Book Co.: New York, 1970.

120. Sridhar, T.; Potter, O. E., Interfacial Areas in Gas-Liquid Stirred Vessels. *Chemical Engineering Science* **1980,** 35 (3), 683-695.

121. Albal, R. S.; Shah, Y. T.; Carr, N. L.; Bell, A. T., Mass Transfer Coefficients and Solubilities for Hydrogen and Carbon Monoxide under Fischer-Tropsch Conditions. *Chemical Engineering Science* **1984,** 39 (5), 905-907.

122. Mizan, T. I.; Li, J.; Morsi, B. I.; Chang, M.-Y.; Maier, E.; Singh, C. P. P., Solubilities and mass transfer coefficients of gases in liquid propylene in a surface-aeration agitated reactor. *Chemical Engineering Science* **1994,** 49 (6), 821-830.

123. Versteeg, G. F.; Blauwhoff, P. M. M.; van Swaaij, W. P. M., The effect of diffusivity on gas-liquid mass transfer in stirred vessels. Experiments at atmospheric and elevated pressures. *Chemical Engineering Science* **1987,** 42 (5), 1103-1119.

124. Matsumura, M.; Masunaga, H.; Kobayashi, J., A correlation for flow rate of gas entrained from free liquid surface of aerated stirred tank. *Journal of Fermentation Technology* **1977,** 55 (4), 388-400.

125. Kara, M.; Sung, S.; Klinzing, G. E.; Chiang, S.-H., Hydrogen Mass Transfer in Liquid Hdrocarbons at Elevated Temperatures and Pressures. *Fuel* **1983,** 62 (12), 1492-1498.

126. Karandikar, B. M.; Morsi, B. I.; Shah, Y. T.; Carr, N. L., Effect of Water on the Solubilities and Mass Transfer Coefficients of Gases in a Heavy Fraction of Fischer-Tropsch Products. *The Canadian Journal of Chemical Engineering* **1987,** 65 (6), 973-981.

127. Hichri, H.; Accary, A.; Andrieu, J., Kinetics and Slurry-Type Reactor Modelling during Catalytic Hydrogenation of o-cresol on Ni/SiO_2. *Chemical Engineering and Processing* **1991,** 30 (3), 133-140.

128. Chang, M.-Y.; Morsi, B. I., Solubilities and Mass Transfer Coefficients of Carbon Monoxide in a Gas-Inducing Reactor Operating with Organic Liquids under High

Pressures and Temperatures. *Chemical Engineering Science* **1992,** 47 (13-14), 3541-3548.

129. Dietrich, E.; Mathieu, C.; Delmas, H.; Jenck, J., Raney-Nickel Catalyzed Hydrogenations: Gas-Liquid Mass Transfer in Gas-Induced Stirred Slurry Reactors. *Chemical Engineering Science* **1992,** 47 (13-14), 3597-3604.

130. Koneripalli, N.; Tekie, Z.; Morsi, B. I.; Chang, M.-Y., Mass Transfer Characteristics of Gases in Methanol and Ethanol under Elevated Pressures and Temperatures. *The Chemical Engineering Journal* **1994,** 54 (2), 63-77.

131. Lockett, M. J.; Safekourdi, A. A., Light Transmission through Bubble Swarms. *AIChE Journal* **1977,** 23 (3), 395-398.

132. Sridhar, T.; Potter, O. E., Interfacial Area Measurements in Gas-Liquid Agitated Vessels: Comparison of Techniques. *Chemical Engineering Science* **1978,** 33 (10), 1347-1353.

133. Midoux, N.; Charpentier, J.-C., Mechanically Agitated Gas-Liquid Reactors. Part 2. Interfacial Area. *International Chemical Engineering* **1984,** 24 (3), 452-481.

134. Muenz, K.; Marchello, J. M., Technique for Measuring Amplitudes of Small Surface Waves. *Review of Scientific Instruments* **1964,** 35 (8), 953-957.

135. Muenz, K.; Marchello, J. M., Surface Motion and Gas Absorption. *AIChE Journal* **1966,** 12 (2), 249-253.

136. Vazquez-Una, G.; Chenlo-Romero, F.; Sanchez-Barral, M.; Perez-Munuzuri, V., Mass transfer enhancement due to surface wave formation at a horizontal gas-liquid interface. *Chemical Engineering Science* **2000,** 55 (23), 5851-5856.

137. Zlokarnik, M., Sorption Characteristics for Gas-Liquid contacting in Mixing Vessels. *Advances in Biochemical Engineering* **1978,** 8, 133-151.

138. Pawlowski, J.; Kricsfalussy, Z., Studies of reaction kinetics in three-phase systems, as exemplified by hydrogenation of dinitrotoluene. *Chemie Ingenieur Technik* **1981,** 53 (8), 652-654.

139. Karandikar, B. M.; Morsi, B. I.; Shah, Y. T., Effect of Water on the Solubility and Mass Transfer Coefficients of CO and H_2 in a Fischer-Tropsch Liquid. *Chemical Engineering Journal* **1986,** 33 (3), 157-168.

140. Eiras, J. G. Characterization of mass transfer in polymerization processes. Unpublished MS Dissertation, University of Pittsburgh, Pittsburgh, 1990.

141. Lee, J. H.; Foster, N. R., Measurement of Gas-Liquid Mass Transfer in Multi-Phase Reactors. *Applied Catalysis* **1990,** 63 (1), 1-36.

142. Lee, J. H.; Foster, N. R., Mass transfer and solubility of O_2 and CH_4 in silicone fluids. *Industrial and Engineering Chemistry Research* **1990,** 29 (4), 691-696.

143. Hichri, H.; Accary, A.; Puaux, J. P.; Andrieu, J., Gas-Liquid Mass-Transfer Coefficients in a Slurry Batch Reactor Equipped with a Self-Gas-Inducing Agitator. *Industrial and Engineering Chemistry Research* **1992,** 31 (8), 1864-1867.

144. Lekhal, A.; Chaudhari, R. V.; Wilhelm, A. M.; Delmas, H., Gas-Liquid Mass Transfer in Gas-Liquid-Liquid Dispersions. *Chemical Engineering Science* **1997,** 52 (21-22), 4069-4077.

145. Tekie, Z.; Li, J.; Morsi, B. I.; Chang, M.-Y., Gas-Liquid Mass Transfer in Cyclohexane Oxidation Process Using Gas-Inducing and Surface-Aeration Agitated Reactors. *Chemical Engineering Science* **1997,** 52 (9), 1541-1551.

146. Tekie, Z.; Li, J.; Morsi, B. I., Mass Transfer Parameters of O_2 and N_2 in Cyclohexane under Elevated Pressures and Temperatures: A Statistical Approach. *Industrial and Engineering Chemistry Research* **1997,** 36 (9), 3879-3888.

147. Fillion, B.; Morsi, B. I., Gas-Liquid Mass-Transfer and Hydrodynamic Parameters in a Soybean Oil Hydrogenation Process under Industrial Conditions. *Industrial and Engineering Chemistry Research* **2000,** 39 (7), 2157-2168.

148. Alghamdi, A. K. A. Mass Transfer Characteristics in a Slurry Agitated Reactor with Organic Liquid Mixtures under High Pressures and Temperatures. Unpublished M.S. Thesis, University of Pittsburgh, Pittsburgh, 2001.

149. Hsu, Y.-C.; Chen, T.-Y.; Chen, J.-H.; Lay, C.-W., Ozone Transfer into Water in a Gas-Inducing Reactor. *Industrial and Engineering Chemistry Research* **2002,** 41 (1), 120-127.

150. Chen, J.-H.; Hsu, Y.-C.; Chen, Y. F.; Lin, C.-C., Application of Gas-Inducing Reactor to Obtain High Oxygen Dissolution in Aeration Process. *Water Research* **2003,** 37 (12), 2919-2928.

151. Soriano, J.-P. Mass Transfer Characteristics in an Agitated Slurry Reactor Operating under Fischer-Tropsch Conditions. Unpublished M.S. Thesis, University of Pittsburgh, Pittsburgh, 2005.

152. Whitman, W. G., Preliminary experimental confirmation of the two-film theory of gas absorption. *Chemical and Metallurgical Engineering* **1923,** 29, 146-148.

153. King, C. J., Turbulent liquid-phase mass transfer at a free gas-liquid interface. *Industrial and Engineering Chemistry Fundamentals* **1966,** 5 (1), 1-8.

154. Higbie, R., The Rate of Absorption of a Pure Gas into a Still Liquid during Short Periods of Exposure. *Transactions of American Institute of Chemical Engineers* **1935,** 31, 365-389.

155. Rose, L. M., *Chemical reactor design in practice*. Elsevier Scientific Pub. Co. ; Distributors for the U.S. and Canada Elsevier/North-Holland: Amsterdam - New York, 1981.

156. Gestrich, W.; Esenwein, H.; Krauss, W., Liquid-Side Mass Transfer Coefficient in Bubble Layers. *Int Chem Eng* **1978,** 18 (1), 38-47.

157. Danckwerts, P. V., Significance of liquid-film coefficients in gas absorption. *Journal of Industrial and Engineering Chemistry (Washington, DC)* **1951,** 43, 1460-1467.

158. Dobbins, W. E., Nature of the oxygen transfer coefficient in aeration systems. *Biological Treatment of Sewage and Industrial Wastes* **1956**, 141-148.

159. Toor, H. L.; Marchello, J. M., Film-Penetration Model for Mass and Heat Transfer. *AIChE Journal* **1958,** 4, 97-101.

160. Kishinevskii, M. K.; Serebryanskii, V. T., Regarding the mechanism of mass transfer at the gas-liquid interface during intensive stirring. *Zhurnal Prikladnoi Khimii (Sankt-Peterburg, Russian Federation)* **1956,** 29, 29-33.

161. Vàzquez, G.; Cancela, M. A.; Riverol, C.; Alvarez, E.; Navaza, J. M., Determination of interfacial areas in a bubble column by different chemical methods. *Industrial and Engineering Chemistry Research* **2000,** 39 (7), 2541-2547.

162. Pearson, R. G., Hard and soft acids and bases (HSAB). I. Fundamental principles. *Journal of Chemical Education* **1968,** 45 (9), 581-587.

163. Pearson, R. G., *Chemical hardness: Applications from Molecules to Solids*. Wiley-VCH: Weinheim, Germany, New York, Chichester, Brisbane, Singapore, Toronto, 1997.

164. Pearson, R. G., Absolute electronegativity and hardness correlated with molecular orbital theory. *Proceedings of the National Academy of Sciences of the United States of America* **1986,** 83 (22), 8440-8441.

165. Burke, J., Solubility Parameters: Theory and Application. In *The Book and Paper Group Annual*, Jensen, C., Ed. Book and Paper Group, American Institute for Conservation of Historic and Artistic Works: Washington, D.C., 1984; Vol. 3, pp 13-58.

166. Hildebrand, J. H.; Prausnitz, J. M.; Scott, R. L., *Regular and Related Solutions; the Solubility of Gases, Liquids, and Solids*. Van Nostrand Reinhold Co.: New York, 1970.

167. Crowley, J. D.; Teague, G. S., Jr.; Lowe, J. W., Jr., A three-dimensional approach to solubility. *Journal of Paint Technology* **1966,** 38 (496), 269-280.

168. Poling, B. E.; Prausnitz, J. M.; O'Connell, J. P., *The Properties of Gases and Liquids*. 5th ed.; McGraw-Hill: New York, 2001.

169. Hansen, C. M., Three-dimensional solubility parameter-key to paint-component affinities: I. Solvents, plasticizers, polymers, and resins. *Journal of Paint Technology* **1967,** 39 (505), 104-117.

170. Barton, A. F. M., *CRC Handbook of Solubility Parameters and Other Cohesion Parameters*. CRC Press: Boca Raton, FL, 1983.

171. Sweeney, C. W.; Ritter, T. J.; McGinley, E. B., Solvent Selection. In *Encyclopedia of Chemical Processing and Design, Volume 52*, McKetta, J. J.; Weismantel, G. E., Eds. Marcel Dekker Inc.: New York, 1995; Vol. 52, pp 458-472.

172. Woelfer, W., Helpful hints for physical solvent absorption. *Hydrocarbon Processing, International Edition* **1982,** 61 (11), 193-197.

173. The Dow Chemical Company, SELEXOL Solvent: For Gas Treating. http://www.dow.com/gastreating/solution/lt_gp.htm (August 16th 2003).

174. Viscous Fluids. http://www.pumpworld.com/centrif9.htm (April 15th 2009).

175. Univar USA Inc. http://www.univarusa.com (January 12th 2009).

176. Andrade, E. N. d. C., The Viscosity of Liquids. *Nature* **1930,** 125 (3148), 309-310.

177. Andrade, E. N. d. C., Theory of viscosity of liquids. *Philos. Mag. (1798-1977)* **1934,** 17, 497-511,698-732.

178. Maciejewski, A., The application of perfluoroalkanes as solvents in spectral, photophysical and photochemical studies. *Journal of Photochemistry and Photobiology, A: Chemistry* **1990,** 51 (2), 87-131.

179. Reed, T. M., III, Physical Chemistry of Fluorocarbons. *Fluorine Chemistry* **1964,** 5, 133-236.

180. Bryce, H. G., Industrial and utilitarian aspects of fluorine chemistry. *Fluorine Chemistry* **1964,** 5, 295-498.

181. Brice, T. J., Fluorocarbons-Their properties and wartime development. *Fluorine Chemistry* **1950,** 1, 423-462.

182. Smart, B. E., Characteristics of C-F Systems. In *Organofluorine Chemistry: Principles and Commercial Applications*, Banks, R. E.; Smart, B. E.; Tatlow, J. C., Eds. Plenum Press: New York, 1994; pp 57-88.

183. Persico, D. F.; Lagow, R. J.; Clark, L. C., Jr.; Huang, H.-N., A general synthesis for symmetrical highly branched perfluoro ethers: a new class of oxygen carriers. *Journal of Organic Chemistry* **1985,** 50 (25), 5156-5159.

184. Banks, R. E.; Smart, B. E.; Tatlow, J. C., *Organofluorine Chemistry: Principles and Commercial Applications*. Plenum Press: New York, 1994.

185. Banks, R. E., *Fluorocarbons and their Derivatives*. 2nd ed.; Macdonald & Co.: London, 1970.

186. Fuchs, R.; Chambers, E. J.; Stephenson, W. K., Enthalpies of interaction of nonpolar solutes with nonpolar solvents. The role of solute polarizability and molar volume in solvation. *Canadian Journal of Chemistry* **1987,** 65 (11), 2624-2627.

187. Fuchs, R.; Peacock, L. A.; Das, K., Enthalpies of interaction of polar and nonpolar solutes with a perfluoro solvent. *Canadian Journal of Chemistry* **1980,** 58 (22), 2301-2304.

188. Patrick, C. R., In *Preparation, Properties, and Industrial Applications of Organofluorine Compounds*, Banks, R. E., Ed. Ellis Horwood Ltd.: Chichester, UK, 1982.

189. Rowlinson, J. S.; Swinton, F. L., *Liquids and Liquid Mixtures*. 3rd ed.; Butterworth: London, 1982.

190. Handa, T.; Mukerjee, P., Surface Tensions of Nonideal Mixtures of Fluorocarbons and Hydrocarbons and Their Interfacial Tensions against Water. *Journal of Physical Chemistry* **1981,** 85 (25), 3916-3920.

191. Mukerjee, P.; Yang, A. Y. S., Nonideality of Mixing of Micelles of Fluorocarbon and Hydrocarbon Surfactants and Evidence of Partial Miscibility from Differential Conductance Data. *Journal of Physical Chemistry* **1976,** 80 (12), 1388-1390.

192. Carlfors, J.; Stilbs, P., The Composition of Mixed Micelles of Fluorocarbon and Hydrocarbon Surfactants as Derived from Nuclear Magnetic Resonance Self-Diffusion Measurements. *Journal of Physical Chemistry* **1984,** 88 (19), 4410-4414.

193. Dorset, D. L., Binary Phase Behavior of Perfluoroalkanes. *Macromolecules* **1990,** 23 (3), 894-901.

194. Battino, R.; Cleve, H. L., Solubility of Gases in Liquids. *Chemical Reviews (Washington, DC, United States)* **1966,** 66 (4), 395-463.

195. Wilhelm, E.; Battino, R., Thermodynamic Functions of the Solubilities of Gases in Liquids at 25^{o}C. *Chemical Reviews (Washington, DC, United States)* **1973,** 73 (1), 1-9.

196. Lowe, K. C., Properties and Biomedical Applications of Perfluorochemicals and Their Emulsions. In *Organofluorine Chemistry: Principles and Commercial Applications*, Banks, R. E.; Smart, B. E.; Tatlow, J. C., Eds. Plenum Press: New York, 1994; pp 555-577.

197. Hamza, M. H. A.; Serratrice, G.; Stebe, M. J.; Delpuech, J. J., Solute-Solvent Interactions in Perfluorocarbon Solutions of Oxygen. An NMR Study. *Journal of the American Chemical Society* **1981,** 103 (13), 3733-3738.

198. Mack, H. G.; Oberhammer, H., An ab initio approach to the interaction of CF_4 and CH_4 with O_2, CO_2, N_2, and CO. The nature of the interaction force in perfluorochemical artificial blood. *Journal of Chemical Physics* **1987,** 87 (4), 2158-2165.

199. Oikawa, S.; Tsuda, M.; Nagayama, K., Ab initio theoretical research on perfluorochemicals as oxygen carriers. *Theoretica Chimica Acta* **1984,** 64 (5), 403-413.

200. Afzal, J.; Ashlock, S. R.; Fung, B. M.; O'Rear, E. A., Interaction between Perfluoro Chemicals and Oxygen in Phosphatidylcholine Vesicles. *Journal of Physical Chemistry* **1986,** 90 (13), 3019-3022.

201. Dias, A. M. A.; Bonifácio, R. P.; Marrucho, I. M.; Pádua, A. A. H.; Costa Gomes, M. F., Solubility of oxygen in n-hexane and in n-perfluorohexane. Experimental determination and prediction by molecular simulation. *Physical Chemistry Chemical Physics B* **2003,** 5 (3), 543-549.

202. Costa Gomes, M. F.; Pádua, A. A. H., Interactions of Carbon Dioxide with Liquid Fluorocarbons. *The Journal of Physical Chemistry B* **2003,** 107 (50), 14020-14024.

203. Wilhelm, E.; Battino, R., Solubility of gases in liquids. 1. Solubility of a series of fluorine-containing gases in several nonpolar solvents. *Journal of Chemical Thermodynamics* **1971,** 3 (3), 379-392.

204. F2 Chemicals Website. http://www.fluoros.co.uk/ (June 2004).

205. Green, S. W.; Slinn, D. S. L.; Simpson, R. N. F.; Woytek, A. J., Perfluorocarbon Fluids. In *Organofluorine Chemistry: Principles and Commercial Applications*, Banks, R. E.; Smart, B. E.; Tatlow, J. C., Eds. Plenum Press: New York, 1994; pp 89-119.

206. Lemoine, R.; Fillion, B.; Morsi, B. I., Hydrodynamic and Mass Transfer Parameters in Agitated Reactors part I: Critical Mixing Speed, Induced Gas Flow Rate, and Wavy Surface in SARs and GIRs. *International Journal of Chemical Reactor Engineering* **2004,** 2 (A29), 1-32.

207. Valley National Gases (in 2009, Matheson Tri-Gas Inc. acquires Valley National Gases). http://www.mathesongas.com/ (March 10th 2011).

208. Reid, R. C.; Prausnitz, J. M.; Poling, B. E., *The Properties of Gases and Liquids*. 4th ed.; McGraw-Hill: New York, 1987.

209. Yaws, C. L., *Chemical Properties Handbook: Physical, Thermodynamic, Environmental, Transport, Safety, and Health related Properties for Organic and Inorganic Chemicals*. McGraw-Hill: New York, 1999.

210. Rackett, H. G., Equation of state for saturated liquids. *Journal of Chemical & Engineering Data* **1970,** 15 (4), 514-517.

211. Andy, J., Personal Communication: Technical Support Chemist, F2 Chemicals. In Preston, UK, 2004.

212. Sastri, S. R. S.; Rao, K. K., A New Group Contribution Method for Predicting Viscosity of Organic Liquids. *The Chemical Engineering Journal* **1992,** 50 (1), 9-25.

213. Wilke, C. R.; Chang, P., Correlation of Diffusion Coefficients in Dilute Solutions. *AIChE Journal* **1955,** 1, 264-270.

214. Tyn, M. T.; Calus, W. F., Estimating liquid molal volume. *Processing (Sutton, England)* **1975,** 21 (4), 16-17.

215. Montgomery, D. C., *Design and Analysis of Experiments*. 3rd ed.; Wiley: New York, 1991.

216. Li, J.; Tekie, Z.; Mohammad, A.; Morsi, B. I., Statistical Assessment of Gas/Liquid Mass Transfer in Slurry-Phase Propylene Polymerization Process. *The Canadian Journal of Chemical Engineering* **1996,** 74 (1), 77-83.

217. Montgomery, D. C., *Design and Analysis of Experiments*. 4th ed.; Wiley: New York, 1997.

218. Box, G. E. P.; Draper, N. R., *Empirical model-building and response surfaces*. Wiley: New York, 1987.

219. Lemoine, R.; Fillion, B.; Behkish, A.; Morsi, B. I.; Smith, A. E., Prediction of the gas-liquid volumetric mass transfer coefficients in surface-aeration and gas-inducing reactors using neural networks. *Chemical Engineering and Processing* **2003,** 42 (8-9), 621-643.

220. Panagiotopoulos, A. Z.; Reid, R. C., New Mixing Rule for Cubic Equations of State for Highly Polar, Asymmetric Systems. In *ACS Symposium Series*, 1986; Vol. 300, pp 571-582.

221. Enick, R. M.; Holder, G. D.; Mohamed, R., Four-Phase Flash Equilibrium Calculations using the Peng-Robinson Equation of State and a Mixing Rule for Asymmetric Systems. *SPE Reservoir Engineering (Society of Petroleum Engineers)* **1987,** 2 (4), 687-694.

222. Morsi, B. I.; Heintz, Y. J.; Lemoine, R. O.; Sehabiague, L. *Development and Testing of Fluorinated Liquids as CO_2 Solvents for High-Temperature and High-Pressure Applications*; Topical Report, U.S. DOE Contract No. DE-AM26-99FT40463, Subcontract No. 735934-30002-00: Pittsburgh, May 2005.

223. Himmelblau, D. M., Solubilities of Inert Gases in H_2O: 0° to near the Critical Point of H_2O. *Journal of Chemical & Engineering Data* **1960,** 5 (1), 10-15.

224. Xu, Y.; Schutte, R. P.; Hepler, L. G., Solubilities of Carbon Dioxide, Hydrogen Sulfide and Sulfur Dioxide in Physical Solvents. *The Canadian Journal of Chemical Engineering* **1992,** 70 (3), 569-573.

225. Schulze, G.; Prausnitz, J. M., Solubilities of Gases in Water at High Temperatures. *Industrial and Engineering Chemistry Fundamentals* **1981,** 20 (2), 175-177.

226. Carroll, J. J.; Slupsky, J. D.; Mather, A. E., The solubility of carbon dioxide in water at low pressure. *Journal of Physical and Chemical Reference Data* **1991,** 20 (6), 1201-1209.

227. Battino, R.; Cleve, H. L.; Young, C. L., *IUPAC Solubility Data Series, Vol. 10: Nitrogen and Air*. Oxford Pergamon Press: 1982.

228. Doraiswamy, L. K.; Sharma, M. M., *Heterogeneous reactions : analysis, examples, and reactor design*. Wiley: New York, 1984.

229. Lachowicz, S. K.; Weale, K. E., Prediction of Gas Solubility in Nonpolar Liquids. *Industrial and Engineering Chemistry, Chemical and Engineering Data Series* **1958,** 3 (1), 162-166.

230. Field, L. R.; Wilhelm, E.; Battino, R., Solubility of gases in liquids. 6. Solubility of nitrogen, oxygen, carbon monoxide, carbon dioxide, methane, and carbon tetrafluoride in methylcyclohexane and toluene at 283 to 313 K. *Journal of Chemical Thermodynamics* **1974,** 6 (3), 237-243.

231. Battino, R.; Rettich, T. R.; Tominaga, T., The solubility of nitrogen and air in liquids. *Journal of Physical and Chemical Reference Data* **1984,** 13 (2), 563-600.

232. Lin, H.-M.; Lee, M.-J.; Lee, R.-J., Phase Equilibria of Toluene in Mixtures with Helium or Nitrogen at High Temperatures. *Journal of Chemical & Engineering Data* **1995,** 40 (3), 653-656.

233. Hildebrand, J. H.; Scott, R. L., *Regular solutions*. Prentice-Hall: Englewood Cliffs, N.J., 1962.

234. Walas, S. M., *Phase equilibria in chemical engineering*. Butterworth: Boston, 1985.

235. King, M. B.; Kassim, K.; Al-Najjar, H., The solubilities of carbon dioxide, hydrogen sulphide and propane in some normal alkane solvents II : Correlation of Data at 25[deg]C in Terms of Solubility Parameters and Regular Solution Theory. *Chemical Engineering Science* **1977,** 32 (10), 1247-1252.

236. Pitzer, K. S.; Lippmann, D. Z.; Curl, R. F., Jr.; Huggins, C. M.; Petersen, D. E., Volumetric and Thermodynamic Properties of Fluids. II. Compressibility Factor, Vapor Pressure, and Entropy of Vaporization. *Journal of the American Chemical Society* **1955,** 77 (13), 3433-3440.

237. Inga, J. R.; Morsi, B. I., Effect of Catalyst Loading on Gas/Liquid Mass Transfer in a Slurry Reactor: a Statistical Experimental Approach. *The Canadian Journal of Chemical Engineering* **1997,** 75 (5), 872-881.

238. Behkish, A. Hydrodynamic and Mass Transfer Parameters in Large-Scale Slurry Bubble Column Reactors. Unpublished Ph.D. Thesis, University of Pittsburgh, Pittsburgh, 2004.

239. Chang, M. Y.; Morsi, B. I., Mass Transfer Characteristics of Gases in Aqueous and Organic Liquids at Elevated Pressures and Temperatures in Agitated Reactors. *Chemical Engineering Science* **1991,** 46 (10), 2639-2650.

240. Deimling, A.; Karandikar, B. M.; Shah, Y. T.; Carr, N. L., Solubility and Mass Transfer of Carbon Monoxide and Hydrogen in Fischer-Tropsch Liquids and Slurries. *Chemical Engineering Journal* **1984,** 29 (3), 127-140.

241. Van't Riet, K.; Bruijn, W.; Smith, J. M., Power Consumption with Aerated Rushton Turbines. *Chemical Engineering Research and Design* **1974,** 52, 88-104.

242. Matsumura, M.; Sakuma, H.; Yamagata, T.; Kobayashi, J., Gas Entrainement in a New Entraining Fermentator. *Journal of Fermentation Technology* **1982,** 60 (5), 457-467.

243. Beenackers, A. A. C. M.; Van Swaaij, W. P. M., Mass transfer in gas-liquid slurry reactors. *Chemical Engineering Science* **1993,** 48 (18), 3109-3139.

244. Oyevaar, M.; Zijl, A.; Westerterp, R., Interfacial Areas and Gas-Hold-Ups at Elevated Pressures in a Mechanically Agitated Gas-Liquid Reactor. *Chemical Engineering and Technology* **1988,** 11 (1), 1-10.

245. Albal, R. S.; Shah, Y. T.; Schumpe, A.; Carr, N. L., Mass Transfer in Multiphase Agitated Contactors. *Chemical Engineering Journal (Amsterdam, Netherlands)* **1983,** 27 (2), 61-80.

246. Ledakowicz, S.; Nettelhoff, H.; Deckwer, W. D., Gas-Liquid Mass Transfer Data in a Stirred Autoclave Reactor. *Industrial and Engineering Chemistry Fundamentals* **1984,** 23 (4), 510-512.

247. Linek, V.; Kordač, M.; Fujasová, M.; Moucha, T., Gas-Liquid Mass Transfer Coefficient in Stirred Tanks Interpreted through Models of Idealized Eddy Structure of Turbulence in the Bubble Vicinity. *Chemical Engineering and Processing* **2004,** 43 (12), 1511-1517.

248. Longanbach, J. R.; Stiegel, G. J.; Rutkowski, M. D.; Buchanan, T. L.; Klett, M. G.; Schoff, R. L. *Capital and Operating Cost of Hydrogen Production from Coal Gasification*; Final Report, U.S. DOE Contract No. DE-AM26-99FT40465, Subcontract No. 990700362: Pittsburgh, April 2003.

249. Welton, T., Room-Temperature Ionic Liquids. Solvents for Synthesis and Catalysis. *Chemical Reviews (Washington, DC)* **1999,** 99 (8), 2071-2083.

250. Meindersma, G. W.; Podt, A.; de Haan, A. B., Selection of Ionic Liquids for the Extraction of Aromatic Hydrocarbons from Aromatic/Aliphatic Mixtures. *Fuel Processing Technology* **2005,** 87 (1), 59-70.

251. Jork, C.; Kristen, C.; Pieraccini, D.; Stark, A.; Chiappe, C.; Beste, Y. A.; Arlt, W., Tailor-Made Ionic Liquids. *The Journal of Chemical Thermodynamics* **2005,** 37 (6), 537-558.

252. Cadena, C. Molecular Modeling of the Thermophysical and Transport Properties of Ionic Liquids. Unpublished Ph.D. Thesis, University of Notre Dame, 2006.

253. Pretti, C.; Chiappe, C.; Pieraccini, D.; Gregori, M.; Abramo, F.; Monni, G.; Intorre, L., Acute Toxicity of Ionic Liquids to the Zebrafish (Danio rerio). *Green Chemistry* **2006,** 8 (3), 238-240.

254. Zhao, D.; Liao, Y.; Zhang, Z., Toxicity of Ionic Liquids. *CLEAN - Soil, Air, Water* **2007,** 35 (1), 42-48.

255. Li, X.; Zhao, J.; Li, Q.; Wang, L.; Tsang, S. C., Ultrasonic Chemical Oxidative Degradations of 1,3-Dialkylimidazolium Ionic Liquids and their Mechanistic Elucidations. *Dalton Transactions* **2007,** (19), 1875-1880.

256. Walker, A. J.; Bruce, N. C., Cofactor-Dependent Enzyme Catalysis in Functionalized Ionic Solvents. *Chemical Communications (Cambridge, United Kingdom)* **2004,** (22), 2570-2571.

257. Hayashi, S.; Hamaguchi, H.-o., Discovery of a Magnetic Ionic Liquid [bmim]$FeCl_4$. *Chemistry Letters* **2004,** 33 (12), 1590-1591.

258. Smiglak, M.; Reichert, W. M.; Holbrey, J. D.; Wilkes, J. S.; Sun, L.; Thrasher, J. S.; Kirichenko, K.; Singh, S.; Katritzky, A. R.; Rogers, R. D., Combustible Ionic Liquids by Design: Is Laboratory Safety Another Ionic Liquid Myth? *Chemical Communications (Cambridge, United Kingdom)* **2006,** (24), 2554-2556.

259. Swatloski, R. P.; Holbrey, J. D.; Rogers, R. D., Ionic Liquids are not Always Green: Hydrolysis of 1-Butyl-3-Methylimidazolium Hexafluorophosphate. *Green Chemistry* **2003,** 5 (4), 361-363.

260. Evonik Industries - Degussa (Evonik Goldschmidt Chemical Corporation). http://corporate.evonik.com/en/Pages/default.aspx (January 12th 2009).

261. Heintz, Y. J.; Sehabiague, L.; Morsi, B. I.; Jones, K. L.; Pennline, H. W., Novel Physical Solvents for Selective CO_2 Capture from Fuel Gas Streams at Elevated Pressures and Temperatures. *Energy & Fuels* **2008,** 22 (6), 3824-3837.

262. Pennline, H. W.; Luebke, D. R.; Jones, K. L.; Myers, C. R.; Morsi, B. I.; Heintz, Y. J.; Ilconich, J. B., Progress in carbon dioxide capture and separation research for gasification-based power generation point sources. *Fuel Processing Technology* **2008,** 89 (9), 897-907.

263. Ethoquad C/25 Product Data Sheet, Akzo Nobel Company. http://files.sc.akzonobel.com/pds/external/763.pdf

264. Harkins, W. D.; Jordan, H. F., A Method for the Determination of Surface and Interfacial Tension from the Maximum Pull on a Ring. *Journal of the American Chemical Society* **1930,** 52 (5), 1751-1772.

265. Rebelo, L. P. N.; Canongia Lopes, J. N.; Esperança, J. M. S. S.; Filipe, E., On the Critical Temperature, Normal Boiling Point, and Vapor Pressure of Ionic Liquids. *The Journal of Physical Chemistry B* **2005,** 109 (13), 6040-6043.

266. Anthony, J. L.; Anderson, J. L.; Maginn, E. J.; Brennecke, J. F., Anion Effects on Gas Solubility in Ionic Liquids. *The Journal of Physical Chemistry B* **2005,** 109 (13), 6366-6374.

267. Anthony, J. L.; Maginn, E. J.; Brennecke, J. F., Solubilities and Thermodynamic Properties of Gases in the Ionic Liquid 1-*n*-Butyl-3-methylimidazolium Hexafluorophosphate. *The Journal of Physical Chemistry B* **2002,** 106 (29), 7315-7320.

268. Kumelan, J.; Perez-Salado Kamps, A.; Tuma, D.; Maurer, G., Solubility of CO_2 in the Ionic Liquid [hmim][Tf_2N]. *The Journal of Chemical Thermodynamics* **2006,** 38 (11), 1396-1401.

269. Shin, E.-K.; Lee, B.-C., High-Pressure Phase Behavior of Carbon Dioxide with Ionic Liquids: 1-Alkyl-3-methylimidazolium Trifluoromethanesulfonate. *Journal of Chemical & Engineering Data* **2008,** 53 (12), 2728-2734.

270. Heintz, Y. J.; Lemoine, R. O.; Sehabiague, L.; Morsi, B. I.; Jones, K. L.; Pennline, H. W. In *Investigation of Perfluorinated Compounds as Physical Solvents for Selective CO_2 Capture at Elevated Pressures and Temperatures*, Proceedings - 22nd Annual International Pittsburgh Coal Conference, Pittsburgh, PA, September 12-15, 2005; Morsi, B. I., Ed. Pittburgh Coal Conference, University of Pittsburgh: Pittsburgh, PA, 2005; pp 34.5/1-34.5/40.

271. Kumelan, J.; Perez-Salado Kamps, A.; Tuma, D.; Maurer, G., Solubility of H_2 in the Ionic Liquid [hmim][Tf_2N]. *Journal of Chemical & Engineering Data* **2006,** 51 (4), 1364-1367.

272. Kohl, A. L.; Riesenfeld, F. C., *Gas Purification*. 4th ed.; Gulf Publishing Company Book Division: Houston, 1985.

273. Heintz, Y. J.; Sehabiague, L.; Morsi, B. I.; Jones, K. L.; Luebke, D. R.; Pennline, H. W., Hydrogen Sulfide and Carbon Dioxide Removal from Dry Fuel Gas Streams Using an Ionic Liquid as a Physical Solvent. *Energy & Fuels* **2009,** 23 (10), 4822-4830.

274. RTI International, Warm-Gas Cleanup Technology. http://www.rti.org/page.cfm?obj=F1EFC93F-B89F-0733-44701578725EBF1A (April 2011).

275. Galán Sánchez, L. M.; Meindersma, G. W.; de Haan, A. B., Solvent Properties of Functionalized Ionic Liquids for CO_2 Absorption. *Chemical Engineering Research and Design* **2007,** 85 (1), 31-39.

276. Ionic Liquids. http://www.organic-chemistry.org/topics/ionic-liquids.shtm (November 9th 2011).

277. Holbrey, J. D.; Seddon, K. R., The phase behaviour of 1-alkyl-3-methylimidazolium tetrafluoroborates; ionic liquids and ionic liquid crystals. *Journal of the Chemical Society, Dalton Transactions* **1999,** (13), 2133-2140.

278. Zhao, H.; Xia, S.; Ma, P., Use of ionic liquids as 'green' solvents for extractions. *Journal of Chemical Technology & Biotechnology* **2005,** 80 (10), 1089-1096.

279. Wasserscheid, P.; Keim, W., Ionische Flüssigkeiten – neue „Lösungen“ für die Übergangsmetallkatalyse. *Angewandte Chemie* **2000,** 112 (21), 3926-3945.

280. Anderson, J. L.; Dixon, J. K.; Brennecke, J. F., Solubility of CO_2, CH_4, C_2H_6, C_2H_4, O_2, and N_2 in 1-Hexyl-3-methylpyridinium Bis(trifluoromethylsulfonyl)imide: Comparison to Other Ionic Liquids. *Accounts of Chemical Research* **2007,** 40 (11), 1208-1216.

281. Maginn, E. J. In *Evaluation of Ionic Liquids in Post-Combustion CO_2 Capture*, Seventh Annual Conference on Carbon Capture and Sequestration, Pittsburgh, PA, May 6, 2008, 2008; Exchange Monitor Publications & Forums: Pittsburgh, PA, 2008.

282. Muldoon, M. J.; Aki, S. N. V. K.; Anderson, J. L.; Dixon, J. K.; Brennecke, J. F., Improving Carbon Dioxide Solubility in Ionic Liquids. *The Journal of Physical Chemistry B* **2007,** 111 (30), 9001-9009.

283. Jork, C.; Seiler, M.; Weyerhausen, B. Novel Working Media for Refrigeration Processes. US 2010/0095703 A1, 2010.

284. Valderrama, J. O.; Rojas, R. E., Critical Properties of Ionic Liquids. Revisited. *Industrial & Engineering Chemistry Research* **2009,** 48 (14), 6890-6900.

285. Valderrama, J. O.; Robles, P. A., Critical Properties, Normal Boiling Temperatures, and Acentric Factors of Fifty Ionic Liquids. *Industrial & Engineering Chemistry Research* **2007,** 46 (4), 1338-1344.

286. Hajipour, S.; Satyro, M. A., Uncertainty analysis applied to thermodynamic models and process design – 1. Pure components. *Fluid Phase Equilibria* **2011,** 307 (1), 78-94.

287. Rudkin, J., Equation predicts vapor pressures. *Chemical Engineering* **1961,** 68 (7), 202-204.

288. Shuster, E.; McIlvried, H. *Systems Analysis Study on the Development of Fluorinated Solvents for Warm-Temperature/High-Pressure CO_2 Capture of Shifted Syngas*; National Energy Technology Laboratory, US Department of Energy Pittsburgh, PA, April 19.

289. Billet, R.; Schultes, M., Predicting mass transfer in packed columns. *Chemical Engineering and Technology* **1993,** 16 (1), 1-9.

290. Banks, R. E., Isolation of Fluorine by Moissan. Setting the Scene. *Journal of Fluorine Chemistry* **1986,** 33 (1-4), 3-26.

291. Greenwood, N. N.; Earnshaw, A., *Chemistry of the Elements*. 1st ed.; Pergamon Press: Oxford, 1984.

292. Banks, R. E.; Tatlow, J. C., Organofluorine Chemistry: Nomenclature and Historical Landmarks. In *Organofluorine Chemistry: Principles and Commercial Applications*, Banks, R. E.; Smart, B. E.; Tatlow, J. C., Eds. Plenum Press: New York, 1994; pp 1-24.

293. Smart, B. E., Fluorocarbons. *The Chemistry of Halides, Pseudo-Halides and Azides* **1983,** 1, 603-655.

294. Banks, R. E.; Sharp, D. W. A.; Tatlow, J. C., *Fluorine: The 1st Hundred Years (1886-1986). [1986; Paris, Fr. In: J. Fluorine Chem., 1986; 33(1-4)]*. 1986.

295. Sen, K. D.; Joergensen, C. K., *Electronegativity*. 1987.

296. Nagle, J. K., Atomic polarizability and electronegativity. *Journal of the American Chemical Society* **1990,** 112 (12), 4741-4747.

297. Allen, L. C.; Egolf, D. A.; Knight, E. T.; Liang, C., Bond Polarity Index. *Journal of Physical Chemistry* **1990,** 94 (14), 5602-5607.

298. Bondi, A., van der Waals volumes and radii. *Journal of Physical Chemistry* **1964,** 68 (3), 441-451.

299. Elliott, A. J., Chlorofluorocarbons. In *Organofluorine Chemistry: Principles and Commercial Applications*, Banks, R. E.; Smart, B. E.; Tatlow, J. C., Eds. Plenum Press: New York, 1994; pp 145-157.

300. Rao, V. N. M., Alternatives to Chlorofluorocarbons (CFCs). In *Organofluorine Chemistry: Principles and Commercial Applications*, Banks, R. E.; Smart, B. E.; Tatlow, J. C., Eds. Plenum Press: New York, 1994; pp 159-175.

301. Cartwright, D., Recent Developments in Fluorine-Containing Agrochemicals. In *Organofluorine Chemistry: Principles and Commercial Applications*, Banks, R. E.; Smart, B. E.; Tatlow, J. C., Eds. Plenum Press: New York, 1994; pp 237-262.

302. Alsmeyer, Y. W.; Childs, W. V.; Flynn, R. M.; Moore, G. G. I.; Smeltzer, J. C., Electochemical Fluorination and Its Applications. In *Organofluorine Chemistry: Principles and Commercial Applications*, Banks, R. E.; Smart, B. E.; Tatlow, J. C., Eds. Plenum Press: New York, 1994; pp 121-143.

303. Slinn, D. S. L.; Green, S. W., In *Preparation, Properties, and Industrial Applications of Organofluorine Compounds*, Banks, R. E., Ed. Ellis Horwood: Chichester, 1982.

304. Dean, J. A.; Editor, *Lange's Handbook of Chemistry*. 13th ed.; 1985.

305. Griller, D.; Kanabus-Kaminska, J. M.; Maccoll, A., Bond Dissociation Energies for Common Organic Compounds. *Theochem, Journal of Molecular Structure* **1988,** 163, 125-131.

306. Wang, S. Y.; Borden, W. T., Why is the π Bond in Tetrafluoroethylene Weaker Than That in Ethylene? An ab Initio Investigation. *Journal of the American Chemical Society* **1989,** 111 (18), 7282-7283.

307. Pickard, J. M.; Rodgers, A. S., π-Bond Dissociation Energy in 1,1-Difluoroethylene. *Journal of the American Chemical Society* **1977,** 99 (3), 695-696.

308. Smart, B. E., In *Molecular Structure and Energetics*, Liebman, J. F.; Greenberg, A., Eds. VCH Publishers: Deerfield Beach, FL, 1986; Vol. 3.

309. Dixon, D. A.; Smart, B. E., Molecular structures, electronic properties and energetics of fluorinated allenes and isomeric acetylenes. *Journal of Physical Chemistry* **1989,** 93 (23), 7772-7780.

310. Smart, B. E., In *The Chemistry of Functional Groups, Suppl. D: The Chemistry of Halides, Pseudo-Halides and Azides, Part. 2*, Patai, S.; Rappoport, Z., Eds. Wiley: New York, 1983.

311. Bruce, M. I.; Cullen, W. R., Chemistry of fluorinated acetylenes. *Fluorine Chemistry Reviews* **1969,** 4, 79-118.

312. McMillen, D. F.; Golden, D. M., Hydrocarbon bond dissociation energies. *Annual Review of Physical Chemistry* **1982,** 33, 493-532.

313. Shin, S. K.; Beauchamp, J. L., Precise Determination of Stabilities of Primary, Secondary, and Tertiary Silicenium Ions from Kinetics and Equilibria of Hydride-Transfer Reactions in the Gas Phase. A Quantitative Comparison of the Stabilities of Silicenium and Carbonium Ions in the Gas Phase. *Journal of the American Chemical Society* **1989,** 111 (3), 900-906.

314. Koch, H. F., Proton-Transfer Reactions between Carbon and Oxygen. *Accounts of Chemical Research* **1984,** 17 (4), 137-144.

315. Stirling, C. J. M., Leaving Groups and Nucleofugality in Elimination and Other Organic Reactions. *Accounts of Chemical Research* **1979,** 12 (6), 198-203.

316. Parker, R. E., Mechanisms of Fluorine Displacement. *Advances in Fluorine Chemistry (M. Stacey, J. C. Tallow, and A. G. Sharpe, Editors, Butterworths)* **1963,** 3, 63-91.

317. Hudlicky, M., *Chemistry of Organic Fluorine Compounds. A Laboratory Manual With Comprehensive Literature Coverage*. 2nd ed.; 1976.

318. Chambers, R. D., *Interscience Monographs in Organic Chemistry: Fluorine in Organic Chemistry*. 1973.

319. Swain, C. G.; Spalding, R. E. T., Mechanism of Acid Catalysis of the Hydrolysis of Benzyl Fluoride. *Journal of the American Chemical Society* **1960,** 82, 6104-6107.

320. Namavari, M.; Satyamurthy, N.; Phelps, M. E.; Barrio, J. R., Halogen Exchange Reactions between Alkyl Halides and Aqueous Hydrogen Halides. A New Method for Preparation of Alkyl Halides. *Tetrahedron Letters* **1990,** 31 (35), 4973-4976.

321. Szucs, S. S., Decomposition of benzyl fluoride. *Chemical and Engineering News* **1990,** 68 (34), 4.

322. Seetula, J. A.; Russell, J. J.; Gutman, D., Kinetics and Thermochemistry of the Reactions of Alkyl Radicals (CH_3, C_2H_5, i-C_3H_7, s-C_4H_9, and t-C_4H_9) with HI: A Reconciliation of the Alkyl Radical Heats of Formation. *Journal of the American Chemical Society* **1990,** 112 (4), 1347-1353.

323. Banks, R. E.; Tatlow, J. C., In *Fluorine: The 1st Hundred Years (1886-1986)*, Banks, R. E.; Sharp, D. W. A.; Tatlow, J. C., Eds. Elsevier: New York, 1986.

324. Bordwell, F. G.; Brannen, W. T., Jr., The effect of the carbonyl and related groups on the reactivity of halides in S_N2 reactions. *Journal of the American Chemical Society* **1964,** 86 (21), 4645-4650.

325. Wakselman, C.; Kaziz, C., In *Fluorine: The 1st Hundred Years (1886-1986)*, Banks, R. E.; Sharp, D. W. A.; Tatlow, J. C., Eds. Elsevier: New York, 1986.

326. Wakselman, C., Single Electron-Transfer Processes in Perfluoroalkyl Halide Reactions. *Journal of Fluorine Chemistry* **1992,** 59 (3), 367-378.

327. Liebman, J. F.; Dolbier, W. R., Jr.; Greenberg, A., Hexafluorocyclopropane and Octafluorocyclobutane: A Study of the Strain Energies. *Journal of Physical Chemistry* **1986,** 90 (3), 394-397.

328. Rahman, M. M.; Secor, B. A.; Morgan, K. M.; Shafer, P. R.; Lemal, D. M., Valence Isomerization Equilibria of Highly Fluorinated Cycloocta-1,3,5-trienes. *Journal of the American Chemical Society* **1990,** 112 (16), 5986-5990.

329. Wall, L. A., Fluoropolymers. In *High polymers*, Wall, L. A., Ed. Wiley-Interscience: New York, 1972; Vol. 25, pp 381-418.

330. Butler, J. N., Thermal decomposition of octafluorocyclobutane. *Journal of the American Chemical Society* **1962,** 84, 1393-1398.

331. Birchall, J. M.; Fields, R.; Haszeldine, R. N.; McLean, R. J., Cyclopropane chemistry. Part 5. Hexafluorocyclopropane as a source of difluorocarbene. *Journal of Fluorine Chemistry* **1980,** 15 (6), 487-495.

332. Aviyente, V.; Inel, Y., Analysis of the Kinetics of the Thermal Decomposition of Pentafluoroethane. *Canadian Journal of Chemistry* **1990,** 68 (8), 1332-1337.

333. Logothetis, A. L., Perfluorocarbon Fluids. In *Organofluorine Chemistry: Principles and Commercial Applications*, Banks, R. E.; Smart, B. E.; Tatlow, J. C., Eds. Plenum Press: New York, 1994; pp 373-396.

334. Dias, A. J.; McCarthy, T. J., Synthesis of a Two-Dimensional Array of Oganic Functional Groups: Surface-Selective Modification of Poly(vinylidene fluoride). *Macromolecules* **1984,** 17 (12), 2529-2531.

335. Brennan, J. V.; McCarthy, T. J., Surface-selective introduction of specific functionality onto poly(vinylidene fluoride). *Polymer Preprints (American Chemical Society, Division of Polymer Chemistry)* **1988,** 29 (2), 338-339.

336. Wang, C. Y.; Tarter, J. G., Determination of Halogens in Organic Compounds by Ion Chromatography after Sodium Fusion. *Analytical Chemistry* **1983,** 55 (11), 1775-1778.

337. Kavan, L.; Dousek, F. P.; Micka, K., Time-Dependent Electrical Resistivity of Carbon. *Journal of Physical Chemistry* **1990,** 94 (12), 5127-5134.

338. Reichardt, C., *Solvents and Solvent Effects in Organic Chemistry*. 2nd ed.; 1988.

339. Freed, B. K.; Biesecker, J.; Middleton, W. J., Spectral Polarity Index: A New Method for Determining the Relative Polarity of Solvents. *Journal of Fluorine Chemistry* **1990,** 48 (1), 63-75.

340. Sánchez, M. A.; Mainar, A. M.; Pardo, J. I.; López, M. C.; Urieta, J. S., Solubility of Nonpolar Gases in 2,2,2-trifluoroethanol and 1,1,1,3,3,3-hexafluoropropan-2-ol at Several Temperatures and 101.33 kPa Partial Pressure of Gas. *Canadian Journal of Chemistry* **2001,** 79 (10), 1460-1465.

341. Kamps, A. P.-S.; Tuma, D.; Xia, J.; Maurer, G., Solubility of CO_2 in the ionic liquid [bmim][PF_6]. *Journal of Chemical & Engineering Data* **2003,** 48 (3), 746-749.

342. Flutec, Electrical /Electronic and Automotive: Why Do They Dissolve Gases? http://www.fluoros.co.uk/a4D3230q/gasexpl.htm (August 13th 2002).

343. Flutec, Electrical /Electronic and Automotive: Excellent Solvents for Gases. http://www.fluoros.co.uk/a4D3230q/gassolub.htm (August 13th 2002).

344. Sargent, J. W.; Seffl, R. J., Properties of Perfluorinated Liquids. *Federation Proceedings* **1970,** 29 (5), 1699-1703.

345. Wesseler, E. P.; Iltis, R.; Clark, L. C., Jr., The Solubility of Oxygen in Highly Fluorinated Liquids. *Journal of Fluorine Chemistry* **1977,** 9 (2), 137-146.

346. Slinn, D. S. L.; Green, S. W., In *Preparation, Properties, and Industrial Applications of Organofluorine Compounds*, Banks, R. E., Ed. Ellis Horwood: Chichester, 1982; p 45.

347. Fowler, R. D.; Burford, W. B., III; Hamilton, J. M., Jr.; Sweet, R. G.; Weber, C. E.; Kasper, J. S.; Litant, I., Synthesis of fluorocarbons. *Journal of Industrial and Engineering Chemistry (Washington, DC)* **1947,** 39, 292-298.

348. Stacey, M.; Sharpe, A. G.; Tatlow, J. C.; Editors, *Advances in Fluorine Chemistry, Vol. 1*. 1960.

349. Stacey, M.; Tatlow, J. C., Exhaustive Fluorinations of Organic Compounds with High-Valency Metallic Fluorides. *Advances in Fluorine Chemistry (M. Stacey, J. C. Tatlow, and A. G. Sharpe, Editors. Academic Press Inc.)* **1960,** 1, 166-198.

350. Pearson, S. F.; Brown, J., Development of a substitute for R-502. *Actes Congrés International du Froid, 18eme* **1991,** 2, 903-909.

351. James, D. R.; Christophorou, L. G.; Pai, R. Y.; Pace, M. O.; Mathis, R. A.; Sauers, I.; Chan, C. C., Dielectric strengths of new gases and gas mixtures. *Gaseous Dielectrics, Proceedings of the International Symposium* **1978,** (CONF-780301), 224-257.

352. Simons, J. H., *Fluorine chemistry*. Academic Press: New York, 1964.

353. Nimitz, J. S.; Tapscott, R. E.; Skaggs, S. R., *Proceedings 1991 International CFC and Halon Alternatives Conference* **1991**.

354. Sianesi, D.; Marchionni, G.; De Pasquale, R. J., Perfluoropolyethers (PFPEs) from Perfluoroolefin Photooxidation. In *Organofluorine Chemistry: Principles and Commercial Applications*, Banks, R. E.; Smart, B. E.; Tatlow, J. C., Eds. Plenum Press: New York, 1994; Vol. Chap. 20, pp 431-461.